ORNL-5104

Cy 1

Mechanical Properties Test Data for Structural Materials Quarterly Progress Report for Period Ending January 31, 1975

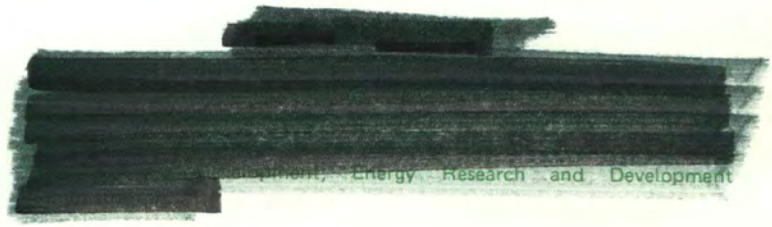

OAK RIDGE NATIONAL LABORATORY
OPERATED BY UNION CARBIDE CORPORATION • FOR THE U.S. ATOMIC ENERGY COMMISSION

Printed in the United States of America. Available from
the Energy Research and Development Administration,
Technical Information Center
P.O. Box 62, Oak Ridge, Tennessee 37830
Price: Printed Copy $10.60 ; Microfiche $2.25

ORNL-5104
UC-79b, -h, -k
(Liquid Metal Fast
Breeder Reactors)

Contract No. W-7405-eng-26

METALS AND CERAMICS DIVISION

MECHANICAL PROPERTIES TEST DATA FOR STRUCTURAL MATERIALS QUARTERLY PROGRESS REPORT FOR PERIOD ENDING JANUARY 31, 1975

Aerojet Nuclear Company

Argonne National Laboratory

Hanford Engineering Development Laboratory

Naval Research Laboratory

Oak Ridge National Laboratory

Westinghouse Advanced Reactors Division

University of Cincinnati

University of California at Los Angeles

General Electric Company

Compiled by M. R. Hill

MARCH 1975

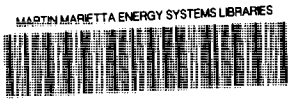

OAK RIDGE NATIONAL LABORATORY
Oak Ridge, Tennessee 37830
operated by
UNION CARBIDE CORPORATION
for the
ENERGY RESEARCH AND DEVELOPMENT ADMINISTRATION

FOREWORD

This is the sixth in a series of progress reports, the purpose of which is to record and distribute quarterly the collected results of all structural materials mechanical properties test programs sponsored by the Reactor Research and Development Division of the USAEC.

To be useful as resource documents, the reports in this series must be published and distributed in a timely manner to those in the reactor design and materials technology community who have a need of mechanical property test data for nuclear reactor and power plant applications. A test and material index is included to increase the effectiveness of the report.

Reports previously issued in this series are as follows: ORNL-4936, period ending October 31, 1973; ORNL-4948, period ending January 31, 1974; ORNL-4963, period ending April 30, 1974; ORNL-4998, period ending July 31, 1974, and ORNL-5103, period ending October 31, 1974. The next quarterly report will be for the period ending April 30, 1975, and contributions are due at ORNL by May 15, 1975.

W. R. Martin
Metals and Ceramics Division
Oak Ridge National Laboratory

CONTENTS

SUMMARY

1. AEROJET NUCLEAR COMPANY

No contribution for this report. During past quarter, ANC has concentrated its Fatigue Program on irradiated specimens and this work has been reported through the HEDL reports.

The Inconel 718 Program activity for the quarter, has involved heat treatment optimization tests to investigate process history and vendor variability effects.

This type of scoping activity has not yielded sufficient reportable data for the current report.

2. ARGONNE NATIONAL LABORATORY

Some considerations involved in the application of strain-range partitioning to the prediction of low-cycle fatigue life for Type 304 stainless steel were discussed in a previous report. These considerations are taken into account in the present report, and strain-range partitioning is used to predict fatigue lives for 20 tension-hold-time tests on Type 304 stainless steel at 593°C. The results indicate that better data correlation is obtained when the inelastic strain associated with an experimentally observed strain-rate-dependent load drop is interpreted as plasticity rather than creep. In addition, a given $\Delta\varepsilon_{cp}$ strain range accumulated in cyclic relaxation appears to be more damaging than when accumulated in cyclic creep.

The low-cycle fatigue behavior of Type 304 stainless steel (Heat 9T2796) has been studied at 593°C (1100°F) from crack-initiation and crack-propagation viewpoints. The fatigue tests were performed on smooth hourglass specimens in air at a strain rate of 4×10^{-3} sec^{-1} and total strain ranges between 0.5 and 2.0%. The crack-initiation-life data obtained from fatigue-striation-spacing measurements and a phenomenological description of fatigue life in terms of crack initiation and crack propagation are presented. With a decrease in total strain range from 2.0 to 0.5%, the percent of life spent in crack initiation increases from 50 to 90%. A quantitative relation for estimating the fraction of life to crack initiation from fatigue life is described.

The low-cycle fatigue properties determined for four heats of Type 304 stainless steel at 593°C (1100°F) and a total strain range of 1% are presented. The tests were performed at cyclic strain rates of 4×10^{-3} sec^{-1} and 4×10^{-5} sec^{-1} without hold times and with tension hold times. The results show that the three heats of steel (Heats 544, 845, and 807) have approximately the same fatigue strength for a specific loading condition, which is in contrast to their widely different creep behavior under uniaxial creep conditions. The fatigue life decreases with more and more contribution of damage accumulation by creep, as expected. The

three heats of material are superior in fatigue strength to that of Heat 796 (reference heat). The improvement in the fatigue behavior of the three heats of steel compared with that of the reference heat of steel is most marked for the cyclic-loading condition used where the damage accumulation by creep is maximum.

The design and analysis of a biaxial tubular fatigue specimen subjected to axial loading and internal pressure are presented. The proposed specimen is shown to be adequate for biaxial low-cycle fatigue and creep testing.

Uniaxial creep-rupture tests are being conducted on Type 304 stainless steel upon exposure to flowing sodium of controlled, nonmetallic element concentrations. The results at 700°C indicate that, for a given sodium-exposure condition, the creep-rupture life increases, whereas the minimum creep rate decreases as the applied stress decreases. The results also indicate that the minimum creep rate increases, whereas the creep-rupture life decreases as the sodium-exposure period increases.

3. HANFORD ENGINEERING DEVELOPMENT LABORATORY

Creep curves obtained from a single specimen of 20% cold worked Type 316 stainless steel tested at 20,000 psi over a series of progressively higher temperatures (850, 1000, 1100°F) show that creep strain increases with increasing temperature. The introduction of only 0.06% creep strain during the 850 and 1000°F loadings appears to significantly affect the creep response at 1100°F. A simple strain hardening rule does not fully account for the effect of prior strain history. Creep response after unloading exhibits measurable strain recovery at all temperatures and is consistent with an anelastic component in the total creep deformation. The magnitude of recovered strain is of the order of 0.02% at both 1000 and 1100°F. To a first approximation, creep response after reloading is consistent with the re-introduction of anelastic strain recovered during the prior unload and the continue accumulation of creep strain as if unloading had not occurred. Test results continue to demonstrate the applicability of the microwave extensometer for sensitive, precise creep strain measurements.

Analytical equations describing thermal creep deformation in pressurized tubes of 20% cold worked Type 316 stainless steel were formulated. These creep equations predict creep strain as a function of stress, time and temperature, and are experimentally verified from 825 to 1400°F for times to 2400 hours over the stress range from zero to as high as 60,000 psi.

Tensile properties of neutron irradiated FTR component structural materials Inconel 718 (to 1×10^{22} n/cm^2, E>0.1 MeV, at 760 and 1100°F), Inconel 600 (to 2.5×10^{21} n/cm^2, E>0.1 MeV, at 700°F), and A-286 (to 2.5×10^{21} n/cm^2, E>0.1 MeV, at 800°F) have been determined. The irradiated materials exhibited good strength and ductility. Irradiations of the Inconel 600 and 718 to higher fluence levels is continuing.

A simplified method of analyzing creep behavior has been used to develop a strain-time relation and an evaluation of the stress required to produce certain creep strain levels as a function of time for CRE308 (FTR Vessel Weld Metal). The technique involves expressing experimentally obtained data in the form $e_c = K^1 t^m \sigma_{tr}^n$ where e_c = creep strain, t = time, σ_{tr} = true stress and K^1, m, and n are constants. Initial indications are that this method is well suited to analysis of weld-deposited materials which often require separated evaluations for materials representing individual weldments.

The effect of several elevated temperature operating environments (e.g. air, nitrogen, liquid sodium) and vacuum on the fatigue-crack growth behavior of reactor structural materials is being determined. Materials tested to-date include annealed Type 304 stainless steel, annealed Inconel 600, and precipitation-heat-treated Inconel 718. Testing is continuing but the results to-date indicate that at elevated temperature, air is the most aggressive environment, followed by nitrogen, and that vacuum and liquid sodium are the least aggressive (most inert).

4. NAVAL RESEARCH LABORATORY

The effect of the fatigue-creep interaction was examined at 1100°F (593°C) for solution annealed and 20% cold-worked Type 316 stainless steel thermally aged at 1100°F (593°C) for 5000 hours and in the unaged condition. For the solution annealed specimens, no effect of hold time on crack growth rate was observed for the thermally aged material. It was found that thermal aging decreased the zero hold time fatigue crack growth rate at all values of ΔK when compared to results on unaged specimens. The results for the 20% cold-worked material show that a 1.0 minute hold time significantly increased the crack growth rate in unaged specimens. Thermal aging also was found to increase the fatigue crack growth rate for hold times of zero and 1.0 minutes when compared with unaged zero hold time results. However, the magnitude of the increase for the aged material at all hold times was considerably less than that produced by a 1.0 minute hold time in the unaged material.

The results show that cyclic rather than static loading was responsible for the crack growth in the thermally aged, solution annealed Type 316 stainless steel. For the 20% cold-worked material, however, the results suggest that the static loading contributed to the fatigue crack growth in both the thermally aged and unaged specimens.

5. OAK RIDGE NATIONAL LABORATORY

Elevated-temperature creep testing of the ORNL reference heat of type 304 stainless steel is continuing, and data have been updated. Some tests have exceeded 18,600 hr. The changes in 10^3-, 10^4-, and 10^5-hr creep-rupture strength due to temperature have been related to the ultimate tensile strength at the creep test temperature.

Data from uniaxial tensile tests following periods of creep on the reference heat of type 304 stainless steel have been examined in terms of prior creep strain and life fraction incurred during prior creep. Increasing prior creep strain decreased the true ultimate tensile strength and uniform elongation in the range 482 to 649°C (900–1200°F). The decrease in residual tensile uniform elongation with increasing creep life fraction was more drastic than the corresponding change in the relative residual ultimate tensile strength.

Ten long-term (50,000 hr) creep tests are in progress on nine different heats of type 304 stainless steel. Two tests ruptured during this quarter after 19,180 and 25,823 hr. The heat-to-heat variation for 20 heats of type 304 stainless steel was presented for several test temperatures and for test times approaching 25,000 hr. The heat-to-heat variation in creep rupture strength was related to the corresponding variation in ultimate tensile strength at the creep test temperature. The variation in ultimate tensile strength has been expressed in terms of the carbon plus nitrogen content and the grain size.

In the Heat-to-Heat Variation Program of type 316 stainless steel a large anisotropy was observed in the creep properties of 0.5-in.-thick (12.7-mm) plates of two heats in the as-received condition. The transverse specimens were 2–3 times stronger than the longitudinal. The heat-to-heat variation observed in creep-rupture strength was related to the corresponding variation in ultimate tensile strength at the creep test temperature. The variation in the ultimate tensile strength was expressed in terms of carbon plus nitrogen and grain size.

Tensile and creep properties were presented for nine heats of type 304 stainless steel, aged for various times up to 10,000 hr at 482, 593, and 649°C (900,1100, and 1200°F). Some results are also presented for the effect of aging under stress on uniform elongation at 593°C (1100°F). The effect of carbon for fixed nitrogen and of nitrogen for fixed carbon on uniform elongation in both unaged and aged conditions has been examined.

Thermal aging under stress produced a more deleterious effect on uniform elongation than plain thermal aging. Increasing nitrogen content decreased the elevated temperature uniform elongation in both the unaged and aged conditions. The reduction in elevated-temperature ductility for the same aging conditions was much greater for type 316 than for type 304 stainless steel.

Thermal aging of one heat of type 304 stainless steel increased the minimum creep rate, decreased the time to rupture, and increased elongation at rupture. Thermal aging produced a transition from intergranular to twin boundary cracking.

Tensile results are presented on four heats of type 316 stainless steel aged for various times up to 4000 hr at 482, 593, and 649°C (900, 1100, and 1200°F). Thermal aging produced only small changes in 0.2% yield and ultimate tensile strength. The elevated-temperature ductility, measured as uniform elongation, total elongation, and reduction of area, was greatly reduced by thermal aging. The uniform elongation for two of the four heats investigated was decreased by aging at 649°C (1200°F) for 4000 hr so as to fall below the minimum expected value curve from the *Nuclear Systems Materials Handbook*.

The limited data on effect of aging on creep properties have been presented and compared with those reported in the literature.

Various failure criteria have been analyzed by use of creep and creep rupture data for several heats of type 304 stainless steel. Rupture life, time to tertiary creep, rupture strength, and various strain limits have been examined by correlation and extrapolation techniques based on standard time-temperature parameters and the minimum commitment method.

Procurement of the reference heat of type 316 stainless is nearing completion.

The operation and expansion of a computerized system for the management of mechanical properties data are continuing. This system includes the Automatic Data Acquisition System (ADAS), the Data Storage and Retrieval System (DSRS), and the Structural Materials Information Center (SMIC).

Two goals of the welding development program at ORNL are developing commercial sources of austenitic welding materials that are ductile under high-temperature creep conditions, and obtaining design data for welds that will be useful in the engineering design codes. In the first task area, SMA type 308 stainless steel test welds with controlled residual elements (CRE) have been made with electrodes supplied by three commercial sources and evaluated by metallography and creep testing at 650°C (1202°F); welds made with electrodes from a fourth source remain to be evaluated. The available results indicate improved strength and ductility for the CRE weld metal from all sources compared with data for welds made with conventional electrodes. In the second task area, the creep-rupture behavior of type 308 CRE weld metal transverse specimens and weldment specimens have been evaluated at 593°C (1100°F) and compared with both longitudinal weld metal and base metal properties. Substantial differences are noted. Strain gage tensile test data for a whole-weld cross section that was strained primarily in the elastic range are presented and evaluated.

High-strain-rate tensile tests were conducted on annealed 2 1/4 Cr-1 Mo steel. Tests were made at 0.16, 1.6, 16, and 144/sec and 25, 454, 510, and 566°C. There was a large increase in strength at room temperature, but only minor changes occurred at the elevated temperatures.

Tensile tests over the range 25 to 566°C were made on specimens taken from three 2 1/4 Cr-1 Mo steel forgings — two produced by the VAR process, one by ESR. Only minor differences in strength and ductility were noted, and the properties were quite typical of annealed commercial material.

Carbides were electrolytically extracted from annealed 2 1/4 Cr-1 Mo steel specimens as annealed, after aging for 26,500 hr at 566°C, and after exposure to sodium (decarburized) for 26,500 hr at 566°C; the carbides were identified by x-ray diffraction. From the before-test material, 1.4% carbide was obtained; this carbide contained M_3C, $M_{23}C_6$, and M_6C, with $M_{23}C_6$ constituting the major portion. In the aged specimen, 2.3 wt % precipitate was extracted, with 60% M_6C, the balance $M_{23}C_6$. The first 20% of the 0.06-in.-thick sodium-decarburized specimen yielded 1.3 wt % precipitate, which contained 94% M_6C, the balance $M_{23}C_6$. The interior of the specimen contained 1.6% carbide, with 86% of it being M_6C.

Recent test results are reported from a test program designed to characterize the fatigue behavior of 2 1/4 Cr-1 Mo steel for steam generator applications. Test results include data obtained in both load and strain control in fully reversed cyclic loading. Comparisons are made between recently obtained data and test results obtained from other sources. Proposed continuous cycle design curves (ASME) were formulated, and equations expressing strain range as a function of design cycles to failure were developed covering material behavior from room temperature to 593°C (1100°F).

Correlations of mechanical properties of 2 1/4 Cr-1 Mo steel in support of the *Nuclear Systems Materials Handbook* are continuing. Time to tertiary creep, true fracture stress, diamond pyramid hardness, Charpy impact energy, and ductile-brittle transition temperature have been investigated.

Creep-rupture studies on variously oriented specimens from a type 304 stainless steel forging with type 308 overlay were extended to 538°C (1000°F).

Results from the creep-rupture tests series on the 1-in. (25-mm) plate of the reference heat of type 304 stainless steel (heat 9T2796) are summarized on a strain component basis by use of stress-strain diagrams. The sum of the loading, transient, and linear strain components is dominated by the loading strain at 482°C (900°F) and by the linear component at 704°C (1300°F) and above.

An approach is presented that shows potential for representing the stress-strain hysteresis loop for type 304 stainless steel. This is based on a combination of a modified Voce equation for representing the cyclic hardening behavior and a Ludwigson-type term for representing the dependence of the flow stress within the hysteresis loop.

Constant-load uniaxial, step-load uniaxial, interrupted uniaxial, and multiaxial creep results on type 304 stainless steel heat 9T2796 5/8-in. (16-mm) bar are updated and discussed. Data are presented graphically and tabularly.

Tensile testing of HTGR structural alloys has continued, including the completion of tests on three heats of 2 1/4 Cr-1 Mo steel and one heat of Hastelloy X. Five creep frames are currently available for testing materials in simulated gas-cooled reactor helium. Subcritical crack growth rate studies are in progress on 2 1/4 Cr-1 Mo steel in air and steam, and work is continuing to allow crack growth and fatigue-life testing in helium.

6. WESTINGHOUSE ADVANCED REACTORS DIVISION

Creep testing of bar- and plate-type specimens was continued using material from the ORNL Type 304 stainless steel reference heat (9T2796). A notched bar test is continuing after having exceeded about twice the expected rupture life of an unnotched specimen. Similar results are reported for a notched bar weld test. Results are also reported for an eccentrically loaded plate specimen and an axial weld specimen.

Creep testing of tubular specimens for the ORNL Type 304 stainless steel reference heat (9T2796) continued, and tests were planned to evaluate the effects of prior creep damage using previously tested specimens.

7. UNIVERSITIES

UNIVERSITY OF CINCINNATI

Work is continuing on the analysis of the creep and tensile test results and on the corresponding substructure characteristics of AISI 304 stainless steel (Reference Heat No. 9T2796). These specimens were tested at temperatures ranging from 538 to 704°C and strain rates from 1.22×10^{-7} sec^{-1} to 8.33×10^{-2} sec^{-1}. Preliminary TEM observations suggest that the microstructure of the specimens tested at the very high strain rates is sufficiently different than those observed in the specimens tested at the lower strain rates and that this microstructural behavior may account for the fact that the apparent stress levels are slightly lower than expected at the very high strain rates.

A family of creep tests have been performed on 304 stainless steel in which the tests have been terminated at different strain levels. Subsequent TEM will be performed to help develop a better understanding of the microstructure changes as a function of the creep strain.

The deformation substructure of Incoloy 800 specimens tested in the low cycle fatigue mode at 760°C suggests that the subgrain size varies inversely with the 2.8 power of the saturation stress level. These results are in reasonable agreement with similar studies on the low cycle fatigue behavior of 316 stainless steel and much different than the relationship established between the subgrain size and the applied stress for the case of undirectional tensile and creep tests.

The misorientation angle between subgrains in the LCF of Incoloy 800 is found to be relatively insensitive to the subgrain diameter, a circumstance which is believed to be consistent with the fact that all specimens evaluated were those which have been tested in fatigue to failure where presumably a saturation misorientation angle (related to the saturation stress level) has been reached in the early part of the fatigue life.

A family of tests have been initiated to study the development of the microstructure of 304 stainless steel tested in the fatigue mode at 650°C. Preliminary observations suggest that the cells are completely formed after a number of cycles equivalent to about 1% of the fatigue life is reached. Cell misorienation continues to increase to some saturation level following a few more cycles of test time.

UNIVERSITY OF CALIFORNIA, LOS ANGELES — (No report.)

8. GENERAL ELECTRIC COMPANY

Preparations are under way for mechanical testing of type 316 stainless steel in carburizing sodium. Chemical and tensile characterization are given for annealed material procured for tubular creep and creep fatigue tests and fracture mechanics bend tests. A test matrix is presented for an impending program of cyclic creep testing of 2 1/4 Cr-1 Mo steel in gettered sodium at 510°C (950°F).

1. AEROJET NUCLEAR COMPANY

W. C. Francis

Aerojet Nuclear Company has no contribution to make to this report. During the past quarter, ANC has concentrated its Fatigue Program on irradiated specimens, and this work has been reported through the HEDL reports.

The Inconel 718 Program activity for the quarter has involved heat treatment optimization tests to investigate process history and vendor variability effects.

This type of scoping activity has not yielded sufficient reportable data for the current reporting period.

2. ARGONNE NATIONAL LABORATORY

R. W. Weeks

2.1 INTRODUCTION

Argonne National Laboratory (ANL) is conducting an extensive program to provide low-cycle, high-temperature fatigue data on Types 304 and 316 stainless steel and to characterize the effects of a sodium environment on the creep and fatigue properties of these materials. The overall program is in support of LMFBR component design. The present report describes (a) the results of a strain-range-partitioning analysis of selected tension-hold-time fatigue data, (b) a study of crack initiation and propagation in low-cycle fatigue, (c) the variations in fatigue life observed among four heats of material, (d) the results of a stress analysis of a proposed biaxial fatigue-specimen design, and (e) the data on the influence of sodium exposure on the uniaxial creep-rupture properties of Type 304 stainless steel.

2.2 FRACTURE AND FATIGUE STUDIES ON STAINLESS STEELS -- D. R. Diercks, P. S. Maiya, and S. Majumdar

2.2.1 Strain-range-partitioning Analysis of Tension-hold-time Data for Type 304 Stainless Steel -- D. R. Diercks

Some considerations involved in the application of strain-range partitioning to the prediction of low-cycle fatigue life for Type 304 stainless steel were discussed in a previous report.[1] A basic difficulty was encountered in partitioning the inelastic strain range for tension-hold-time tests at elevated temperatures. This difficulty was related to the load drop that was observed to accompany an abrupt change in plastic strain rate. The author suggested that the inelastic strain associated with this load drop (hereinafter referred to as "mixed" strain, ε_m) be interpreted as a c strain rather than a p strain. In addition, a testing mode was suggested whereby unambiguous strain range versus fatigue-life data could be generated. The present report describes the results obtained when strain-range partitioning is used to

predict fatigue lives for 20 tension-hold-time tests on Type 304 stainless steel at 593°C (Table 2.1), taking the above considerations into account.

Before the results of the analysis are reported, however, the procedure used for calculating the fatigue lives should be discussed further. All data analyzed were generated with a strain rate of 4×10^{-3} sec^{-1} during the cycling between hold times. However, continuous cycling data generated at ANL indicate longer fatigue lives at a total strain rate of 4×10^{-2} sec^{-1} than at 4×10^{-3} sec^{-1} (see pp curves of Fig. 2.1). In terms of strain-range partitioning, this means that the 4×10^{-3} sec^{-1} strain rate is not fast enough to eliminate all creep effects, and some cc strain ε_{cc} is accumulated while cycling at this strain rate. Using a linear summation-of-damage approximation, the resultant damage D_{cc} may be expressed as

$$D_{cc} = 1 - N^*/N_{pp}. \tag{1}$$

Here, N* is the number of cycles to failure under pure cyclic conditions at 4×10^{-3} sec^{-1}, evaluated at the inelastic strain range $\Delta\varepsilon_{inel}$ (since $\Delta\varepsilon_{inel} \approx \Delta\varepsilon_{pp}$), and N_{pp} is the number of cycles to failure for the same inelastic strain range at 4×10^{-2} sec^{-1}. (It is assumed that no cc damage is incurred at 4×10^{-2} sec^{-1}.) For a tension-hold-time test at 4×10^{-3} sec^{-1}, the pp, cp, and cc damage components are present, and one has at failure

$$D_{pp} + D_{cp} + D_{cc} = 1. \tag{2}$$

Combining Eqs. (1) and (2), one obtains

$$D_{pp} + D_{cp} = N^*/N_{pp}. \tag{3}$$

The interaction damage rule originally proposed by Manson[2] was used to calculate cyclic lives under conditions of combined strain.

Table 2.1. Cyclic Relaxation Data for Type 304 Stainless Steel. The test temperature is 593°C (1100°F), and the total strain rate during cycling is 4×10^{-3} sec^{-1}

Test Number	Tension Hold Time, min	Total Strain Range	$\Delta\varepsilon_{inel}$	$\Delta\varepsilon_{pp}$[a]	$\Delta\varepsilon_{cp}$	$\Delta\varepsilon_{m}$	N_f	Time to Failure, min
198	1	0.00501	0.00280	0.00262	0.00003	0.00015	10,441	10,607
135	1	0.00997	0.00698	0.00674	0.00004	0.00020	1,664	1,730
176	1	0.01011	0.00731	0.00710	0.00004	0.00017	1,328	1,437
401	1	0.00995	0.00676	0.00652	0.00004	0.00020	1,235	1,285
543	1	0.02048	0.01677	0.01641	0.00015	0.00021	378	440
154	10	0.00503	0.00285	0.00276	0.00003	0.00006	3,803	38,107
189	10	0.01005	0.00735	0.00700	0.00010	0.00025	553	5,563
150	10	0.01011	0.00739	0.00711	0.00007	0.00021	636	6,378
442	10	0.01243	0.00957	0.00925	0.00011	0.00021	656	6,642
416	15	0.00595	0.00381	0.00361	0.00005	0.00015	2,765	41,671
418	15	0.01004	0.00748	0.00713	0.00008	0.00027	666	10,030
412	15	0.02004	0.01659	0.01603	0.00025	0.00031	237	3,579
579	60	0.00551	0.00350	0.00332	0.00009	0.00009	1,253	75,140
152	60	0.00987	0.00738	0.00702	0.00017	0.00019	338	20,234
463	60	0.01984	0.01666	0.01615	0.00031	0.00020	112	6,677
443	180	0.00594	0.00399	0.00380	0.00009	0.00010	1,284	230,971
512	180	0.00621	0.00418	0.00392	0.00010	0.00016	1,251	223,795
509	180	0.01020	0.00757	0.00719	0.00022	0.00016	170	29,976
510	180	0.02024	0.01744	0.01675	0.00048	0.00021	63	10,990
528	600	0.01034	0.00856	0.00815	0.00028	0.00013	212	125,675

[a]Value includes any cc strain that may occur during cycling.

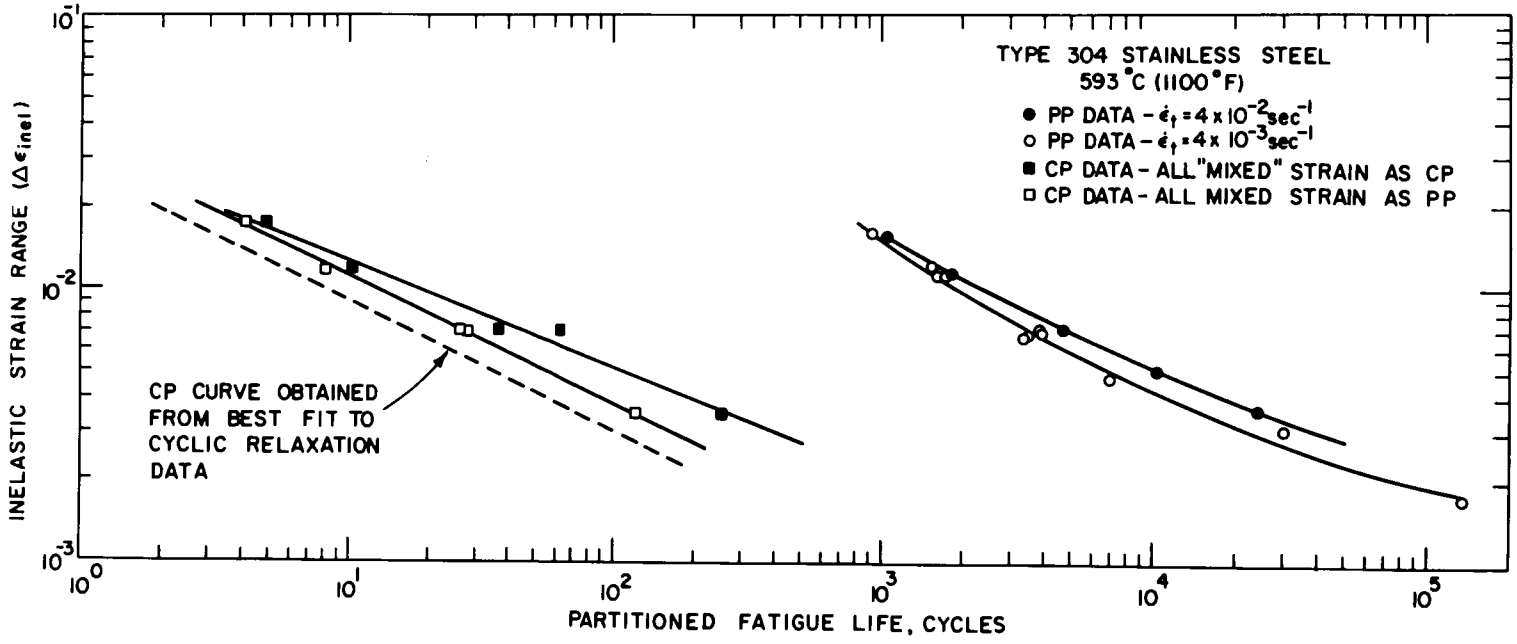

Fig. 2.1. Inelastic Strain Range vs Partitioned Fatigue-life Curves Obtained for the $\Delta\varepsilon_{pp}$ and $\Delta\varepsilon_{cp}$ Strain-range Components.

In this damage rule, the damage fraction D_{cp} due to cp strain is given by

$$D_{cp} = F_{cp} \frac{N_f}{N_{cp}} , \tag{4}$$

where F_{cp} is the cp fraction of the inelastic strain range, and N_f is the experimental (or predicted) cyclic life. The definition of the pp damage fraction D_{pp} is completely analogous. Substituting these definitions of damage into the failure criterion of Eq. (3), we obtain

$$F_{pp} \left(\frac{N_f}{N_{pp}} \right) + F_{cp} \left(\frac{N_f}{N_{cp}} \right) = \frac{N^*(\Delta\varepsilon_{pp})}{N_{pp}(\Delta\varepsilon_{pp})} . \tag{5}$$

The quantities N* and N_{pp} on the right-hand side of the equation are evaluated at the $\Delta\varepsilon_{pp}$ strain range, since they correct for the cc strain that takes place during the nominal pp cycling. The quantities N_{pp} and N_{cp} on the left-hand side of the equation are evaluated at the inelastic strain range, in accordance with the requirements of the interaction damage rule.

The data from which the $\Delta\varepsilon_{inel}$ versus N_{cp} relationships were experimentally determined are presented in Table 2.2. (The "modified cyclic creep" waveform used to generate these data is described in Ref. 1.) Equation (5) was solved for N_{cp}, and the resultant relation was used to compute N_{cp} values from the data in Table 2.2. The N* and N_{pp} values were determined from the appropriate curves in Fig. 2.1. The N_{cp} values obtained, assuming $\Delta\varepsilon_m$ and $\Delta\varepsilon_{cp}$ to be equivalent, are plotted versus the inelastic strain range as the solid squares in Fig. 2.1. If $\Delta\varepsilon_m$ and $\Delta\varepsilon_{pp}$ are taken to be equivalent, the open squares in Fig. 2.1 are obtained. The best-fit lines through the two sets of points differ significantly, with the open squares showing noticeably less scatter. The equations for both N_{cp} curves are given in Table 2.3.

Table 2.2. Modified Cyclic Creep Data Used to Experimentally Determine the N_{cp} Partitioned Life. The test temperature is 593°C (1100°F), and the total strain rate during cycling is 4×10^{-3} sec^{-1} in all cases

Test Number	Total Strain Range	$\Delta\varepsilon_{inel}$	$\Delta\varepsilon_{pp}$ [a]	$\Delta\varepsilon_{cp}$	$\Delta\varepsilon_{m}$	N_f	Time to Failure, min
634	0.00597	0.00352	0.00331	0.00010	0.00011	2,176	75,782
575	0.00986	0.00702	0.00679	0.00010	0.00013	1,055	3,613
553	0.00982	0.00708	0.00684	0.00017	0.00007	685	7,366
569	0.01471	0.01186	0.01126	0.00048	0.00012	166	8,512
580	0.01988	0.01746	0.01627	0.00101	0.00018	73	7,457

[a] Value includes any cc strain that may occur during cycling.

Table 2.3. Equations for the Various N_{pp} and N_{cp} Partitioned Life Relationships Obtained in Study

A. $\Delta\varepsilon_{pp}$ versus N_{pp} Relationships

$\dot{\varepsilon}_t = 4 \times 10^{-2}$ sec^{-1}

$$\log_e \Delta\varepsilon_{pp} = 1.163 - 0.979 \cdot \log_e N_{pp} + 0.0305 \cdot (\log_e N_{pp})^2$$
$$\text{or } \log_e N_{pp} = 16.0444 - (219.2958 + 32.7858 \cdot \log_e \Delta\varepsilon_{pp})^{1/2}$$

$\dot{\varepsilon}_t = 4 \times 10^{-3}$ sec^{-1}

$$\log_e \Delta\varepsilon_{pp} = 2.464 - 1.268 \cdot \log_e N_{pp} + 0.0444 \cdot (\log_e N_{pp})^2$$
$$\text{or } \log_e N_{pp} = 14.2859 - (148.5878 + 22.5288 \cdot \log_e \Delta\varepsilon_{pp})^{1/2}$$

B. $\Delta\varepsilon_{cp}$ versus N_{cp} Relationships ($\Delta\varepsilon_{cp} = A \cdot N_{cp}^{B}$)

Interpretation of $\Delta\varepsilon_m$	Strain Rate for $\Delta\varepsilon_{pp}$ Data	A	B	Standard Deviation	rms Scatter Factor
$\Delta\varepsilon_{cp}$ relationships experimentally determined from modified cylic creep data					
cp	4×10^{-2}	0.0292	-0.387	0.565	1.76
pp	4×10^{-2}	0.0255	-0.467	0.502	1.65
$\Delta\varepsilon_{cp}$ relationships obtained from best fit to cyclic-relaxation data					
cp	4×10^{-2}	0.0339	-0.408	0.561	1.75
pp	4×10^{-2}	0.0267	-0.475	0.329	1.39
cp	4×10^{-3}	0.0371	-0.471	0.560	1.75
pp	4×10^{-3}	0.0285	-0.561	0.327	1.39

Equation (5) can now be used to compute predicted cyclic lives N_f for the data of Table 2.1, using the calibration curves of Fig. 2.1. Let us first consider the case for which the $\Delta\varepsilon_m$ and $\Delta\varepsilon_{cp}$ strain ranges are taken to be equivalent. The calculated cyclic lives thus obtained are plotted versus experimental life in Fig. 2.2. Agreement between the two is fair, with a distribution of $\log_e(N_{calc})$ about $\log_e(N_{exper})$ that has a standard deviation, σ, of 0.565. An "rms scatter factor" may be defined as $\exp(\sigma)$, and for the data of Fig. 2.2 this factor has a value of 1.76. It is interesting to note from Fig. 2.2 that cyclic lives are underpredicted for the five tests with a 1-min-tension hold time and overpredicted for the eight tests with 60 to 600-min hold times.

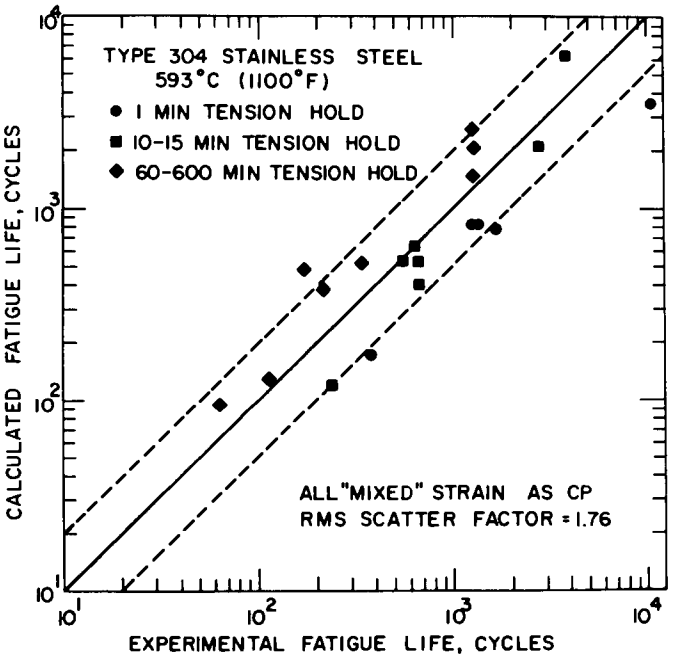

Fig. 2.2. Calculated Cyclic Life vs Experimental Life for All Mixed Strain Taken as cp. The upper cp curve of Fig. 2.1 was used to determine the partitioned lives.

For the case in which the $\Delta\varepsilon_m$ and $\Delta\varepsilon_{pp}$ strain ranges are taken to be equivalent, as this author recommends, the predicted versus

experimental life plot of Fig. 2.3 results. The standard deviation is now 0.502, and the scatter factor is 1.65. Note that the method now shows a decided tendency to overpredict cyclic lives, suggesting that the cp strain accumulated in cyclic relaxation is somehow more damaging than is indicated by the five modified cyclic creep tests of Table 2.2. Previous workers have assumed that cp strains accumulated in tensile relaxation and in tensile creep are completely equivalent insofar as damage is concerned. However, when the data of Table 2.1 were re-analyzed ($\Delta\varepsilon_m$ included in $\Delta\varepsilon_{pp}$) to determine the $\Delta\varepsilon_{incl}$ versus N_{cp} relation that would minimize the error in predicted life, the dashed line of Fig. 2.1 resulted. This line falls almost parallel to, but to the left of, the N_{cp} line obtained from the five modified cyclic creep tests, indicating that the cp strain accumulated in relaxation is more damaging. When the cyclic lives, which were calculated using the dashed N_{cp} curve of Fig. 2.1, are plotted versus experimental life, Fig. 2.4 results. The standard deviation is now a 0.329, and the scatter factor is 1.39.

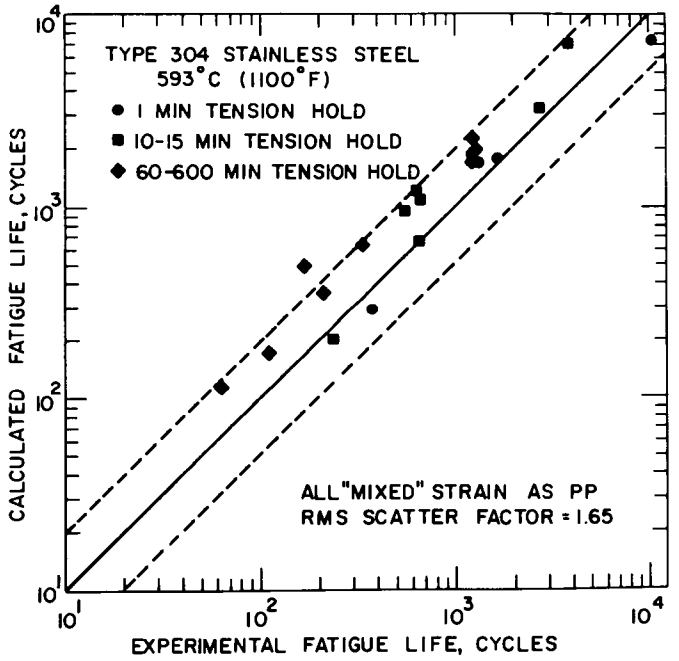

Fig. 2.3. Calculated Cyclic Life vs Experimental Life for All Mixed Strain Taken as pp. The middle cp curve of Fig. 2.1 was used to determine the partitioned lives.

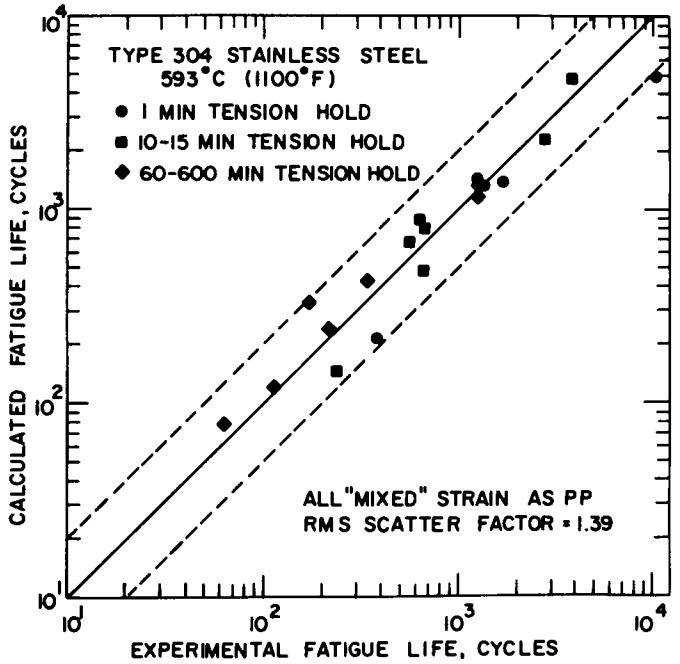

Fig. 2.4. Calculated Cyclic Life vs Experimental Life for a Best-fit Analysis of the Cyclic-relaxation Data, with All Mixed Strain Taken as pp. The analysis yielded the dashed cp curve plotted in Fig. 2.1.

As a possible explanation for the above observations, it should be noted that the strain rates during relaxation were generally less than those during creep through the same $\Delta\varepsilon_{cp}$ strain range, in some cases by an order of magnitude. The longer times spent in relaxation offer more opportunity for time-dependent phenomena, such as oxidation, to occur and thus to contribute to failure. A time-dependent contribution as well as a strain-dependent contribution to damage may thus be present.

A best-fit analysis of the data of Table 2.1 was also performed with $\Delta\varepsilon_m$ assumed to be equivalent to $\Delta\varepsilon_{cp}$. Since the resultant N_{cp} curve was found to coincide almost exactly with the curve obtained from the modified creep data (solid squares in Fig. 2.1), this curve is not shown in Fig. 2.1, but its equation is given in Table 2.3. Also, the experimental lives calculated using this N_{cp} curve are almost identical to those plotted in Fig. 2.2, and no separate plot is presented. The

standard deviation and the scatter factor are found to be 0.561 and 1.75, respectively, as compared with 0.565 and 1.76 for Fig. 2.2. No simple explanation can be offered for the coincidence of the N_{cp} curves in this case. However, the relatively poor data correlation obtained even from a best-fit analysis indicates the inappropriateness of equating the $\Delta\varepsilon_m$ and $\Delta\varepsilon_{cp}$ strain ranges.

Two other interesting results were obtained from the strain-range-partitioning analysis. First, the correction for the cc strain taking place at a strain rate of 4×10^{-3} sec^{-1} may not have been necessary. Equally good life predictions are obtained if the 4×10^{-3} sec^{-1} strain rate is assumed to produce pure pp strain. Second, the universalized functional relationship between $\Delta\varepsilon_{cp}$ and N_{cp} suggested by Manson[2] was found to differ significantly from the relationship observed here. The explanation appears to be that Manson's relationship was obtained using a linear summation-of-damage analysis, and cannot, in general, be expected to agree with relationships obtained using an interaction damage analysis, as was done here. The reader is referred to a forthcoming paper for more details.[3]

2.2.2 Considerations of Crack Initiation and Crack Propagation in Low-cycle Fatigue -- P. S. Maiya

Fatigue failure is the certain result of nucleation and growth of highly localized microcracks. In most cases, fatigue cracks initiate from the surface. Therefore, studies concerned with crack initiation (nucleation and early growth of a crack across a few grain diameters from the surface) are important, more so, if the useful life of a structural component is dictated by crack-initiation considerations. Several investigators[4-7] have indicated the importance of distinguishing between crack initiation and crack propagation from an engineering as well as a mechanistic viewpoint. Yet the majority of the low-cycle fatigue design data generated on Type 304 stainless steel and the analyses do not consider crack initiation and crack propagation separately, partly because of the difficulties associated with the crack-initiation studies. The present report will discuss the low-cycle fatigue behavior of Type

304 stainless steel (Heat 9T2796) at 593°C (1100°F) and the crack-initiation and crack-propagation aspects of fatigue life in smooth specimens.

Several hourglass-shape specimens (0.25-in. minimum diam) were solution annealed for 30 min at 1092°C (1998°F) and aged for 1000 hr at 593°C (1100°F). Following the heat treatment, the specimens were mechanically polished in the longitudinal direction to obtain smooth surfaces (surface finish $\approx$ 0.0075 μm, rms value). The resultant surface finish is much better than that of the hourglass-shape specimens that are used to obtain most of the low-cycle fatigue design data. The fatigue tests were performed in air in servocontrolled, hydraulically actuated fatigue machines in axial strain control at a strain rate of $\sim 4 \times 10^{-3}$ sec^{-1} and at total strain ranges between 0.5 and 2.0%. The fractured surfaces were examined by scanning-electron microscopy to obtain information on crack growth versus strain cycles as a function of strain range.

The low-cycle fatigue lives of the smooth specimens with a surface finish of $\approx$ 0.0075 μm are approximately the same as those obtained from specimens with a surface finish close to or better than 0.3 μm (rms value) under the axial push-pull cyclic-loading conditions.

All specimens were tested to failure (complete separation). The fractured surfaces showed fatigue striations, as observed by scanning-electron microscopy. From striation-spacing measurements, plots of crack length a versus strain cycles N for different values of strain range were constructed as shown in Fig. 2.5a and b. The trend of the results suggests that the number of cycles to initiate a crack in smooth specimens decreases markedly as the strain range increases. The same data, when plotted as ln a versus strain cycles N, yield linear relationships, as demonstrated in Fig. 2.6a and b. When the total strain range is approximately $\geq$ 2.0%, crack propagation appears to be faster than that predicted by the relation ln a proportional to N for shorter crack length ($\sim$ a <0.8 mm). The results are consistent with a similar

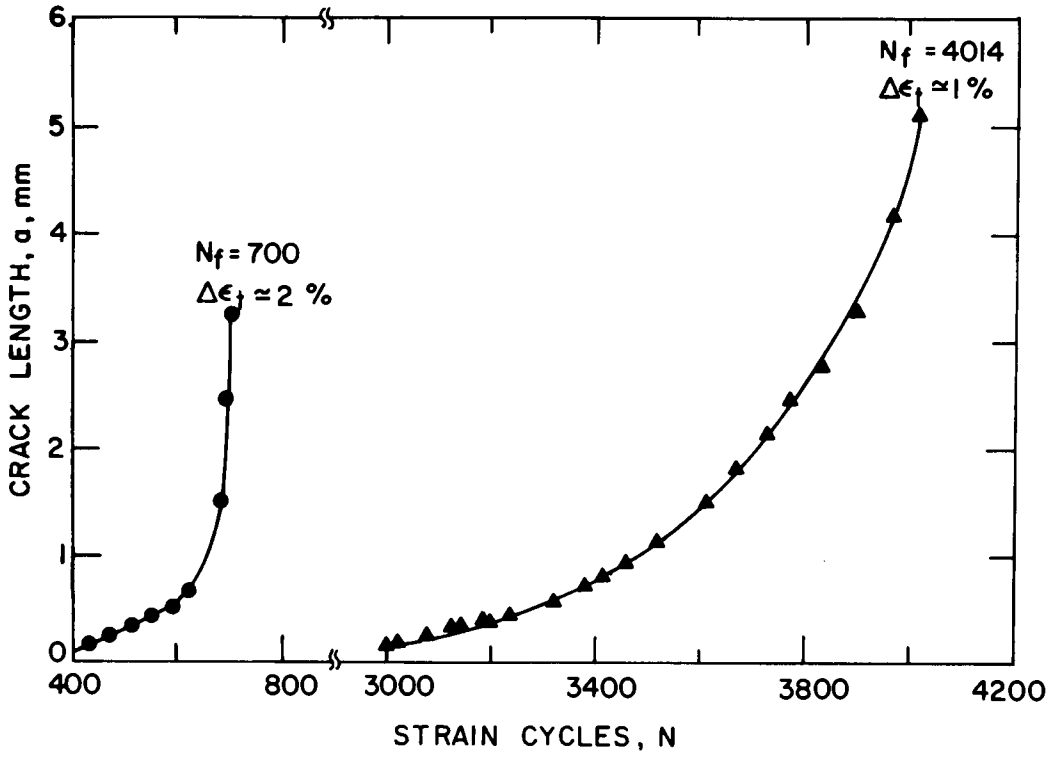

(a)

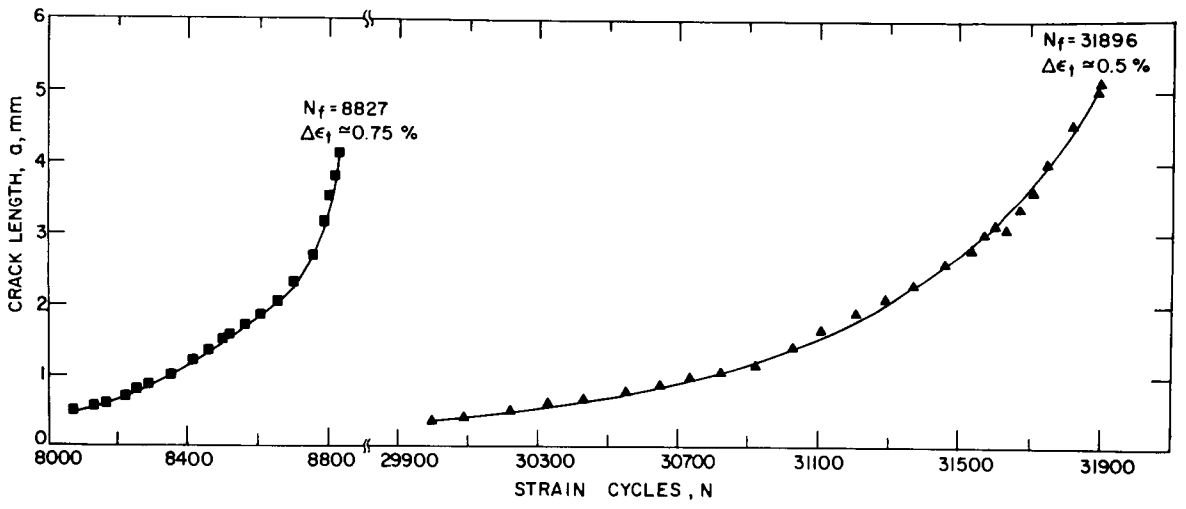

(b)

Fig. 2.5. Effect of Strain Range on Crack Initiation and Stage I and Stage II Growth in Type 304 Stainless Steel at 593°C.

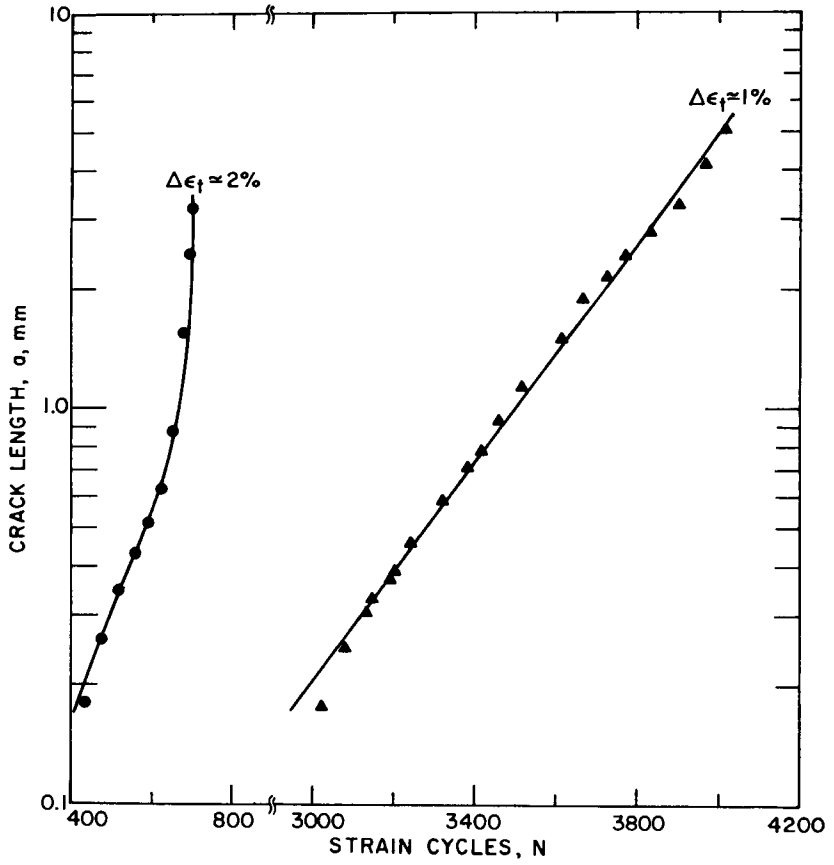

(a)

Fig. 2.6. Plots of ln a vs N for Different Plastic Strain Ranges.

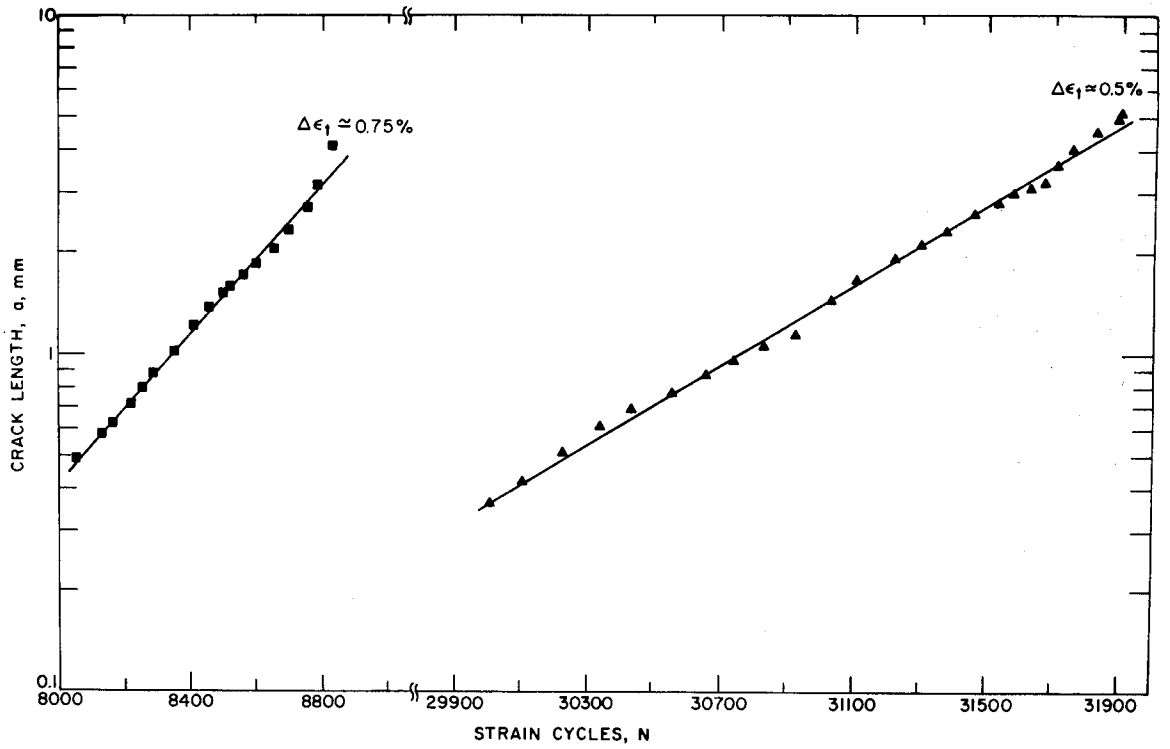

(b)

behavior observed by Solomon[8] in his crack-growth studies. This type of crack-growth behavior at large plastic strain ranges is believed to result from the formation and link-up of several microcracks ahead of the main crack.

The ln a versus N plots (Fig. 2.6a and b) have been used to determine the number of cycles N_o to initiate a crack of length a_o ($\sim$ 1 grain diam $\approx$ 0.1 mm) by extrapolation.

The fatigue life of a smooth specimen $N_f(S)$ is the sum of $N_o(S)$ and $N_p(S)$, where $N_o(S)$ is the number of cycles to initiate a crack of length 0.1 mm, and $N_p(S)$ is the number of cycles for crack propagation

$$N_f(S) = N_o(S) + N_p(S). \tag{6}$$

If one postulates Coffin-Manson law for both crack initiation and crack propagation, then

$$N_o(S) = A\ (\Delta\varepsilon_p)^{-\alpha}, \tag{7}$$

$$N_p(S) = B\ (\Delta\varepsilon_p)^{-\beta}, \tag{8}$$

and, hence,

$$N_f(S) = A\ (\Delta\varepsilon_p)^{-\alpha} + B\ (\Delta\varepsilon_p)^{-\beta}, \tag{9}$$

where A, B, α, and β are constants, and $\Delta\varepsilon_p$ is the plastic-strain range. The values of the constants A, B, α, and β, determined from the least-squares fit of the data, are 0.0122, 3.911, 2.474, and 1.103, respectively.

Fig. 2.7 shows that the fatigue life can be phenomenologically described by Eqs. (7)-(9). The description of total life in terms of crack initiation and crack propagation (Fig. 2.7) shows that the propagation component of fatigue life becomes important only when N_f is less than 300 cycles.

It is noteworthy that, although a_o has been assumed to be equal to 0.1 mm, the actual choice of a_o is not critical to the quantitative estimation of the fraction of life in crack initiation. For example, as shown in Fig. 2.8, the variation of $N_o(S)$ with $\Delta\varepsilon_p$ is not sensitive to the choice of crack lengths between 0.1 and 0.8 mm ($\sim$1-8 grain diameters) for $\Delta\varepsilon_p < 1\%$. Thus, it is clear that, at least for stainless steel, crack-initiation life can be directly determined from the ln a versus N plots. Therefore, the procedure in some cases obviates the need to extrapolate the crack-growth behavior data. However, the definition of crack-initiation life $N_o(S)$ must include crack-initiation length a_o.

It is observed that, in a smooth specimen at 593°C and total strain ranges between 0.5 and 2.0%, crack initiation occupies a significant fraction of total life. This is clear from a plot of plastic-strain

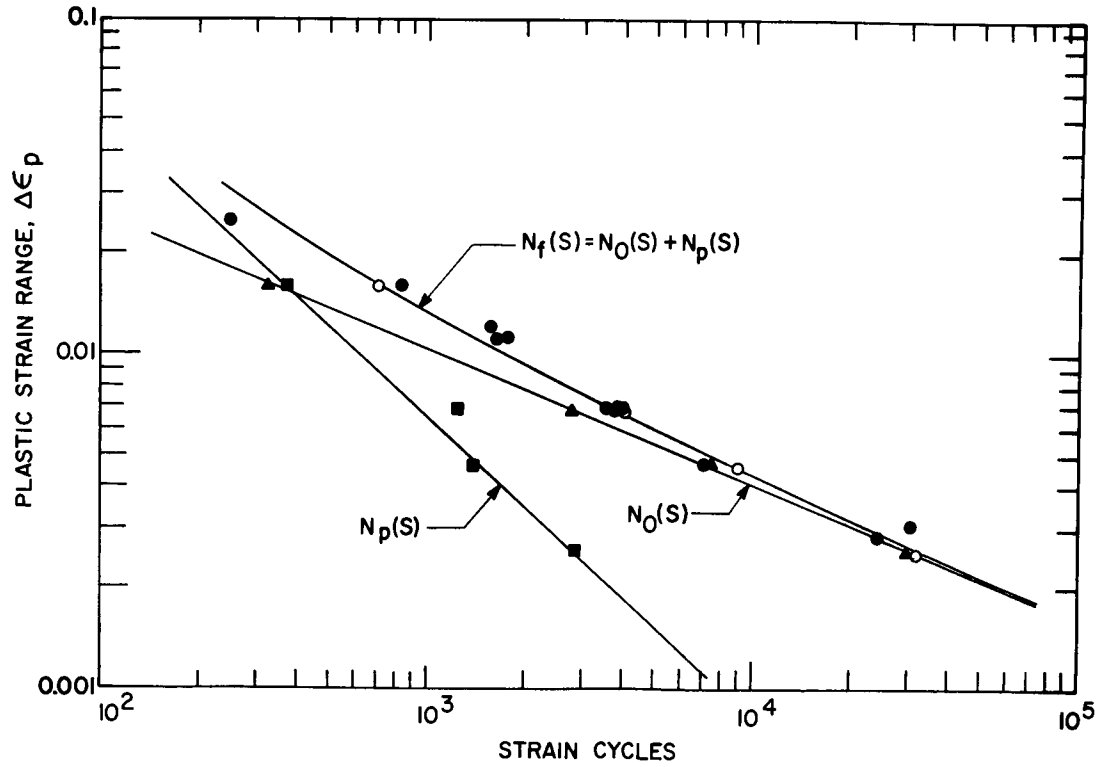

Fig. 2.7. Description of Total Fatigue Life in Terms of Crack Initiation and Crack Propagation for Type 304 Stainless Steel at 593°C. The open circles represent fatigue life of specimens with a surface finish $\approx$ 0.0075 μm and the solid circles approximately $\leq$ 0.3 μm.

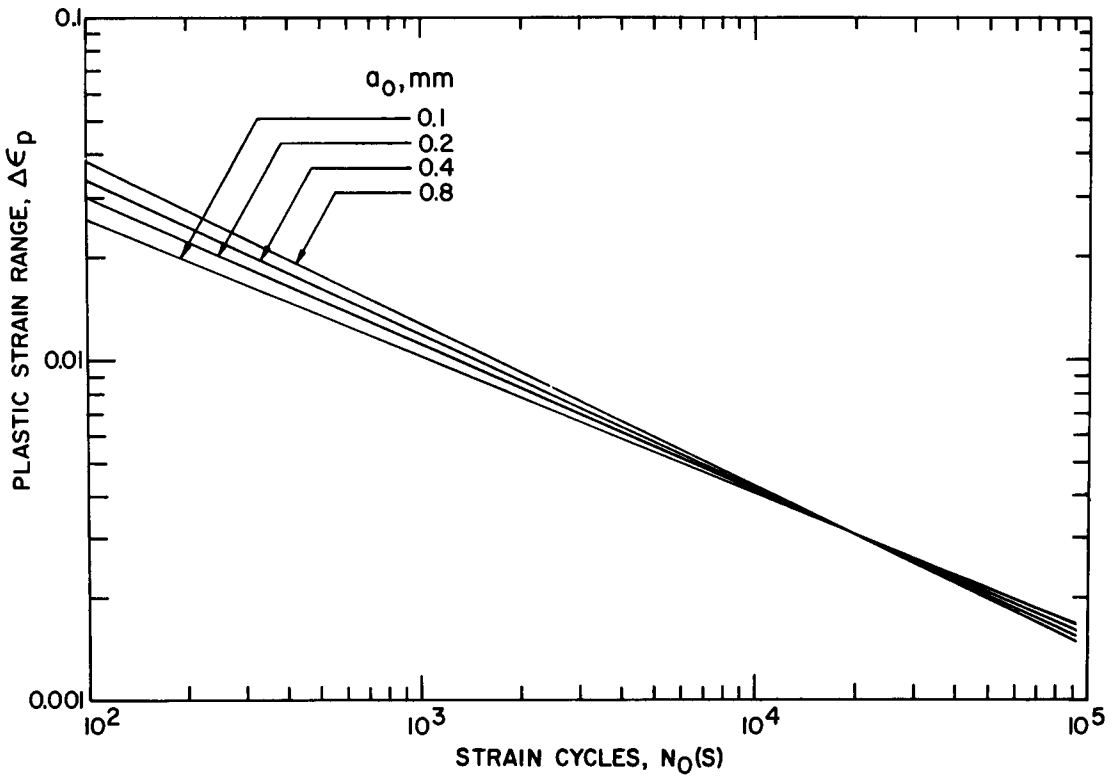

Fig. 2.8. Effect of Plastic-strain Range on Number of Cycles to Crack Initiation for Different Crack-initiation Lengths.

range versus fraction of life spent in crack initiation (Fig. 2.9), which shows that even when the plastic strain range is as high as 1% the percent of life consumed in crack initiation is greater than 60%. At lower strain ranges, crack initiation governs the major portion of fatigue life in smooth specimens.

At present, no method is available that has the capability of predicting the crack-initiation life. Furthermore, quantitative data on crack initiation for any material are scanty. Several years ago, Manson proposed an equation of the following form for estimating $N_o(S)$ in a ductile material:

$$N_f(S) - N_o(S) = N_p(S) = PN_f(S)^{-c}, \qquad (10)$$

where P and c are adjustable constants. The form of Eq. (10) is based on crack-growth considerations, and the constant c was chosen to be

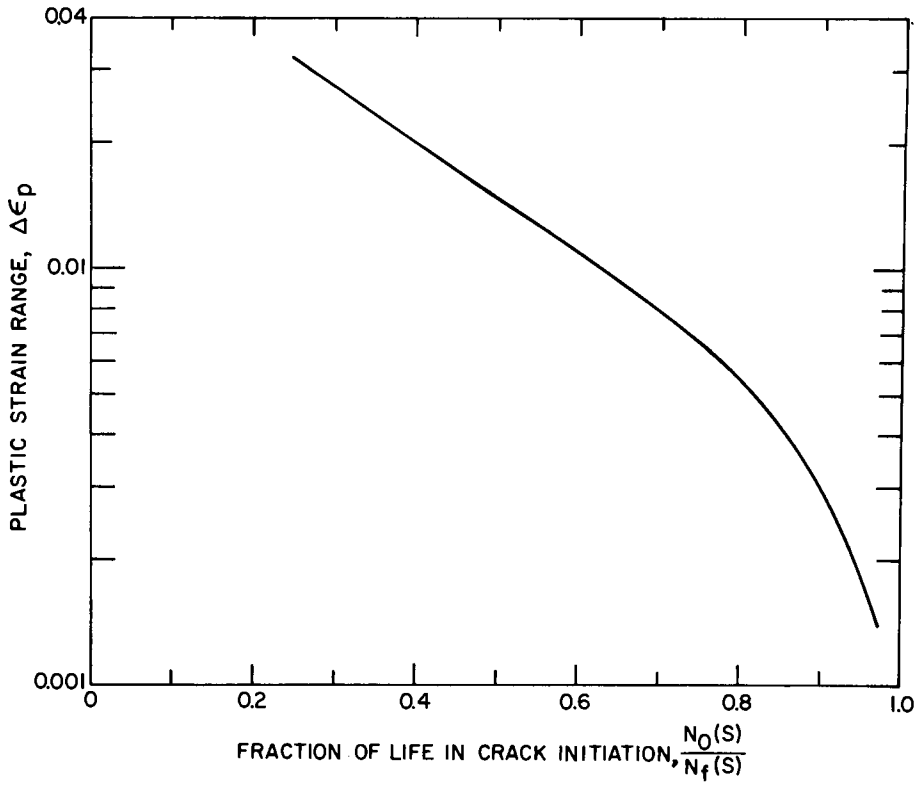

Fig. 2.9. Effect of Plastic-strain Range on the Fraction of Life Spent in Crack Initiation.

equal to 0.6, which is consistent with the Method of Universal Slopes that Manson proposed for estimating fatigue life at room temperature. Assuming $PN_f(S)^{0.6} < N_f(S)$ and $a_o = 0.0762$ mm, his equation for crack initiation can be written in the following form:

$$\frac{N_o(S)}{N_f(S)} = 1 - 6.2\ N_f(S)^{-0.4}, \tag{11}$$

which is valid for $N_f > 730$ cycles. The crack-initiation data generated for Type 304 stainless steel at 593°C can be fit into Eq. (10) to obtain

$$\frac{N_o(S)}{N_f(S)} = 1 - 13.57\ N_f(S)^{-0.48}. \tag{12}$$

A comparison of Eqs. (11) and (12), shown in Fig. 2.10, reveals that, despite the different materials Manson considered and the assumptions involved in the hypothesized crack initiation in Eq. (11), the predictive capabilities of Eqs. (11) and (12) for estimating $N_o(S)$ are not too divergent when N_f > 3500-4000 cycles.

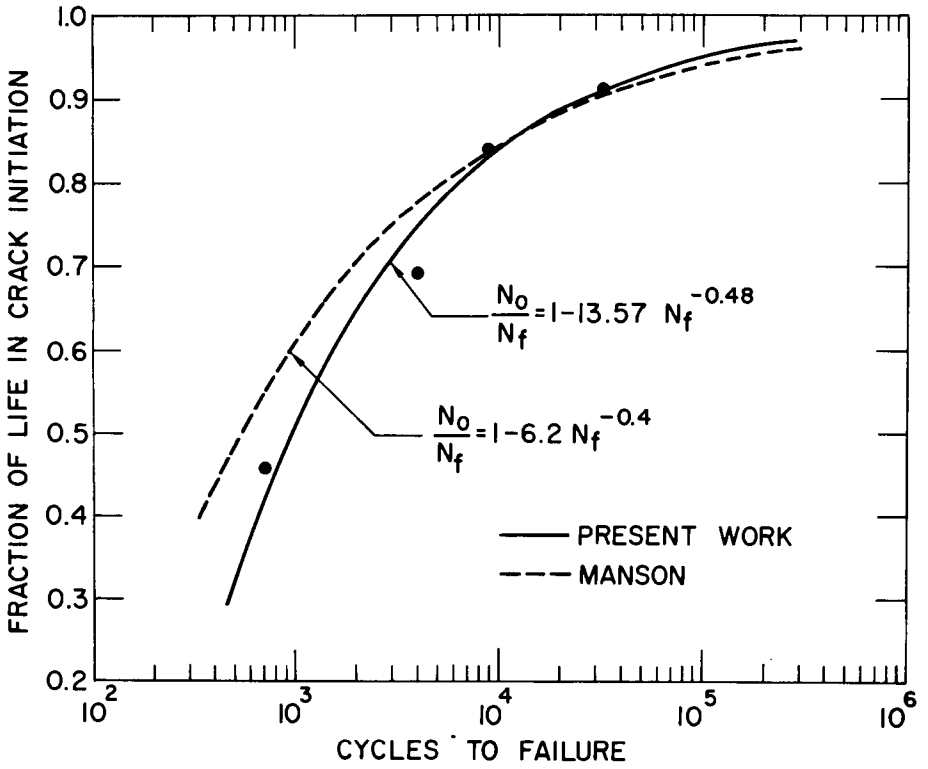

Fig. 2.10. Relation between Fraction of Life in Crack Initiation and Fatigue Life of Smooth Specimens.

Surface replica studies will be performed on stainless steel specimens subjected to interrupted fatigue tests at various stages of life. These studies, as well as those concerned with the determination of crack-initiation life, are expected to yield useful information on the crack-nucleation site and crack-initiation process and valuable data for designers. In addition, it is clear that several variables (e.g., surface notches, creep, and environment) affecting crack initiation should be investigated. Only then will it be possible to achieve an understanding of the effect of a specific variable on fatigue life.

2.2.3 Effect of Heat-to-heat Variations on the Low-cycle Fatigue Behavior of Type 304 Stainless Steel -- P. S. Maiya

The majority of the elevated-temperature, low-cycle fatigue tests have been performed on specimens obtained from a single heat of Type 304 stainless steel (Heat 9T2796), which was produced as a reference heat for all LMFBR testing programs. One of the ANL commitments to the LMFBR program is to evaluate the effect of different heats of Type 304 stainless steel using the ANL data generated on the reference heat as a basis for comparison. The work has been coordinated with the heat-to-heat studies of the Structural Materials Test Program at Oak Ridge National Laboratory (ORNL) so that the same heats of steel will be used in both programs while establishing the range of property parameters required for design purposes. The three heats of material selected and supplied by ORNL are designated as 346544, 346845, and X22807. The hourglass-shape specimens were fabricated at Tasco Tool and Specimen Company, Oak Ridge, Tennessee. The longitudinal axis of most of the specimens was parallel to the direction of rolling. A few specimens of each heat were obtained with the longitudinal axis parallel to the transverse direction. The present report describes the low-cycle fatigue properties determined for specimens (obtained from various heats of material) with the longitudinal axis parallel to the direction of rolling.

The chemical analysis[9] of the various heats of material of interest in the present study is summarized in Table 2.4. All specimens were solution annealed for 30 min at 1092°C (1998°F) and aged for 1000 hr at 593°C (1100°F). The tests were performed in air in servocontrolled, hydraulically actuated fatigue machines in axial strain control at cyclic strain rates of 4×10^{-3} sec^{-1} and 4×10^{-5} sec^{-1} with zero hold time. The tests were, in addition, performed at strain rates of 4×10^{-3} sec^{-1} and 4×10^{-5} sec^{-1} with tension hold times of 1 and 60 min, respectively. The total strain range, in all fatigue tests, is 1%, and the test temperature is 593°C (1100°F).

The optical micrographs of the aged specimens from the four heats of material (Heat Nos. 796, 544, 845, and 807) are displayed in Fig. 2.11. The grain-size measurements were made on several photomicrographs, such

Table 2.4. Chemical Analysis (wt %) of Various Heats of Type 304 Stainless Steel

Elements	Heat Numbers[a]			
	9T2796	346544	346845	X22807
C	0.047	0.063	0.057	0.029
N	0.031	0.019	0.024	0.021
P	0.029	0.023	0.023	0.024
B	-	0.0002	0.0002	0.0005
O	0.011	0.0081	0.0092	0.0100
H	0.0006	0.0006	0.0013	0.0012
S	0.012	0.006	0.006	0.023
Mn	1.22	0.99	0.92	1.26
Si	0.47	0.47	0.53	0.5
Mo	0.10	0.20	0.1	0.2
Ti	0.01	0.036	0.033	0.025
Cu	0.10	0.12	0.11	0.11
Co	0.05	0.05	0.07	0.03
Pb	0.01	0.01	0.01	0.01
Sn	0.02	0.01	0.01	0.01
Ta + Nb	0.08	0.02	0.03	0.02
Cr	18.5	18.40	18.4	18.8
Ni	9.58	9.12	9.28	9.67
Fe	Bal.			

[a]Hereafter, only the last three digits of the heat number will be used to identify the heat.

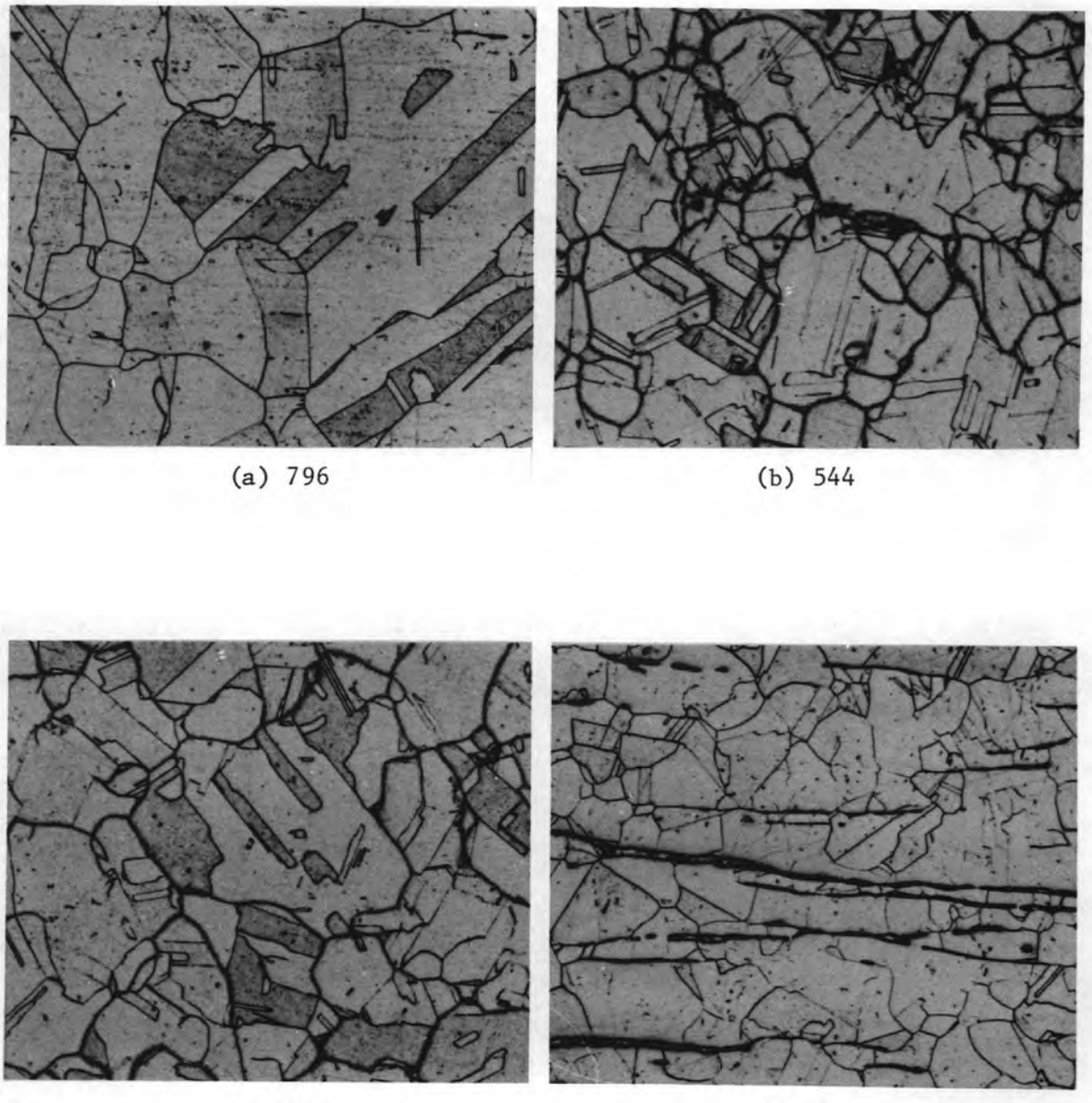

(a) 796 (b) 544

(c) 845 (d) 807

Fig. 2.11. Type 304 Stainless Steel. Etched with oxalic acid. Specimens solution annealed and aged. The dark bands in (d) were found to be Cr-rich phases. Mag. 100X. Heat number is indicated.

as those shown in Fig. 2.11, using the intercept method described by Hilliard,[10] and the results are shown in Table 2.5. As can be observed, the grain size of the reference heat of material is larger than that of the three heats of steel, which have, approximately, the same grain size. No noticeable texture was observed in the grain-size distribution in any of the heats of material investigated.

The low-cycle fatigue results obtained for the three heats of stainless steel (Heat Nos. 544, 845, and 807) are compared with the data obtained from the reference heat of material (Heat No. 796). The results are tabulated, according to the type of cyclic loading variables used, in Tables 2.6-2.9.

Tables 2.6 and 2.7 show the results obtained at a cyclic strain rate of 4×10^{-3} sec^{-1} with zero hold time and with a tension hold time of 1 min, respectively. Tables 2.8 and 2.9 summarize the results obtained at a strain rate of 4×10^{-5} sec^{-1} with zero hold time and with a tension hold time of 60 min, respectively. The cyclic-loading variables listed in Tables 2.6-2.9 indicate an increasing order of contribution to damage accumulation by creep.

The significant points that emerge from the comparison of the fatigue behavior of the four heats of stainless steel are the following: (a) The three heats of steel (Heat Nos. 544, 845, and 807) have approximately the same fatigue strength for each cyclic-loading condition, which is in contrast to their widely different creep behavior[9] under pure uniaxial creep conditions. As expected, fatigue life decreases with more and more damage accumulation by creep. (b) The three heats of material are superior in fatigue strength to that of Heat No. 796 (reference heat). The improvement in the fatigue behavior of the three heats of steel is most marked for the cylic-loading conditions used where the damage accumulation by creep is maximum. For example, at a strain rate of 4×10^{-5} sec^{-1} with a tension hold time of 60 min (Table 2.9), the three heats of steel show an improvement in fatigue life by a factor of better than two, when compared with the reference heat.

Microstructural examinations of specimens obtained from all heats of stainless steel are being made by means of scanning-electron

Table 2.5. Grain Sizes of Various Heats of Type 304 Stainless Steel[a]

Heat No.	Average Intercept, μm	ASTM
796	133	2.4
544	84	3.7
845	98	3.3
807	80	3.9

[a]Solution annealed at 1092°C (1998°F) and aged for 1000 hr at 593°C (1100°F).

Table 2.6. Low-cycle Fatigue Behavior of Various Heats of Type 304 Stainless Steel. Strain rate = 4×10^{-3} sec^{-1} and hold time = 0

Test No.	Heat No.	Total Strain Range, %	Plastic Strain Range, %	Stress Range ($\Delta\sigma$) at $N_f/2$, ksi	Cycles to Failure, N_f	Time to Failure, min
464	796	1.022	0.693	72.516	3826	317.49
557	544	0.999	0.663	74.207	3870	322.09
559	845	0.990	0.650	74.990	4376	364.19
626	807	0.990	0.687	66.848	4022	336.83

Table 2.7. Low-cycle Fatigue Behavior of Various Heats of Type 304 Stainless Steel at 593°C (1100°F). The cyclic strain rate = 4×10^{-3} sec^{-1} and tension hold time = 1 min

Test No.	Heat No.	Total Strain Range, %	Plastic Strain Range, %	Stress Range ($\Delta\sigma$) at $N_f/2$, ksi	Relaxed Stress Range ($\Delta\sigma_r$) at $N_f/2$, ksi	Cycles to Failure, N_f	Time to Failure, min
682	796	1.010	0.704	72.407	67.526	1670	1768.65
565	544	1.00	0.699	71.947	67.305	2712	2914.28
560	845	1.00	0.690	72.407	68.339	3034	3263.36
562	807	0.99	0.721	63.322	59.254	2755	2963.13

Table 2.8. Low-cycle Fatigue Behavior of Various Heats of Type 304 Stainless Steel. The cyclic strain rate = 4×10^{-5} sec^{-1} and hold time = 0

Test No.	Heat No.	Total Strain Range, %	Plastic Strain Range, %	Stress Range ($\Delta\sigma$) at $N_f/2$, ksi	Cycles to Failure, N_f	Time to Failure, min
151	796	0.997	0.665	73.268	851	7083.55
594	544	0.995	0.660	73.898	1658	13853.29
567	845	0.999	0.676	71.051	1707	14207.00
586	807	1.020	0.688	73.176	1637	14528.9

Table 2.9. Low-cycle Fatigue Behavior of Various Heats of Type 304 Stainless Steel at 593°C (1100°F). The cyclic strain rate = 4×10^{-5} sec^{-1} and tension hold time = 60 min

Test No.	Heat No.	Total Strain Range, %	Plastic Strain Range, %	Stress Range ($\Delta\sigma$) at $N_f/2$, ksi	Relaxed Stress Range ($\Delta\sigma_r$) at $N_f/2$, ksi	Cycles to Failure, N_f	Time to Failure, min
441	796	0.994	0.725	68.377	59.401	305	20757.30
621	544	1.016	0.720	73.858	65.121	751	51044.36
595	845	1.004	0.776	56.678	50.441	644	52312.85
612	807	1.01	0.7857	57.567	49.459	874	59612.46

microscopy and X-ray analysis. Preliminary observations made on the fractured surfaces of specimens fatigue tested to failure indicate that all three heats of steel are more resistant to intergranular fracture than the reference heat of material, which is consistent with the observed fatigue results. No correlation is obvious between chemical composition and fatigue behavior nor between creep behavior and fatigue properties. However, it should be mentioned that the reference heat of steel has a larger grain size than that of the other three heats of stainless steel. Furthermore, relying on the reported chemical analysis,[9] the concentration of Ta + Nb in the three heats of steel is approximately the same and is lower than that of the reference heat of material. However, this is only an observation, since the influence of these variables on fatigue behavior is not known.

2.2.4 Design and Analysis of a Biaxial Fatigue Specimen -- S. Majumdar

The design and analysis of the biaxial tubular fatigue specimen subjected to axial loading and internal pressure have been completed. In the specimen design, two competing factors had to be taken into account:

a. Because of the nature of internal pressure loading, an unavoidable gradient exists in the stresses and strains through the wall of the specimen. The gradient is larger the smaller the radius-to-thickness ratio. To keep this gradient small, so that the stress and strain distribution are as close to homogeneous as possible and also to keep the radial stress small compared with the hoop stress, the radius-to-thickness ratio should be large.

b. On the other hand, increasing the radius-to-thickness (r/t) ratio reduces the buckling load of the specimen so that the safe maximum axial stress and strain ranges of the specimen become limited.

For example, Fig. 2.12 shows the buckling stress and strain as a function of r/t for Type 304 stainless steel at room temperature and 1000°F (538°C). It should be noted that the analysis is based on a shell-type buckling mode of the specimen and accounts for plastic

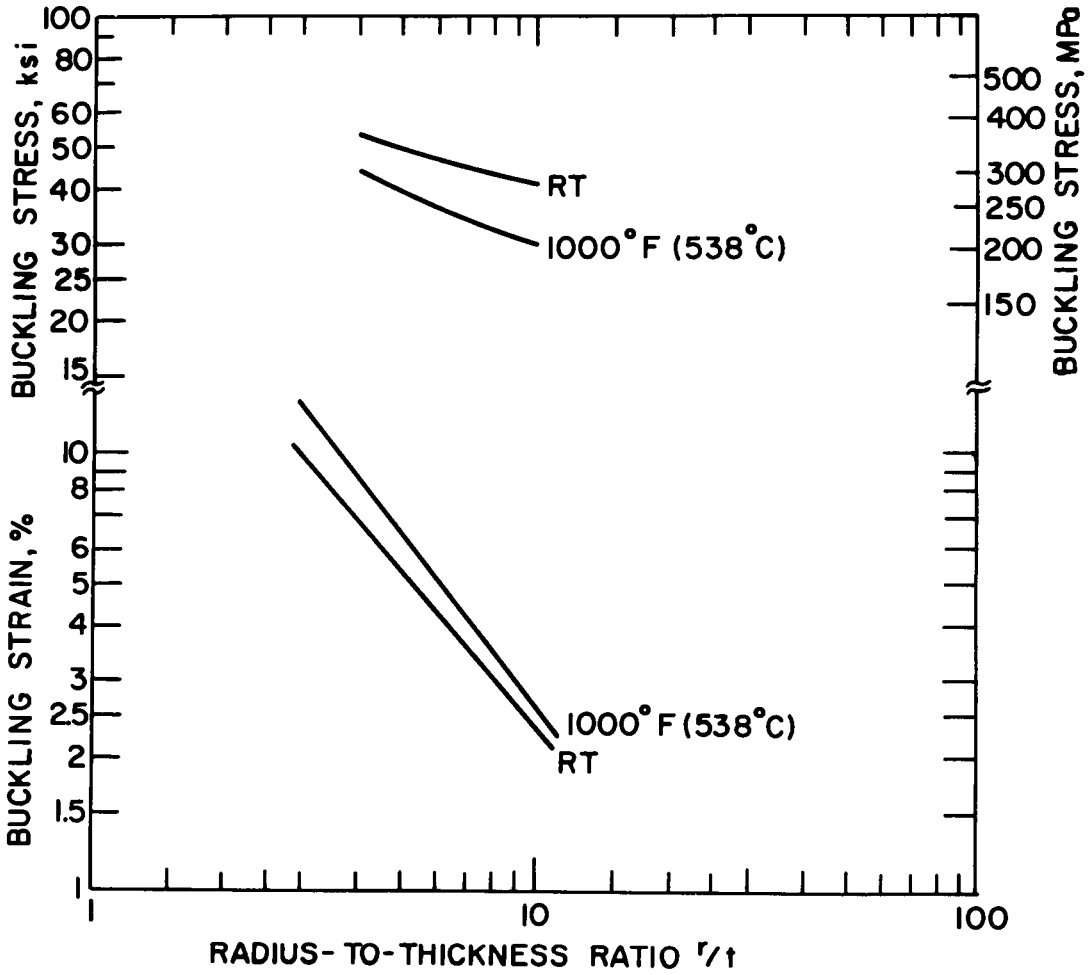

Fig. 2.12. Plastic Buckling of a Type 304 Stainless Steel Hollow Cylinder under Axial Load.

yielding.[11] Euler (beam-type) buckling loads, for the length of the specimen considered, are higher than the shell-type buckling values. Based on Fig. 2.12, a value of r/t = 10 was chosen so that a maximum axial strain range of ±1% can be safely applied to the specimen. In addition, the internal pressure will have a stabilizing influence on the specimen. The geometry to be analyzed is shown in Fig. 2.13, where one-half of a longitudinal cross section of the specimen is shown.

The purpose of the stress analysis was threefold. First, the analysis would provide the location and magnitude of the maximum stress and strain that occurs in the specimen outside the gauge section (1 in. at the center) due to stress concentration effects. Secondly, since the axial and hoop strains in the tests will be measured indirectly via the displacements at the outer surface of the specimen while the maximum stresses and strains in the gauge section will mostly occur at the inner surface, the analysis would provide the errors to be expected in determining the maximum stress and strain ranges in the gauge section. Finally, the analysis would indicate the error involved in the usual practice of computing the third component (through the thickness) of the strain from the two measured strains by using the condition of incompressibility.

2.2.4.1 Loading Cases

The following loading conditions were analyzed:

a. Keeping the internal pressure equal to zero, the axial load was increased to 1821 lb (8100 N), and the specimen was allowed to creep for 50 hr at 1100°F (593°C).

b. Keeping the axial load equal to zero, the internal pressure was increased to 1920 psi (13.2 MPa) at 500°F (260°C).

c. Keeping the axial load equal to zero, the internal pressure was increased to 1920 psi (13.2 MPa), and the specimen was allowed to creep for 25 hr at 1100°F (593°C).

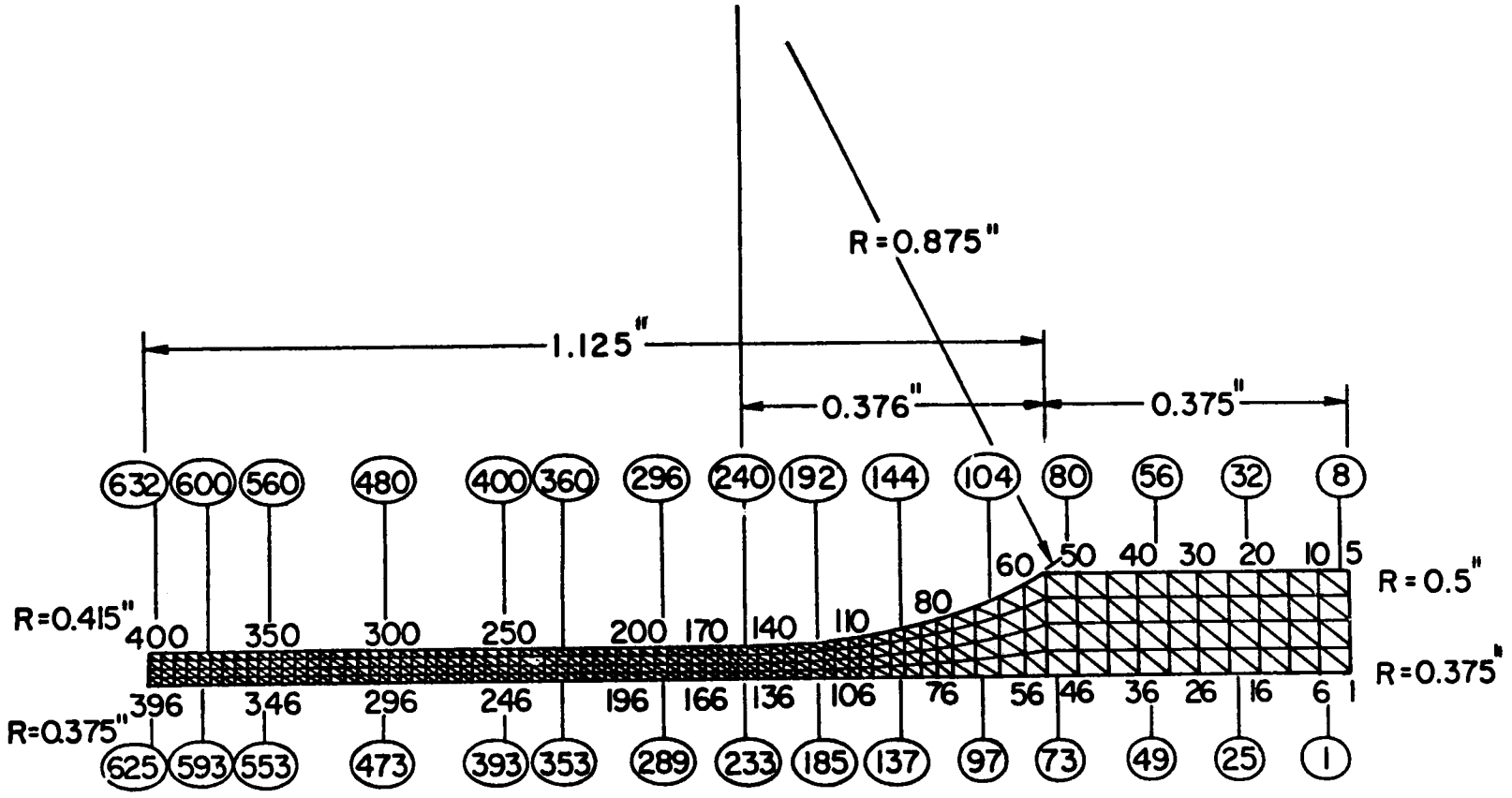

Fig. 2.13. Finite-element Model of Biaxial Fatigue Specimen.

d. Keeping the axial end displacement equal to zero, the internal pressure was increased to 1920 psi (13.2 MPa), and the specimen was allowed to creep for 25 hr at 1100°F (593°C).
e. The axial load was increased to 961 lb (4275 N) (compressive), followed by increased internal pressure to 1470 psi (10.1 MPa) at 1100°F (593°C).
f. The internal pressure was increased to 1470 psi (10.1 MPa), followed by increased axial load to 961 lb (4275 N) (compressive) at 1100°F (593°C).

2.2.4.2 Method of Analysis

The analyses were carried out by the CREEP-PLAST finite-element program.[12] Material properties of Type 304 stainless steel (annealed), as recommended in the LMFBR Handbook,[13] are incorporated in the CREEP-PLAST program. A finite-element model consisting of 400 nodes and 632 elements (Fig. 2.13) was used. Any additional refinement of the model was found to be unnecessary.

2.2.4.3 Results

A study of the deformation of the specimen shows that, in addition to stress concentration effects due to change in the cross-sectional area, significant shell-type bending stresses are generated due to eccentricity and a difference in the bending stiffness of the section at the ends of the specimen from that at the middle. Details of the stress-strain distribution in the specimen for the various loading cases may be obtained from Ref. 14. Distribution of stress and strain at the outer and inner surfaces of the specimen that correspond to loading case e are shown in Figs. 2.14 and 2.15.

2.2.4.4 Discussion

The various loading cases analyzed show that the maximum strain gradients (both axial and through the thickness) to be expected in the gauge section of the specimen are of the order of 10%. Although the hoop and axial stress distribution may be nonuniform, the effective

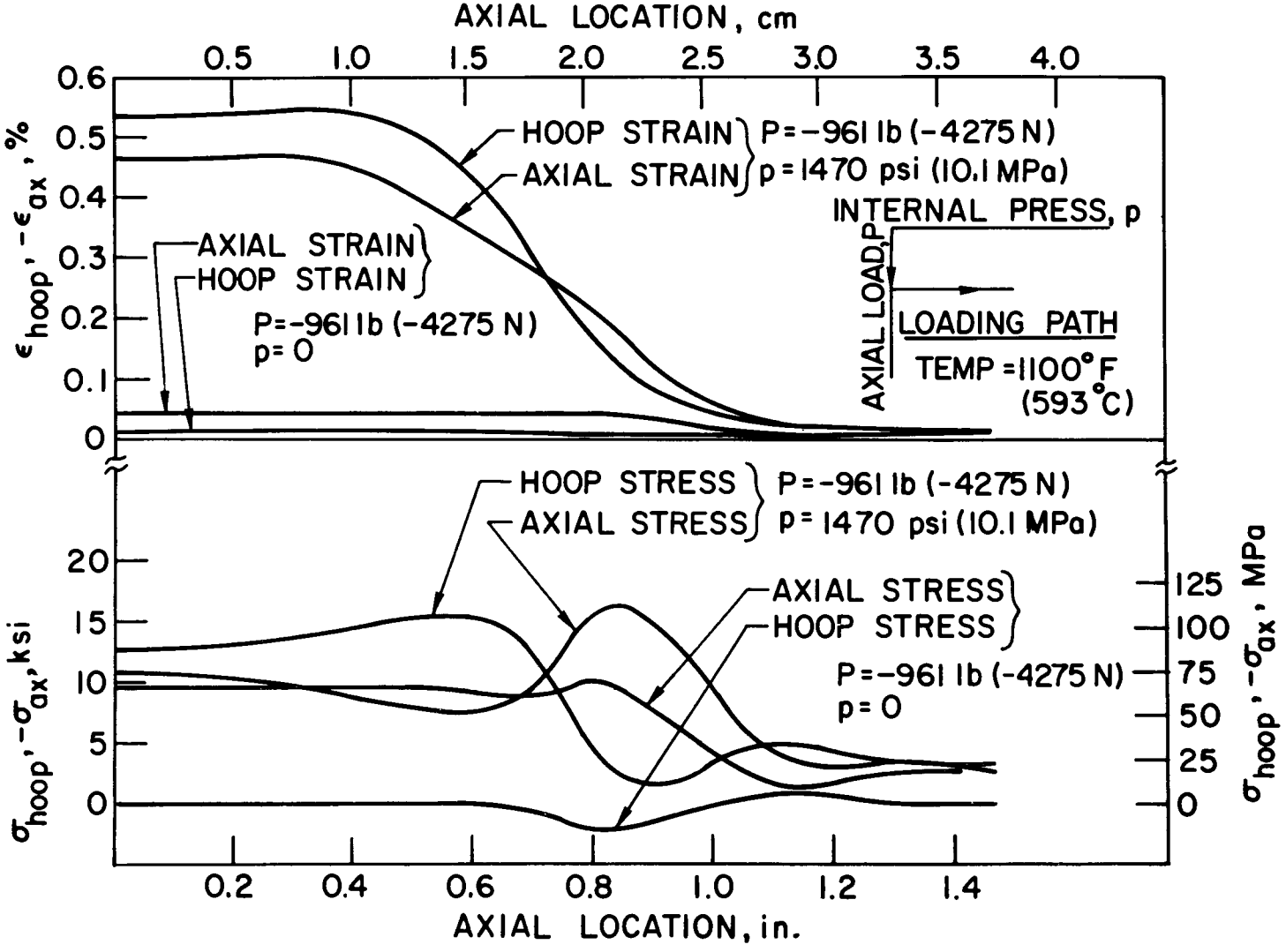

Fig. 2.14. Variation of Stress-Strain Outer Surface (Case e).

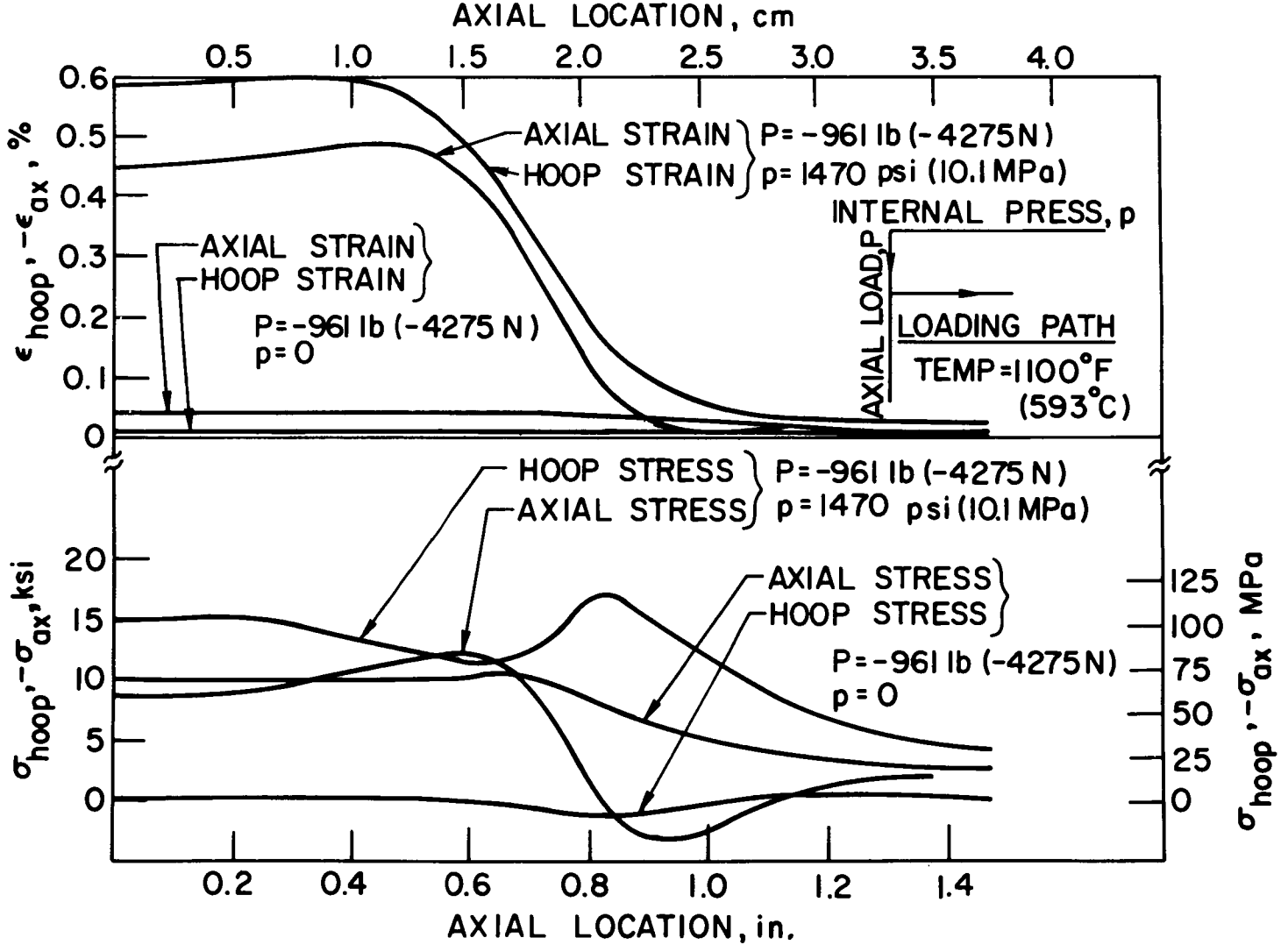

Fig. 2.15. Variation of Stress-Strain Inner Surface (Case e).

stress distribution is uniform throughout the gauge section. The maximum strains always occur in the gauge section except for (low stress) elastic loading. Thus, in general, the failure of the specimen, due to low-cycle (high stress) fatigue, is expected to occur in the gauge section.

In tests with tubular specimens, all displacement measurements are made on the outer surface of the specimen so that the strains at the outer surface are measured directly. However, the maximum hoop strain often occurs at the inner surface of the specimen. A method of estimating the hoop strain at the inner surface is to divide the radial displacement at the outer surface by the inner radius. Similarly, an estimate of the axial strain at the inner surface can be obtained by assuming the strain at the inner surface is equal to that at the outer surface. A comparison between the various surface-strain values, as computed by the program, and the strains that would be calculated from the knowledge of the outside-surface displacements alone shows that the axial strain distribution through the thickness of the wall is uniform in all cases and can be estimated to within 2% from the measured displacements at the outer surface. The hoop strains at both the inner and outer surfaces can be obtained from the radial displacement at the outer surface to within 2%, except for the case of pure axial loading. For pure axial loadings, the hoop strain occurs as a result of Poisson's ratio effect and not hoop stress. Thus, no gradient occurs in the hoop strain through the thickness of the specimen wall. Consequently, the estimate of the hoop strain at the inner surface, obtained by dividing the radial displacement at the outer surface by the internal radius of the tube, overestimates the actual value by 11%. In the case of combined internal pressure and axial loading, the accuracy of measuring the hoop strain at the inner surface by this method improves with increasing internal pressure. In all cases, the method of calculating the radial strain indirectly by using incompressibility results in considerable error and may be as much as 42% in some cases. This error is larger the smaller the loading, as might be expected.

2.2.4.5 Conclusions

The biaxial fatigue specimen, as depicted in Fig. 2.13, is acceptable for low-cycle fatigue testing under combined axial load and internal pressure. Failure in these tests should occur in the gauge section.

The axial strain can be estimated to within 2% accuracy from displacements measured over a 1-in.-gauge length at the outer surface of the specimen. The hoop strain at the outer surface can be obtained directly by measuring the radial displacements at the outer surface. Hoop strain at the inner surface, as calculated by dividing the radial displacement at the outer surface by the internal radius of the tube, can lead to a maximum error of 11% in the case of pure axial loading. The accuracy improves as the internal pressure is increased.

The third component (radial) of the strain cannot be reliably obtained from the other two by using the condition of incompressibility. Auxiliary tests with the same material must be conducted to determine its effective Poisson ratio for various levels of loading.

2.3 SODIUM EFFECTS ON LMFBR MATERIALS -- T. F. Kassner

2.3.1 Influence of Sodium Environment on the Uniaxial Creep-rupture Properties of Austenitic Stainless Steels -- K. Natesan, D. L. Smith, J. Y. N. Wang, O. K. Chopra, and G. J. Zeman

The effect of carburization on the creep-rupture properties of Types 304, 316, and Ti-modified 316 stainless steel, after exposure to well-characterized sodium at temperatures between 550 and 700°C, is being determined. Since the composition and microstructure of the material in the vicinity of the sodium-steel interface can have a strong influence on crack initiation and propagation, the degree of carburization resulting from the sodium environment needs to be correlated with the mechanical-property changes in the material.

Uniaxial creep-rupture specimens of AISI Type 304 stainless steel, which were fabricated according to ASTM Standard E8-69, were exposed to flowing sodium at 700°C for 120 to 1512 hr to yield $\sim$4, 8, and 15-mil-penetration depths for carbon. The 15-mil-thick specimens were subsequently used in uniaxial creep-rupture tests to obtain the creep

curves and creep-rupture life. Figures 2.16-2.18 show the creep strain versus time at 700°C as a function of applied stress between 125 and 55.5 MPa (18-8 ksi) for specimens exposed to a flowing sodium environment for 120, 504, and 1512 hr, respectively. The creep-rupture life and the minimum creep rate calculated from the curves (Figs. 2.16-2.18) for various sodium exposure and testing conditions are tabulated in Table 2.10. The results show that, for a given sodium-exposure condition, the creep-rupture life increases, whereas the minimum creep rate decreases as the applied stress decreases. The results also indicate that the minimum creep rate increases, whereas the creep-rupture life decreases as the sodium-exposure period increases. Figure 2.19 shows the uniaxial creep curves at an applied stress of 90 MPa (13 ksi) for Type 304 stainless steel specimens exposed for various times in flowing sodium.

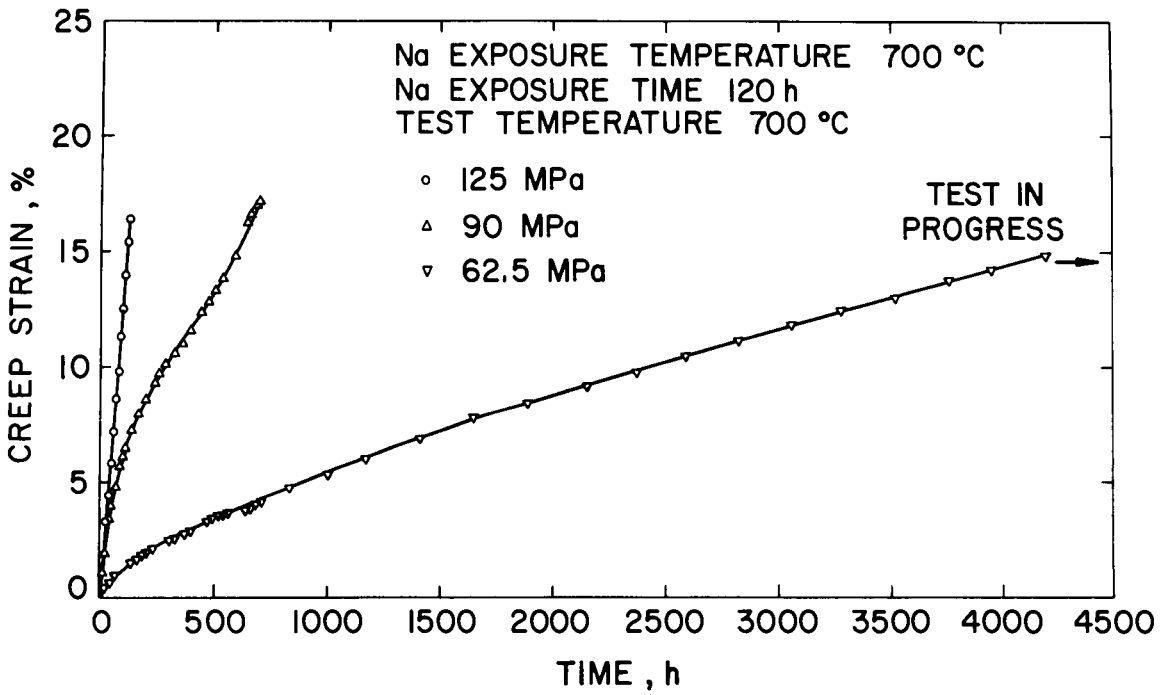

Fig. 2.16. Uniaxial Creep Curves as a Function of Applied Stress for AISI Type 304 Stainless Steel Specimens Preexposed to Flowing Sodium at 700°C for 120 hr.

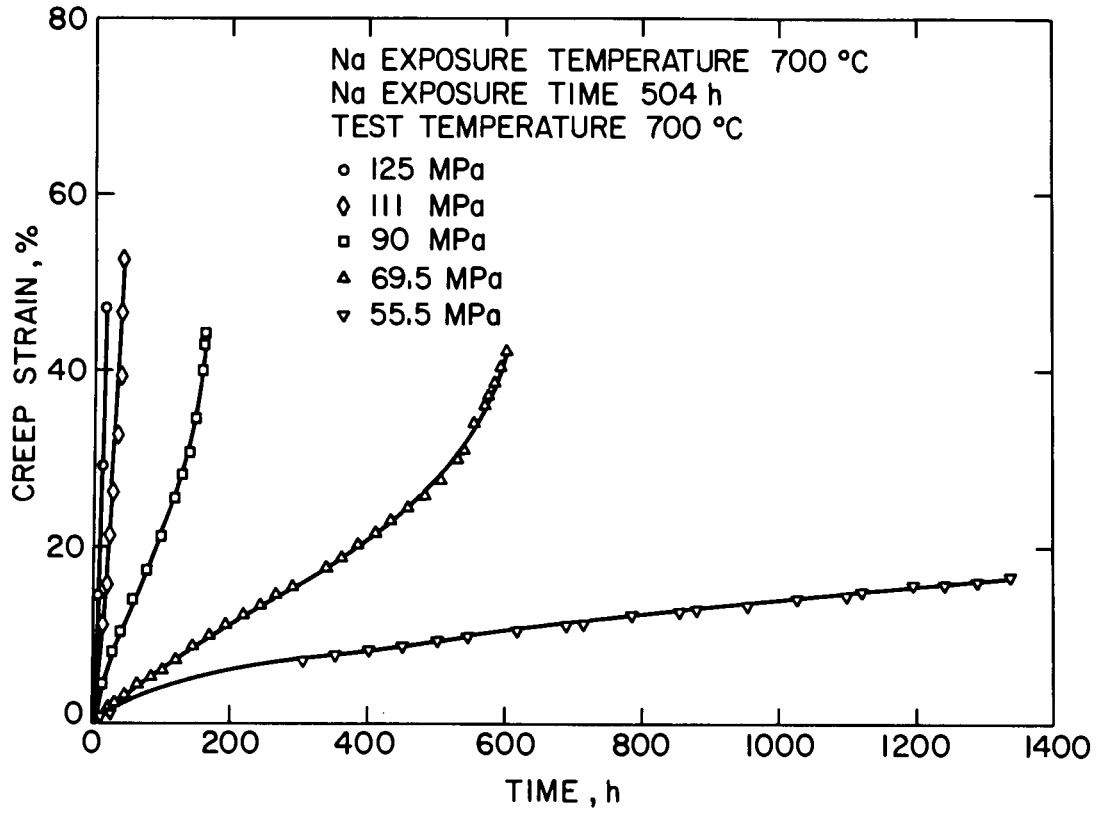

Fig. 2.17. Uniaxial Creep Curves as a Function of Applied Stress for AISI Type 304 Stainless Steel Specimens Preexposed to Flowing Sodium at 700°C for 504 hr.

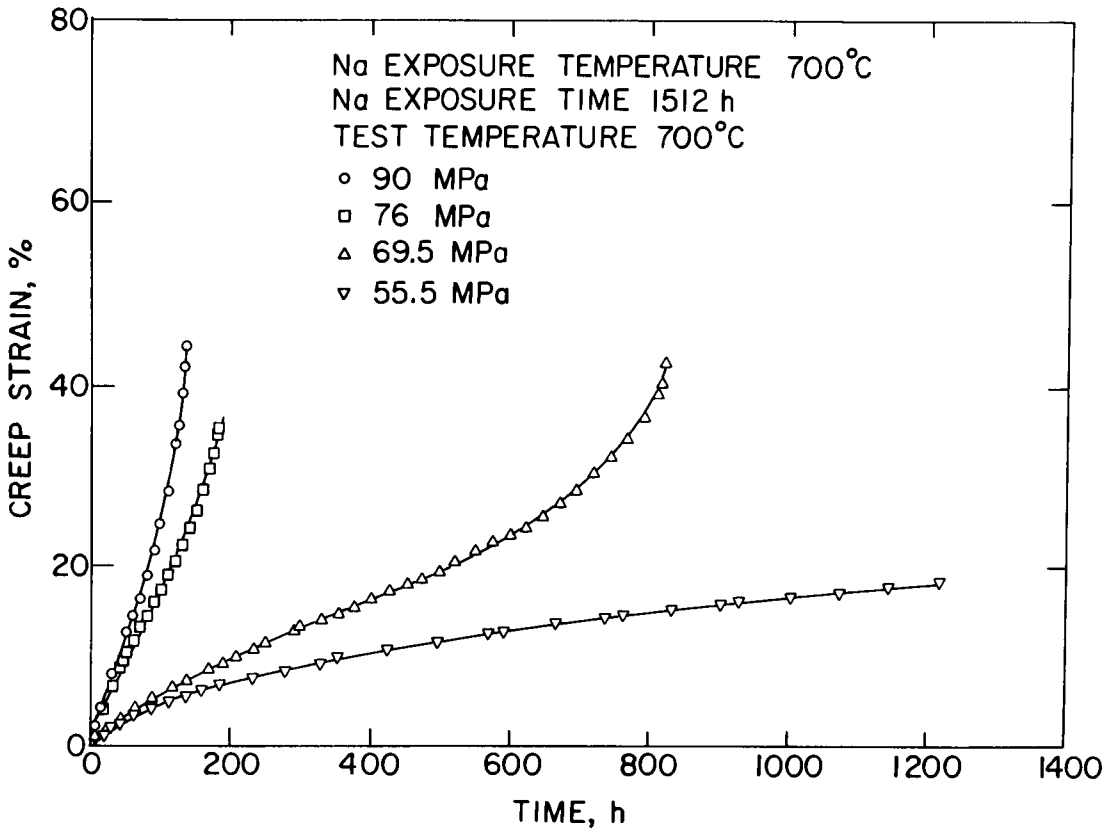

Fig. 2.18. Uniaxial Creep Curves as a Function of Applied Stress for AISI Type 304 Stainless Steel Specimens Preexposed to Flowing Sodium at 700°C for 1512 hr.

Table 2.10. Creep-rupture Behavior of AISI Type 304 Stainless Steel (Heat 9T2796) upon Exposure to Sodium Environment at 700°C

Na Exposure Time, hr	Carbon Penetration Depth, mils	Applied Stress, MPa (ksi)	Rupture Life, hr	Minimum Creep Rate, %/hr	Strain at Rupture, %
120	∿4	62.5 (9)	(a)	0.0020	(a)
		90 (13)	678	0.0145	17.2
		125 (18)	125.5	0.134	16.4
504	∿8	55.5 (8)	1337	0.0097	16.6
		69.5 (10)	600.8	0.045	42
		90 (13)	159.5	0.190	44
		111 (16)	36.5	High	52.4
		125 (18)	12.5	High	47
1512	∿15	55.5 (8)	1218	0.011	18.4
		69.5 (10)	822	0.043	42.6
		76.5 (11)	182.2	0.128	35.6
		90 (13)	135.5	0.218	44

[a]Test in progress.

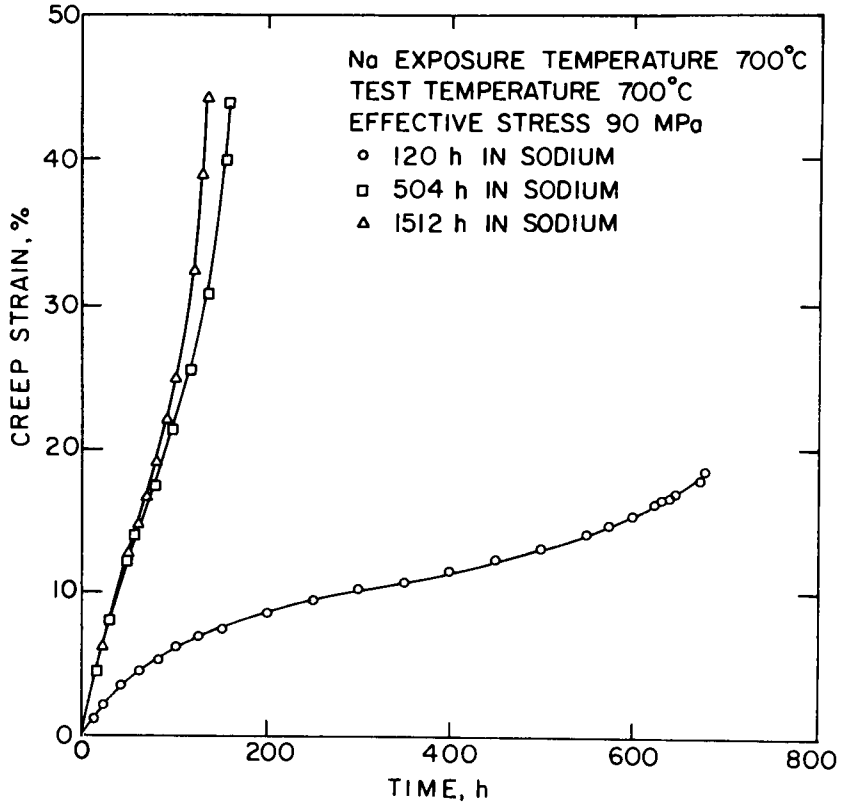

Fig. 2.19. Uniaxial Creep Curves at an Applied Stress of 90 MPa for Type 304 Stainless Steel Specimens Exposed for Various Times in Flowing Sodium.

The surface carbon concentrations in the mechanical test specimens are being determined from combustion analyses of 2-mil-thick foils of the same material that were equilibrated in sodium during the specimen-exposure period. The surface carbon concentration values that ranged from 0.06 to 0.07 wt % and from 0.25 to 0.30 wt % at 700 and 650°C, respectively, are being used with a kinetic analysis for carbon diffusion[15] to obtain the carbon-concentration profiles and the average carbon concentration in the specimens after exposure to sodium. The mechanical test specimens are also being analyzed to determine the average carbon concentrations, and these values will be compared with those calculated using the kinetic analysis. The equivalence of the calculated and experimentally determined average carbon concentrations in the material

will establish the reliability of the computed carbon-concentration profiles in the sodium-exposed specimens. The constancy of the depth of penetration of carbon in the specimens will be used as a basis for a comparison of the mechanical-property data at various temperatures.

Microstructural examination of the tested specimens is being conducted using optical metallography, SEM, and TEM techniques. Preliminary results show a significant increase in carbide precipitation with an increase in sodium-exposure time. The microstructures of a small number of specimens examined to date indicate an absence of any external effects (e.g., sodium cleaning) that could influence the creep properties, which gives credence to the postexposure testing approach for quantitative evaluation of the influence of the sodium environment on the mechanical behavior of materials.

Creep testing of specimens that have been exposed to flowing sodium at 650 and 600°C has been initiated. Types 316 and Ti-modified 316 stainless steel specimens that have been exposed to flowing sodium will be tested upon completion of the test program on Type 304 stainless steel.

2.4 REFERENCES

1. Mechanical Properties Test Data for Structural Materials Quarterly Progress Report for Period Ending July 31, 1974, Oak Ridge National Laboratory, ORNL-4998, pp. 15-22.

2. S. S. Manson, "The Challenge to Unify Treatment of High Temperature Fatigue -- A Partisan Proposal Based on Strain-Range Partitioning," in Fatigue at Elevated Temperatures, Am Soc. Testing and Materials, ASTM (1973), pp. 744-782.

3. D. R. Diercks, "The Application of Strain-range Partitioning to the Prediction of Elevated-temperature, Low-cycle Fatigue Life for Type 304 Stainless Steel," submitted to the Second National Congress on Pressure Vessel and Piping, San Francisco, June 1975.

4. J. A. Bennett, Proc. Intl. Conf. on Fatigue of Metals, Institute of Mechanical Engineers, London, 1956, p. 548.

5. P. J. E. Forsyth, Proc. Crack Propagation Symp., Cranfield, England, 1962, Vol. 1, p. 76.

6. S. S. Manson, Experimental Mechanics 5, 193 (1965).

7. S. S. Manson, Intl. J. Fracture Mechanics 2, 327 (1966).

8. H. D. Solomon, Met. Trans. 4, 341 (1973).

9. H. E. McCoy, "Tensile and Creep Properties of Several Heats of Type 304 Statinless Steel," Oak Ridge National Laboratory, ORNL-TM-4709 (November 1974).

10. J. E. Hilliard, Metal Progr. 5, 99 (1964).

11. "Buckling of Thin-walled Circular Cylinders," National Aeronautics and Space Administration, NASA SP-8007 (September 1965).

12. J. A. Clinard and J. S. Crowell, "ORNL User's Manual for CREEP-PLAST Computer Program," Oak Ridge National Laboratory, ORNL-TM-4062 (November 1973).

13. "Liquid Metal Fast Breeder Reactor Materials Handbook," Hanford Engineering Development Laboratory, HEDL-71-32 (June 1971).

14. S. Majumdar, "Design and Analysis of Biaxial Fatigue Specimen," to be published.

15. R. B. Snyder, K. Natesan, and T. F. Kassner, "Kinetics of the Carburization-Decarburization Process of Austenitic Stainless Steels in Sodium," J. Nucl. Mater. 50, 259-274 (1974).

3. HANFORD ENGINEERING DEVELOPMENT LABORATORY

T. T. Claudson

3.1 INTRODUCTION

The objectives of the structural materials investigation conducted at the Hanford Engineering Development Laboratory are to provide control data for the in-reactor and postirradiation tests and to provide direct and timely assistance to FFTF and Demonstration plant structural design and analysis programs. The HEDL efforts involve evaluation of mechanical properties at high strain rates, creep testing and analysis, fatigue crack growth, and tensile tests of such materials as FFTF weldments, vessel and piping, core support structures, reflectors as well as duct and cladding. Those test results and analyses appropriate to the "Structural Materials Quarterly Report" will be reported herein; however those investigations associated with irradiation effects per se will continue to be reported in the "Irradiation Damage to Reactor Structural Materials" Quarterly Report published at HEDL.

3.2 IRRADIATION DAMAGE TO REACTOR METALS - T. T. Claudson and H. H. Yoshikawa

3.2.1 Low Temperature Creep of 20% Cold Worked Type 316 Stainless Steel

3.2.1.1 Objective

The objectives of this work are: (1) to accurately measure thermal creep deformation in 20% cold worked Type 316 stainless steel, and (2) to further demonstrate the application of microwave extensometers for high precision creep strain measurements.

3.2.1.2 Accomplishments and Status

3.2.1.2.1 Scope of Work. A creep test on 20% cold worked Type 316 stainless steel using a high precision microwave extensometer to measure

strain was continued to further explore creep response under varying load and temperature. This test was initiated at 850°F, and the load history and strain response were reported previously.[1,2] The temperature was then raised to 1000°F, and the specimen was stressed to 20,000 psi for 960 hours, unloaded to 220 psi for 240 hours, reloaded to 20,000 psi for 625 hours, and unloaded again to 220 psi for 335 hours. After this final unloading, the test temperature was increased to 1100°F in 5 hours, and then held constant for 43 hours. The specimen was then loaded in increments of about 2,000 psi to a total stress of 20,000 psi within about 7 minutes. After 980 hours at a stress of 20,000 psi, the specimen was unloaded to 220 psi for a period of 290 hours and then reloaded to 20,000 psi.

3.2.1.2.2 Results. Strain measurements obtained during loading at 1100°F are summarized in Figure 3.1, along with earlier results at 850 and 1000°F. The small departure from elastic behavior at high stresses (i.e., a strain of 18×10^{-6} at 20,000 psi) is probably a result of creep during the finite loading time. A value of 2.16×10^{6} psi was obtained for Young's modulus at 1100°F; this value is slightly lower (by about 4%) than the results reported by Garofalo et. al.[3]

Complete results of creep strain measurements at both 1000 and 1100°F are presented in Figures 3.2 and 3.3. Since the elastic extensions and contractions accompanying stress changes were larger than the time dependent deformation, these strain contributions were subtracted out and are tabulated separately in the figures. These elastic strain measurements agree to within about one percent.

The previous report[2] presented 1000°F results through about 260 hours following the reload. The additional results in Figure 3.2 confirm the observation that the measured strain after reloading is slightly larger than predicted from reoccurrence of anelastic strain and continued plastic creep strain. Recovery strains following the second unloading are very similar to those observed during the first unloading for short times, but are slightly smaller at long recovery times.

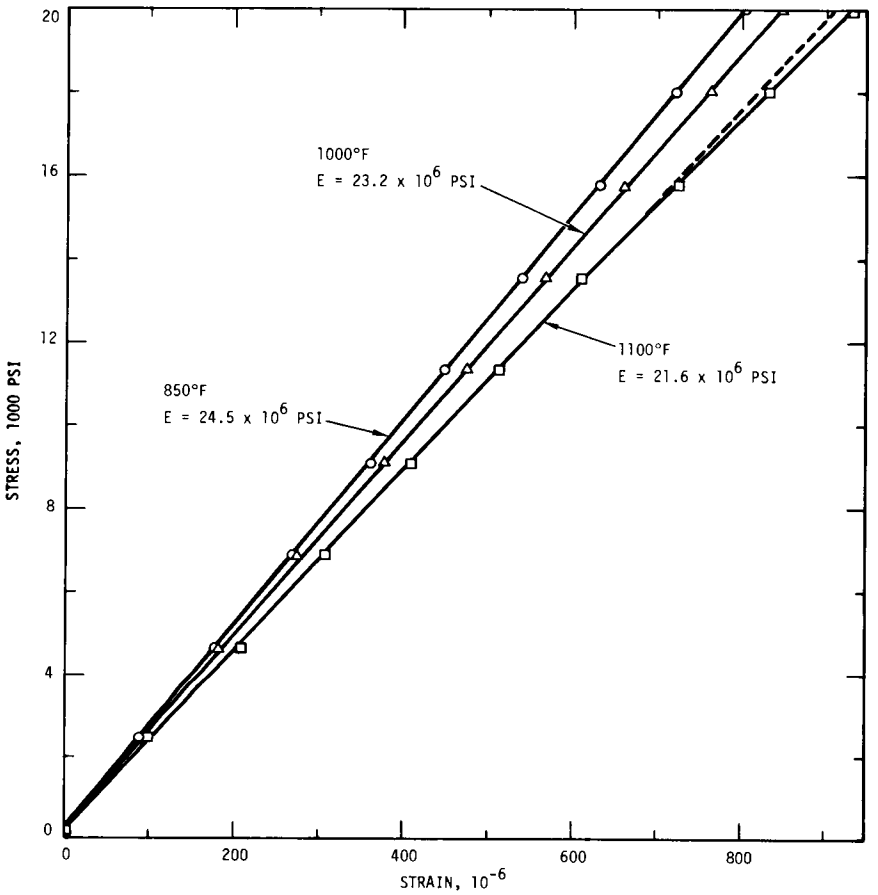

FIGURE 3.1. Loading Curves for 20% Cold Worked Type 316 Stainless Steel at 850, 1000 and 1100°F.

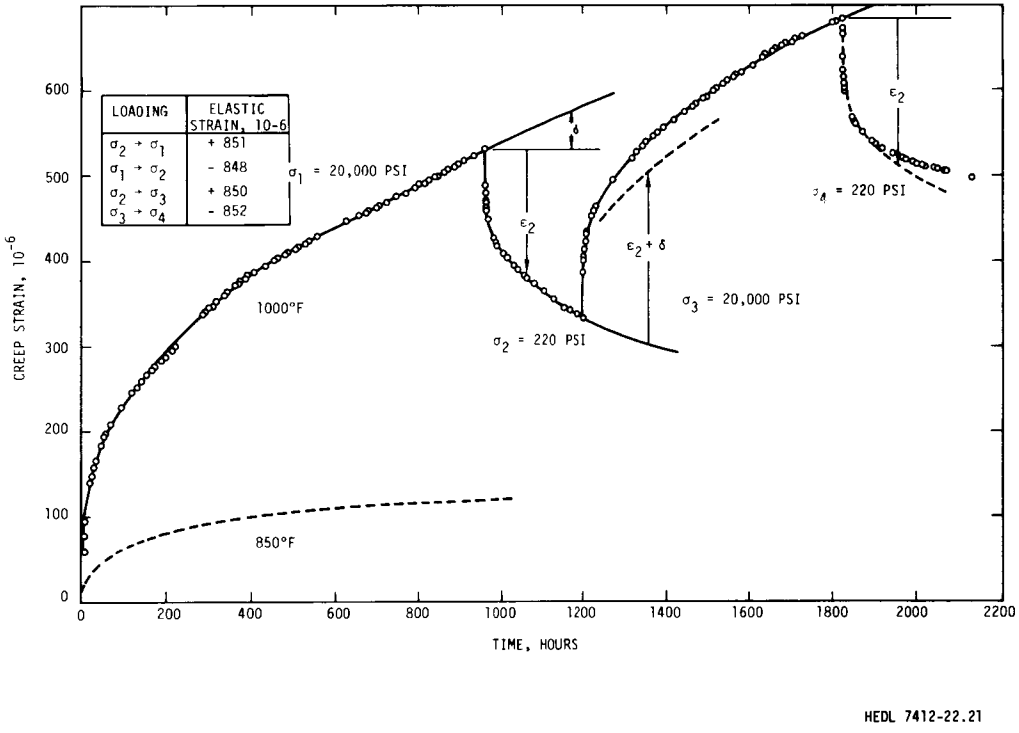

HEDL 7412-22.21

FIGURE 3.2. Creep Curve for 20% Cold Worked Type 316 Stainless Steel at 1000°F.

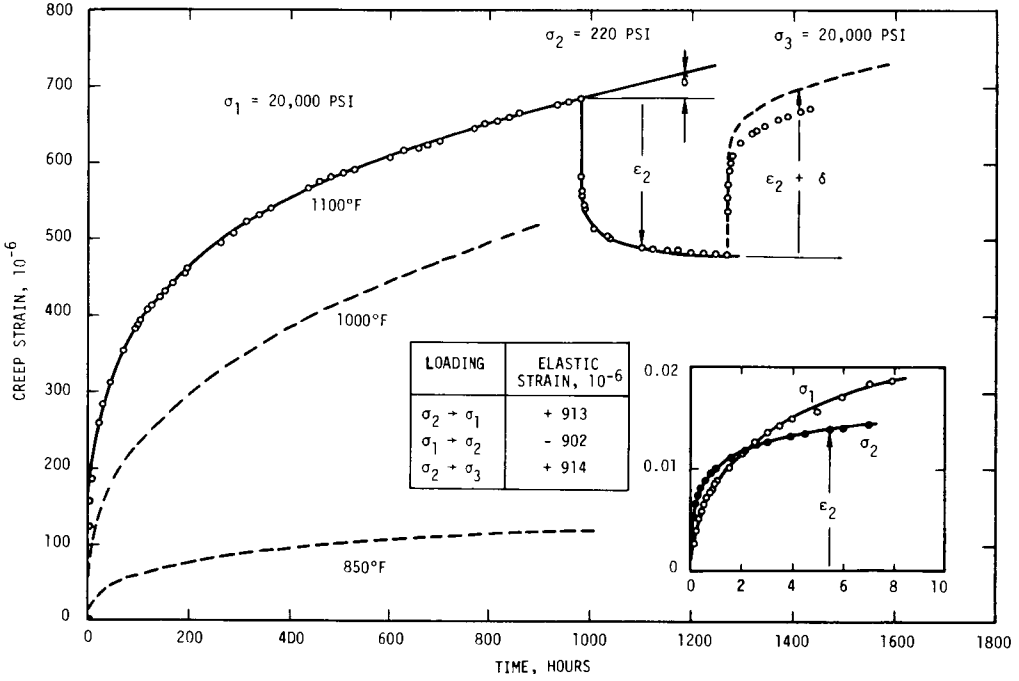

HEDL 7412-22.25

FIGURE 3.3. Creep Curve for 20% Cold Worked Type 316 Stainless Steel at 1100°F.

The initial creep rate is substantially higher at 1100°F than at the lower temperatures (Figure 3.3), but creep rate decreases more rapidly with time, so that after 1000 hours, similar creep rates are observed at 1000 and 1100°F. As a result, the creep strain at 1100°F is only about 28% larger than the creep strain at 1000°F after 1000 hours. At 1100°F, strain recovery occurs rapidly after unloading and the rate of strain recovery is higher than the initial forward creep rate, as shown in the inset of Figure 3.3. This behavior is observed at each of the three test temperatures. Creep strain accrues rapidly after reloading, but the observed strains are slightly smaller than predicted from a re-occurrence of anelastic strain and continued plastic creep strain, as shown by the construction in Figure 3.3.

3.2.1.2.3 Evaluation of Results. The creep curves after the first loading show a progressive increase in creep strain with increasing temperature (see Figure 3.3), but the creep rate at 1100°F seems to decrease more rapidly as deformation proceeds than we would expect. That is, the creep rate after 1000 hours does not reflect a strong temperature dependence in the 1000-1100°F range. One possible explanation for this observation is that the prior creep deformation at 1000°F hardens the material so that creep rates at 1100°F are then lower than for a virgin specimen. To examine the present results for this history effect, we compared our results with those obtained from pressurized tube specimens[4] using several hypotheses.* In Figure 3.4, we show the effective strain-time curves at an effective stress of 20,000 psi for virgin specimens as computed from the creep equation describing the pressurized tube results. We also present the current data for the virgin specimen at 850°F; the last measured strain at 850°F was 0.01%, although some additional strain recovery did occur on final unloading and heating to 1000°F. The present data at 1000°F are plotted in Figure 3.4 using two different assumptions:

*Since creep curves for virgin specimens at 1000 and 1100°F were not obtained in the present work, it was necessary to use the pressurized tube results to represent creep behavior for virgin material. The pressurized tubes and the present specimen were made from the same heat of steel and are all 20% cold worked, although the detailed fabrication history is somewhat different.

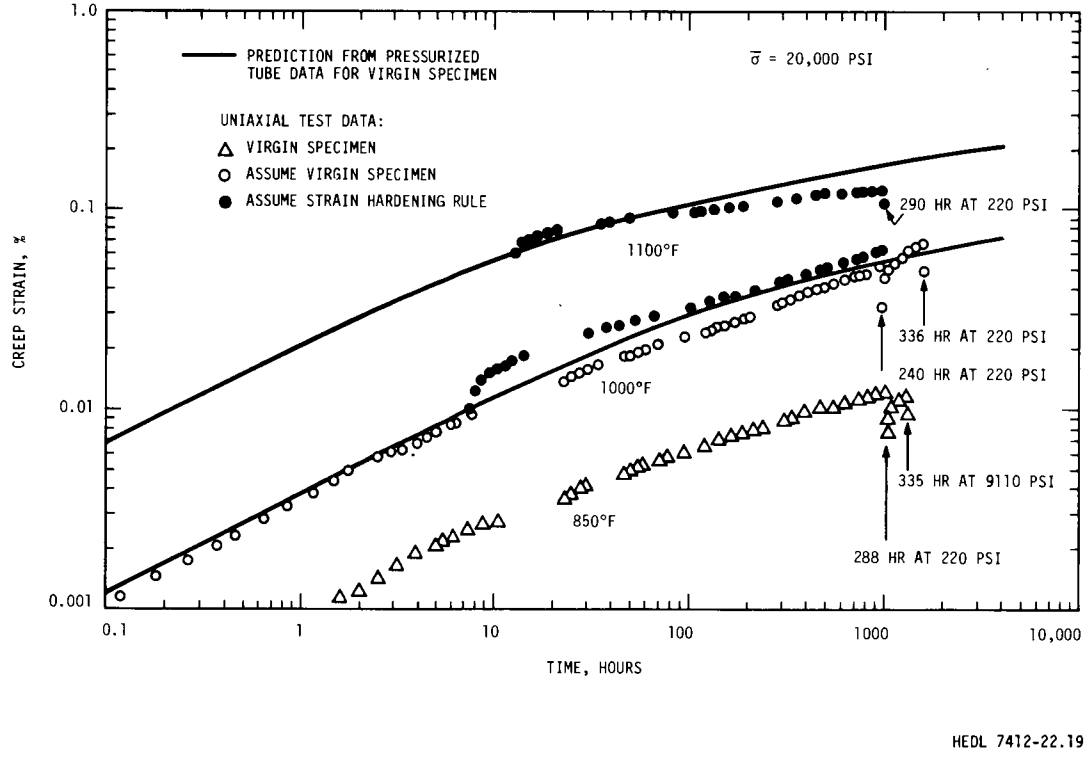

FIGURE 3.4. Creep Response of 20% Cold Worked Type 316 Stainless Steel Under Varying Load and Temperature.

(a) the prior creep at 850°F has no effect, so the creep response is that of a virgin specimen, and (b) the effect of prior creep at 850°F is accounted for assuming a strain hardening rule. Both assumptions give reasonable agreement with predicted response of a virgin specimen, since the initial departure of the strain hardening assumption from the predicted curve can be rationalized as anelastic strain which would not have occurred if the specimen had not been unloaded at 850°F. However, for the assumption of virgin specimen behavior at 1100°F, the current results give strains a factor of 2 to 3 smaller than predicted values. The strain hardening assumption gives somewhat better agreement as shown in Figure 3.4, but the construction shown still predicts a strain value of 0.108% at 1000 hours for the present test, while we observed a strain of only 0.068%. We therefore conclude that, while prior strain history apparently has an effect on the 1100°F creep response, the simple strain hardening rule does not fully explain the observed decrease in creep rate over the first 1000 hours of testing.

Creep recovery results for all three test temperatures are presented in Figure 3.5. The time dependence of strain recovery is essentially the same at 860 and 1000°F, with the magnitude of strain recovery being about four times larger at 1000°F. On the other hand, the total strain recovery is comparable in magnitude at both 1000 and 1100°F, but the recovery occurs more rapidly at the higher temperature. The magnitude of creep strain recovery observed in these tests is only a small fraction of the elastic strain.

The observed creep response after reloading is slightly different at the three test temperatures. Creep deformation after reloading is in good agreement with that predicted from the reoccurrence of anelastic strain and continued plastic creep strain at 850°F,[2] but is slightly higher than predicted at 1000°F (Figure 3.2) and slightly lower than predicted at 1100°F (Figure 3.3). Our earlier view[2] was that the reloading results at 1000°F suggested possible static thermal recovery during the prior unload period. However, in view of the fact that the 1100°F results show no evidence of enhanced creep strain after reloading, it now appears that static thermal recovery is not significant in these

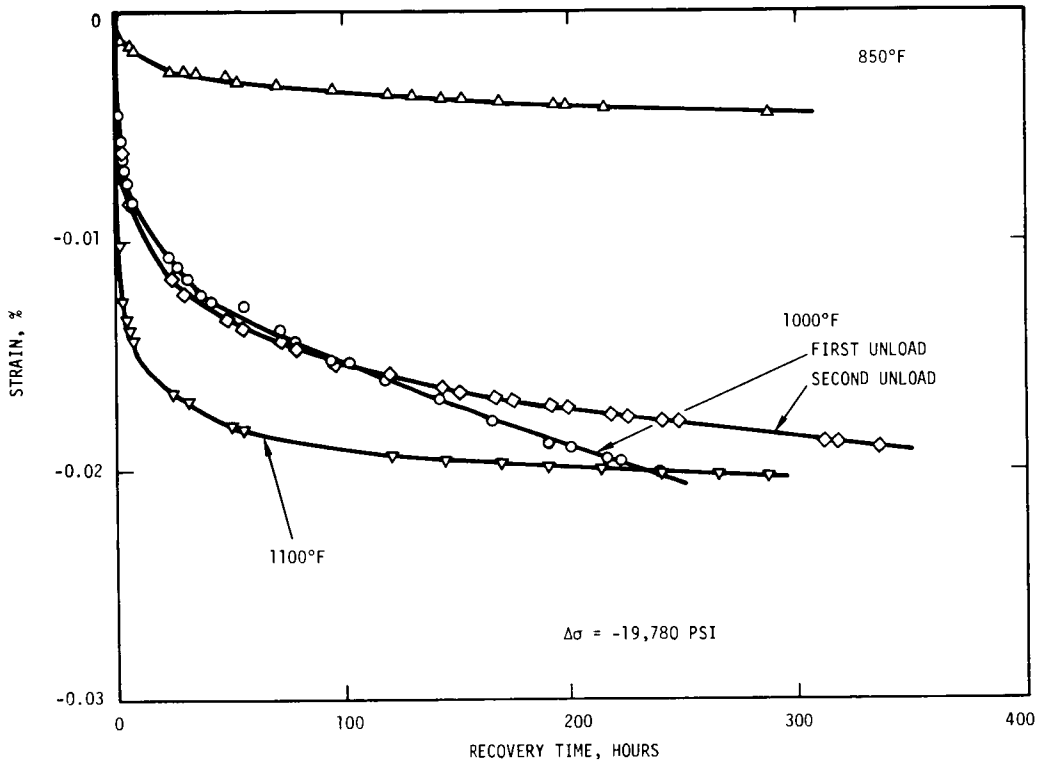

HEDL 7412-22.20

FIGURE 3.5. Creep Recovery Results for 20% Cold Worked Type 316 Stainless Steel at 850, 1000 and 1100°F.

experiments. We presently have no physical explanation for the slight differences in observed and predicted response after reloading.

The microwave extensometer employed in this test has now operated for about 5600 hours over the temperature range from 850 to 1100°F. Strain measurement sensitivity is still of the order of 10^{-6}, and the reproducibility of the elastic extension and contraction measurements which were made periodically throughout the test indicate that the extensometer calibration has not changed perceptibly during service. Such results continue to demonstrate the applicability of microwave extensometers for sensitive, precise creep strain measurements.

3.2.1.2.4 Conclusions and/or Recommendations. Creep curves obtained from a single specimen of 20% cold worked Type 316 stainless steel tested at 20,000 psi over a series of progressively higher temperatures (850, 1000, 1100°F) show that creep strain increases with increasing temperature. The introduction of only 0.06% creep strain during the 850 and 1000°F loadings appears to significantly affect the creep response at 1100°F. A simple strain hardening rule does not fully account for the effect of prior strain history. Creep response after unloading exhibits measurable strain recovery at all temperatures and is consistent with an anelastic component in the total creep deformation. The magnitude of recovered strain is of the order of 0.02% at both 1000 and 1100°F. To a first approximation, creep response after reloading is consistent with the re-introduction of anelastic strain recovered during the prior unload and the continued accumulation of creep strain as if unloading had not occurred. Test results continue to demonstrate the applicability of the microwave extensometer for sensitive, precise creep strain measurements.

3.2.2 Thermal Creep in Pressurized Tubes of 20% Cold Worked Type 316 Stainless Steel

3.2.2.1 Objective

The purpose of this work is to determine the thermal creep deformation of pressurized tubes of 20% cold worked Type 316 stainless steel.

Results of these experiments will be compared with companion in-reactor tests to define the irradiation creep component of in-reactor deformation.

3.2.2.2 Accomplishments and Status

3.2.2.2.1 Scope of Work. Experimental measurements of creep strains in pressurized tube samples of 20% cold worked Type 316 stainless steel were reported previously.(5) These specimens covered the temperature range from 825 to 1400°F for times to 2400 hours at stresses up to 60,000 psi. In this report, we present the results of a detailed analysis of these data which yield an analytical description of the experimental results. This description of thermal creep behavior finds application in the analysis and interpretation of in-reactor creep experiments, and also in inelastic analysis of reactor components.

Experimental details were reported previously,(5) but several features will be repeated here for clarity. We computed stresses using the thin-wall approximations:

$$\sigma_\theta = \frac{p\ d_m}{2w}$$

$$\sigma_z = \frac{p\ d_m}{4w}$$

$$\sigma_r = 0$$

where σ_θ, σ_z, and σ_r are the circumferential (hoop), axial, and radial stresses, respectively, p is the difference between internal and external pressures, d_m is the midwall tube diameter, and w is the tube wall thickness. Effective stress is given by:

$$\sigma_e = \frac{1}{\sqrt{2}} \left[(\sigma_\theta-\sigma_z)^2 + (\sigma_z-\sigma_r)^2 + (\sigma_r-\sigma_\theta)^2\right]^{1/2}$$

$$= \frac{\sqrt{3}}{2}\ \sigma_\theta$$

This computation of effective stress is in good agreement with the midwall effective stress computed from exact elastic solutions for a

pressurized tube. We expect midwall stresses to change very little as a result of stress redistribution accompanying creep deformation. Consequently, we elected to describe deformation in terms of midwall hoop strain, since the selection of hoop strain at the external or internal diameter would result in a greater distortion of the correct effective stress-effective strain relation. Measured hoop strains at the external diameter were converted to midwall hoop strain based on conservation of volume with zero axial strain; for the present specimen geometry, measured strains were multiplied by 1.15 to obtain midwall hoop strains.

Specimens employed in this study were pressurized and sealed, so assuming uniform deformation, the pressure-volume product is constant as the specimen deforms. As a result, the stress does not increase with strain as it does in a specimen subjected to a constant pressure, but remains nearly constant.

3.2.2.2.2 Results. Experimental hoop strain values for various creep times and stresses are tabulated in Ref. 5. Our analysis begins with a description of the relation between strain and stress with time as a parameter. This starting point contrasts with that frequently used in describing uniaxial creep results, which begins with a formulation of the time dependence of creep strain with stress as a parameter. The basic reason for this difference is the widely spaced time intervals between strain measurements in the present experiment, but it is interesting to note that early attempts to begin the analysis with a strain-time relation failed to identify an analytical form which would apply over the complete time and temperature ranges. As we shall see, however, a consistent description of time dependence is obtained when we begin with the strain-stress relation.

The experimental results consistently show a linear dependence of strain on stress at low stress levels, with a much stronger stress dependence appearing at higher stress levels. As illustrated in Figure 3.6, we described this behavior as the sum of two strain components, one which exhibits a linear stress dependence and one which exhibits some stronger stress dependence. In evaluating the slope, $C(t)$, of the

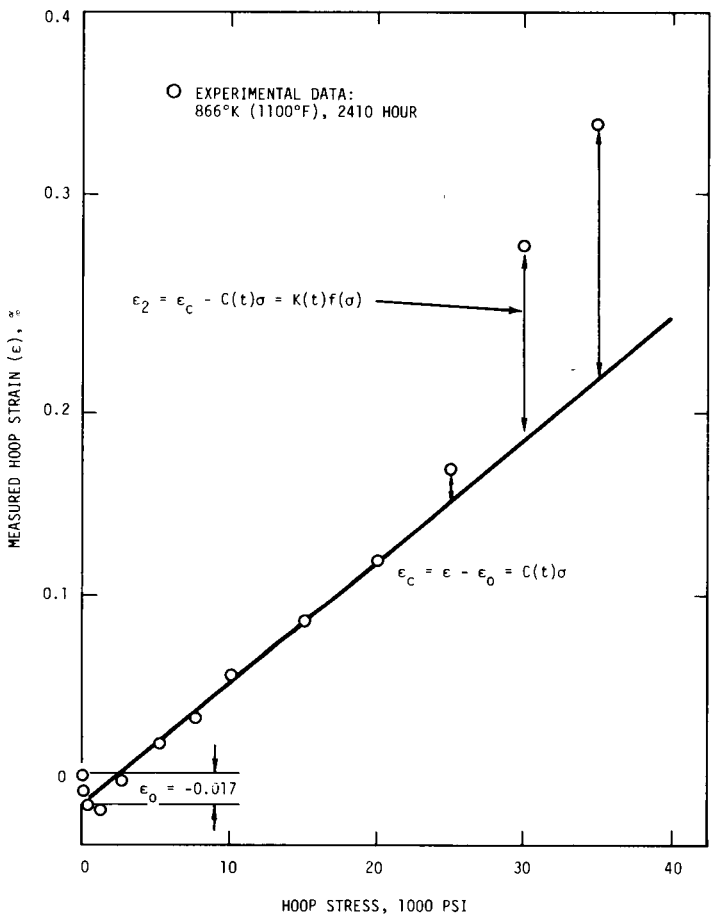

HEDL 7412-22.2

FIGURE 3.6. Illustration of Analysis Procedure for Strain-Stress Data.

linear strain-stress relation, the fit to the experimental data was allowed to intercept the strain axis at non-zero values (Figure 3.6). These strain intercept values, ε_o, were generally in the range ± 0.02%, which is considered to be within the measurement uncertainty, and showed no systematic variation with either time or temperature. We then define creep strain, ε_c, as:

$$\varepsilon_c = \varepsilon - \varepsilon_o$$

where ε is the measured hoop strain and ε_o is the intercept strain which may be either positive or negative. Our description of the two strain components is then given by :

$$\varepsilon_1 = C(t)\ \sigma$$

$$\varepsilon_2 = \varepsilon_c - \varepsilon_1 = \varepsilon_c - C(t)\ \sigma$$

Values of C(t) were determined from each set of strain-stress data, and are plotted against log (t) in Figure 3.7. These results were described by an equation of the form:

$$C(t) = A \cosh^{-1} (1 + rt)$$

where $\cosh^{-1} x = \ln (x + \sqrt{x^2+1})$, as shown in Figure 3.7. Swindeman and Pugh[6] suggested the inverse hyperbolic cosine function for describing creep data, but did not explore its application in detail. This function has the characteristics of ln (1+rt) at long times, but does not decrease as rapidly as ln (1+rt) at short times. Blackburn et. al.[7] reported results of a uniaxial creep test on a rod specimen at conditions within the present linear stress dependence range (i.e., 850°F, 20,000 psi). These data are plotted in Figure 3.8, along with analytical descriptions based on both $\cosh^{-1}$ (1+rt) and ln (1+rt). The $\cosh^{-1}$ (1+rt) function clearly yields the better description of the uniaxial experiment results, and was therefore selected for describing the present C(t) results. Values of the parameters A and r derived from the C(t) results in Figure 3.8 are presented in Figure 3.9, along with the analytical description

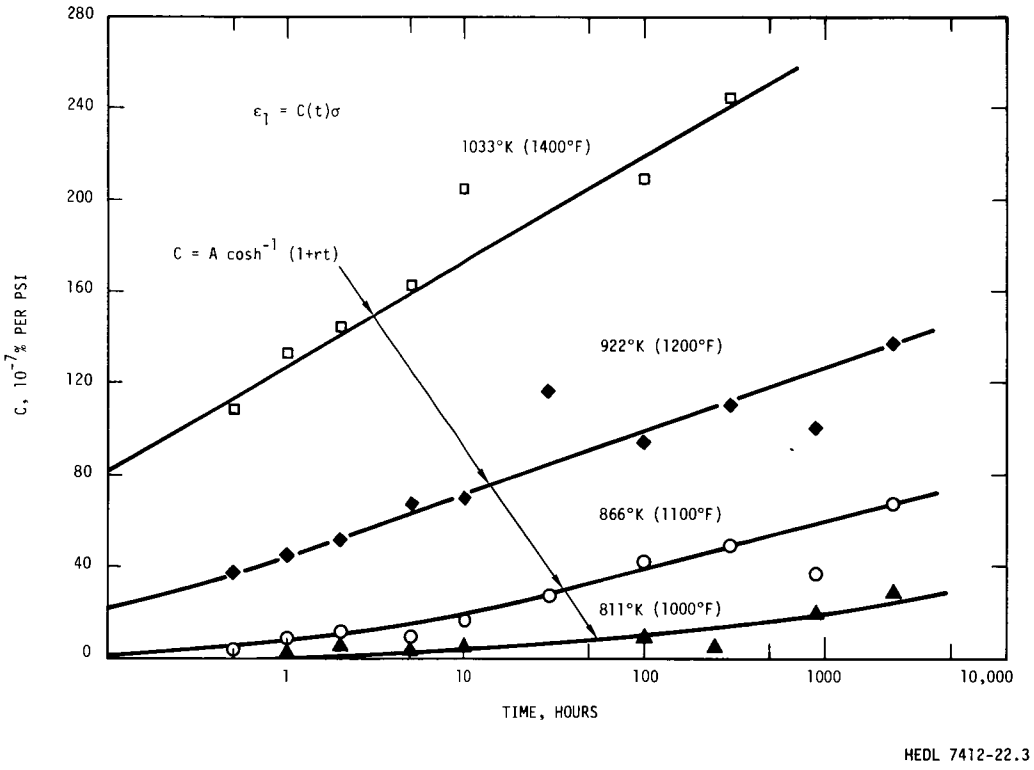

FIGURE 3.7. Experimental Results and Analytical Description for C(t).

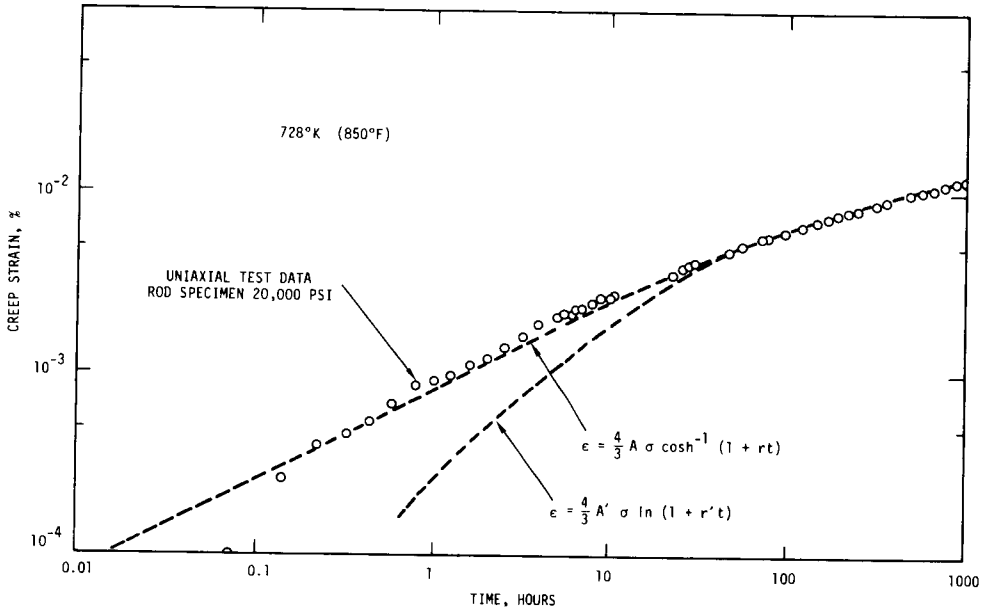

HEDL 7412-22.7

FIGURE 3.8. Analytical Descriptions of Creep Data Using $\cosh^{-1}$ (1 + rt) and ln (1 + rt) Functions.

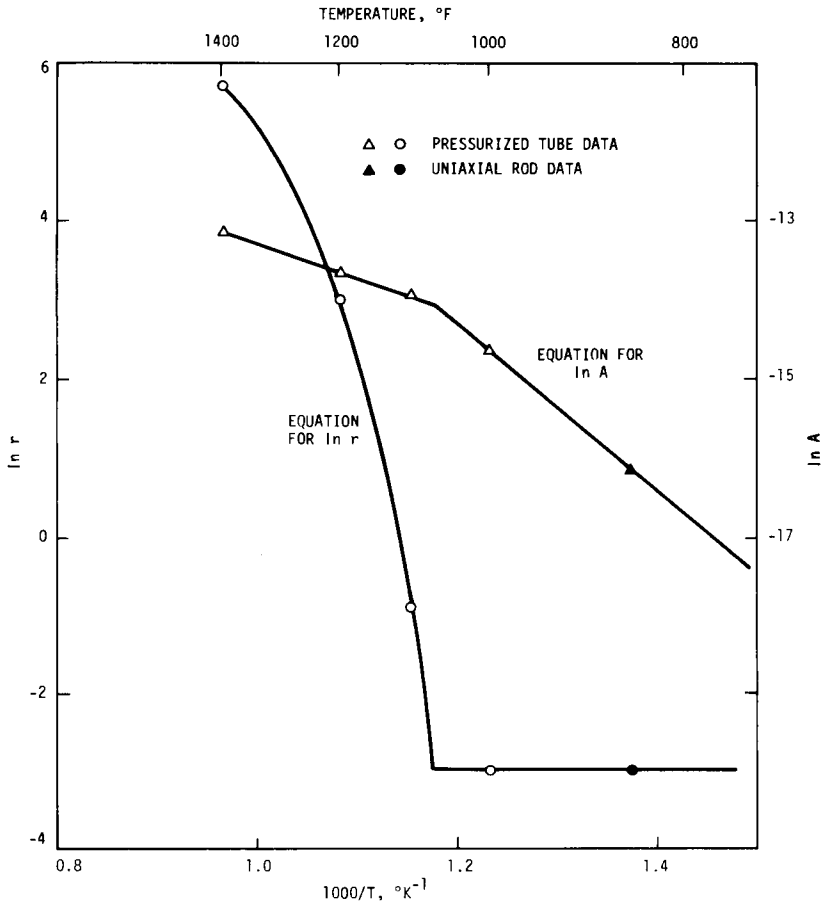

FIGURE 3.9. Temperature Dependence of A and r in the Relation $\varepsilon^c = A\sigma \cosh^{-1}(1 + rt)$.

of the temperature dependence of these parameters. The complete equations describing the strain component with linear stress dependence are as follows:

$$\varepsilon_1 = A\sigma \cosh^{-1}(1+rt)$$

$$\ln A = \begin{cases} -8.94451 - \dfrac{4331.4}{T} \\ \text{or} \\ -1.3748 - \dfrac{10747.1}{T} \end{cases}$$

whichever yields the smaller value of ln A,

$$\ln r = \begin{cases} 291.069 - \dfrac{926425.0}{T} + \dfrac{1.0114 \times 10^9}{T^2} - \dfrac{3.70757 \times 10^{11}}{T^3} \\ \text{or} \\ -2.99573 \end{cases}$$

whichever yields the larger value of ln r,,

where T is temperature in °K ($T = \frac{5(F-32)}{9} + 273.15$, where F is temperature in °F).

We turn now to a description of the strain component ε_2, which exhibits a strong stress dependence. We represent this strain component with an equation of the form:

$$\varepsilon_2 = K(t)\ \sigma^n$$

Figure 3.10 shows a plot of log ε_2 against log σ for the 2410-hour data illustrating this relation. We obtain an n value of 6.3 at temperatures of 1200°F and below and a value of 4.4 at 1400°F. The results in Figure 3.10 for the three lower temperatures yield a well-defined n value which represents the data well over the whole time range. The n value at 1400°F is not as well-defined by the results in Figure 3.10, and the selected value of 4.4 was judged to give the best overall representation of all

the 1400°F data. The temperature dependence of n is described by the following equations:

For $T \leq 922.039°K$ (1200°F)

$$n = 6.3$$

For $T > 922.039°K$ (1200°F)

$$n = -124.539 + 0.283804\ T - 1.539 \times 10^{-4}\ T^2$$

The polynomial coefficients were evaluated by requiring that n = 6.3 at 1200°F, n = 4.4 at 1400°F, and $\frac{dn}{dT} = 0$ at 1200°F, thus providing a smooth transition from the constant n value at lower temperatures.

Values of K(t) at each time where non-linear stress dependence was observed were obtained from a series of plots similar to Figure 3.10. The variation of K(t) with time is illustrated in Figure 3.11. At short times, K(t) can be represented by the relation:

$$K(t) = K_1\ t^m$$

where m is 0.533 at 1200°F and below, but is 1.172 at 1400°F. The temperature dependence of m is given by the equations:

For $T \leq 922.039°K$ (1200°F)

$$m = 0.533$$

For $T > 922.039°K$ (1200°F)

$$m = 44.5365 - 0.0954482\ T + 5.17593 \times 10^{-5}\ T^2$$

Polynomial coefficients were evaluated by requiring that m = 0.533 at 1200°F, m = 1.172 at 1400°F, and $\frac{dm}{dT} = 0$ at 1200°F, thus assuring a smooth transition from the constant m value at lower temperatures. There is clearly a departure from the $K_1 t^m$ relation at longer times in the direction of a stronger time dependence for the results at 1000, 1200 and 1400°F. This behavior was described by adding another term, $K_2 t^{2.5}$, to the above relation, as illustrated in Figure 3.11. The equation describing K(t) thus becomes:

$$K(t) = K_1 t^m + K_2 t^{2.5}$$

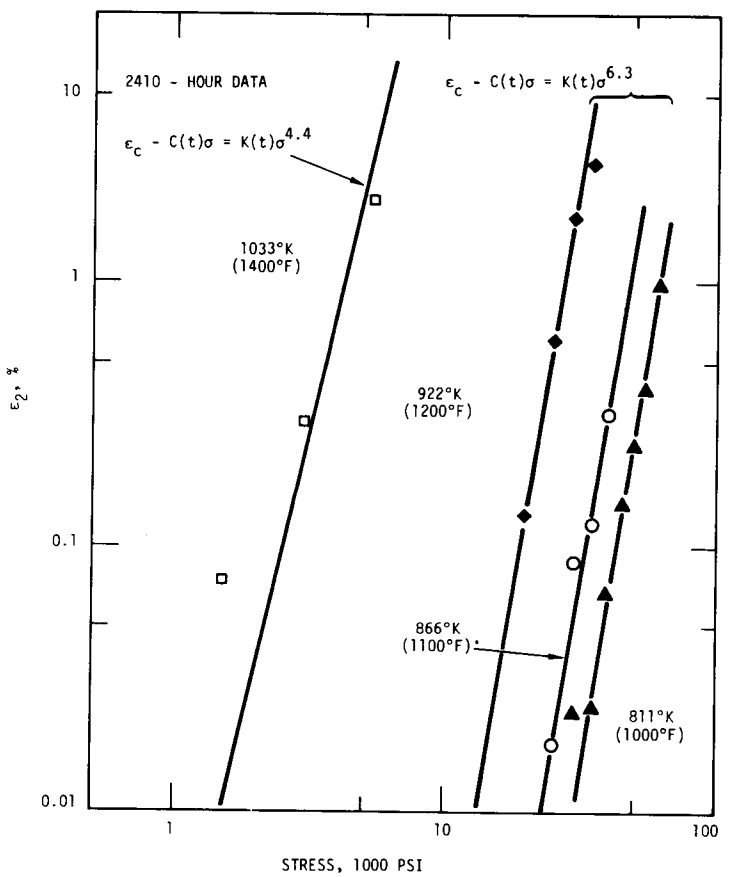

HEDL 7412-22.4

FIGURE 3.10. Illustration of the Stress Dependence of Strain Component ε_2.

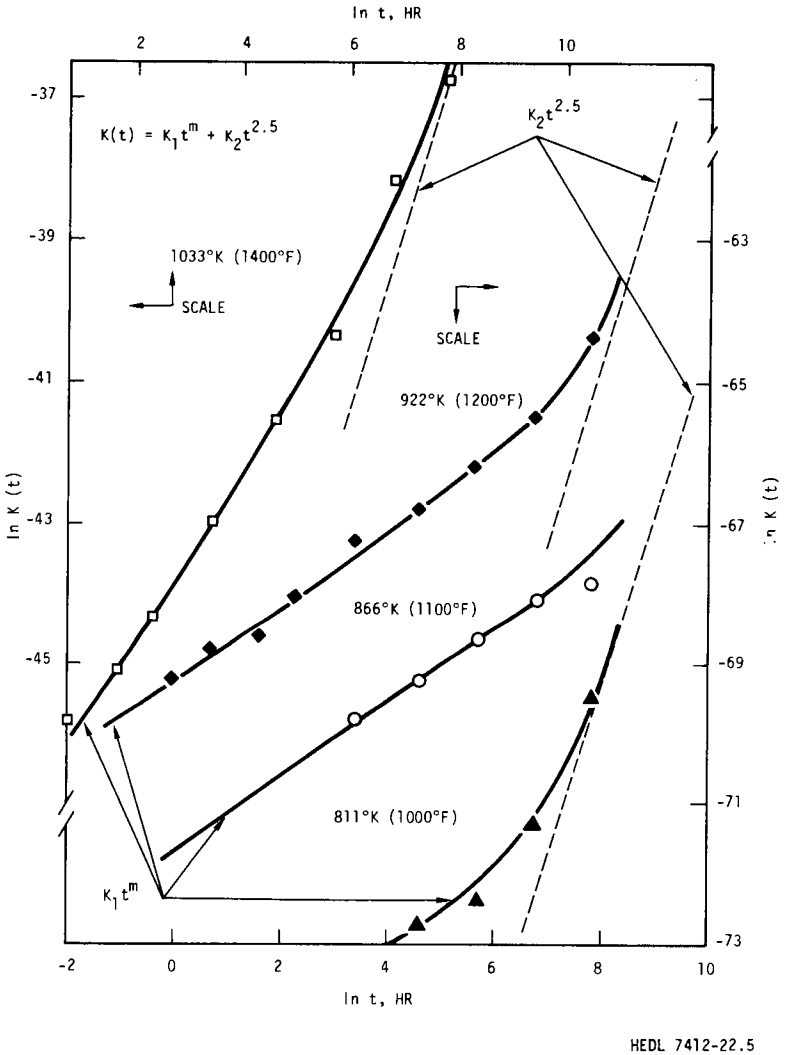

FIGURE 3.11. Time Dependence of K(t) in the Relation $\varepsilon_2 = K(t)\sigma^n$.

Values of K_1 and K_2 obtained from Figure 3.11 are presented in Figure 3.12, where the temperature dependence of these parameters is given by the equations:

For 1033.15°K (1400°F) ≥ T ≥ 810.928°K (1000°F)

$$\ln K_1 = 5131.26 - \frac{1.35198\text{x}10^7}{T} + \frac{1.17285\text{x}10^{10}}{T^2} - \frac{3.39674\text{x}10^{12}}{T^3}$$

For T < 810.928°K (1000°F)

$$\ln K_1 = 35.3606 - \frac{89658.6}{T}$$

For 1033.15°K (1400°F) ≥ T ≥ 866.483°K (1100°F)

$$\ln K_2 = 1179.06 - \frac{2.19791\text{x}10^6}{T} + \frac{9.52226\text{x}10^8}{T^2}$$

For 866.483°K (1000°F) > T ≥ 810.928°K (1000°F)

$$\ln K_2 = -89.2335$$

For T < 810.928°K (1000°F)

$$\ln K_2 = -453.917 + \frac{5.91409\text{x}10^5}{T} - \frac{2.39794\text{x}10^8}{T^2}$$

The extrapolation of $\ln K_1$ below 1000°F is made using the slope of the third order polynomial for the high temperature range evaluated at 1000°F. This assures a smooth transition in the temperature dependence of K_1. Extrapolation of $\ln K_2$ below 1000°F is based on a second order polynomial in 1/T, with coefficients evaluated to give $\ln K_2 = -89.2335$ at 1000°F, $d \ln K_2/d(\frac{1}{T}) = 0$ at 1000°F, and $\ln K_2 = -96$ at 825°F. This again assures a smooth transition in the temperature dependence of K_2, and the value of $\ln K_2$ imposed at 825°F assures that the strain contribution from the term containing K_2 is negligible at this low temperature. We impose this latter requirement since the experimental hoop strain data at 825°F show no evidence of non-linear stress dependence (see Figure 3.21).

Our final description of creep strain is therefore:

$$\varepsilon^c = A\sigma \cosh^{-1}(1+rt) + K_1\sigma^n t^m + K_2\sigma^n t^{2.5}$$

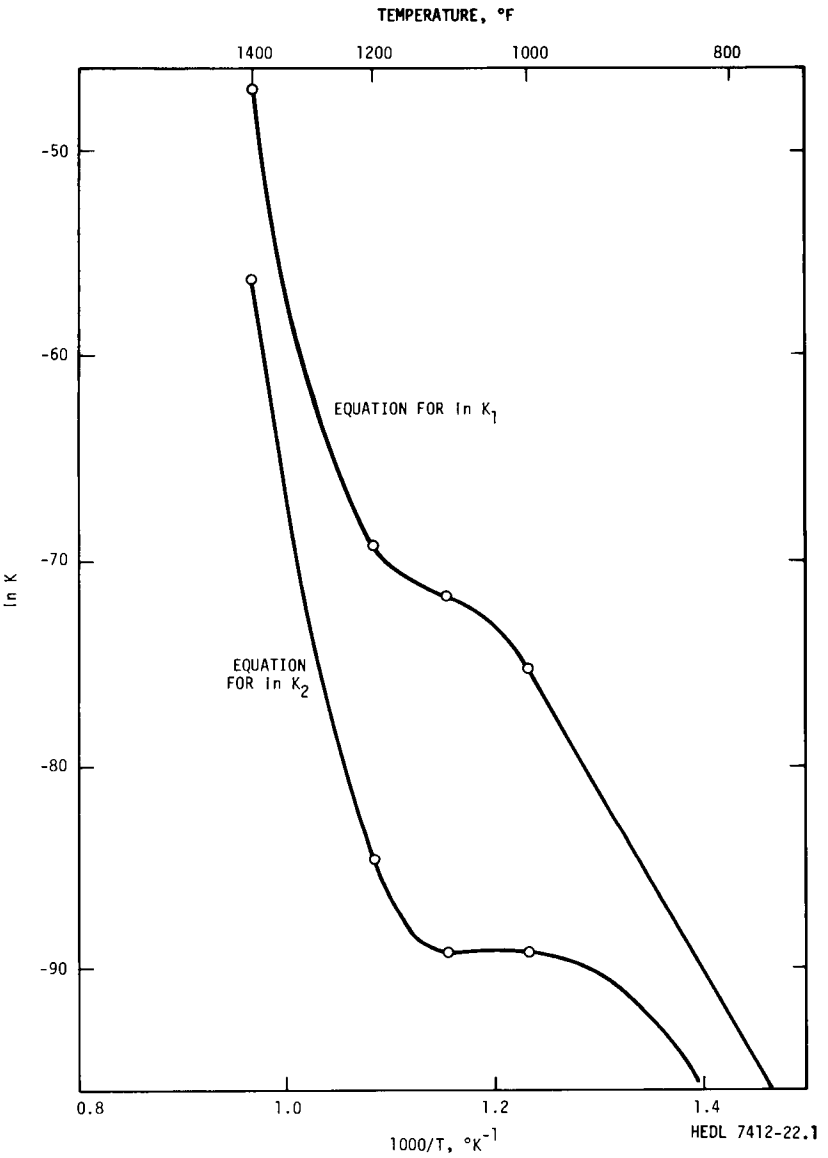

FIGURE 3.12. Temperature Dependence of K_1 and K_2 in the Relation $\varepsilon_2 = K_1\sigma^n t^m + K_2\sigma^n t^{2.5}$

Using the numerical values of the parameters A, r, K_1, K_2, n and m obtained from the equations given earlier, this relation predicts the midwall hoop strain, ε^c, in percent when hoop stress is given in psi (using thin-wall approximation), and time, t, is given in hours.

3.2.2.2.3 Evaluation of Results. The description of creep behavior given by the equations derived in the preceding section is compared with the experimental data in Figures 3.13-3.21. Comparisons in Figures 3.13-3.16 are shown on log ε^c against log t plots, with experimental points plotted as the measured strain minus ε_o (see Figure 3.6). In general, the analytical description of the experimental results is good at 1400°F (Figure 3.13), although the equations overpredict creep strain for longer times at 5.4 ksi and underpredict strain at long times at 1.5 ksi. Specimen failure is observed at the three highest stresses as evidenced by a constant value of creep strain for the longer times. At 1200 and 1100°F, the creep equations again provide a good description of the experimental data (Figures 3.14 and 3.15). The comparison for 1000°F shown in Figure 3.16 shows substantial scatter in the experimental results. We estimate the experimental uncertainty for our strain measurements to be in the range ± 0.02 to ± 0.04%, so the scatter appears very large in logarithmic coordinates at these low strain values. However, when the comparison is viewed in linear coordinates (see Figure 3.20), the description appears quite reasonable.

Figures 3.17-3.20 present comparisons of creep equations and experimental data in linear strain-time coordinates. The computed creep curves show the typical features of creep behavior: an initial period of primary creep, a minimum creep rate, and then accelerating creep in third stage. A number of the low stress curves appear to exhibit a steady-state creep rate, even though a steady-state creep term is not included in the analytical equations.

Experimental data at 825°F did not give a clear picture of creep behavior because the small strains were near the limit of detectability. However, the results shown in Figure 3.21 indicate that the procedure of deriving the creep equation from the uniaxial data at 850°F and

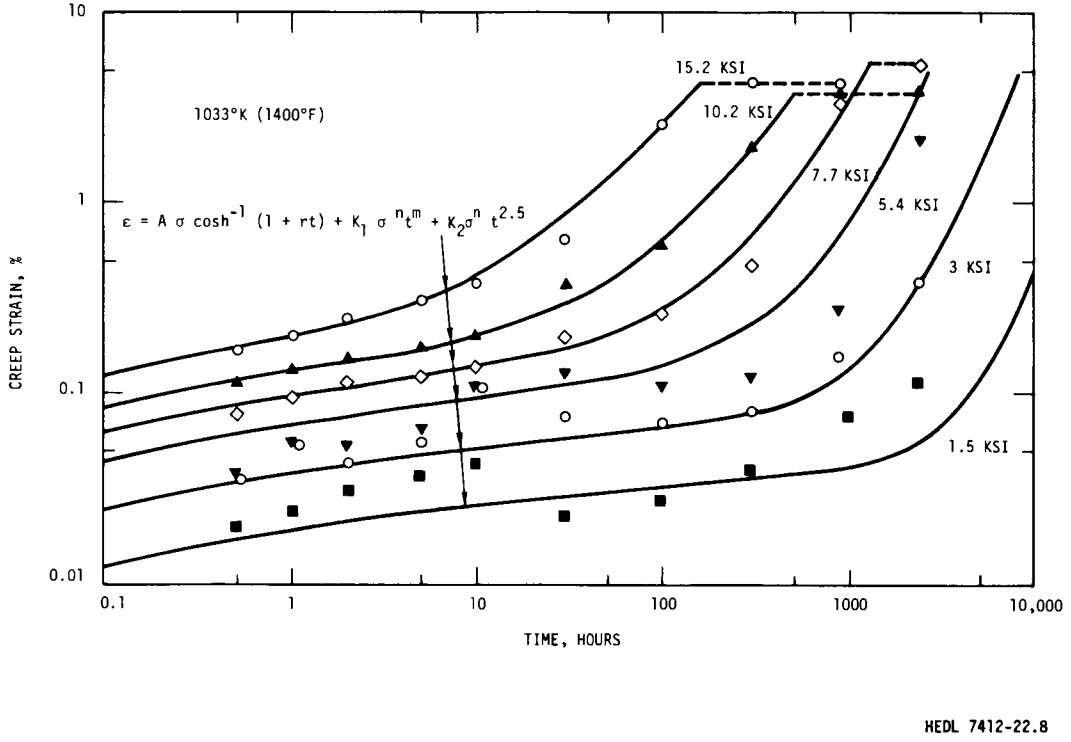

FIGURE 3.13. Comparison of Analytical Creep Equation Preditions with Experimental Data at 1400°F.

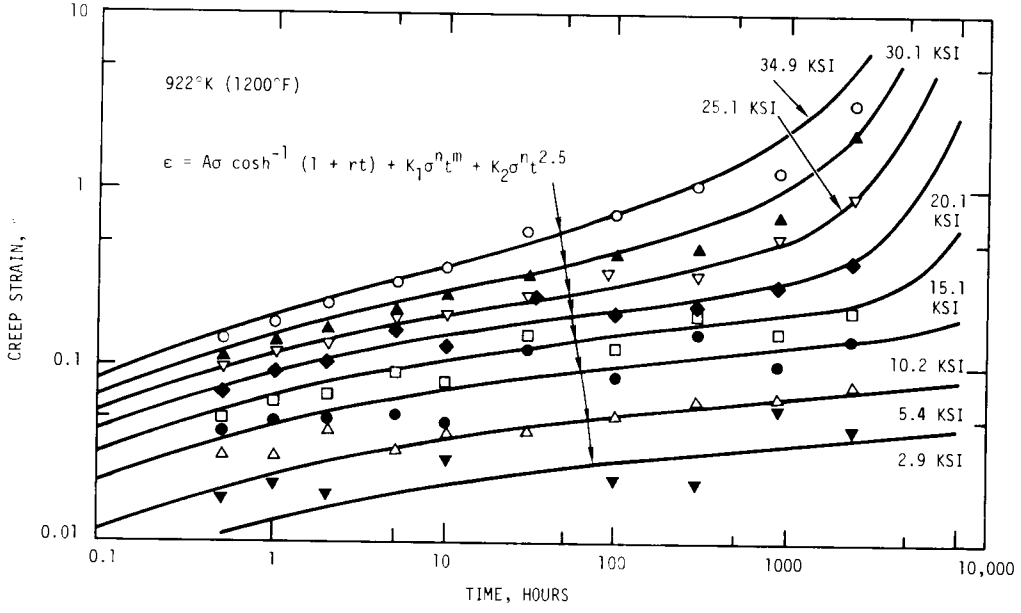

HEDL 7412-22.9

FIGURE 3.14. Comparison of Analytical Creep Equation Predictions with Experimental Data at 1200°F.

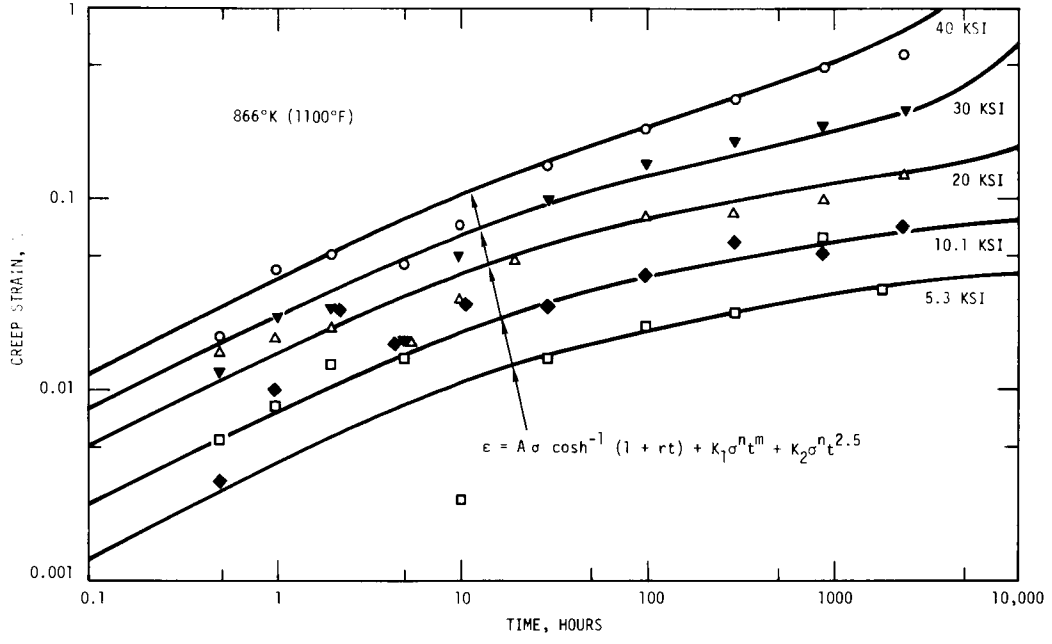

HEDL 7412-22.10

FIGURE 3.15. Comparison of Analytical Creep Equation Predictions with Experimental Data at 1100°F.

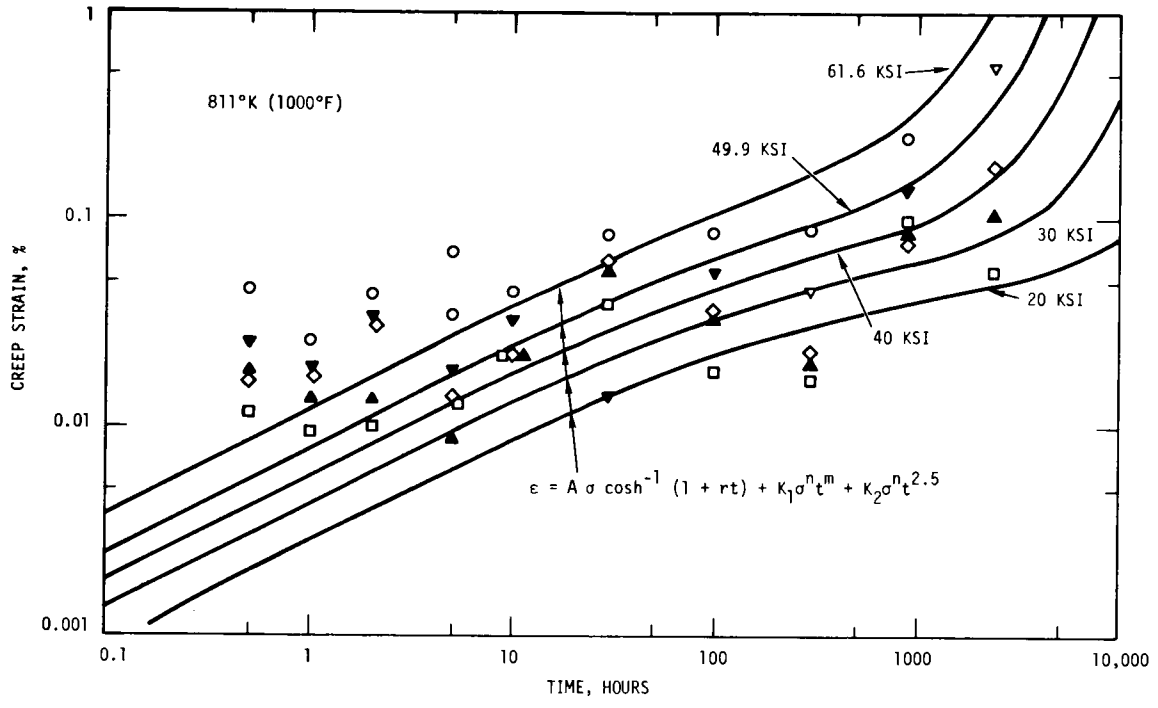

HEDL 7412-22.11

FIGURE 3.16. Comparison of Analytical Creep Equation Predictions with Experimental Data at 1000°F.

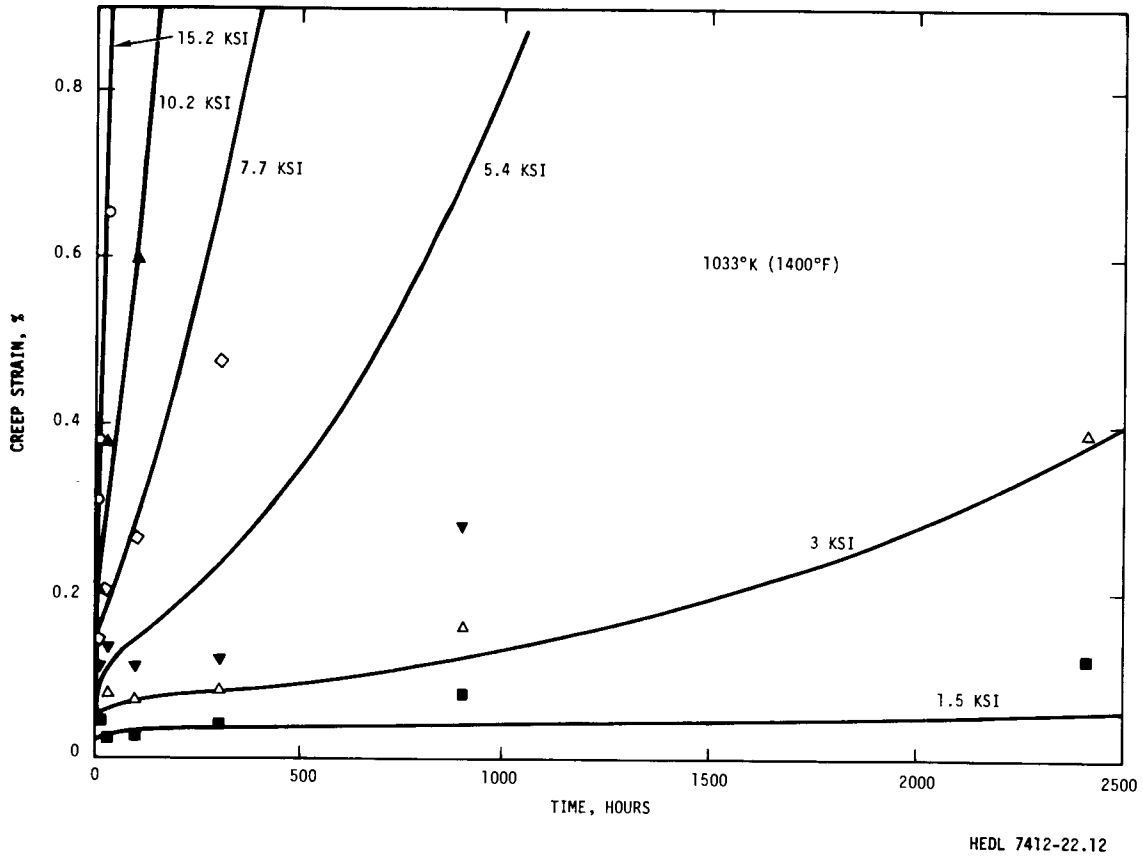

FIGURE 3.17. Comparison of Analytical Creep Equation Predictions with Experimental Data at 1400°F.

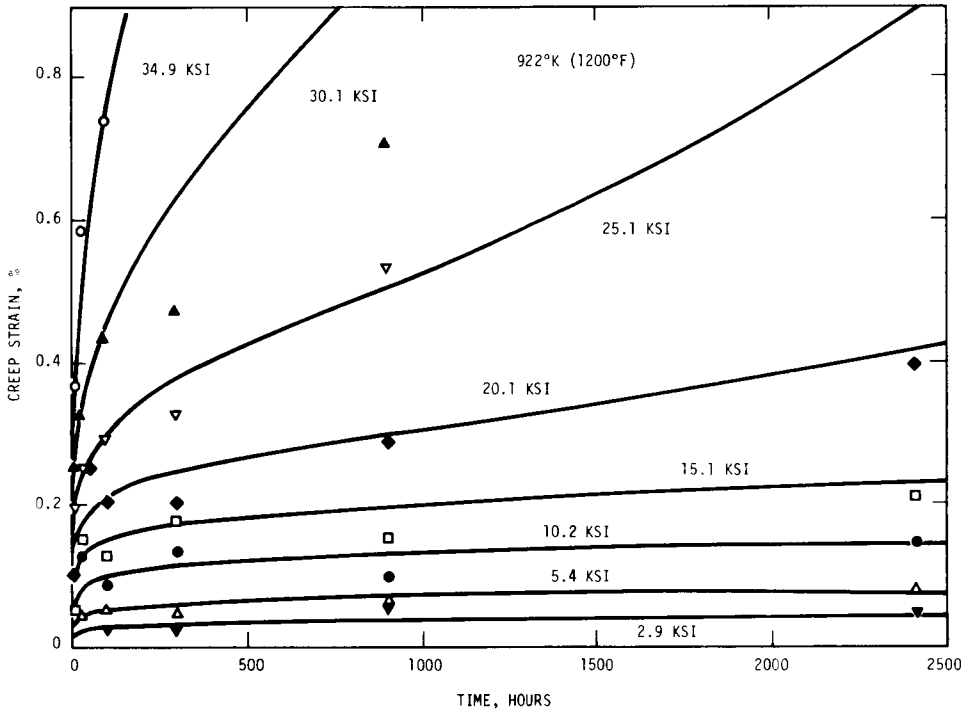

FIGURE 3.18. Comparison of Analytical Creep Equation Predictions with Experimental Data at 1200°F.

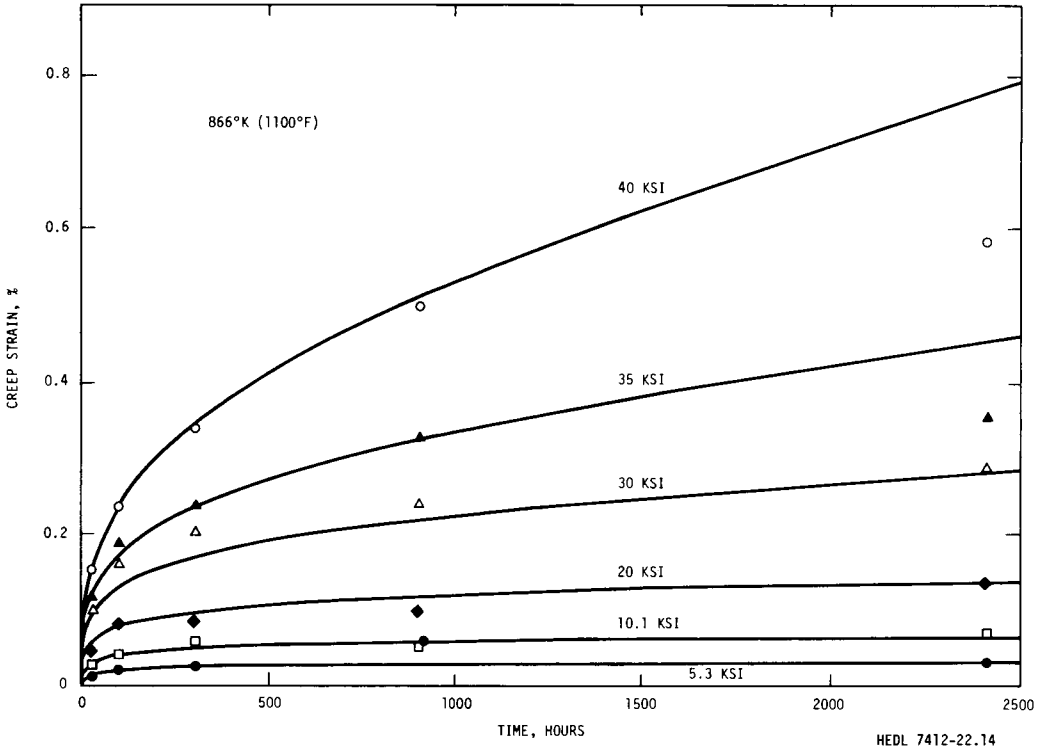

FIGURE 3.19. Comparison of Analytical Creep Equation Predictions with Experimental Data at 1100°F.

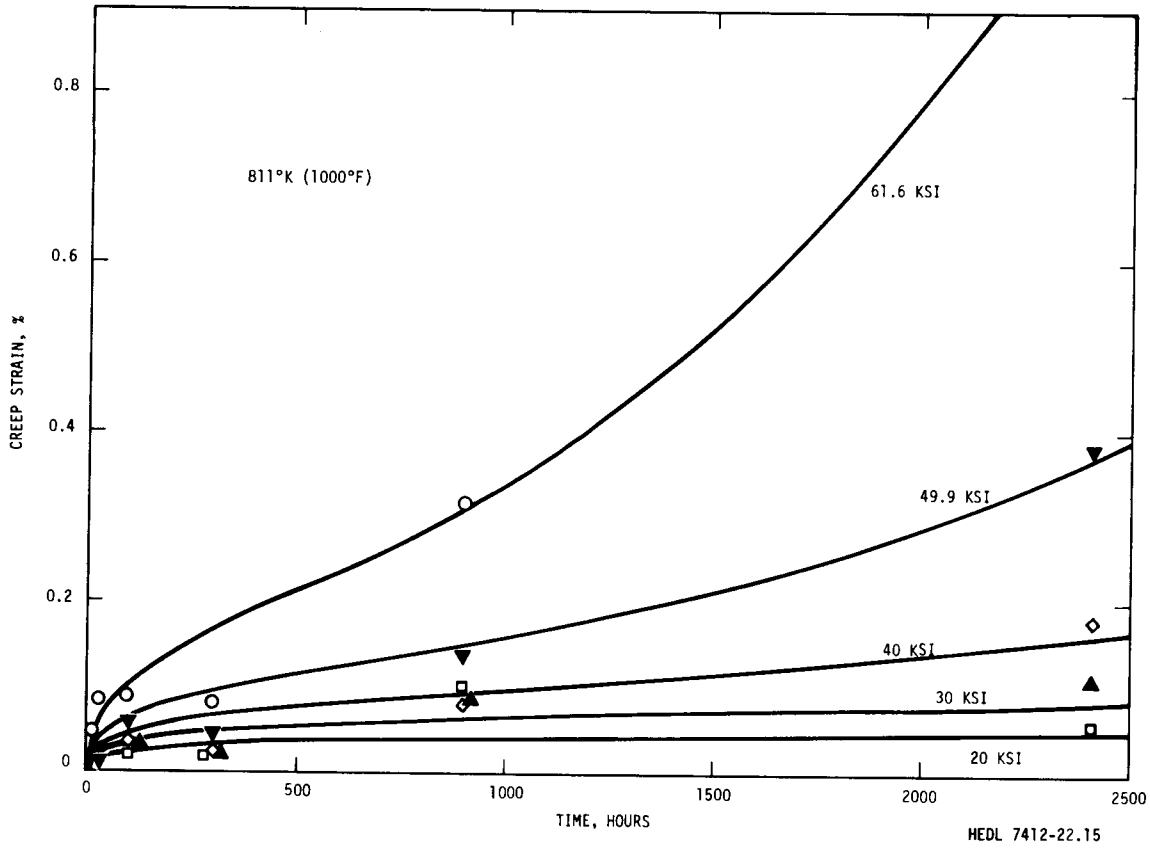

FIGURE 3.20. Comparison of Analytical Creep Equation Predictions with Experimental Data at 1000°F.

suppressing strain contribution from terms containing K_1 and K_2 yields a very reasonable representation of the data. (Note: Strain values plotted in Figure 3.21 were not adjusted by subtracting ε_o.)

Lovell[8] formulated creep equations for 20% cold worked Type 316 stainless steel based on results from uniaxial creep tests, but these equations tend to overpredict the present pressurized tube results.[5] We have made a detailed comparison of the data reported by Lovell for tube and rod specimens with the present experimental results on pressurized tubes.* One illustration of these comparisons is shown in the isochronous effective strain-effective stress plot of Figure 3.22. (Note: Plotted strain values for biaxial tests were not adjusted by subtracting ε_o.) Although the scatter is larger in the uniaxial results, we find basically good agreement between the uniaxial and biaxial results at low stresses, particularly for the tube material. However, at high stresses larger strains are observed in uniaxial tests than are predicted from extrapolation of the biaxial data. These observations were quite general for the temperature range from 1000 to 1400°F for times to 2400 hours. Since the pressurized tube data give a more complete definition of the low stress range, we prefer the present creep equations for describing both uniaxial and biaxial results.

The present creep equations may find application as input to constitutive equations for inelastic analysis of reactor components. Most computer programs require the materials creep description in terms of creep strain rate rather than creep strain for such calculations. We have therefore examined the behavior of the time derivative of present creep equations. Figures 3.23-3.25 show the relation between creep rate and creep strain at 1000, 1200 and 1400°F. The relation is smooth and continuous, as it should be for application in inelastic analyses. We also found that the creep rate was a smooth, continuous function of temperature.

---

*The tube material is identical in the two studies and the rod material was fabricated from the same heat of steel.

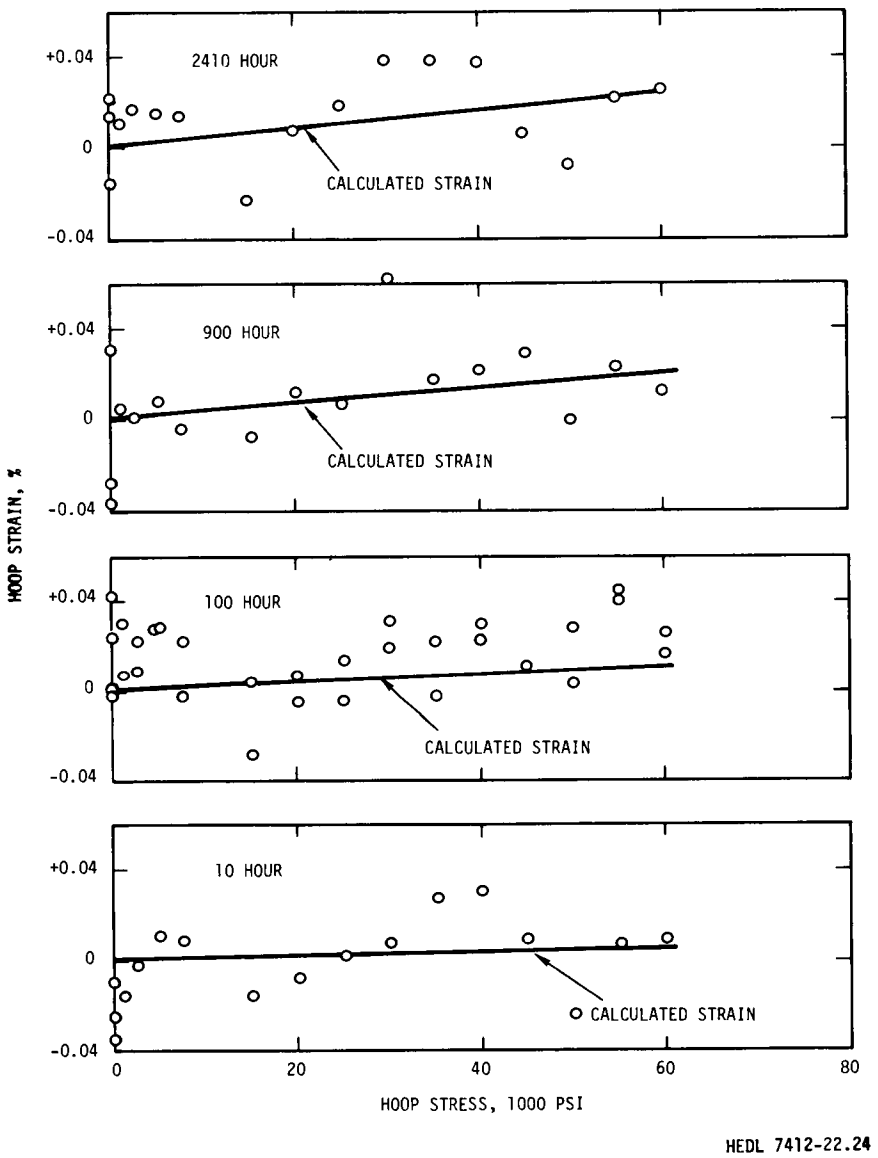

FIGURE 3.21. Comparison of Analytical Creep Equation Predictions with Experimental Data at 825°F.

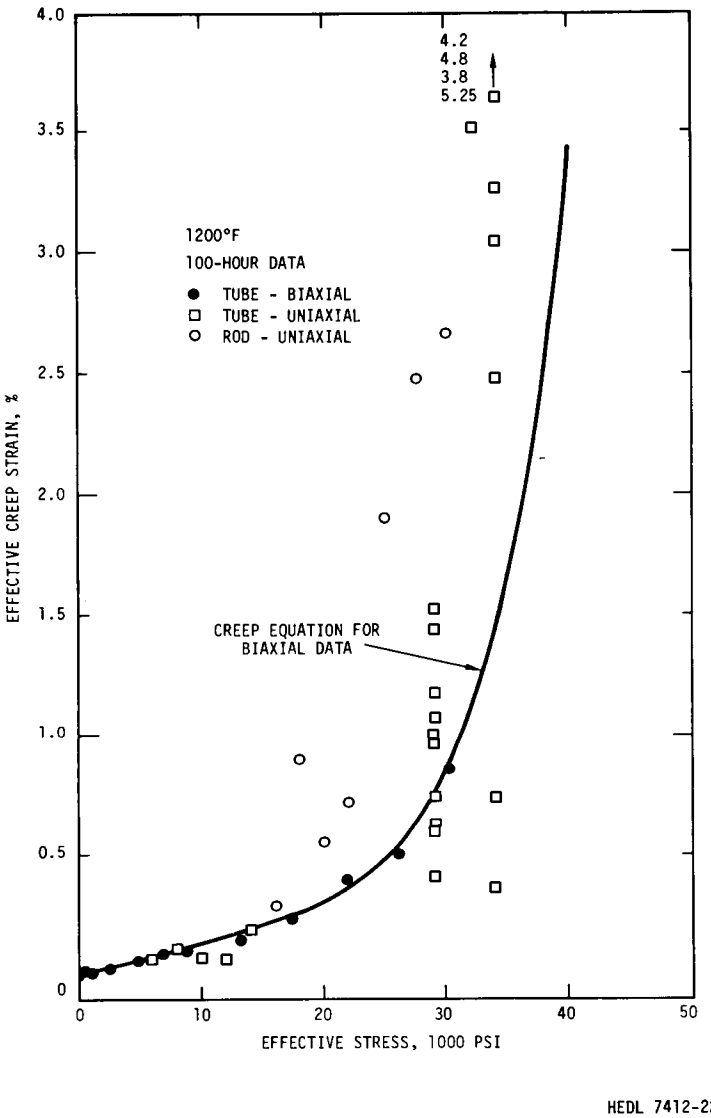

FIGURE 3.22. Comparison of 100-Hour Creep Data at 1200°F for Uniaxial and Biaxial Loading.

One problem for the application of the current creep equation in inelastic analyses is the definition of creep rate at t = 0. The equation for creep rate is:

$$\frac{d\varepsilon^c}{dt} = \frac{A\sigma r}{\sqrt{2rt+r^2t^2}} + mK_1{}^n\sigma t^{m-1} + 2.5K_2\sigma^n t^{1.5}$$

If $m < 1$, both the first and second terms give infinite creep rates at t = 0. To circumvent this singularity we propose specifying a finite, constant creep rate over some short time interval from t = 0 to $t = t_o$. The creep rate beyond t_o is then given by the time derivative of the creep equation. We examined this procedure to select a value of t_o which would not significantly alter the agreement between the creep equation and the experimental data. We arrived at the following procedure for using the creep equations in inelastic analysis:

$$\frac{d\varepsilon^c}{dt} = \frac{d\varepsilon_1{}^c}{dt} + \frac{d\varepsilon_2{}^c}{dt} + \frac{d\varepsilon_3{}^c}{dt}$$

For t = 0

$$\frac{d\varepsilon_1{}^c}{dt} = \frac{A\sigma r}{\sqrt{0.002\ r + 1x10^{-6}\ r^2}}$$

$$\frac{d\varepsilon_2{}^c}{dt} = \begin{cases} mK_1\sigma^n\ (0.001)^{m-1} & \text{for } m < 1 \\ K_1\sigma^n & \text{for } m = 1 \\ 0 & \text{for } m > 1 \end{cases}$$

$$\frac{d\varepsilon_3{}^c}{dt} = 0$$

For t > 0

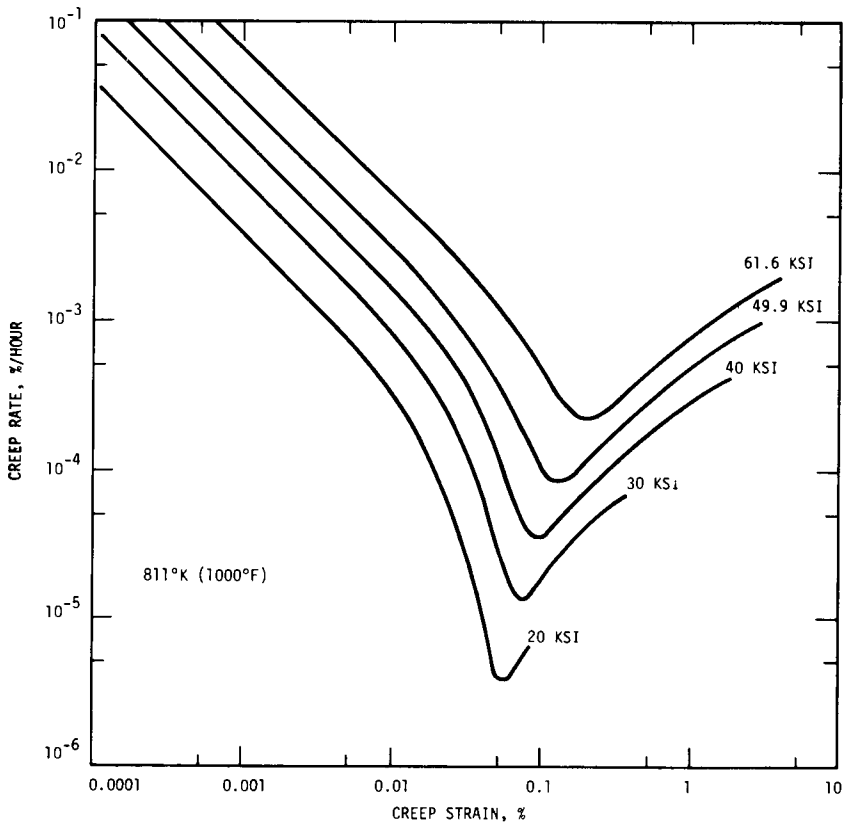

HEDL 7412-22.18

FIGURE 3.23. Computed Relation Between Creep Rate and Creep Strain at 1000°F.

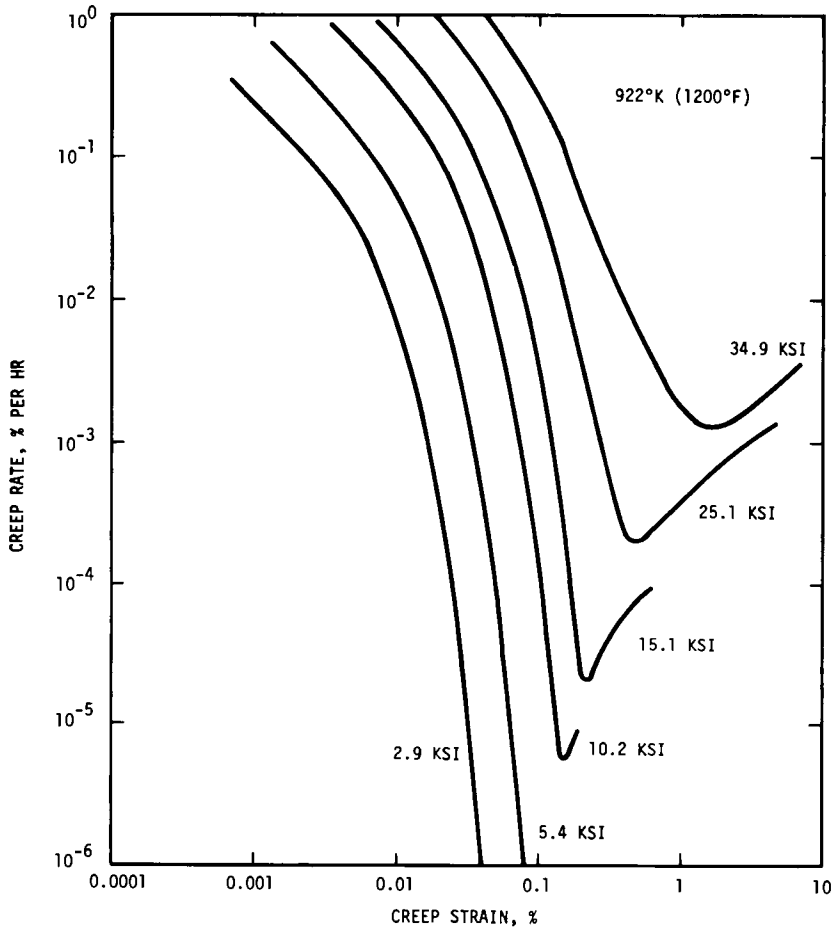

FIGURE 3.24. Computed Relation Between Creep Rate and Creep Strain at 1200°F.

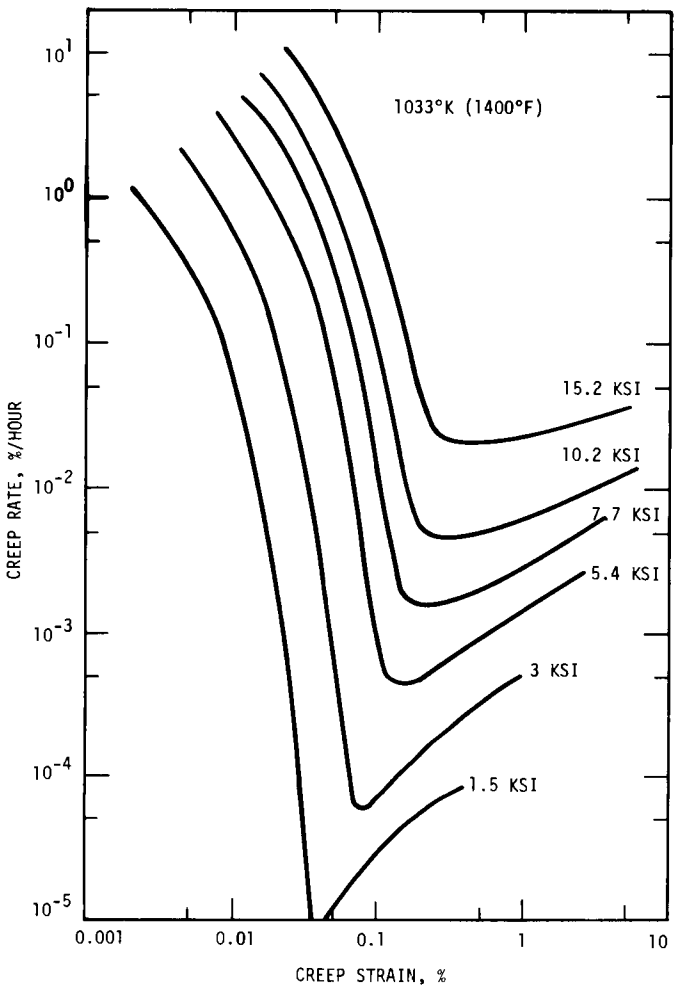

HEDL 7412-22.16

FIGURE 3.25. Computed Relation Between Creep Rate and Creep Strain at 1400°F.

$$\frac{d\varepsilon_1^c}{dt} = \begin{cases} \dfrac{A\sigma r}{\sqrt{2rt + r^2t^2}} \\ \text{or} \\ \dfrac{A\sigma r}{\sqrt{0.002\ r + 1x10^{-6}\ r^2}} \end{cases}$$

whichever yields the smaller value of $\frac{d\varepsilon_1^c}{dt}$

$$\frac{d\varepsilon_2^c}{dt} = \begin{cases} mK_1\sigma^n\ t^{m-1} \\ \text{or} \\ mK_1\sigma^n\ (0.001)^{m-1} \quad \text{[applied only if } m < 1\text{]} \end{cases}$$

whichever yields the smaller value of $\frac{d\varepsilon_2^c}{dt}$

$$\frac{d\varepsilon_3^c}{dt} = 2.5\ K_2\sigma^n\ t^{1.5}$$

The corresponding equations for strain are:

$$\varepsilon^c = \varepsilon_1^c + \varepsilon_2^2 + \varepsilon_3^c$$

For $t \leq 0.001$ hours

$$\varepsilon_1^c = \frac{A\sigma r\ t}{\sqrt{0.002\ r + 1x10^{-6}\ r^2}}$$

$$\varepsilon_2^c = \begin{cases} m\ K_1\sigma^n\ (0.001)^{m-1}\ t & \text{for } m < 1 \\ K_1\sigma^n\ t^m & \text{for } m \geq 1 \end{cases}$$

$$\varepsilon_3^c = K_2\sigma^n\ t^{2.5}$$

For $t > 0.001$ hours

$$\varepsilon_1^c = A\sigma\ \cosh^{-1}\ (1+rt) + \frac{0.001\ A\sigma r}{\sqrt{0.002\ r + 1x10^{-6}r^2}}$$

$$- A\sigma\ \cosh^{-1}\ (1+0.001\ r)$$

$$\varepsilon_2^c = \begin{cases} K_1\sigma^n\, t^m + mK_1\sigma^n\,(0.001)^m - K_1\sigma^n\,(0.001)^m & \text{if } m < 1 \\ K_1\sigma^n\, t^m & \text{if } m \geq 1 \end{cases}$$

$$\varepsilon_3^c = K_2\sigma^n\, t^{2.5}$$

To convert these equations to effective strain, $\bar{\varepsilon}$, and effective stress, $\bar{\sigma}$, units, replace ε by $\sqrt{3/2}\ \bar{\varepsilon}$ and σ by $2/\sqrt{3}\ \bar{\sigma}$.

3.2.2.2.4 Conclusions and/or Recommendations. The analytical equations developed here are a good representation of the thermal creep deformation of 20% cold worked Type 316 stainless steel over the temperature range from 825 to 1400°F for times to 2400 hours at stresses from zero to as high as 60,000 psi.

3.2.2.2.5 Expected Achievements. Experimental tests are still in progress, and 4000-hour creep data should be obtained during the next quarter.

3.3 LMFBR STRUCTURAL MATERIALS - T. T. Claudson and H. H. Yoshikawa

3.3.1 LMFBR Structural Materials Application

3.3.1.1 Accomplishments and Status

An initial characterization of the effect of neutron irradiation on the tensile properties of three reactor structural materials (Inconel 718, Inconel 600, and A-286) has been completed. Materials and irradiation conditions were representative of reactor components and operating conditions. Tensile test conditions included temperatures from room temperature to 1100°F and a strain rate of 3×10^{-5} in/in/sec. Preliminary results from these tests are presented herein.

Specimen irradiations were performed in Row II of EBR-II in subassembly X-195. Irradiation conditions for the test material were:

Inconel 718 - 760°F to 1.0×10^{22} n/cm^2 (E>0.1 MeV)
-1100°F to 0.9×10^{22} n/cm^2 (E>0.1 MeV)
Inconel 600 - 760°F to 0.25×10^{22} n/cm^2 (E>0.1 MeV)
A-286 - 800°F to 0.3×10^{22} n/cm^2 (E>0.1 MeV)

All specimens irradiated at temperatures of 760°F were irradiated in EBR-II coolant (weeper capsules). The higher irradiation temperatures (800 and 1100°F) were obtained by subcapsule gas gapping and were verified by melt sentinels.

3.3.1.2 Results

3.3.1.2.1 Inconel 718. The effect of test temperature on the ultimate and 0.2% yield strength of unirradiated and irradiated Inconel 718 is illustrated in Figure 3.26. As shown in the figure, strength properties of unirradiated material decrease with increasing test temperature. Neutron irradiation at 760°F to ∿1 x 10^{22} n/cm^2 (E>0.1 MeV) has little effect on either the ultimate or 0.2% yield strength, however, irradiation at 1100°F to the same fluence significantly reduces the 0.2% yield strength and has little effect on the ultimate strength.

The ductility (total elongation and reduction of area) of unirradiated Inconel 718 is influences by test temperature as illustrated in Figure 3.27. Both ductility properties initially decrease with increasing temperature to a temperature of ∿450°F. From ∿450 to 600°F substantial increases in ductility are observed and at temperatures above 800°F ductility decreases with increasing test temperature. The enhanced ductility observed in the 600-1100°F temperature range is believed to be the result of dynamic strain aging since pronounced serrations were observed in these stress-strain curves.

Neutron irradiation at 760°F to ∿1 x 10^{22} n/cm^2 (E>0.1 MeV) significantly decreased (by approximately 50%) the total elongation at all test temperatures. Reduction of area values were unchanged by irradiation at 760°F except at the highest test temperature (1000°F) where irradiated values were substantially lower than unirradiated values.

Irradiation at 1100°F appears to slightly enhance the ductility of the subject material at room temperature and 450°F (Figure 3.27). At the higher test temperatures (1100 and 1200°F) both total elongation and reduction of area are greatly reduced and approach ∿2% at the highest test temperature. Helium embrittlement may be responsible for the lack of high temperature ductility.

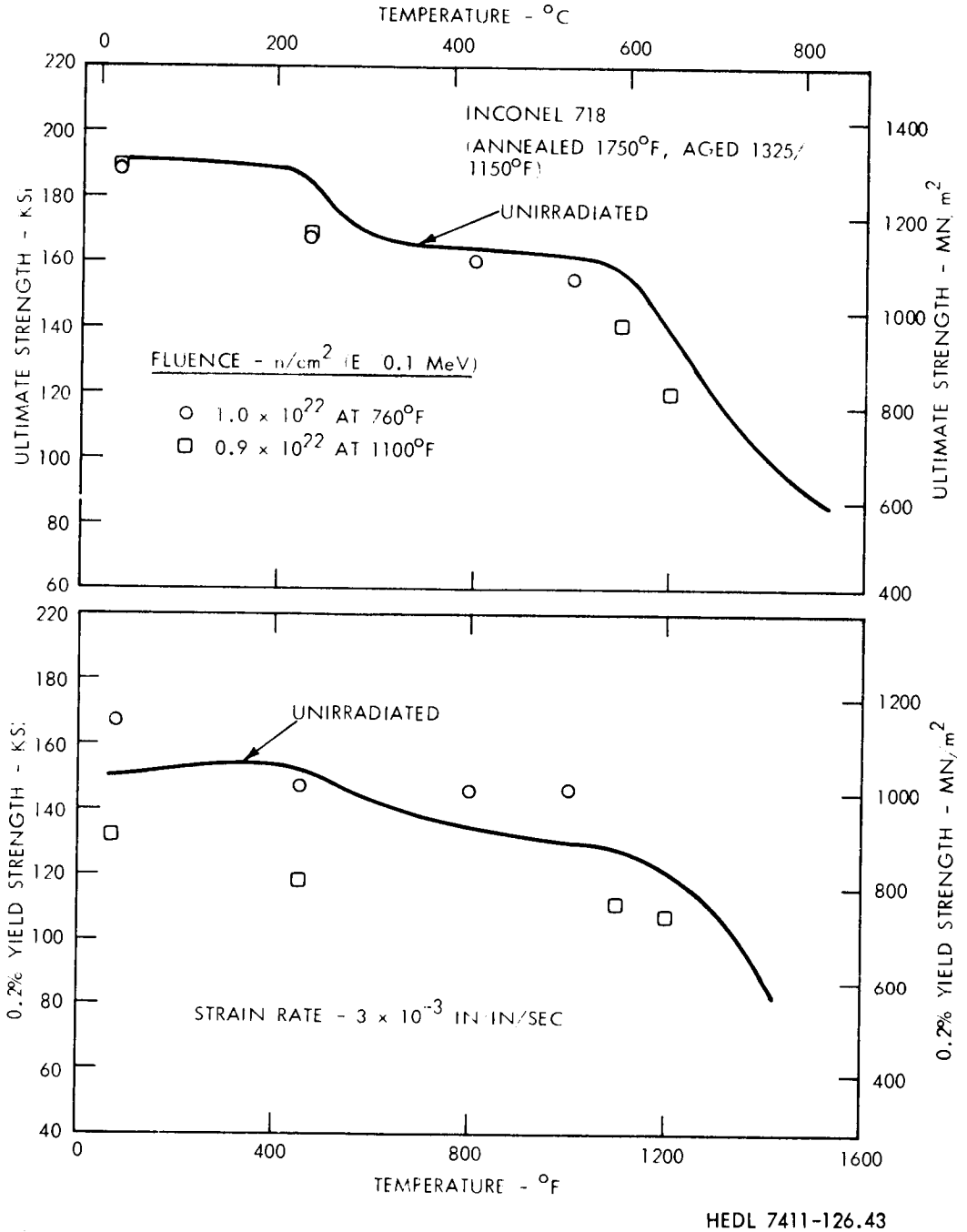

FIGURE 3.26. Strength of Unirradiated and Irradiated Inconel 718.

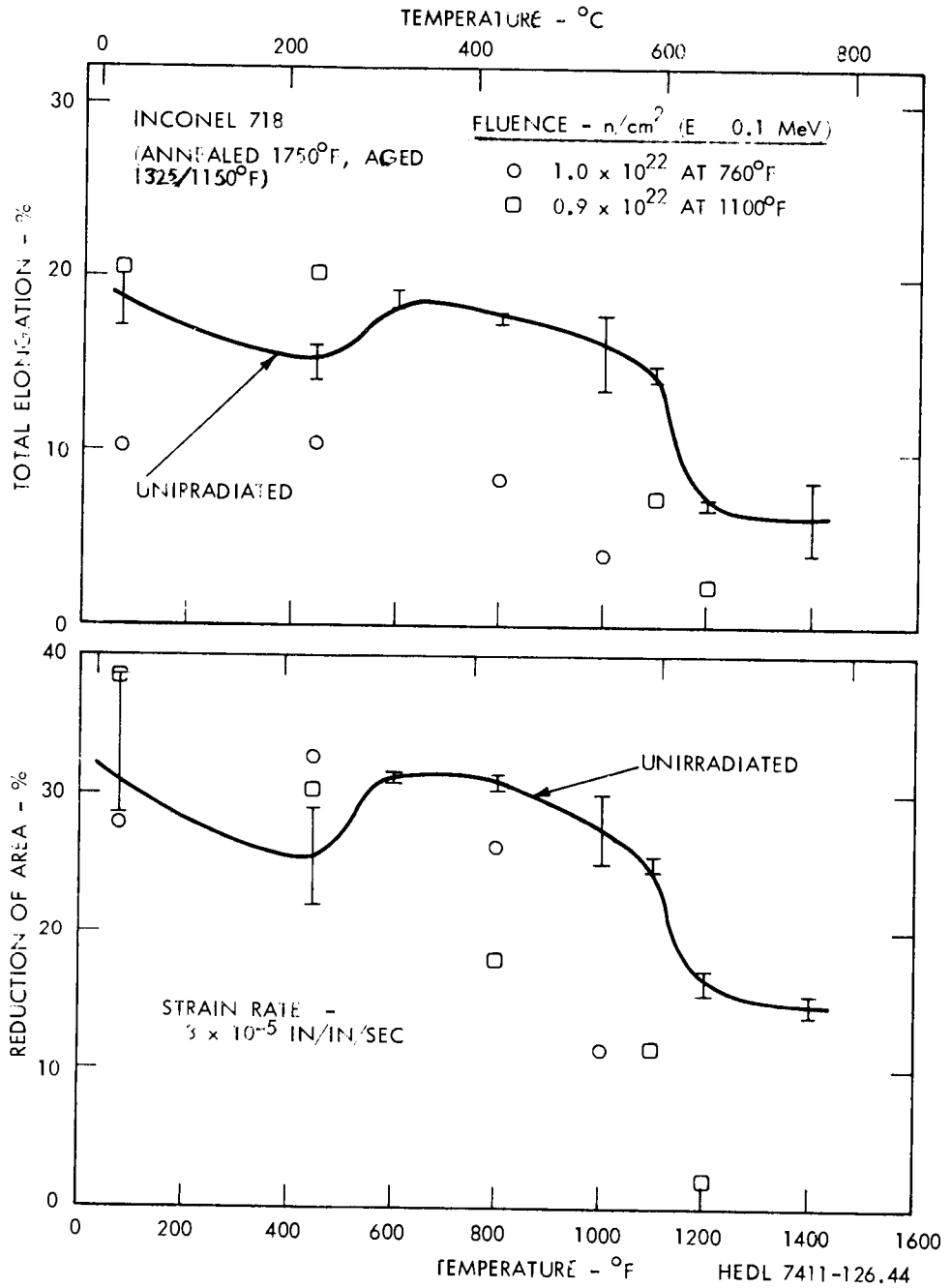

FIGURE 3.27. Ductility of Unirradiated and Irradiated Inconel 718.

3.3.1.2.2 Inconel 600. Elevated temperature tensile properties of unirradiated and irradiated Inconel 600 are presented in Figures 3.28 and 3.29. Irradiation effects data are presented for an irradiation temperature of 700°F and fluences of 1.3 and 2.5 x 10^{21} n/cm^2 (E>0.1 MeV).

The ultimate and 0.2% yield strengths of unirradiated Inconel 600 decrease with increasing test temperature (Figure 3.28). Similar behavior is noted for irradiated material. Irradiation hardening of the Inconel 600 slightly increases ultimate strength and significantly increases the yield strength (values for the higher fluence are approximately double unirradiated values) at all test temperatures.

The effect of test temperature on the ductility (total elongation and reduction of area) of Inconel 600 is illustrated in Figure 3.29. For temperatures to 800°F ductility remains constant for unirradiated material. Similar behavior is observed for irradiated material, however total elongation values are slightly reduced as a result of neutron irradiation. For temperatures from 800 to 1200°F ductility of both unirradiated and irradiated material decrease with temperature. The large decreases observed for irradiated material are believed to result from helium embrittlement. Above 1200°F ductility of unirradiated material rapidly increases with temperature. Although tests were not performed on irradiated material in this temperature region, it is anticipated helium embrittlement would severely restrict ductility.

3.3.1.2.3 A-286. A-286 elevated temperature tensile properties are illustrated in Figure 3.30. The heat treatment of the material prior to testing and irradiation included annealing at 1800°F for 30 minutes and precipitation hardening at 1325°F for 16 hours. As shown in Figure 3.30, the ultimate and 0.2% yield strength of unirradiated A-286 decreases with increasing temperature. Similar behavior is observed for material irradiated at 800°F to 2.5 x 10^{21} n/cm^2 (E>0.1 MeV) and the strength of irradiated and unirradiated material is nearly identical at all test temperatures.

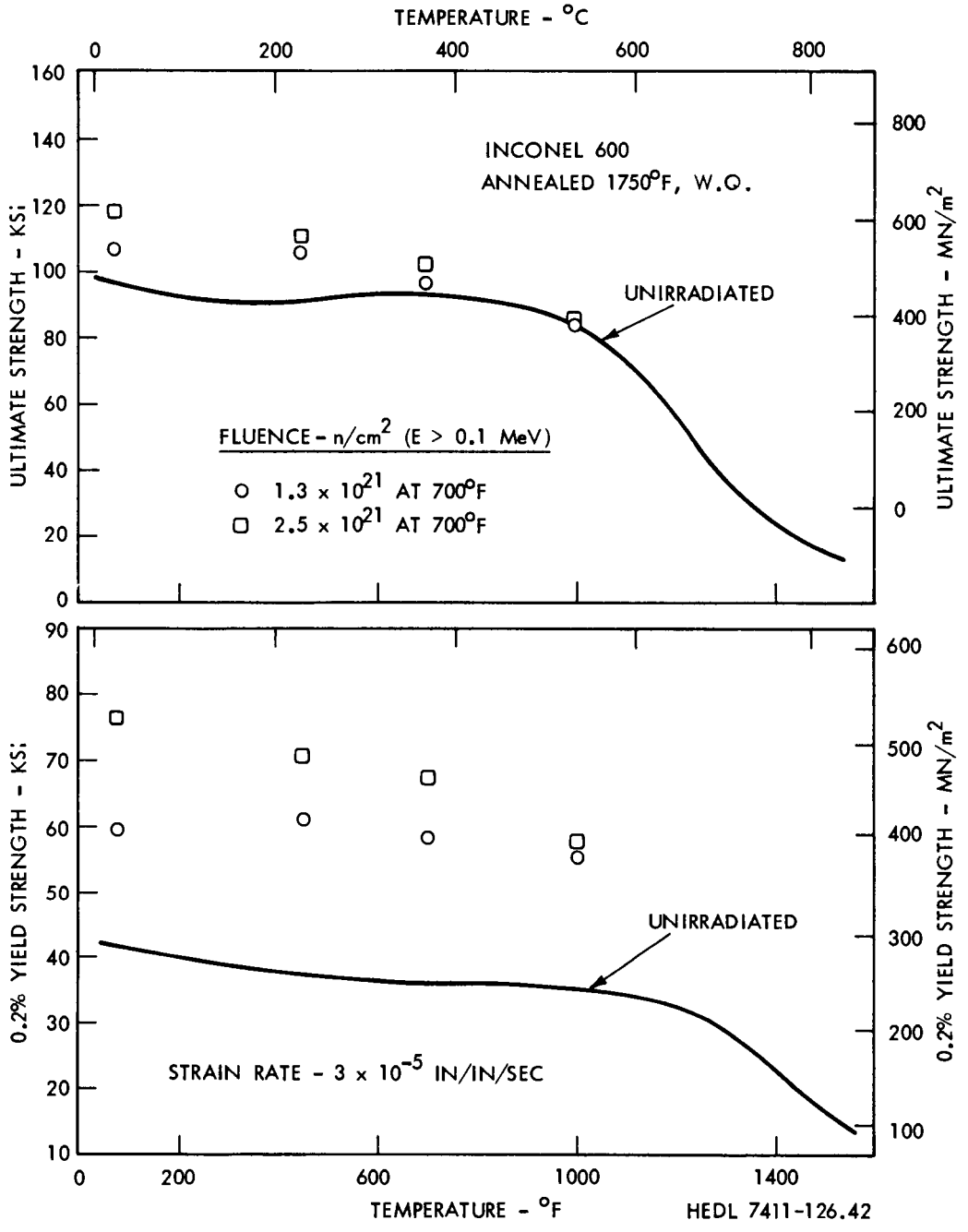

FIGURE 3.28. Strength of Unirradiated and Irradiated Inconel 600.

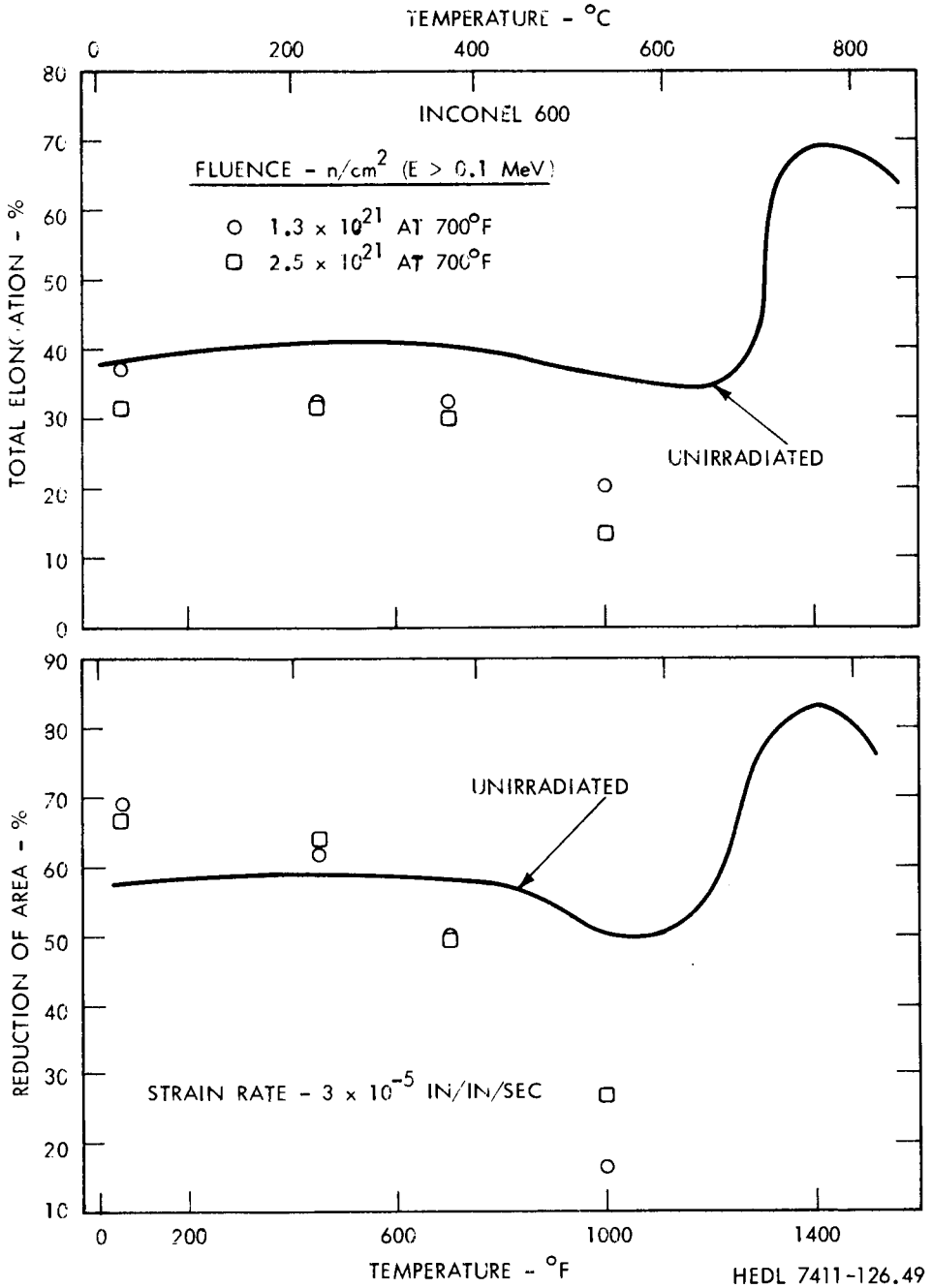

FIGURE 3.29. Ductility of Unirradiated and Irradiated Inconel 600.

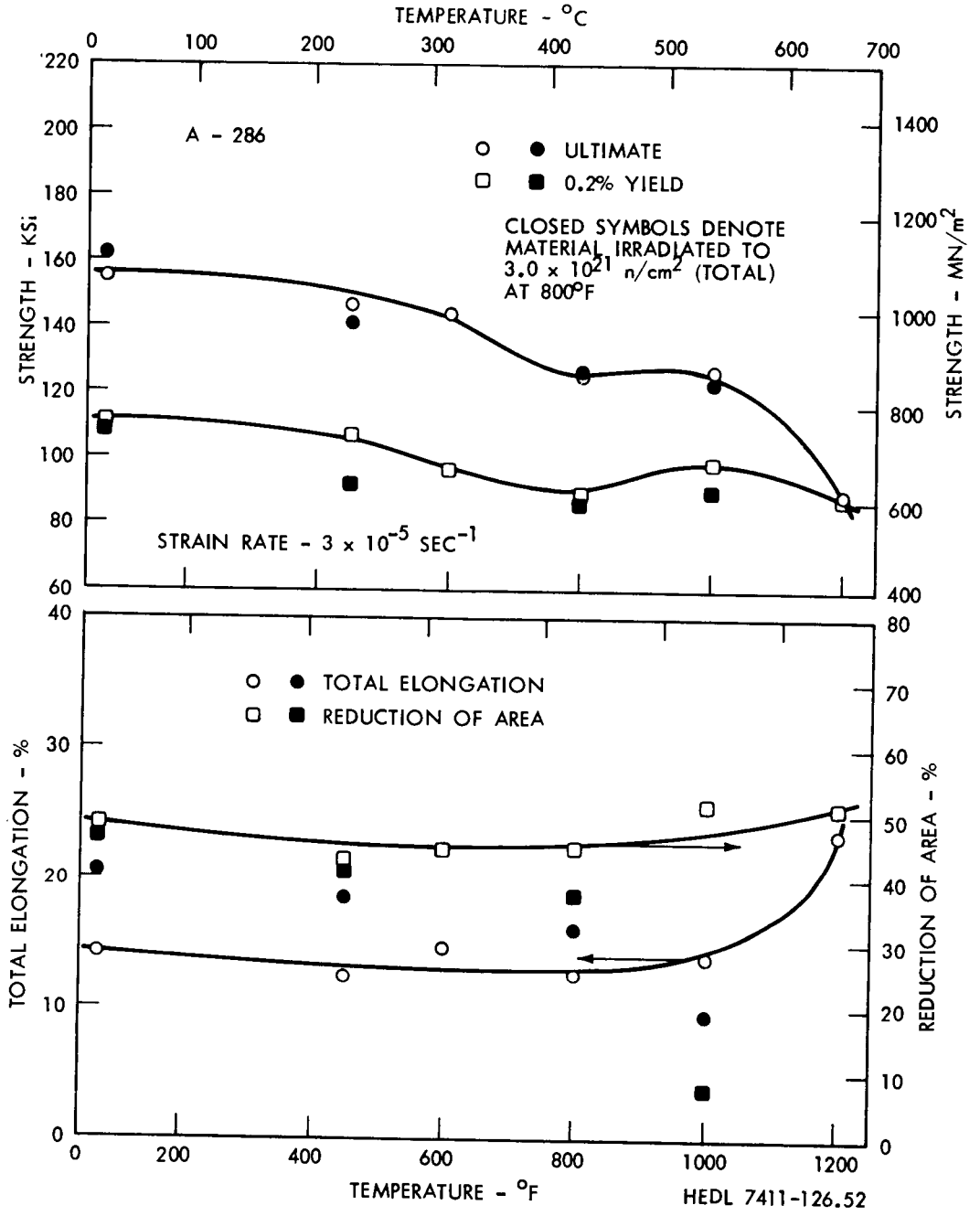

FIGURE 3.30. A-286 Tensile Properties.

The total elongation and reduction of area of unirradiated A-286 remain essentially constant with temperature to 1000°F and slightly increase with temperature from 1000 to 1200°F. Neutron irradiation slightly enhances total elongation and reduces reduction of area values for test temperatures to 1000°F. At a test temperature of 1200°F both total elongation and reduction of area are reduced by irradiation.

3.3.1.2.4 Expected Achievements. Testing of Inconel 718 tensile specimens irradiated at 1100 and 1200°F to $\sim 3 \times 10^{22}$ n/cm^2 (E>0.1 MeV) will be completed during the next reporting period.

3.3.2 Weld Materials Properties

3.3.2.1 Accomplishments and Status

Complete description of the behavior of structural materials for elevated-temperature (>800°F for austenitic stainless steels) service requires consideration of both the short-term tensile (time-independent) and long-term creep (time-dependent) stress-strain relationships. A variety of methods have been used to provide descriptions of the inter-relationships among stress, strain, time and temperature which vary widely in complexity and in suitability for general use. In order for a property description to apply broadly, the formulation must be based on data which are statistically representative of those material variables which might reasonably be expected to affect the properties. In this regard, weld-deposited materials pose a particularly difficult problem in that welding can introduce a large number of important variables (joint configuration, state of prestrain, microstructural variations, etc.) to which most wrought products are not subject. Thus, a useful data treatment technique for weld materials is, ideally, one which is relatively simple and which lends itself to repeated use in a reasonable time. Perhaps the most straight forward method of obtaining a strain-time relation, is that in which isochronous stress-strain curves are established directly from conventional specimen-elongation vs. time curves and the stress and temperature dependence are then derived from

the isochronous curves. In the present report, this technique is applied to as-deposited CRE (Controlled Residual Element) 308 (Reactor Vessel Weld Metal) which was tested at 1000°F over a range of initial stresses from 30 to 50 ksi. The materials and weldments have been described in detail elsewhere[9].

Important to this simplified treatment is the establishment of a linear relationship between stress and strain parameters. For the subject CRE 308, it was found that a plot of Log creep strain (e_c) vs. Log true stress (σ_{tr}) produced this linear relation (Figure 3.31). Thus the basic expression $e_c = K\sigma^n$ applies. The isochronous curves of Figure 3.31 were formed by visually fairing a straight line through points cross-plotted from the experimental elongation vs. time-under-load curves. The data were cross plotted directly except for the conversion of the nominal stress (σ_o) to true stress [$\sigma_{tr} = \sigma_o(1 + e_c + e_t)$, e_t = tensile loading strain]. By taking e_c values corresponding to incremental times of 10, 30, 100, 300, 1000, and 3,000 hours and establishing isochronous curves for each time increment, the constant K can be evaluated as a function of time, K(t). The stress exponent, n, was required to remain constant and was established from the slope of the isochronous stress-strain curve which defined the overall relation [K(30), in this treatment]. The other curves were then constructed parallel to the 30 hour isochronous curve.

The time dependence of the constant K is determined in Figure 3.32. K(t) values, evaluated at $e_c = 1$, are plotted against time and a constant K^1 and slope M are defined by the resulting linear relation, $K(t) = K^1 t^m$. A useful feature of this technique lies in the opportunity to make iterative judgement as to specific placement of the lines in Figure 3.31 and the points in Figure 3.32. Assuming the validity of the linearity of the two relations (in Log-Log planes), adjustments can be made in either the isochronous curve location (left or right shift) or the position of a point in the Log K(t) vs. Log t plot.

Once the strain-time relation has been established to this extent ($e_c = K^1 \sigma_{tr}^{\ n} t^m$), the analysis may continue in a variety of ways. For example, stress values associated with specific creep strains as a

function of time may be taken directly from Figure 3.31. This is illustrated by the CRE 308 (1000°F) example in Figure 3.33, which shows the true stress required to produce 0.1, 0.5 and 1% creep strains as a function of time from 10, to 100,000 hours. Such determinations are valuable for assignment of stresses in structures and, as has been shown, can be obtained simply and directly. The isostrain curves of Figure 3.33 are based upon experimental data for times to 3000 hours and for longer times, represent extrapolations. It is important to note however, that the extropolations are not based upon the projection of the isostrain curves but rather are taken from the 10,000-and 100,000-hour isochronous curves shown as dashed lines in Figure 3.31 which were, in turn taken from extrapolation of the Log K(t) vs. Log t plot of Figure 3.32. Thus, the extrapolation is effected by extending a relationship in which linearity is reasonably assured.

Another extension of the technique involves formulating analytic strain-time relations. Starting with the equation developed above.

$$e_c = K^1 \sigma_{tr}^{\ n} t^m$$

we can see that for constant-load conditions we are faced with the open form equation

$$e_c = K^1 \left[\sigma_o (1 + e_c + e_t)\right]^n t^m.$$

Depending upon the degree of refinement desired, this expression may be solved by an iterative numerical procedure or it may be approximated in closed form by ignoring higher-order terms in the evaluation of the stress function. In the present treatment n = 11 and the resulting approximation leads to the solution

$$e_c = \frac{K^1 t^m \sigma_o^{\ n} (1 + 11\ e_t)}{1 - 11\ K^1 t^m \sigma_o^{\ n}}$$

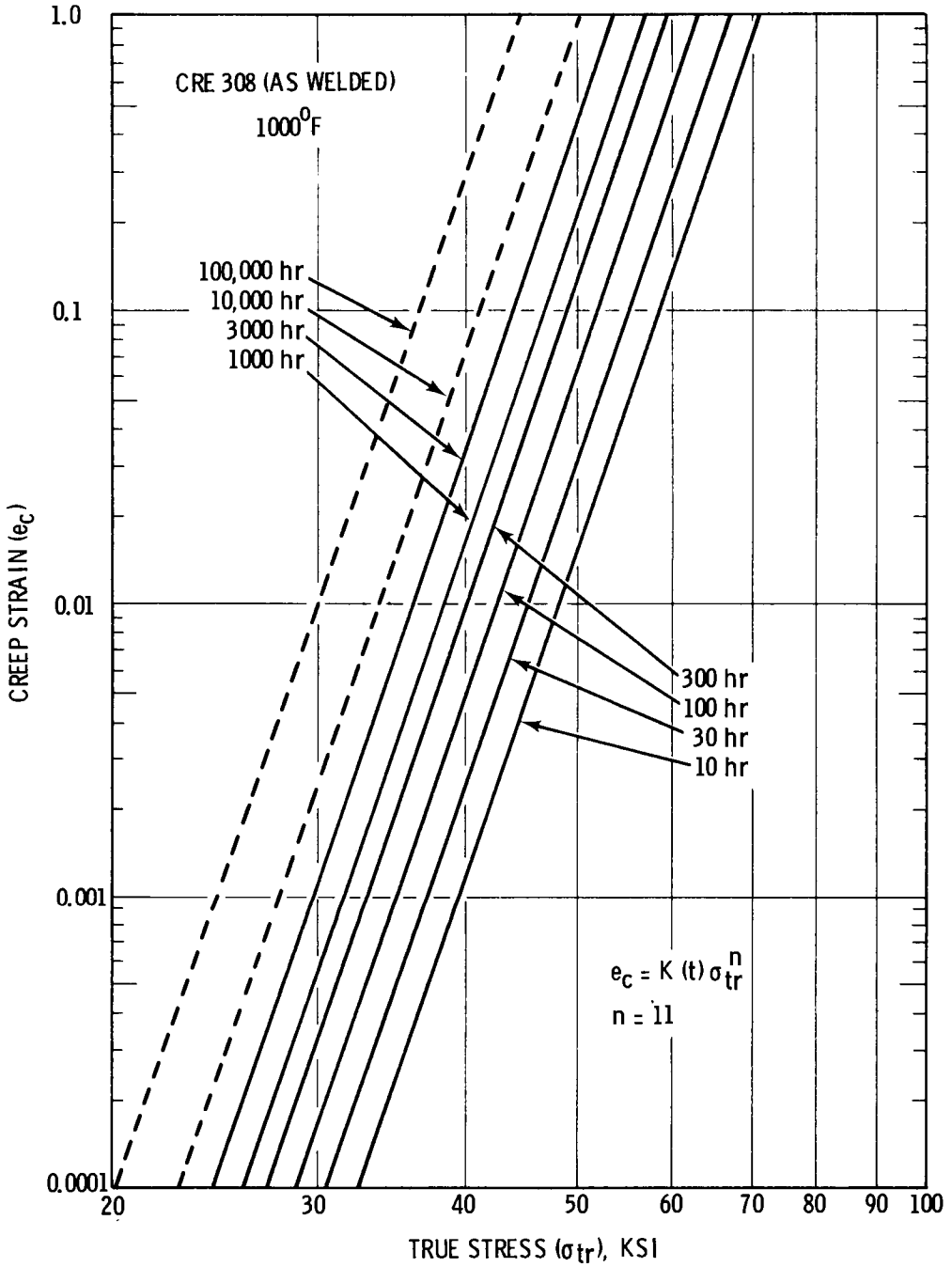

FIGURE 3.31. Isochronous Stress-Strain Relation for CRE 308 at 1000°F.

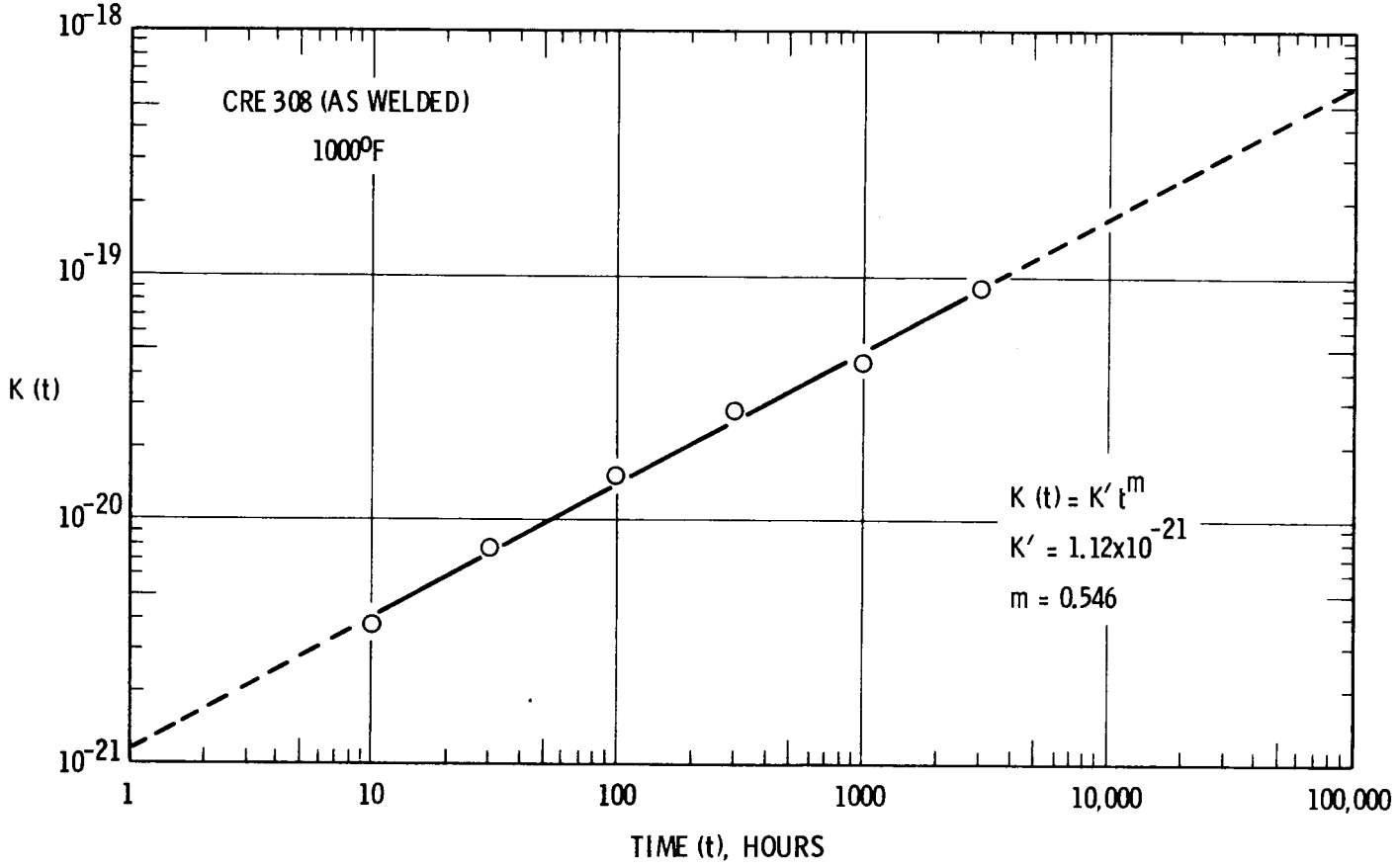

FIGURE 3.32. Formulation of the Time Dependence of the Creep Stress-Strain Relation for CRE 308 at 1000°F.

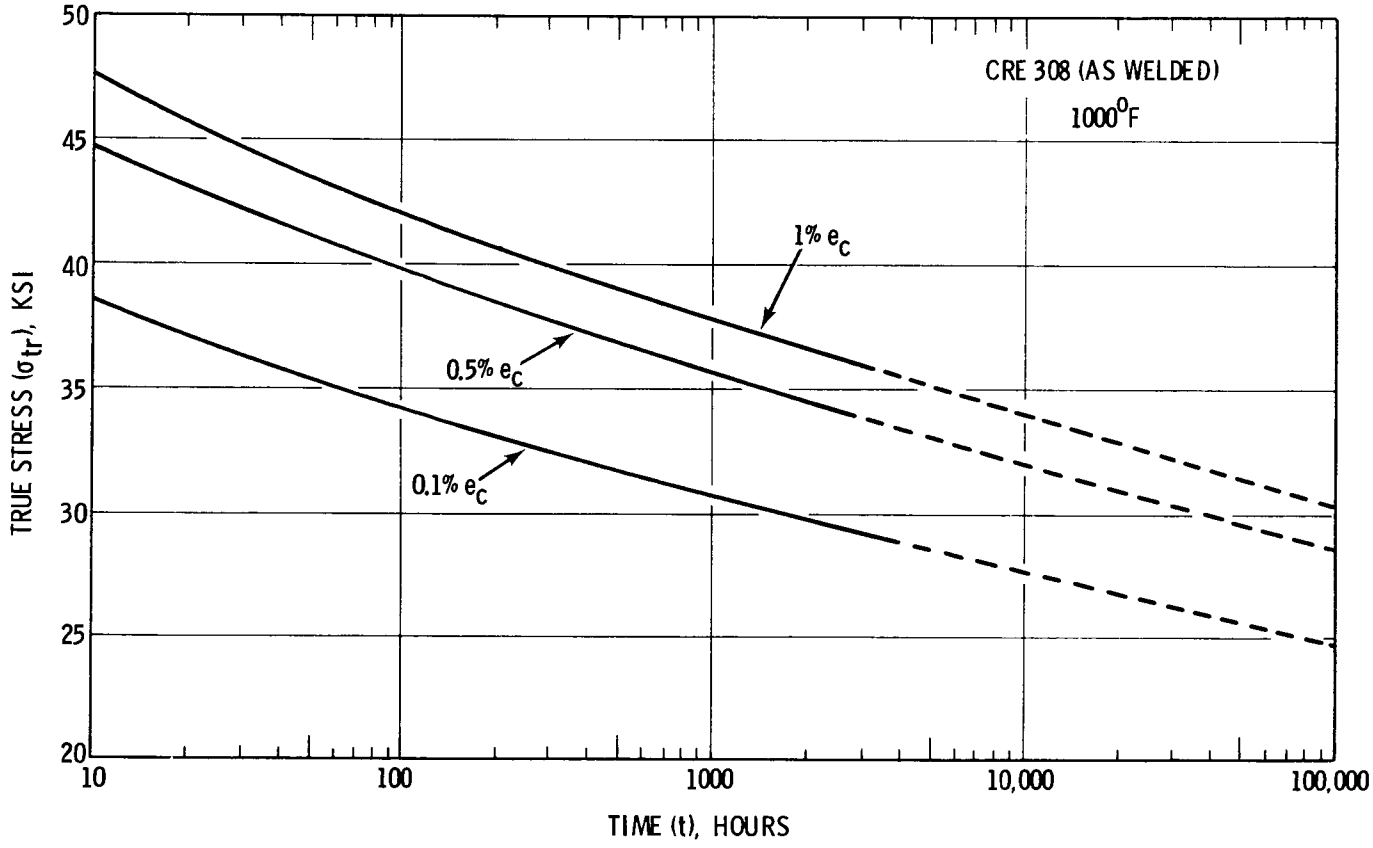

FIGURE 3.33. Stress to Produce Specific Creep Strains as a Function of Time Under Stress.

where $K^1 = 1.12 \times 10^{-21}$

$m = 0.546$

$n = 11$

e_t = strain value taken from tensile test at stress of σ_o.

3.3.2.1.1 Expected Achievements. Similar data treatments are in progress for other weldments in the program: 308, 308L, 316 and 16-8-2. Promising early results suggest that the above-described method will be valuable in detecting and describing the effects of thermal aging and neutron irradiation.

3.4 MATERIALS SAFETY AND ENGINEERING - T. T. Claudson and H. H. Yoshikawa

3.4.1 Subcritical Crack Growth

3.4.1.1 Accomplishments and Status

Linear-elastic fracture mechanics techniques were used to characterize the effect of various elevated temperature operating environments (e.g., air, nitrogen, liquid sodium) and vacuum on the fatigue-crack propagation behavior of reactor structural materials. The materials studies to-date include annealed Type 304 stainless steel, annealed Inconel 600, and precipitation-heat treated Inconel 718. Each of the materials investigated were from the same material heats utilized in previous investigations at HEDL: Type 304 stainless (Allegheny Ludlum heat 55697)[10,11], Inconel 600 (Huntington heat NX-9929-1A)[12], and Inconel 718 (Huntington heat 52C9EK)[13].

The test utilizing an air environment were done in an air-circulating furnace. The sodium environment chamber and the vacuum chamber have been described in Reference 10. The same chamber used for vacuum testing was also employed for the nitrogen environment tests. All tests in liquid sodium were conducted in "low oxygen" sodium (1-3 ppm Oxygen) except Specimen No. 59 which was tested in "high oxygen" sodium (20-40 ppm Oxygen).

The vacuum tests were conducted in 6.7-8.6 x 10^{-6} torr vacuum. The nitrogen environment tests were conducted at one atmosphere in ultra-high-purity nitrogen (0_2<8ppm).

All tests were conducted using feedback-controlled electro-hydraulic equipment utilizing load as the control parameter. The loading waveforms employed were either sinusoidal or "sawtooth." The tests in nitrogen, vacuum and sodium environments used a fracture face marking technique, employing periodic changes in stress ratio, to obtain the basic crack length versus cycles data. (See Reference 10 for more details). Test results were plotted in form crack growth rate as a function of the effective stress intensity factor (see Reference 11 for a discussion of K_{eff}).

The results for annealed Type 304 S.S. tested at 800°F and 1000°F are given in Figures 3.34 and 3.35, respectively. The results for annealed Inconel 600 and precipitation-heat-treated Inconel 718, both tested at 800°F, are given in Figures 3.36 and 3.37, respectively.

It will be noted (Figures 3.34 and 3.35), that, for annealed Type 304, the effects of vacuum and liquid sodium environments are approximately equivalent, and both environments produce fatigue-crack growth rates far lower than does an air environment at the same value of K_{eff}. The results for nitrogen fall between the results for air and for sodium/vacuum, indicating that nitrogen is not as inert as a vacuum but is less aggressive than air. These results are in qualitative agreement with results [14] for Inconel 718 tested at room temperature in air, nitrogen and vacuum. Crack growth rates that were lower in a nitrogen environment at 1200°F than an air environment at the same temperature have also been noted for annealed Types 316 and 321 stainless steels[15]. The results for a nitrogen environment are important since a nitrogen cover gas is used for the primary piping in the FFTF.

The effect of a liquid sodium environment on the crack growth behavior of annealed Inconel 600 and precipitation-heat-treated Inconel 718 is given in Figures 3.36 and 3.37, respectively. As with the previous observations for annealed Type 304 S.S., a sodium environment has the effect of significantly reducing the crack growth rates in these two nickel-base

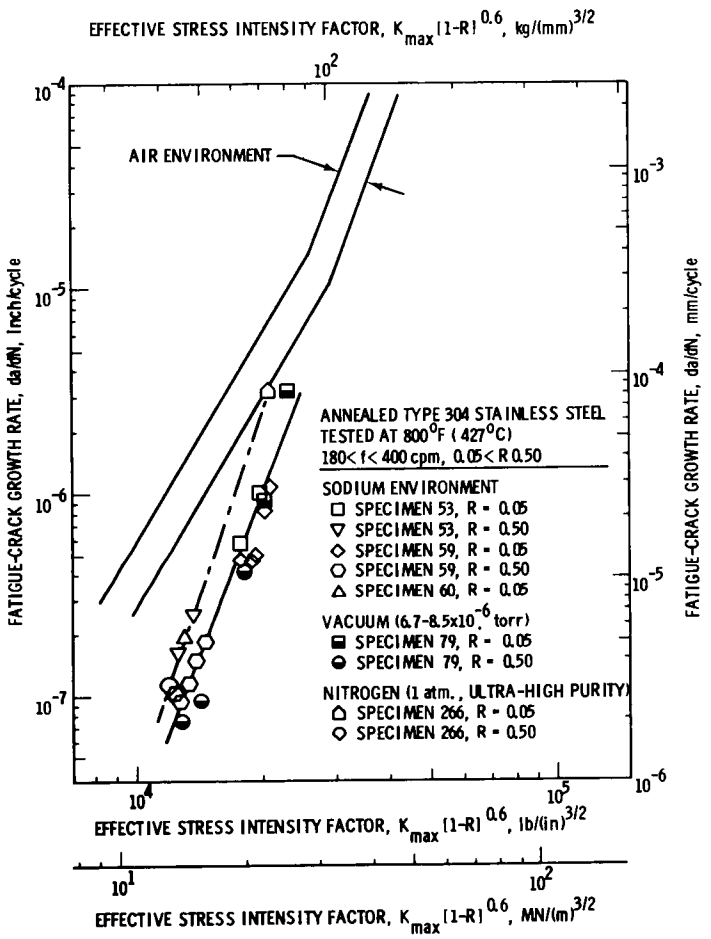

FIGURE 3.34. Fatigue-crack growth behavior of annealed Type 304 S.S. in air, vacuum, nitrogen and sodium environments at 800°F. (Air environment data from Reference 16.)

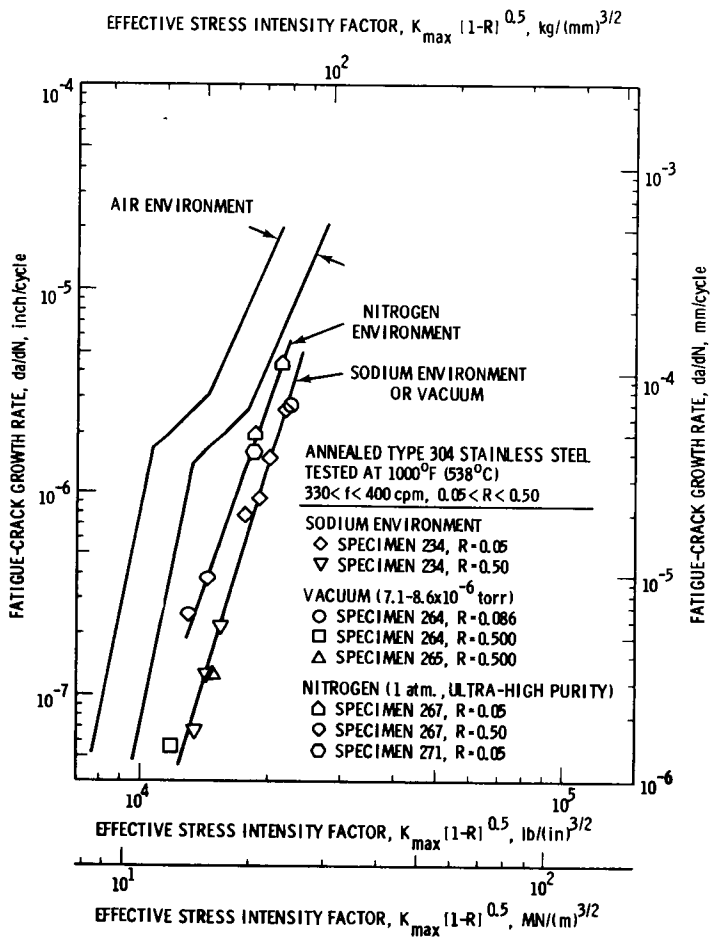

FIGURE 3.35. Fatigue-crack growth behavior of annealed Type 304 S.S. in air, vacuum, nitrogen and sodium environments at 1000°F. (Air environment data from Reference 11.)

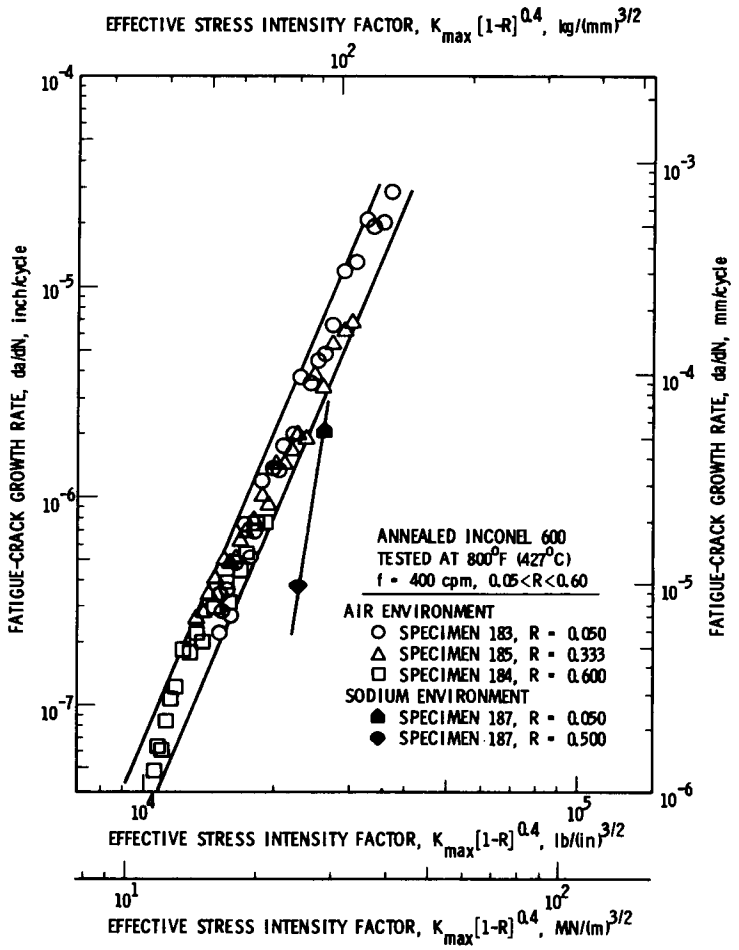

FIGURE 3.36. Fatigue-crack growth behavior of annealed Inconel 600 in air and sodium environments at 800°F.

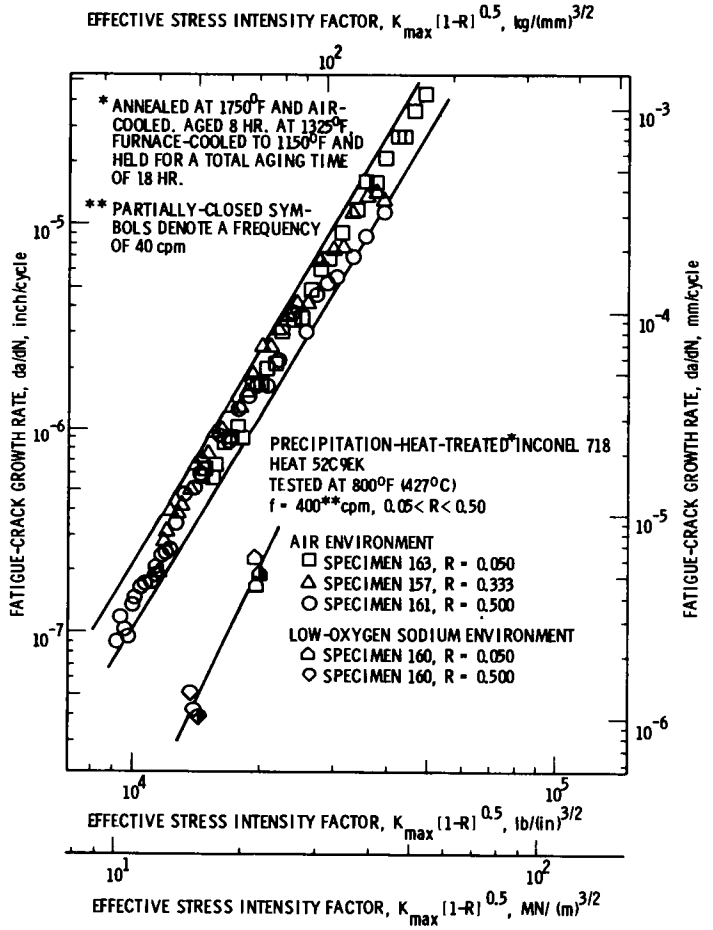

FIGURE 3.37. Fatigue-crack growth behavior of precipitation-heat-treated Inconel 718 in air and sodium environments at 800°F.

alloys are considered preliminary as additional in-sodium tests are planned for each material.

A small amount of in-sodium testing on Inconel 718 was done at a cyclic frequency of 40 cpm instead of 400 cpm. As may be seen in Figure 3.37, there appears to be little or no effect upon the crack growth behavior of reducing the cyclic frequency one decade. Previous results[13] on this alloy tested in an air environment at 800°F indicated a slight increase in the crack growth rate as the frequency was reduced from 400 cpm to 40 cpm.

3.4.1.2 Expected Achievements

The results described are part of a larger effort to determine the effects of temperature, cyclic frequency, stress ratio, head treatment, neutron irradiation and operating environments upon the crack growth behavior of reactor structural alloys. Work on these parameters is continuing.

3.5 REFERENCES

1. L. D. Blackburn, R. W. Barker and R. T. Billeter, *HEDL Quarterly Progress Report, April, May, June 1974, HEDL-TME 74-2,* Vol. 1, p. B-4.
2. L. D. Blackburn and R. W. Barker, *HEDL Quarterly Progress Report, July, August, September 1974, HEDL-TME 74-3,* Vol. 1, p. B-13.
3. F. Garofalo, P. R. Malenoch and G. V. Smith, "The influence of Temperature on the Elastic Constants of Some Commercial Steels," *Symposium on Determination of Elastic Constants,* ASTM STP 129, American Society for Testing and Materials, Philadelphia, Pennsylvania, 1952, p. 10.
4. L. D. Blackburn and E. R. Gilbert, *HEDL Quarterly Progress Report, October, November, December 1974, HEDL-TME 74-4,* Vol. 1.
5. L. D. Blackburn and E. R. Gilbert, *HEDL Quarterly Progress Report, July, August, September 1974, HEDL-TME 74-3,* Vol. 1, p. B-23.
6. R. W. Swindeman and C. E. Pugh, "Creep Studies on Type 304 Stainless Steel (Heat 8043813) Under Constant and Varying Loads," *ORNL-TM-4427,* June 1974.

7. L. D. Blackburn, R. W. Barker and T. R. Billeter, *HEDL Quarterly Progress Report, April, May, June 1974, HEDL-TME 74-2,* Vol. 1, p. B-4.
8. A. J. Lovell, "Creep of 20% C.W. Type 316 Stainless Steel," *HEDL-TME 73-65,* October 1973.
9. A. L. Ward, "Austenitic Stainless Steel Weld Materials - A Data Compilation and Review," *HEDL-TME 74-25,* May, 1974.
10. L. A. James and R. L. Knecht, "Fatigue-Crack Propagation Behavior of Type 304 Stainless Steel in a Liquid Sodium Environment," *Metallurgical Transactions,* Vol. 6, No. 1, January 1975.
11. L. A. James, "The Effect of Stress Ratio on the Elevated Temperature Fatigue-Crack Propagation of Type 304 Stainless Steel," *Nuclear Technology,* Vol. 14, No. 2, May 1972, pp. 163-170.
12. L. A. James, "The Effect of Temperature Upon the Fatigue-Crack Growth Behavior of Two Nickel-Base Alloys," *Journal of Engineering Materials and Technology,* Vol. 95, No. 4, October 1973, pp. 254-256.
13. L. A. James/R. L. Knecht, "Subcritical Crack Growth," in *Report HEDL TME-74-3,* Vol. 1, Exhibit C, 1974.
14. J. D. Frandsen, P. J. Stocker and H. L. Marcus, "Fatigue Crack Propagation of Inconel 718 in Gaseous Environments," *Report SCTR-72-15, North American Rockwell Science Center,* November 1972.
15. M. W. Mahoney and N. E. Paton, "The Influence of Gas Environments on Fatigue Crack Growth Rates in Types 316 and 321 Stainless Steel," *Nuclear Technology,* Vol. 23, No. 3, September 1974, pp. 290-297.
16. L. A. James, "Estimation of Crack Extensions in a Piping Elbow Using Fracture Mechanics Techniques," *Journal of Pressure Vessel Technology,* Vol. 96, No. 4, November 1974, pp. 273-278.

4. NAVAL RESEARCH LABORATORY

L. E. Steele

4.1 INTRODUCTION - L. E. Steele

The research program of the NRL, Engineering Materials Division, Thermostructural Materials Branch, includes the study of the behavior of structural materials useful in reactor construction. This report is developed using such data to support the ERDA objective of compiling structural materials properties data for the use in national reactor development programs. The NRL program is sponsored by the Office of Naval Research, the Energy Research & Development Administration, the U. S. Nuclear Regulatory Commission, and the U. S. Army Engineer Power Group. The unirradiated materials properties data contributed here include those developed in the course of research for these sponsors in the areas of high temperature materials, radiation damage, and fracture mechanics.

4.2 EFFECT OF HOLD TIME ON FATIGUE CRACK PROPAGATION IN THERMALLY AGED, SOLUTION ANNEALED AND 20% COLD-WORKED TYPE 316 STAINLESS STEEL - D. J. Michel, H. H. Smith and H. E. Watson

4.2.1 Background

The fatigue crack growth resistance of austenitic stainless steels (SS) and nickel-base alloys is being investigated for high temperature structural applications. The purpose of this work is to determine the effect of high temperature time-dependent processes, such as thermal aging and creep, on the fatigue crack growth resistance of these alloys. It is also intended to correlate crack growth behavior with microstructural changes produced by extended elevated temperature exposure.

In a previous report[1], it was shown that prior high temperature thermal aging altered the fatigue properties of Type 316 SS. As a continuation of that study, this report presents results of the combined effect of cyclic and static loading on crack growth rates in thermally aged and unaged Type 316 SS.

4.2.2 Materials and Test Procedures

The effect of the fatigue-creep interaction was investigated at

1100°F (593°C) for solution annealed and 20% cold-worked Type 316 SS unaged and after thermal aging at 1100°F (593°C) for 5000 hours. The chemical composition of the material, the specimen design, and the general test procedures have been previously reported.[2] Briefly, single-edge-notched cantilever specimens were cycled under zero-to-tension loading in a saw-tooth mode to a constant maximum load. To examine the fatigue-creep interaction, tension loads were imposed on the test specimen during each cycle by holding the load at the maximum value for a time of 1.0 minutes before returning to zero load. The loading and unloading rates remained constant for all hold times.

4.2.3 Results and Discussion

The experimental data were analyzed to yield crack growth rate, da/dN, as a function of the stress intensity factor range, ΔK. For the solution annealed, thermally aged Type 316 SS tested at 1100°F (593°), Fig. 4.1 indicates that a 1.0 minute hold time produced a negligible effect on crack growth rate when compared to the results for the zero hold time tests. This indicates that the cyclic rather than the static portion of the tests produced the majority of the crack growth. However, it is important to note that regardless of the hold time, thermal aging reduced the fatigue crack growth rate of solution annealed Type 316 SS at all values of ΔK when compared to results for unaged material.

Figure 4.2 summarizes the results for the effects of hold time on fatigue crack growth rate in 20% cold-worked, thermally aged and unaged Type 316 SS tested at 1100°F (593°C). The results (Fig. 4.2) show that in the unaged condition the fatigue crack growth rate was increased by a factor of approximately 15 when a 1.0 minute hold time was imposed at the maximum cyclic load. The addition of thermal aging, however, is seen to increase the fatigue crack growth rate for zero hold time by approximately a factor of 5 at all values of ΔK when compared to the zero hold time results for unaged material. A 1.0 minute hold time for the thermally aged material increased the fatigue crack growth rate by nearly a factor of 10 at all values of ΔK when compared with the zero hold time results for the unaged material. It is seen, however, that the effects of hold time when combined with thermal aging do not produce an

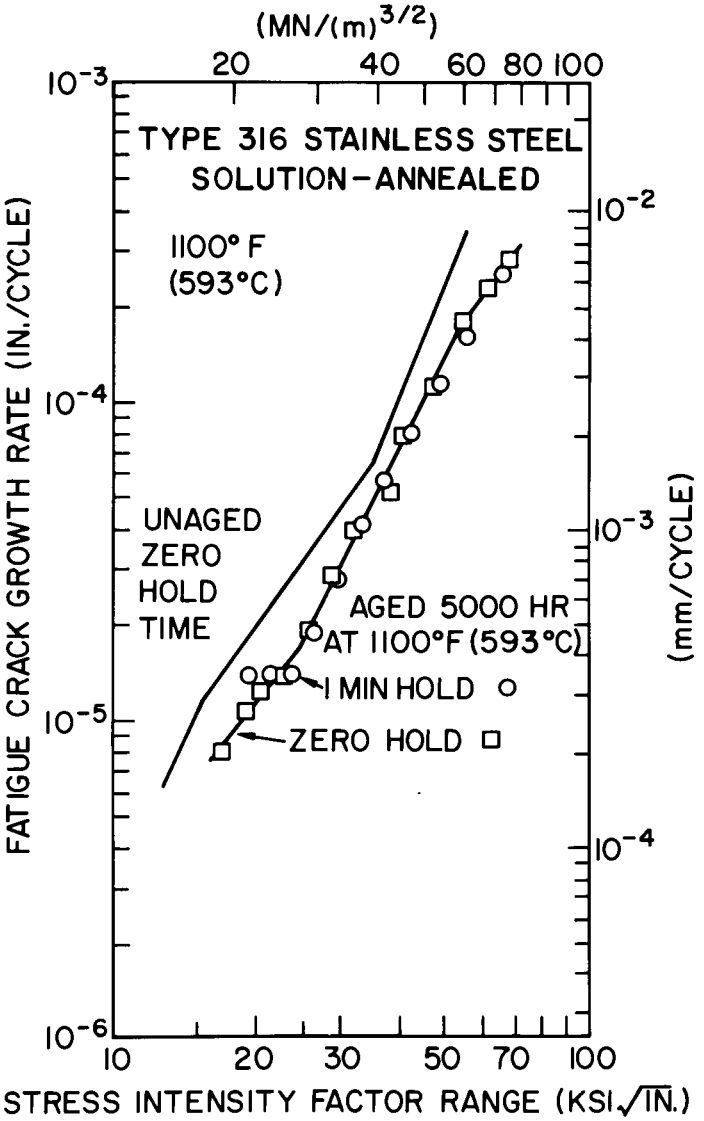

Fig. 4.1 - Effect of hold time on fatigue crack growth rates in solution annealed, unaged and thermally aged Type 316 stainless steel as a function of the stress intensity factor range.

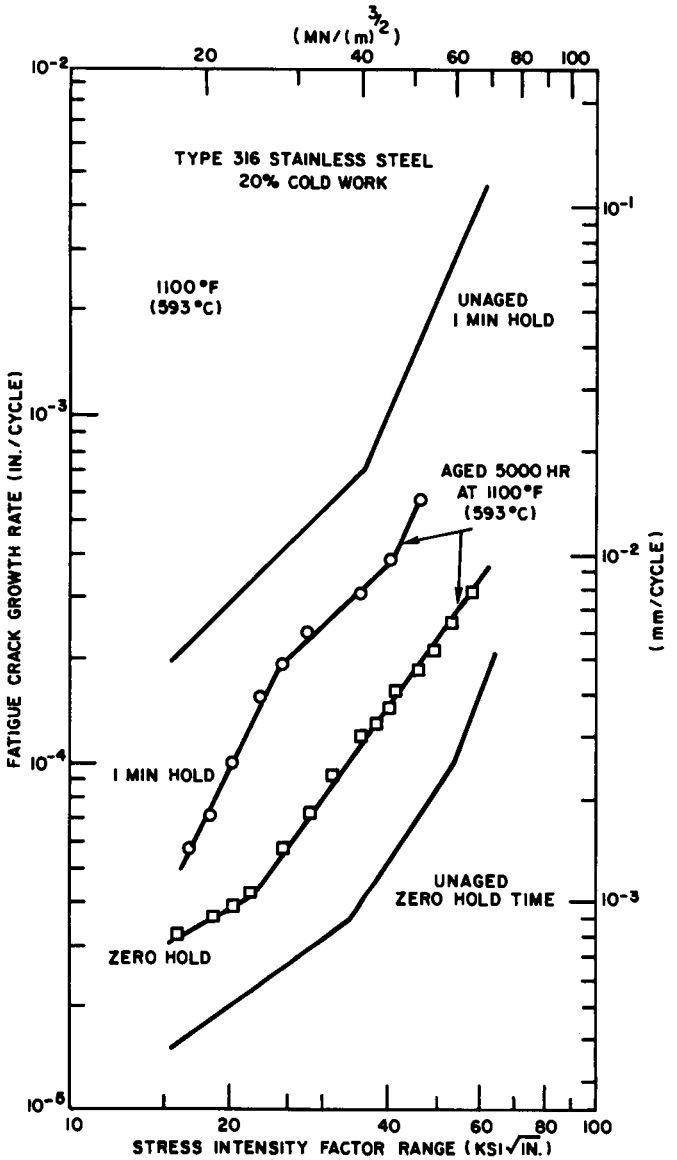

Fig. 4.2 - Effect of hold time on fatigue crack growth rates in 20% cold-worked, unaged and thermally aged Type 316 stainless steel as a function of the stress intensity factor range.

increase in fatigue crack growth rate comparable to that produced by the 1.0 minute hold time in the unaged material. The results for the unaged material strongly suggest that, during the 1.0 minute hold time tests, a time dependent mechanism contributed to the increase in crack growth observed. A similar but less significant contribution of this phenomenon is suggested by the results on the aged material. Additional experiments are in progress to examine this effect in more detail in order to separate the effects of the time dependent variables cyclic frequency, thermal recovery, and creep.

4.3 REFERENCES

1. D. J. Michel, H. H. Smith, and H. E. Watson, "Fatigue Crack Growth in Thermally Aged Types 304 and 316 Stainless Steel Plate," in Mechanical Properties Test Data for Structural Materials, Quarterly Progress Report for period ending July 31, 1974, ORNL-4998, Oak Ridge National Laboratory, Oak Ridge, Tennessee, September 1974, pp. 103-110.

2. D. J. Michel and H. H. Smith, "Fatigue Crack Growth in Type 316 Stainless Steel," in Mechanical Properties Test Data for Structural Materials, Quarterly Progress Report for period ending January 31, 1974, ORNL-4948, Oak Ridge National Laboratory, Oak Ridge, Tennessee, March 1974, pp. 157-165.

5. OAK RIDGE NATIONAL LABORATORY

W. R. Martin

5.1 INTRODUCTION

The ORNL mechanical properties effort comprises several programs. The program Mechanical Properties and Behavior for Structural Materials deals with materials of general applicability to the LMFBR program. Other programs are concerned with the mechanical properties of weldments in LMFBR components, the specific materials of interest for LMFBR steam generators, collection and correlation of mechanical data needed for design on high-temperature LMFBR systems, and materials for the primary circuit and steam generators of HTGR systems.

5.2 MECHANICAL PROPERTIES AND BEHAVIOR FOR STRUCTURAL MATERIALS — C. R. Brinkman

The objective of this program is to collect mechanical property data and material behavior for LMFBR structural and component materials. Included in the scope of this effort are the following: (1) basic tensile, creep, creep-rupture, and relaxation base-line data that are directly applicable to design criteria and methods for types 304 and 316 stainless steel reference heats and cyclic stress-strain tests performed with emphasis on loading and aging history effects, (2) find the variations in properties for several heats of types 304 and 316 stainless steel to allow establishment of minimum and average values of specific properties and the equation parameters required for design purposes. This work will include determination of property variation of samples from different mill products within a given heat of stainless steel.

5.2.1 Mechanical Property Characterization of Type 304 Stainless Steel Reference Heat — V. K. Sikka, E. Lee, and E. B. Patton

5.2.1.1 Creep and Rupture Properties of the 2-in. (51-mm) Plate of Reference Heat

Several creep tests on 2-in. (51-mm) plate of the reference heat of type 304 stainless steel (9T2796) continued. The test times and creep

strains for all tests have been updated and are summarized in Table 5.1. Three creep tests have exceeded test times over 18,600 hr and two other tests have exceeded 16,360 hr. All creep tests are progressing smoothly and will be continued during the next quarter.

The stress-rupture data on 2-in. (51-mm) and 1-in. (25.4-mm) plate of the reference heat were reported earlier.[1,2] The minimum commitment method[3] was applied (see Sect. 5.2.3) to the creep-rupture data available at present to extrapolate it to test times approaching 10^5 hr. The extrapolated values of 10^3-, 10^4-, and 10^5-hr creep-rupture strengths have been plotted in Fig. 5.1 as functions of ultimate tensile strength at the creep temperature. The figure shows that the creep-rupture strength data over the temperature range 538 to 704°C (1000–1300°F) can be related to the ultimate tensile strength by a relation of the form:

$$S_R^{\,t} = \alpha \exp(\beta S_u^{\,R}) \quad , \tag{1}$$

where $S_R^{\,t}$ = creep rupture strength for a time t, $S_u^{\,R}$ = ultimate tensile strength at a strain rate R, and α, β = constants. The 10^5-hr minimum-expected creep-rupture strength values reported by Smith[4] for both types 304 and 316 stainless steel have also been plotted as functions of minimum-expected ultimate tensile strength values at the same temperature. The minimum-expected values are over a temperature range of 538 to 816°C (1000–1500°F) and can still be related by the relation presented in Eq. (1).

It should be pointed out that the positions of isotime lines in Fig. 5.1 are functions of tensile strain rate, because of strain rate sensitivity of the ultimate tensile strength. The relation observed in Fig. 5.1 appears to have potential since it may be possible to show that the results of a short-term tensile test at a given temperature are indicative of long-term creep rupture strength. Work is continuing to extend the relation in Eq. (1) to data from other sources and on other types of stainless steels.

Table 5.1. Creep Tests on Type 304 Stainless Steel Reference Heat 9T2796 2-in.-thick (51-mm) Plate[a]

Test	Temperature		Stress		Time in Test	Strain, %		Ratio of Creep Stress to Yield Stress[b]	Comments[c]
	(°C)	(°F)	ksi	MPa	(hr)	Loading	Creep		
11595	427	800	20.0	138	12,862	2.67	0.073	1.57	
12368	427	800	18.0	124	9,925	1.91	0.020	1.42	
12472	427	800	16.0	110	9,175	1.17	0.056	1.26	
12570	427	800	14.9	97	8,850	0.83	0.040	1.10	
11569	482	900	20.0	138	13,072	3.27	0.128	1.70	
12375	482	900	18.0	124	9,755	2.40	0.065	1.53	
11675	482	900	16.0	110	2,451	1.48	0.032	1.36	Discontinued
11693	482	900	14.0	97	2,202	0.92	0.14	1.19	Discontinued
11830	482	900	12.0	83	1,682	0.35	0.04	1.02	Discontinued
13152	482	900	10.0	69	7,843	0.089	0.08467	0.85	
13020	482	900	10.0	69	7,500	0.085	0.025	0.85	
10489	538	1000	20.0	138	18,100	3.80	0.612	1.80	
12250	538	1000	18.0	124	10,400	2.62	0.274	1.62	
11625	538	1000	16.0	110	12,800	1.79	0.248	1.44	
10491	538	1000	14.0	97	18,105	1.16	0.250	1.26	
12444	538	1000	14.0	97	9,349	1.18	0.180	1.26	
12445	538	1000	14.0	97	4,498	1.17	0.090	1.26	Discontinued
11568	538	1000	12.0	83	12,974	0.53	0.110	1.08	
11626	538	1000	10.0	69	12,735	0.071	0.095	0.90	
11641	538	1000	8.0	55	3,170	0.040	0.027	0.72	Discontinued
10853	593	1100	18.0	124	4,547	2.84	5.94	1.65	Ruptured
10852	593	1100	16.0	110	14,647	2.29	3.55	1.47	Ruptured
13947	593	1100	16.0	110	2,900	2.13	1.04	1.47	
10554	593	1100	14.0	97	8,710	1.40	0.65	1.28	Discontinued

Table 5.1. (Continued)

Test	Temperature		Stress		Time in Test	Strain, %		Ratio of Creep Stress to Yield Stress[b]	Comments[c]
	(°C)	(°F)	ksi	MPa	(hr)	Loading	Creep		
11596	593	1100	12.0	83	12,926	0.52	0.420	1.10	
10490	593	1100	10.0	69	18,081	0.22	0.357	0.92	
13710	593	1100	10.0	69	2,010	0.096	0.156	0.92	Discontinued
14163	593	1100	10.0	69	2,853	0.228	0.110	0.92	
11227	593	1100	8.0	55	6,103	0.041	0.080	0.73	Discontinued
12459	593	1100	5.0	34	10,100	0.024	0.095	0.46	
10855	649	1200	16.0	110	304	2.41	12.0	1.57	Ruptured
10854	649	1200	14.0	97	761	1.60	13.0	1.37	Ruptured
11563	649	1200	12.0	83	2,674	0.59	13.4	1.18	Ruptured
11226	649	1200	10.0	69	7,278	0.18	7.0	0.98	Ruptured
10851	649	1200	8.0	55	16,210	0.044	1.78	0.78	
12255	649	1200	5.0	34	992	0.030	0.08	0.49	Discontinued
12443	649	1200	5.0	34	10,060	0.024	0.126	0.49	
12460	649	1200	3.0	21	10,075	0.020	0.20	0.29	
10856	704	1300	10.0	69	568	0.067	15.6	0.90	Ruptured
11562	704	1300	10.0	69	653	0.12	22.5	0.90	Ruptured
11222	704	1300	8.0	55	2,760	0.031	16.4	0.72	Ruptured
12254	704	1300	5.0	34	10,050	0.030	1.773	0.45	
12461	704	1300	3.0	21	10,050	0.018	0.374	0.27	
12462	704	1300	2.0	14	9,865	0.010	0.228	0.18	

[a]Annealed 0.5 hr at 1093°C before testing. All tests loaded at a strain rate of 0.004/min.

[b]Yield stresses used in this ratio were 12,700 psi (88 MPa) at 427°C (800°F), 11,800 psi (81 MPa) at 482°C (900°F), 11,100 psi (77 MPa) at 538°C (1000°F), 10,900 psi (75 MPa) at 593°C (1100°F), 10,200 psi (70 MPa) at 649°C (1200°F), 11,100 psi (77 MPa) at 704°C (1300°F).

[c]Unless otherwise noted, tests in progress.

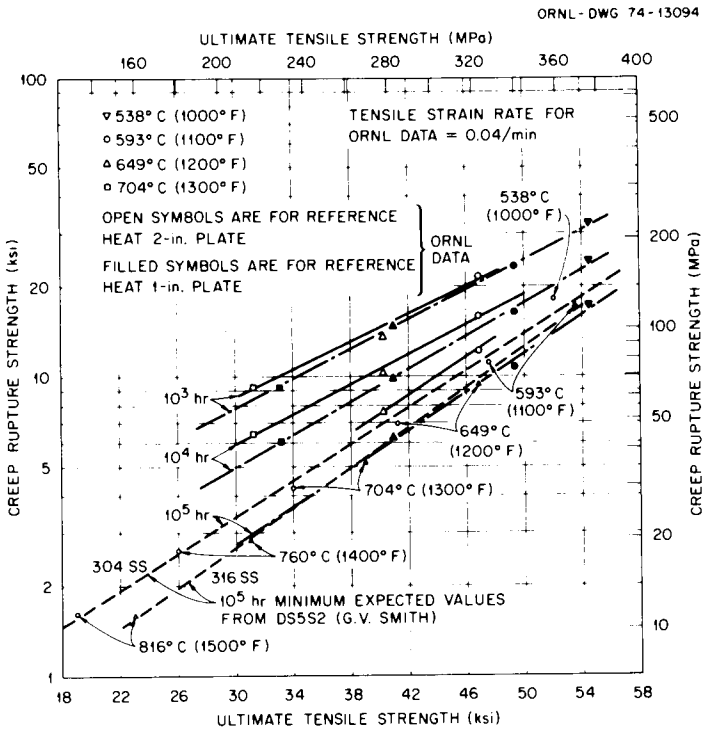

Fig. 5.1. The Relationship Between the Creep-Rupture Strength and Ultimate Tensile Strength at the Same Test Temperature for the Reference Heat of Type 304 Stainless Steel.

5.2.1.2 Uniaxial Tensile Tests Following Periods of Creep

Two additional creep tests to be discontinued after 10,000 hr are in progress, and other tests will be started as creep machines become available. During the last quarter we examined the available ORNL[5] and HEDL[6] data from uniaxial tests following periods of creep. Figure 5.2 shows the effect of prior creep strain (loading plus creep strain) on true ultimate tensile strength and true uniform elongation. The effect of life fraction accrued during prior creep on the relative residual ultimate tensile strength and relative residual uniform elongation is shown in Fig. 5.3. Following are the definitions of the terms used in Fig. 5.3.

$$\text{Creep Life Fraction, } L_c = \Delta t / t_r \ ,$$

where Δt = prior creep time,

t_r = time to rupture.

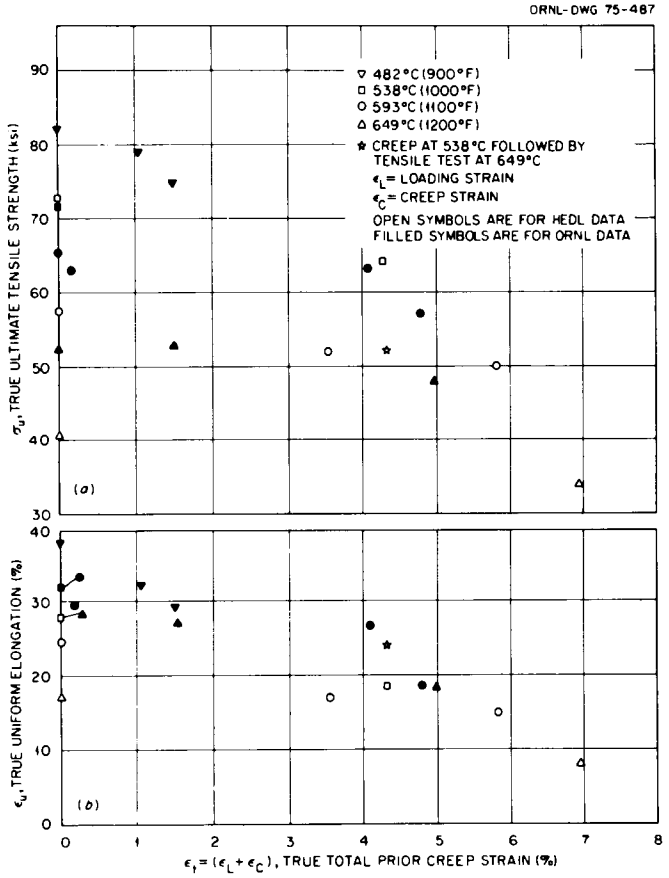

Fig. 5.2. (a) True Ultimate Tensile Strength and (b) True Uniform Strain as Functions of True Total Prior Creep Strain for the Reference Heat of Type 304 Stainless Steel

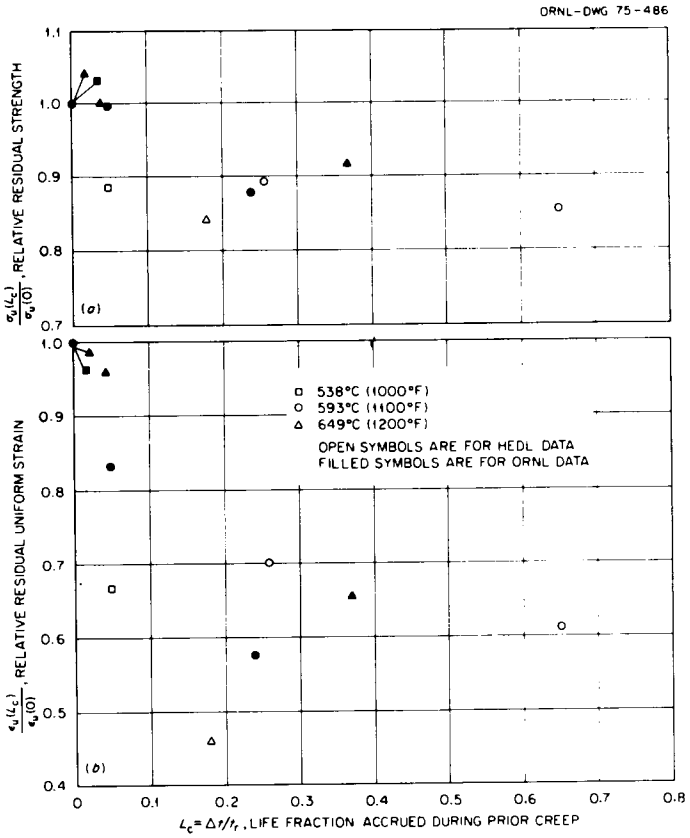

Fig. 5.3. (a) Relative Residual Strength and (b) Relative Residual Uniform Strain as Functions of Life Fraction Accrued During Prior Creep for the Reference Heat of Type 304 Stainless Steel.

$$\text{Relative Residual Strength after Life Fraction } L_c = \sigma_u(L_c)/\sigma_u(0) ,$$

where $\sigma_u(0)$ = true ultimate tensile strength without prior creep,
$\sigma_u(L_c)$ = true ultimate tensile strength with life fraction L_c.

$$\text{Relative Residual Uniform Elongation after Life Fraction } L_c = \varepsilon_u(L_c)/\varepsilon_u(0) ,$$

where $\varepsilon_u(0)$ = true uniform elongation without prior creep,
$\varepsilon_u(L_c)$ = true uniform elongation with life fraction L_c.

The data presented in Figs. 5.2 and 5.3 show the following trends.

1. Increasing prior creep strain decreases the true ultimate tensile strength and uniform elongation in the temperature range investigated, 482 to 649°C (900–1200°F).

2. The increasing life fraction accrued during creep decreases the residual ultimate tensile strength and uniform elongation. The decrease in relative residual uniform elongation with increasing prior creep life fraction is much more drastic than the corresponding change in the relative residual ultimate tensile strength.

Work will continue in this area, and results will be plotted as they become available.

5.2.2 Heat-to-Heat Variation of Mechanical Properties of Types 304 and 316 Stainless Steel — V. K. Sikka, E. Lee, and E. B. Patton

5.2.2.1 Long-Term Creep Tests in Heat-to-Heat Variation Study of Type 304 Stainless Steel

Ten long-term creep tests are in progress on several heats of type 304 stainless steel at 593°C (1100°F). Two tests had ruptured during the previous quarter, after 14,077 and 22,622 hr. Two more tests have ruptured during this quarter. One test conducted on heat 551 at 593°C (1100°F) and 25 ksi (172 MPa) ruptured after 19,180.3 hr. The other test completed on heat 697 at 593°C (1100°F) and 17 ksi (117 MPa) ruptured after 25,823 hr.

The creep curves for the ruptured tests are being updated. The creep curves on the remaining six long-term tests have been updated, and the data are summarized in Table 5.2. Table 5.3 lists the strain values at several times for the ten long-term tests mentioned above and the additional tests in progress on the weak, medium, and strong heats. The creep strain values at 593°C and 17 ksi (117 MPa) show a factor of 5 variation after a test time of 20,000 hr. For the weak, medium strong, and reference heats, the creep strain values at 593°C (1100°F) and 10 ksi (69 MPa) also show approximately a factor of 5 variation after a test time of 5000 hr.

The time-to-rupture data at several temperatures for 20 heats of type 304 stainless steel are plotted in Fig. 5.4 and compared with the minimum expected value curve from ASME Code Case 1592. HEDL data,[7] from one heat (697) also being investigated at ORNL, have been included in Fig. 5.4. The figure shows that for all heats of type 304 stainless steel in both the as-received and reannealed conditions the times to rupture are above the code minima for test temperatures of 538 and 593°C (1000 and 1100°F). At 649°C (1200°F), data from the reference heat (796) 2-in. (51-mm) plate in the reannealed condition lie on or slightly above the ASME Code Case 1592 minimum curve. The important point to note from Fig. 5.4 and Tables 5.2 and 5.3 is that large variations were observed in creep-rupture properties of the heats of type 304 stainless steel at all test temperatures used in this investigation. Reannealing the as-received material lowers the time to rupture in some cases, but the variations in properties among the heats were still observed.

The relation between the creep-rupture strength and the ultimate tensile strength, observed for the reference heat of type 304 stainless steel, has been extended in Fig. 5.5 to explain the heat-to-heat variation. The 10^3-hr creep rupture strength for seven heats of type 304 stainless steel in both the as-received and reannealed conditions is plotted as a function of ultimate tensile strength determined from tensile tests conducted at a strain rate of 0.04/min for test temperatures of 538, 593, and 649°C (1000, 1100, and 1200°F). It is evident that the variation in the creep-rupture strength at 593°C (1100°F) for the various heats is related to the corresponding change in the ultimate tensile strength. Furthermore, it appears that the changes in the creep-rupture strength due to temperature

Table 5.2. Status of Several Long-Term Creep Tests of Type 304 Stainless Steel at 593°C (1100°F)

Test	Heat	Condition[a]	Stress, (ksi)	Stress, (MPa)	Test Time[b] (hr)	Strain, % Loading	Strain, % Creep	Minimum Creep Rate (%/hr)	Time to Rupture (hr)
10396	60551	A 479	25.0	172	Ruptured	1.81	6.31	1.4×10^{-4}	19,180
10395	346845	A 240	25.0	172	Ruptured	1.37	11.35	1.4×10^{-4}	14,077
9499	300380	Reannealed	17.0	117	25,600	0.72	1.01	~0	
9483	600414	Reannealed	17.0	117	25,672	1.49	0.97	1.1×10^{-5}	
9464	337330	A 240	17.0	117	25,935	−0.20	0.15	5.5×10^{-6}	
9446	9T2796	A 479	17.0	117	25,940	0.13	1.77	2.1×10^{-5}	
9443	337187	A 240	17.0	117	Ruptured	0.47	10.18	9.7×10^{-5}	22,622
9371	55697	A 479	17.0	117	Ruptured	0.62	8.27	1.4×10^{-4}	25,823
9221	600414	A 240	17.0	117	28,074	0.18	0.76	1.0×10^{-5}	
9508	346544	A 240	17.0	117	25,500	0.22	4.20	3.5×10^{-5}	

[a]As received per indicated specification or reannealed 0.5 hr at 1065°C (1950°F).

[b]Unless otherwise noted tests are in progress.

Table 5.3. Summary of Creep Data for Several Heats of Type 304 Stainless Steel at 593°C (1100°F)

Heat	Treatment[a]	Stress (ksi)	Stress (MPa)	Strain (%) ε_L	Strain (%) ε_{pc}	Minimum Creep Rate (%/hr)	Creep Strain, %, at indicated Time in hr[b] 100	1000	5000	10,000	15,000	20,000	25,000	Time to Rupture (hr)
807	Reannealed	10	69	0.068	0.1625	2.05×10^{-5}	0.031	0.145	0.258	D				
807	Reannealed	10	69	0.058			0.067	0.191	0.311	I				
807	Reannealed	10	69	0.079			0.048	0.191	0.369	I				
544	Reannealed	10	69	0.059			0.026	0.065	0.169	I				
544	Reannealed	10	69	0.053			0.015	0.039	0.102	D				
845	Reannealed	10	69	0.051	~0.03	8.7×10^{-6}	0.028	0.039	0.071	I				
845	Reannealed	10	69	0.068	~0.011	5.4×10^{-6}	0.010	0.014	0.044	D				
796K	Reannealed	10	69	0.218	~0.21	8.5×10^{-6}	0.038	0.096	0.248	0.304	I			
796P	Reannealed	10	69	0.16			0.06	0.105	0.21		I			
796P	Reannealed	10	69	0.11			0.02	0.05	D					
796P	Reannealed	10	69	0.18			0.03	0.105	I					
380	Reannealed	17	117	0.72			0.149	0.337	0.666	0.835	0.906	0.920	I	
414	Reannealed	17	117	1.48			0.125	0.289	0.623	0.813	0.888	0.924	I	
813	Reannealed	17	117	1.16	0.11	2.75×10^{-5}	−0.014	0.103	D					
813	A 240	17	117	0.31	0.316	2.525×10^{-5}	0.133	0.290	D					
796R	A 479	17	117	0.0	0.61	1.95×10^{-5}	0.109	0.323	0.612	0.788	0.863	1.024	1.471	
544	A 240	17	117	0.22	1.125	3.5×10^{-5}	0.313	0.671	1.287	1.482	1.727	2.329	I	
330	A 240	17	117	0.0	0.735	1.168×10^{-5}	0.137	0.363	0.763	0.842	0.932	0.971	1.022	
697	A 240	17	117	0.62	0.125	1.368×10^{-4}	−0.020	0.151	0.873	1.493	2.238	3.07	4.896	
414	A 240	17	117	0.18			0.100	0.170	0.385	0.596	0.650	0.700		
187	A 240	17	117	0.47	1.15	9.6×10^{-5}	0.431	0.819	1.491	1.929	2.448	3.50	9.03 R	22,622
551	A 240	25	172	1.80	1.42	1.9×10^{-4}	0.200	0.900	2.200	3.300	4.050	I		
845	A 240	25	172	1.40	1.80	1.6×10^{-4}	0.600	1.300	2.700	3.550	11.450 R			14,077

[a] Reannealed is for 0.5 hr at 1065°C (1950°F).

[b] R = ruptured before indicated time and strain shown is that at rupture; D = discontinued before time indicated; I = in test.

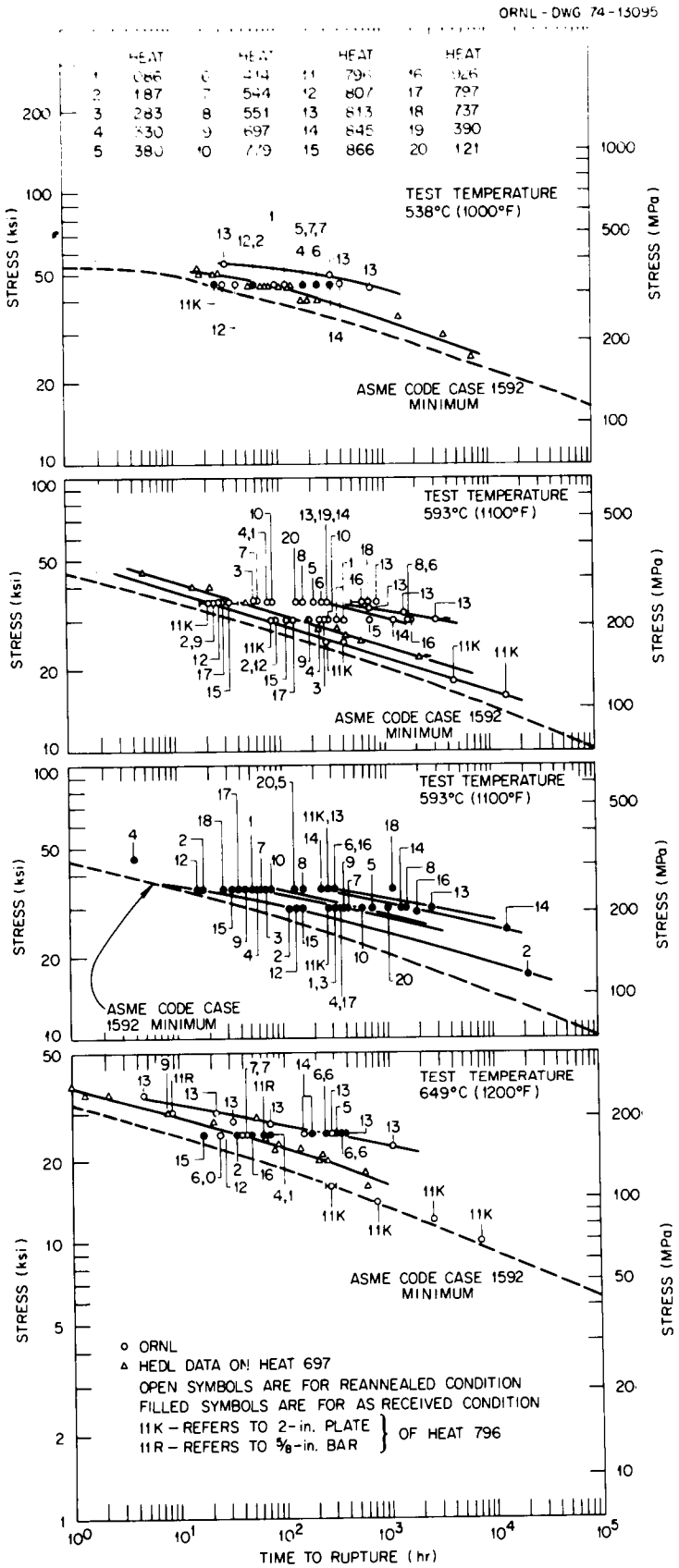

Fig. 5.4. Comparison of Stress-Rupture Results at 538, 593, and 649°C (1000, 1100, and 1200°F) for 20 Heats of Type 304 Stainless Steel in Both As-Received and Reannealed Conditions with ASME Code Case 1592 Minimum Value Curve.

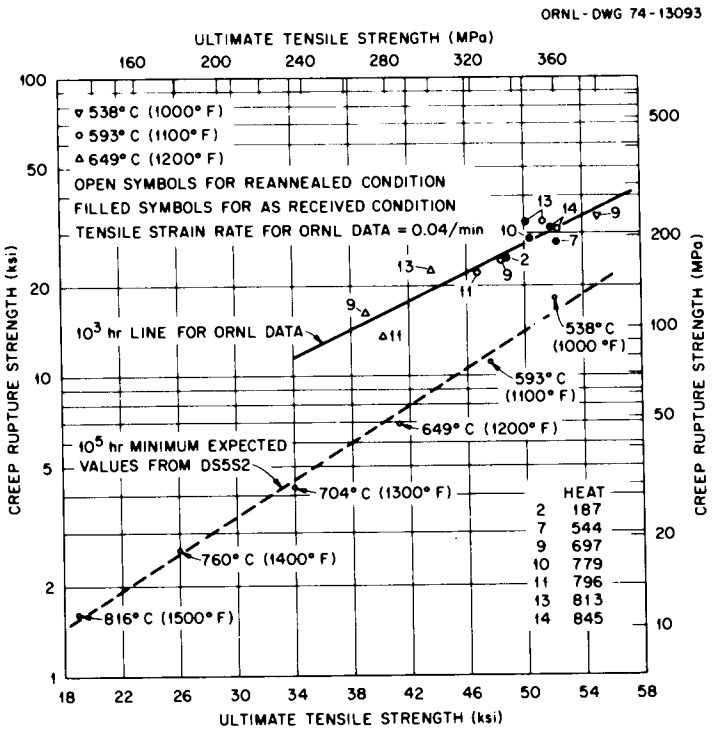

Fig. 5.5. Relationship Between the Creep-Rupture Strength and Ultimate Tensile Strength at the Same Test Temperature for Various Heats of Type 304 Stainless Steel.

can also be related to the changes in the ultimate tensile strength. The relation between the 10^5-hr minimum-expected creep-rupture strength and minimum-expected ultimate tensile strength values reported by Smith[4] is also included for comparison in Fig. 5.5.

In Fig. 5.6 the ultimate tensile strength data at four different temperatures are plotted as functions of $(C + N)d^{-1/2}$, where $(C + N)$ is the sum of the weight percentages of carbon and nitrogen and d is the average grain diameter in micrometers, for 19 heats of type 304 stainless steel in the reannealed condition. The least squares analysis for the data at different test temperatures gave the constants in Table 5.4 for a fit to

$$S_u = A + B(C + N)d^{-1/2} \quad .$$

Thus, we have seen from the data analyzed that the variation in creep rupture strength for various heats can be qualitatively related to ultimate tensile strength for the times considered, which in turn can be related to $(C + N)d^{-1/2}$.

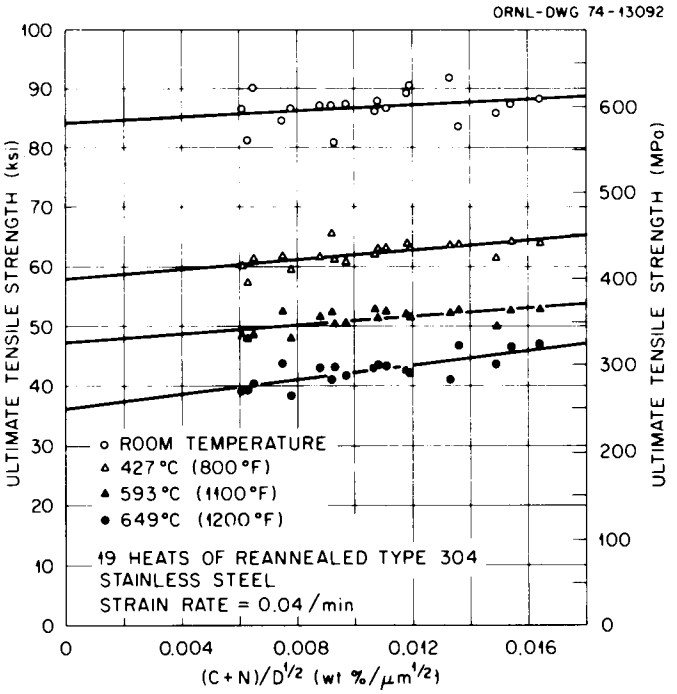

Fig. 5.6. Ultimate Tensile Strength as a Function of $(C + N)d^{-1/2}$ for 19 Heats of Type 304 Stainless Steel.

Table 5.4. Effect of Interstitial Content and Grain Size on the Ultimate Tensile Strength of Types 304 and 316 Stainless Steel

Stainless Steel Type	Test Temperature (°C)	Test Temperature (°F)	Constants of $S_u = A + B(C + N)d^{-1/2}$ A, ksi	A, MPa	B for S in ksi	B for S in MPa
304	Room		84.1 ± 2.3	580	245.9 ± 210.5	1695
	427	900	57.8 ± 1.3	399	401.1 ± 114.6	27.65
	593	1100	47.3 ± 1.1	326	352.7 ± 104.2	2432
	649	1200	36.2 ± 1.3	250	606.6 ± 122.4	4182
316	Room		74.8 ± 1.2	516	513.6 ± 56.5	3541
	427	900	61.9 ± 1.3	427	390.5 ± 57.1	2692
	593	1100	52.5 ± 1.3	362	449.1 ± 60.4	3096
	649	1200	44.9 ± 0.53	310	377.8 ± 24.5	2665

Work is continuing to find factors necessary to account for variation observed in creep curves for various heats of type 304 stainless steel.

5.2.2.2 Heat-to-Heat Variation of Type 316 Stainless Steel

In the heat-to-heat variation program on type 316 stainless steel, we performed creep tests on 0.5-in. (12.7-mm) plate of heats 212 and 613 in both longitudinal and transverse directions. The creep tests were performed on material in the as-received condition and at a test temperature of 593°C (1100°F) and a stress of 35 ksi (241 MPa). The curves for longitudinal and transverse specimens of heat 212 are shown in Fig. 5.7 and for heat 613 in Fig. 5.8. The loading strain and rupture elongation were not greatly different for either heat in both longitudinal and transverse directions. For heat 212, time to rupture for the transverse specimen was 2.07 times that in the longitudinal specimen, whereas for heat 613 it was 2.67 times. We are performing the similar creep tests on material in the reannealed condition.

Figure 5.9 compares time-to-rupture data for seven heats of type 316 stainless steel with the ASME Code Case 1592 minimum and with other data from the literature.[7,8] The ORNL data on six out of seven heats of type 316 stainless steel showed a rather close agreement, but heat 686 (supplied by Allegheny Ludlum) was extremely strong. For example, at 593°C (1100°F) and a stress of 35 ksi (241 MPa), the time to rupture for heat 686 was 3900 hr, compared with 465 hr for heat 613. The large error bands shown in Fig. 5.9 for Garofalo et al.[8] data are partially due to the machine variability and partially to the normal data scatter.

The relation between the creep-rupture strength and ultimate tensile strength observed[9] for type 304 stainless steel has been extended to type 316 stainless steel in Fig. 5.10. The heat-to-heat variation in 10^3-hr creep-rupture strength for ORNL data and the variation due to test temperature in the HEDL data[7] have been correlated with the ultimate tensile strength. The HEDL data show a slight shift in data points to the left, which can be explained perhaps as being due to a lower strain rate (0.0018/min) used by HEDL, as compared with 0.04/min used by ORNL. In

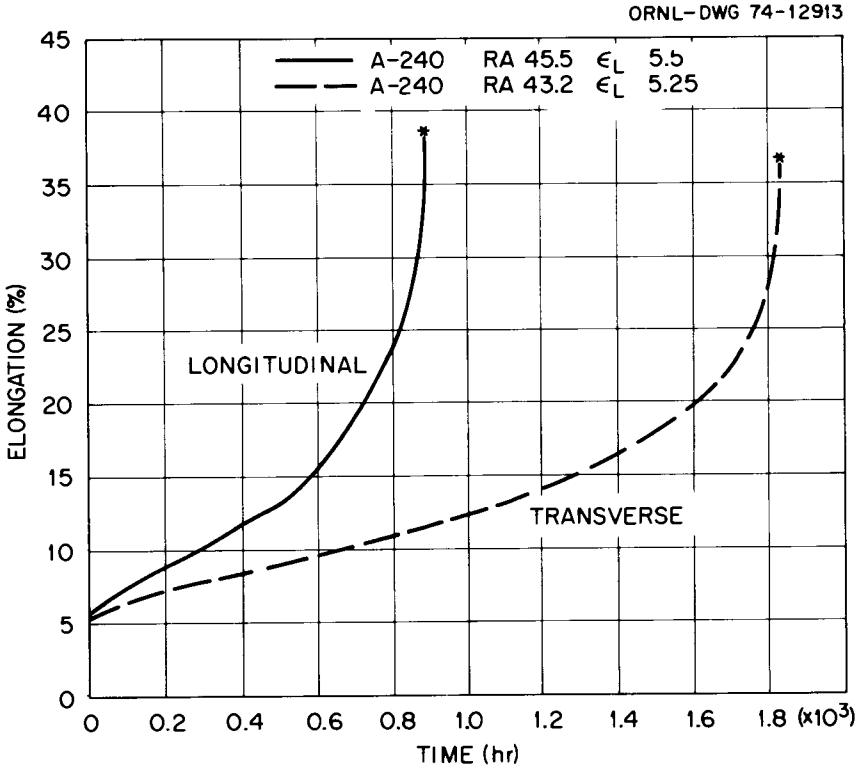

Fig. 5.7. Comparison of Creep Curves for Specimens in the Longitudinal and Transverse Directions for Heat 212 of Type 316 Stainless Steel in the As-Received Condition. The creep tests were performed at 593°C (1100°F) and 30 ksi (207 MPa).

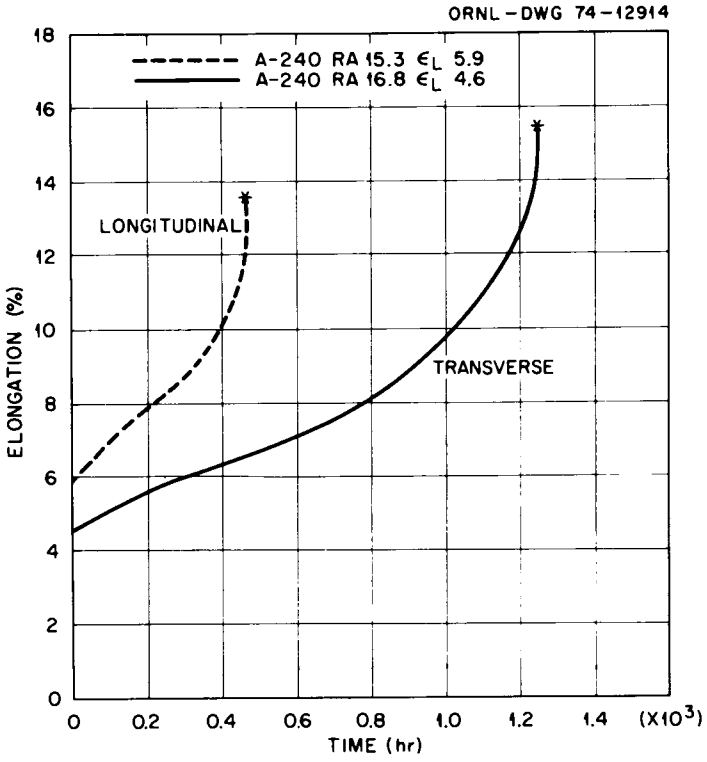

Fig. 5.8. Comparison of Creep Curves for Specimens in the Longitudinal and Transverse Directions for Heat 613 of Type 316 Stainless Steel in the As-Received Condition. The creep tests were performed at 593°C (1100°F) and 30 ksi (207 MPa).

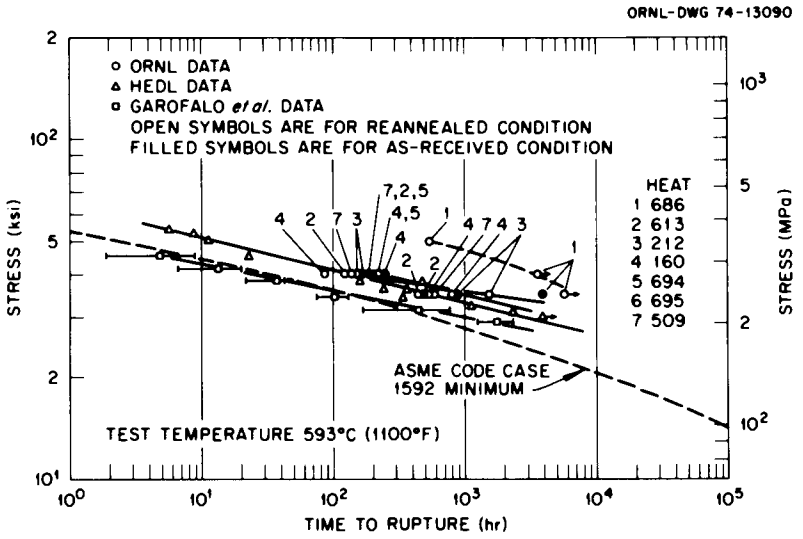

Fig. 5.9. Comparison of Stress-Rupture Results at 593°C (1100°F) for Seven Heats of Type 316 Stainless Steel with ASME Code Case 1592 Minimum Value Curve and with Data from the literature.

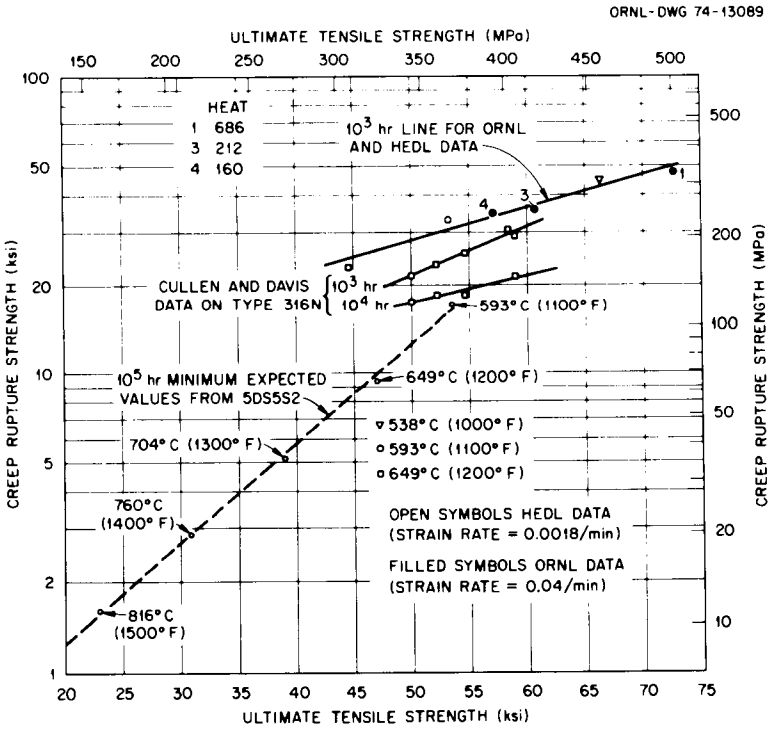

Fig. 5.10. Relationship Between the Creep-Rupture Strength and Ultimate Tensile Strength at the Same Test Temperature for Various Heats of Type 316 Stainless Steel. Cullen and Davis data are at 649°C (1200°F).

Fig. 5.10 we have also examined the data from Cullen and Davis[10] for type 316 stainless steel, where the nitrogen content was varied from 0.039 to 0.15% and the creep-rupture strength was determined at 649°C (1200°F). The plot of Cullen and Davis data in Fig. 5.10 shows that the increase in the 10^3- and 10^4-hr creep rupture strength due to increasing nitrogen content can be related to the corresponding increase in the ultimate tensile strength at the same temperature. The plot of minimum-expected 10^5-hr creep-rupture strength and ultimate strength values reported by Smith[4] for a temperature range of 593 to 816°C (1100–1500°F) again shows an excellent relationship.

A literature review was presented in an earlier report[11] on the importance of carbon, nitrogen, and grain size to tensile properties of stainless steels. We have tried to explain the observed variation in ultimate tensile strength in terms of $(C + N)d^{-1/2}$, where $(C + N)$ is the sum of weight percentages of carbon and nitrogen. The grain size, d, is an average grain diameter in micrometers, determined by the intercept method. In Fig. 5.11, the ultimate tensile strength data at four different temperatures are plotted as functions of $(C + N)d^{-1/2}$ for seven heats of type 316 stainless steel in the reannealed condition. Table 5.4 gives the least squares fit through experimental data to the equation $S_u = A + B(C + N)d^{-1/2}$ for different test temperatures.

Thus, we have again shown that the variation in creep-rupture strength for various heats can be qualitatively related to ultimate tensile strengths for the times considered, which in turn can be related to $(C + N)d^{-1/2}$.

Work is continuing to extend the relation between creep-rupture strength and ultimate tensile strengths for data available in the literature and to properties like stress required to reach a given strain. Complete verification of this technique will of course continue to depend on the results of long-term tests still in progress.

5.2.2.3 Effect of Aging on Tensile and Creep Properties of Type 304 Stainless Steel

The scope and the status of the aging program on nine heats of type 304 stainless steel were presented in earlier reports.[12–15] During the last quarter, we examined the effect of thermal aging on several tensile and creep properties.

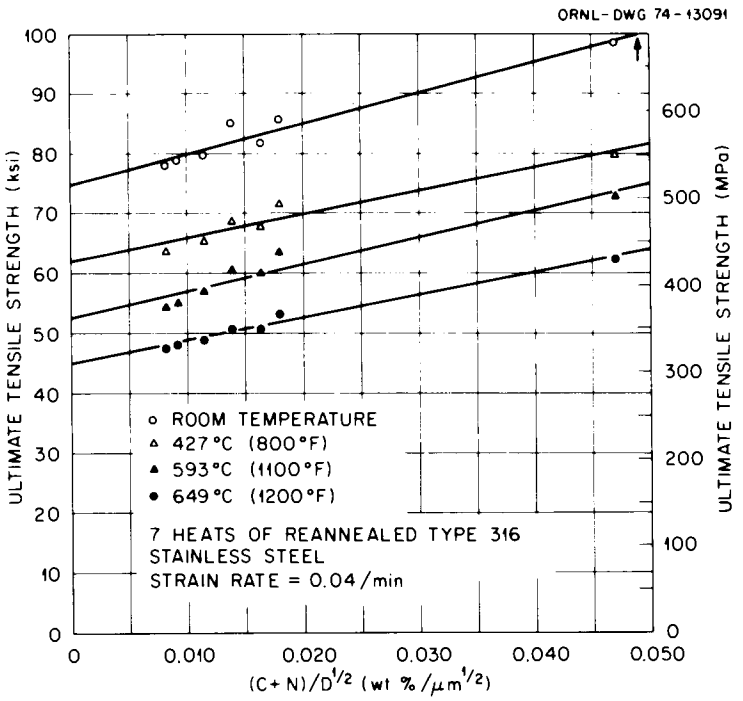

Fig. 5.11. Ultimate Tensile Strength as a Function of $(C + N)d^{-1/2}$ for Seven Heats of Type 316 Stainless Steel.

5.2.2.3.1 Tensile Properties. Figure 5.12 shows the uniform elongation at 593°C (1100°F) as a function of aging temperature for a fixed aging time of 4000 hr for several heats of type 304 stainless steel in the as-received condition. A similar plot for the reannealed condition is shown in Fig. 5.13. From Figs. 5.12 and 5.13 it can be noted that the uniform elongation remains unchanged for an aging temperature of 482°C (900°F), whereas it shows a small and large decrease for aging temperatures of 593 and 649°C (1100 and 1200°F), respectively. For the as-received condition uniform elongation at 593°C (1100°F) dropped from 33–40% for the unaged condition to 28–30% after aging at 649°C (1200°F) for 4000 hr. A similar drop for the reannealed condition was from 36–39% to 29–32%.

The uniform elongation at 593°C (1100°F) for two heats, 845 and 926, of type 304 stainless steel is plotted in Fig. 5.14 as a function of aging temperature for aging times of 4000 and 10,000 hr. The most important point to note is that although uniform elongation remains unchanged for aging at a temperature of 482°C (900°F) for an aging time

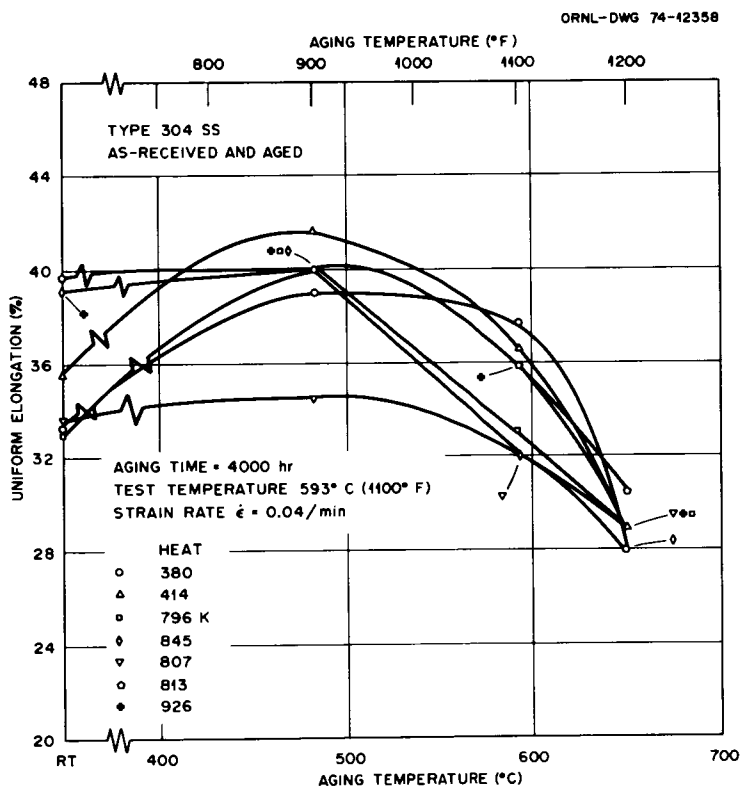

Fig. 5.12. Effect of Aging Temperature on Uniform Elongation of As-Received Type 304 Stainless Steel Aged for 4000 hr and Tested at 593°C (1100°F).

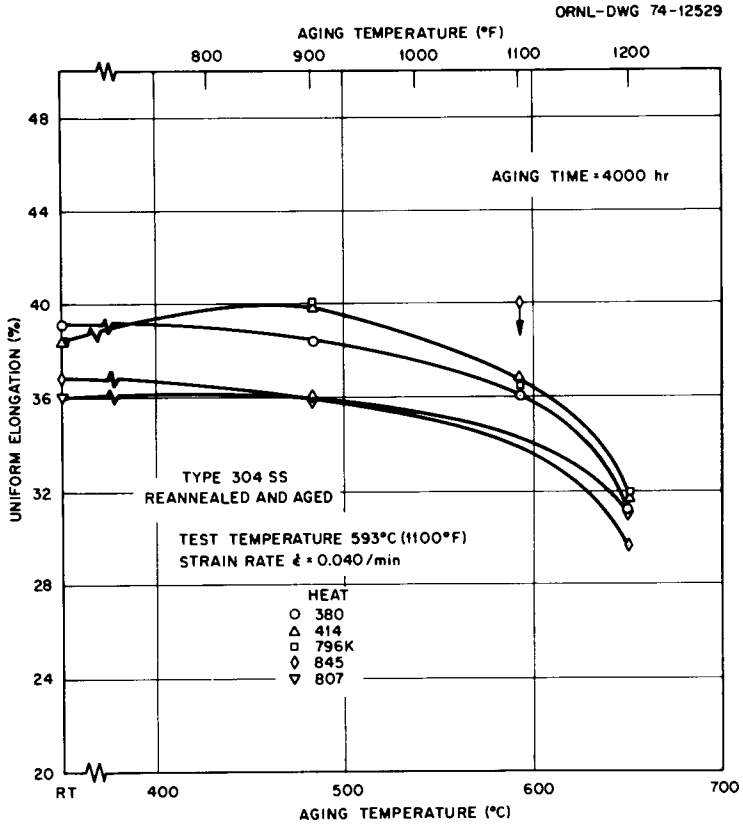

Fig. 5.13. Effect of Aging Temperature on Uniform Elongation of Reannealed Type 304 Stainless Steel Aged for 4000 hr and Tested at 593°C (1100°F).

of 4000 hr, it does show a decrease for an aging time of 10,000 hr. Furthermore, the decrease in uniform elongation at a given aging temperature is greater for an aging time of 10,000 hr than for 4000 hr. For example the drop in uniform elongation for both heats, 845 and 926, aged at 649°C (1200°F) is from 39 to 28–30% for an aging time of 4000 hr and from 39 to 23–24% for an aging time of 10,000 hr.

The uniform elongation at 593°C (1100°F) for the reference heat of type 304 stainless steel is compared in Fig. 5.15 for specimens aged with and without stress (pre-creeping). Aging at 593°C (1100°F) for 500 hr under a stress of 20 ksi (138 MPa) produced a decrease in uniform elongation from 38 to 20.2% as compared with essentially no change produced by thermal aging for 4000 hr at the same temperature. Thus, it seems that although thermal aging produces small changes in uniform elongation, aging under stress (a more realistic situation for a component in service) can produce rather severe reductions in uniform elongation. More work is continuing in this area on the reference heat of type 304 stainless steel.

Uniform elongation for unaged and thermally aged specimens of various heats of type 304 stainless steel is compared with the minimum-expected value curve from the *Nuclear Systems Materials Handbook* (plate-bars) in Figs. 5.16 and 5.17 for the as-received-and-aged condition, and for the reannealed-and-aged condition, respectively. The uniform elongations in the present investigation are measured for specimens of 1.25-in. (31.8-mm) gage length, whereas the Handbook values are for 2-in. (50.8-mm) gage length. Uniform elongation is known[16] to be independent of gage length, and thus the present results can be compared with those from the Handbook without any correction.

Figure 5.16 shows that for the as-received condition of type 304 stainless steel, aging for 10,000 hr at 649°C (1200°F) still maintains the uniform elongation at 593°C (1100°F) above the minimum-expected value curve. For the reannealed condition of type 304 stainless steel, aging data are available only for an aging time of 4000 hr at various aging temperature. For all combinations of aging time and temperature, uniform elongation at 593°C (1100°F) stays much above the minimum-expected value

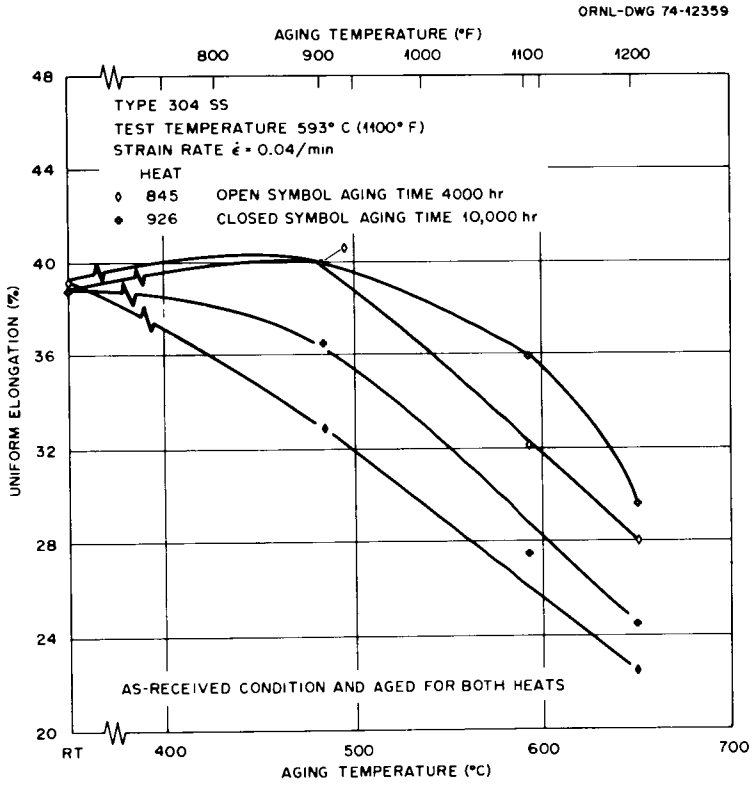

Fig. 5.14. Effect of Aging Temperature on Uniform Elongation of As-Received Type 304 Stainless Steel Aged for 4000 and 10,000 hr and Tested at 593°C (1100°F).

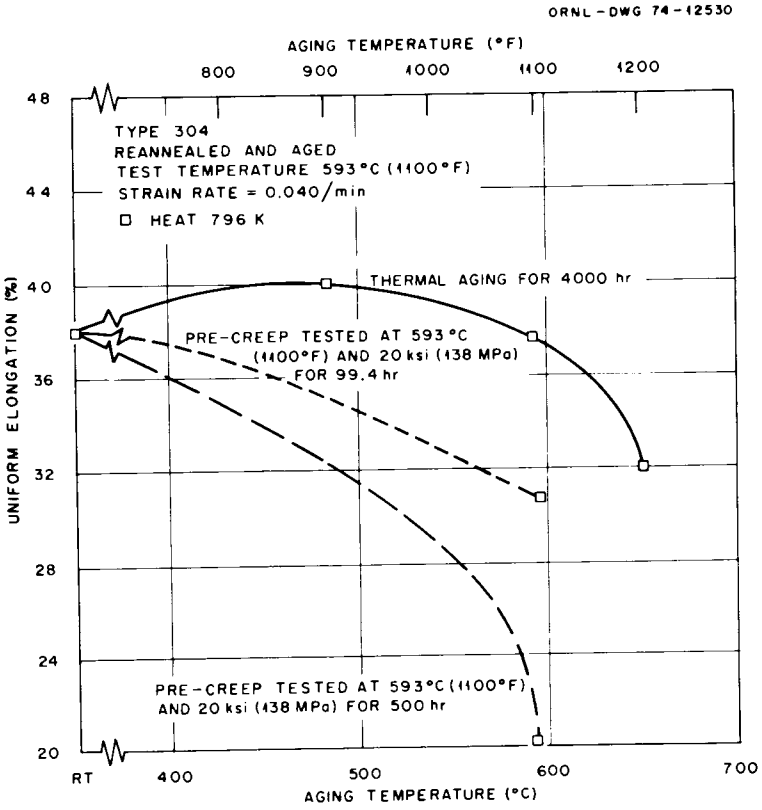

Fig. 5.15. Effect of Thermal Aging and Precreeping on Uniform Elongation at 593°C (1100°F) for Reannealed Heat 796 of Type 304 Stainless Steel.

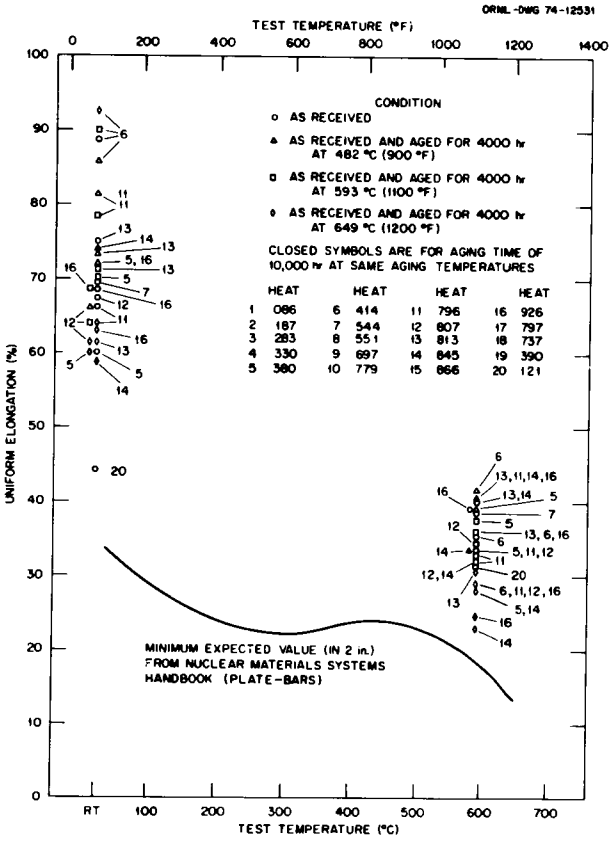

Fig. 5.16. Comparison of Uniform Elongation of Type 304 Stainless Steel for As-Received and As-Received-and-Aged Conditions with Minimum-Expected Values from the *Nuclear Systems Materials Handbook.*

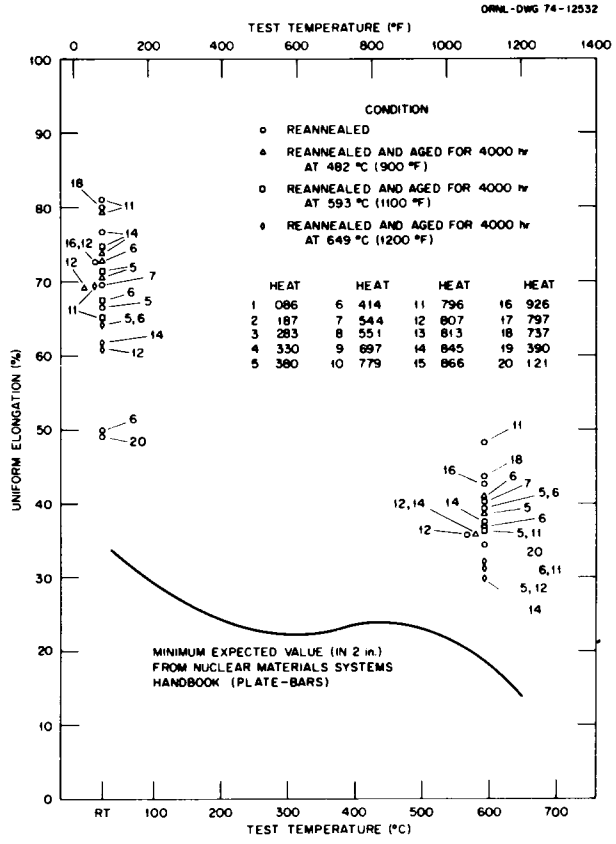

Fig. 5.17. Comparison of Uniform Elongation of Type 304 Stainless Steel for Reannealed and Reannealed-and-Aged Conditions with Minimum-Expected Values from the *Nuclear Systems Materials Handbook.*

curve in Fig. 5.17. The uniform elongation for type 316 stainless steel in the unaged and aged conditions is compared with the minimum-expected value curve from the *Nuclear Systems Materials Handbook* in Sect. 5.2.2.4, and for some heats aging conditions used in the present investigation can bring the uniform elongation well below the minimum-expected value curve (see Fig. 5.35).

The effect of carbon, for a fixed nitrogen content (0.019–0.033%), on uniform elongation at 593°C (1100°F) for unaged and aged type 304 stainless steel is shown in Fig. 5.18. A similar plot showing the effect of nitrogen for a fixed carbon content (0.057–0.065%) is shown in Fig. 5.19. It can be noted from Fig. 5.18 that for a small nitrogen content, increasing carbon increases the uniform elongation for the unaged condition. For the aged condition, 4000 hr at 649°C (1200°F), uniform elongation appears to be independent of carbon content up to 0.062%, where a marked decrease occurs. More data are needed to define the drop observed, and thus it is marked by a dotted line in Fig. 5.18.

For a fixed carbon content (0.057–0.065%), Fig 5.19 shows that increasing nitrogen decreases the uniform elongation at 593°C (1100°F) for both the unaged and aged type 304 stainless steel. At very low nitrogen, 0.019%, and carbon content of 0.065%, uniform elongation appears to drop very sharply. Thus, while increasing carbon content tends to increase the uniform elongation at 593°C (1100°F) in the unaged condition or has no effect on the aged condition, increasing nitrogen tends to slightly decrease the uniform elongation for both unaged and aged conditions of type 304 stainless steel.

From Fig. 5.18 we note that the effect of increasing carbon content on the uniform elongation in the unaged condition disappears for the aged condition. This may imply that the carbon in solution (in the unaged condition) increases the uniform elongation but has no effect when it precipitates as carbides (in the aged condition). Based on similar lines, increasing nitrogen, which decreases the uniform elongation, (Fig. 5.19) when in solution (in the unaged condition) must stay in solution even on aging or must have the same effect even when precipitated as nitrides.

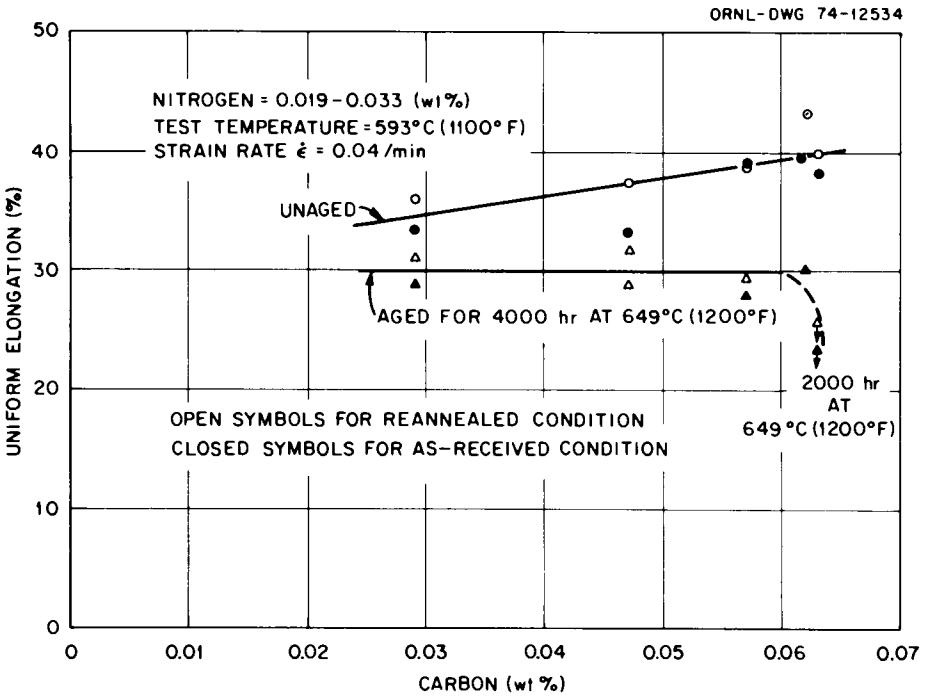

Fig. 5.18. Effect of Carbon on Uniform Elongation at 593°C (1100°F) of Various Heats of Type 304 Stainless Steel in Unaged and Aged Conditions.

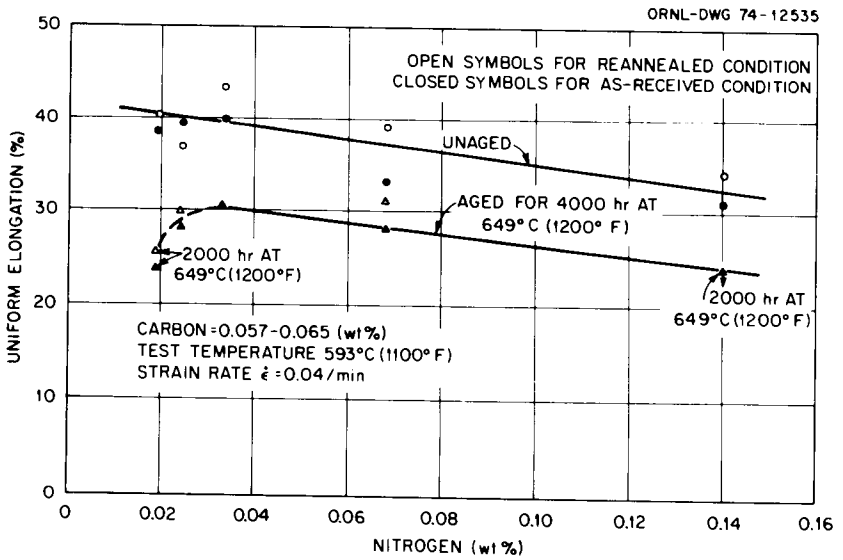

Fig. 5.19. Effect of Nitrogen on Uniform Elongation at 593°C (1100°F) of Various Heats of Type 304 Stainless Steel in Unaged and Aged Conditions.

5.2.2.3.2 Creep Properties. The effect of aging on creep properties of the reference heat and heat 845 was reported[15] last quarter. The data on effect of aging on the creep properties of heats 926, 544, 121, and 380 are summarized in Tables 5.5 through 5.7 Consistent with the previous observations on heats 845 and 796, we note the following on heats 926, 544, 121, and 380.

1. Both minimum creep rate and time to rupture increase for heat 380, whereas minimum creep rate increases with decrease in time to rupture for heats 926, 544, and 121.

2. Loading strain decreases on aging for all heats.

3. Strain in all stages (first, second, and third) increases on aging for all heats. Thereby, total elongation at rupture and reduction of area also increase.

4. The durations of second- and third-stage creep decrease on aging for all heats except heat 380, for which they increase.

The effect of aging temperature on creep curves for heats 845 and 926 are shown in Figs. 5.20 and 5.21. The effect of aging time on creep curves for heat 845 is shown in Fig. 5.22.

From Tables 5.5 through 5.7 and Figs. 5.20 and 5.21, it can be noted that the effect of aging is negligible for an aging temperature of 482°C (900°F) but becomes important for aging temperatures of 593 and 649°C (1100 and 1200°F). The effect of increasing aging time for an aging temperature of 649°C (1200°F) on creep curves of heat 845, Fig. 5.22, is rather small as compared with the effect of increasing aging temperature for a given aging time, Figs. 5.20 and 5.21.

Garofalo et al.[8] investigated the effect of pretreatment at 816°C (1500°F) for 24 hr on creep properties of type 316 stainless steel at a test temperature of 593°C (1100°F). They found that at equivalent stress levels there was no systematic change in minimum creep rate, but secondary creep strain increased. The time to rupture and rupture elongation both increased. The present ORNL results on type 304 stainless steel (and type 316 stainless steel, see Sect. 5.2.2.4) clearly show that aging for times up to 10,000 hr at temperatures of 482, 593, and 649°C (900, 1100, and 1200°F) increase the minimum creep rate and decrease the time to

Table 5.5. Creep[a] Properties of Aged Heats 926, 544, 121, and 380 of Type 304 Stainless Steel — Creep-Rupture Data

Condition	Treatment			Stages (hr)		Minimum Creep Rate (% hr^{-1})	Rupture Strain (%)	Reduction of Area (%)
	Time (hr)	Temperature (°C)	Temperature (°F)	Loading e_L	Rupture t_r	ε_{mcr}	ε_f	R_A
				Heat 926				
Reannealed	0.5	1065	1950	7.60	2580.2	2.025×10^{-3}	28.0	31.67
As-received and aged	10,000	482	900	4.42	3249.5	1.975×10^{-3}	26.20	31.37
As-received and aged	10,000	593	1100	2.10	930.8	2.85×10^{-2}	51.23	54.9
As-received and aged	10,000	649	1200	2.83	780.6	3.5×10^{-2}	64.77	52.9
				Heat 544				
As-received				4.60	431.0	1.66×10^{-2}	20.7	21.1
As-received and aged	1000	649	1200	2.39	246.0	1.33×10^{-1}	58.8	45.7
As-received and aged	2000	649	1200	2.198	223.5	1.48×10^{-1}	63.7	54.9
Reannealed	0.5	1065	1950	5.84	356.1	2.16×10^{-2}	23.6	22.8
Reannealed and aged	2000	593	1100	4.22	349.0	3.50×10^{-2}	26.0	25.1
Reannealed and aged	1000	649	1200	2.36	293.0	9.15×10^{-2}	51.82	48.4
Reannealed and aged	2000	649	1200	2.98	156.4	1.56×10^{-1}	43.98	37.6
				Heat 121				
As-received				6.76	1055.9	4.875×10^{-3}	18.67	22.32
As-received and aged	2000	482	900	7.18	1059.8	4.750×10^{-3}	19.79	29.0
As-received and aged	2000	649	1200	3.49	640.30	2.90×10^{-2}	46.84	71.59
				Heat 380				
Reannealed	0.5	1065	1950	9.82	741.5	3.2×10^{-3}	13.42	11.50
Reannealed and aged	1000	649	1200	3.37	1645.8	1.15×10^{-2}	39.32	38.35

[a]All creep tests were performed at a stress of 30 ksi (207 MPa) and a test temperature of 593°C (1100°F).

Table 5.6. Creep[a] Properties of Aged Heats 926, 544, 121, and 380 of Type 304 Stainless Steel — Strain Measures

Condition	Treatment			Strain, %						Strain Ratio, %		Stable Creep Strain $\epsilon_s = t_r \epsilon_m$ (%)
	Time (hr)	Temperature (°C)	Temperature (°F)	End of Primary ϵ_1	End of Secondary: Actual, ϵ_1	End of Secondary: 0.2% Offset, ϵ_{ss}	Creep Strain ϵ_{cs}	$\epsilon_2 - \epsilon_1$	$\epsilon_{cs} - \epsilon_2$	$\frac{\epsilon_2 - \epsilon_1}{\epsilon_{cs}}$	$\frac{\epsilon_{cs} - \epsilon_2}{\epsilon_{cs}}$	
						Heat 926						
Reannealed	0.5	1065	1950	1.625	3.25	4.125	20.4	1.625	17.15	7.97	84.1	5.22
As-received and aged	10,000	482	900	1.580	3.30	4.080	21.78	1.720	18.48	7.90	84.8	6.42
As-received and aged	10,000	593	1100	5.00	14.125	16.50	49.13	9.125	35.005	18.57	71.3	26.53
As-received and aged	10,000	649	1200	2.50	12.50	15.50	61.94	10.00	49.44	16.14	79.8	27.32
						Heat 544						
As-received				2.90	5.35	6.20	16.10	2.45	10.75	15.22	66.8	7.15
As-received and aged	1000	649	1200	2.00	16.50	18.50	36.38	14.50	39.88	25.72	70.7	32.72
As-received and aged	2000	649	1200	2.50	18.2	19.6	61.46	15.70	43.26	25.54	70.4	33.08
Reannealed	0.5	1065	1950	3.50	6.0	6.90	17.8	2.50	11.80	14.04	66.3	7.69
Reannealed and aged	2000	593	1100	4.375	9.63	10.63	21.78	5.255	12.15	24.13	55.8	12.22
Reannealed and aged	1000	649	1200	3.750	14.125	17.00	49.46	10.375	35.335	20.98	71.4	26.81
Reannealed and aged	2000	649	1200	3.00	14.50	16.25	41.00	11.50	26.50	28.05	64.6	24.40
						Heat 121						
As-received				2.20	4.20	5.10	11.91	2.00	7.71	16.79	64.7	5.15
As-received and aged	2000	482	900	2.30	4.25	5.00	12.61	1.95	7.61	15.46	60.35	5.03
As-received and aged	2000	649	1200	2.625	10.00	11.50	43.35	7.375	33.35	17.01	76.93	18.57
						Heat 380						
Reannealed	0.5	1065	1950	1.4375	2.8375	3.375	3.60	1.40	0.7625	38.9	21.18	2.373
Reannealed and aged	1000	649	1200	4.250	12.750	14.50	35.95	8.50	23.20	23.6	64.53	18.93

[a]All creep tests were performed at a stress of 30 ksi (207 MPa) and a test temperature of 593°C (1100°F).

Table 5.7. Creep[a] Properties of Aged Heats 926, 544, 121, and 380 of Type 304 Stainless Steel — Time Parameters

Condition	Treatment			Time, hr			Duration, hr		Time Ratio, %	
	Time (hr)	Temperature (°C)	Temperature (°F)	End of Primary t_1	End of Secondary		Third Stage $t_r - t_2$	Second Stage $t_2 - t_1$	$\frac{t_2 - t_1}{t_r}$	$\frac{t_r - t_2}{t_r}$
					Actual, t_2	0.2% Offset, t_{ss}				
				Heat 926						
Reannealed	0.5	1065	1950	350.0	1125.0	1425	1455.2	775	30.0	56.4
As-received and aged	10,000	482	900	250.0	1225.0	1375	2024.5	975	30.0	62.3
As-received and aged	10,000	593	1100	110.0	420.0	500	510.8	310	33.3	54.9
As-received and aged	10,000	649	1200	40.0	300.0	400	480.6	260	33.3	61.6
				Heat 544						
As-received				100.0	242.5	282.5	188.5	142.5	33.1	43.7
As-received and aged	1000	649	1200	9.38	118.8	131.2	127.2	109.4	44.5	51.7
As-received and aged	2000	649	1200	10.00	115.3	123.5	108.2	105.3	47.1	48.4
Reannealed	0.5	1065	1950	75.0	187.5	222.5	168.6	112.5	31.6	47.3
Reannealed and aged	2000	593	1100	62.5	212.6	237.5	136.4	150.1	43.0	39.1
Reannealed and aged	1000	649	1200	22.5	135.0	162.5	158.0	112.5	38.4	53.9
Reannealed and aged	2000	649	1200	12.0	85.0	95.0	71.4	73.0	46.7	45.7
				Heat 121						
As-received				165.0	560.0	710.0	495.9	395	37.4	46.96
As-received and aged	2000	482	900	180.0	570.0	680.0	489.8	390	36.8	46.22
As-received and aged	2000	649	1200	45.0	295.0	335.0	345.3	250	39.0	53.93
				Heat 380						
Reannealed	0.5	1065	1950	185	617.5	730.0	124.0	432.5	58.3	16.72
Reannealed and aged	1000	649	1200	190	930.0	1050.0	715.8	740.0	44.96	43.50

[a]All creep tests were performed at a stress of 30 ksi (207 MPa) and a test temperature of 593°C (1100°F).

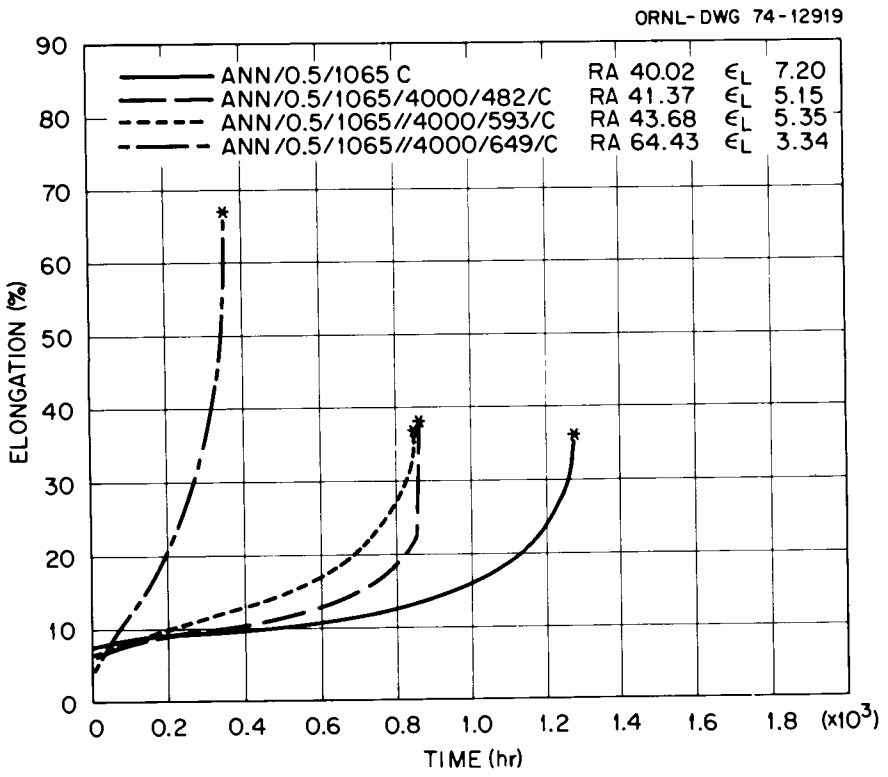

Fig. 5.20. Effect of Aging Temperature on Creep Curves for Heat 845 of Type 304 Stainless Steel. Creep tests were performed at 593°C (1100°F) and 30 ksi (207 MPa).

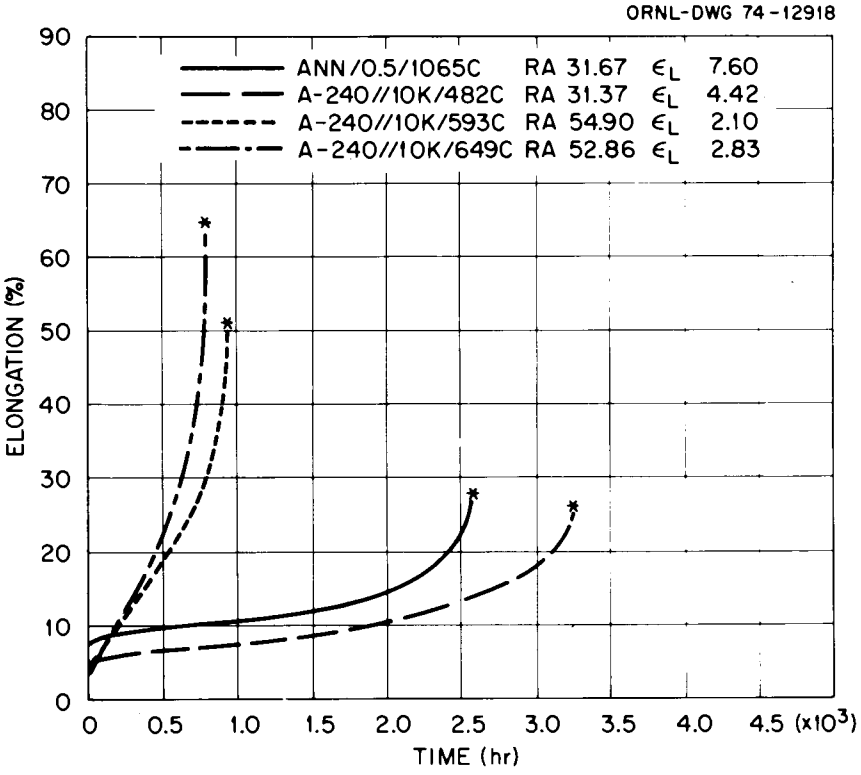

Fig. 5.21. Effect of Aging Temperature on Creep Curves for Heat 926 of Type 304 Stainless Steel. Creep tests were performed at 593°C (1100°F) and 30 ksi (207 MPa). 10 K stands for aging time of 10,000 hr.

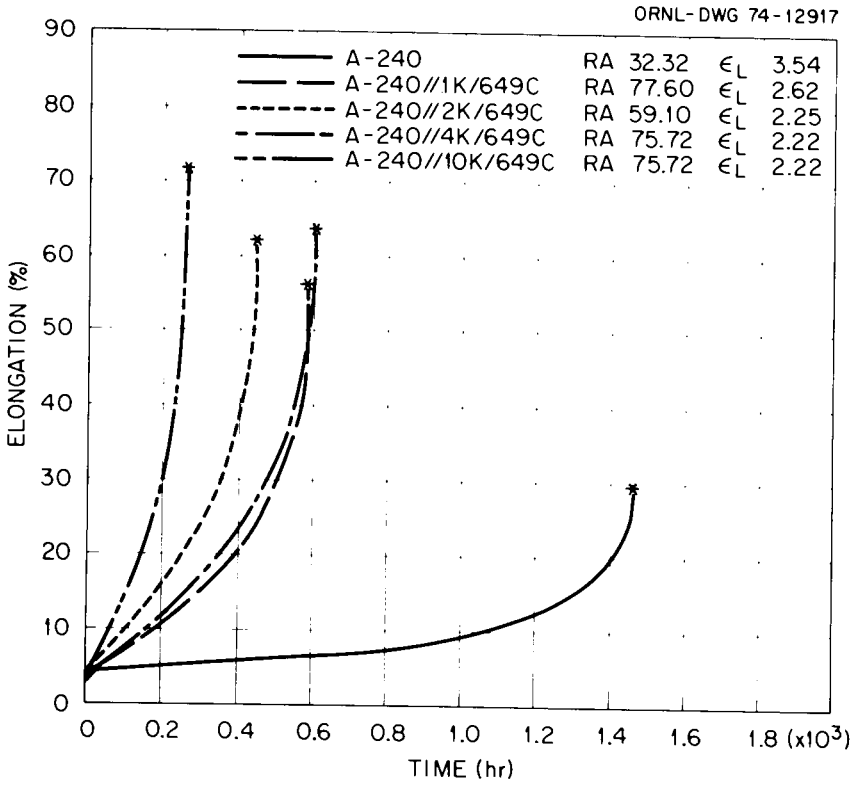

Fig. 5.22. Effect of Aging Time on Creep Curves for Heat 845 of Type 304 Stainless Steel. Creep tests were performed at 593°C (1100°F) and 30 ksi (207 MPa). 1 K, 2 K etc. stand for aging time of 1000, 2000 hr etc.

rupture for all heats except 796 and 380, for which both minimum creep rate and time to rupture increased. The change in minimum creep rate and time to rupture increased with increasing aging temperature and was greatest for 649°C (1200°F).

Thus, a comparison of ORNL results on the aged specimens with those of Garofalo et al.[8] shows a contrast that, while the present results indicate a decrease in time to rupture for most of the heats of type 304 stainless steel, their results show an increase. The major difference between the aging treatments is that Garofalo et al. used a higher temperature, 816°C (1500°F), and shorter time, 24 hr, whereas we used lower temperatures 482 to 649°C (900–1200°F), and longer times, 1000 to 10,000 hr.

In a recent study, Etienne et al.[17] performed detailed electron microscopy on type 304 stainless steel aged for long times at temperatures in the range 500 to 800°C (932–1472°F). They reported the precipitate size both at grain boundaries and in the matrix. We have summarized

their results in Table 5.8 for aging conditions used in the present investigation. It can be noted that no grain boundary or matrix carbides are formed for aging temperatures below 500°C (932°F) for aging times greater than 10,000 hr. Even for an aging temperature of 500°C (932°F),

Table 5.8. Summary[a] of Carbide Particle Sizes at Grain Boundary and in Matrix for Various Aging Times and Temperatures for Type 304 Stainless Steel Containing 0.04% C

Aging Temperature		Aging Time (hr)	Carbide Particle Size, μm	
°C	°F		Grain boundary	Matrix
<500	<932	>10,000	NO	NO
500	932	<10,000	NO	initiated
500	932	10,000	NO	<0.020
538	1000	200	initiated	NO
538	1000	1000	0.10	NO
538	1000	10,000	0.20–0.30	0.020–0.050
593	1100	100	initiated	NO
593	1100	1000	>0.20	<0.020
593	1100	10,000[b]	0.40–0.60	0.10
650	1200	10	initiated	NO
650	1200	100	~0.2	NO
650	1200	1000	0.4	NO
650	1200	10,000	1.0	0.05–0.10

[a]Numbers in this table are derived from Fig. 225.4 of C. F. Etienne, W. Portland, and H. B. Zeedijk, "On the Capability of Austenitic Steel to Withstand Cyclic Deformation During Service at Elevated Temperature," presented at the International Conference on Creep and Fatigue in Elevated Temperature Applications, Philadelphia, September 1973, and Sheffield UK, April 1974.

[b]ORNL data on one heat of type 304 stainless steel aged for 22,622 hr at 593°C gave precipitate sizes of 0.23 and 0.13 μm for grain boundary and matrix, respectively.

aging time up to 10,000 hr did not produce any carbide at the grain boundaries, but some had started to form in the matrix. The aging at 593°C (1100°F) for 10,000 hr (Table 5.8) produced carbides of 0.40 to 0.60 μm at the grain boundaries and 0.10 μm in the matrix. At ORNL we estimated the size of carbide precipitate particles in heat 187 of type 304 stainless steel, which was aged at 593°C (1100°F) for 22,622 hr. The micrographs showing the precipitate at the grain boundary and in the matrix are presented in Figs. 5.23 and 5.24, respectively.

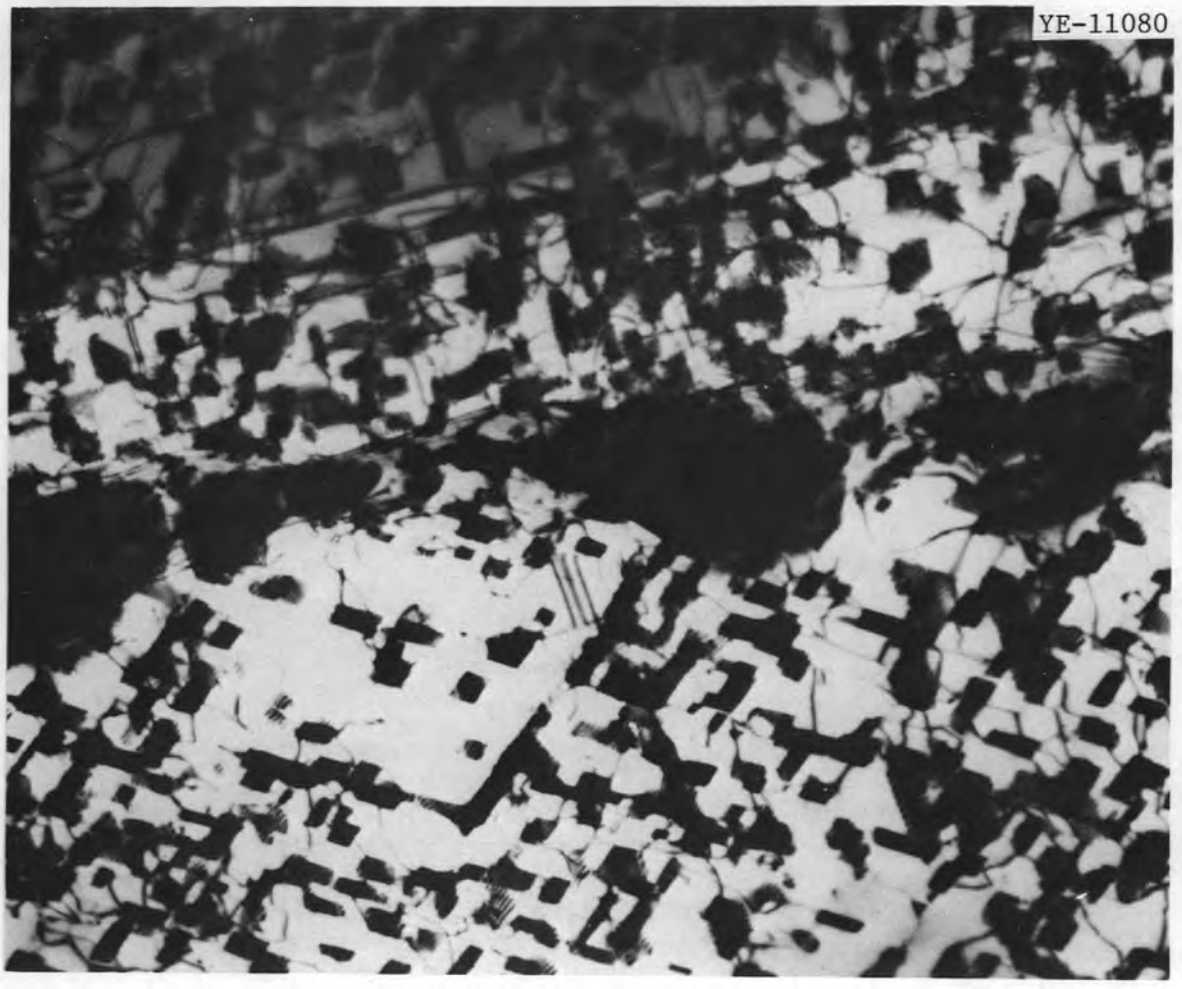

Fig. 5.23. Transmission Electron Micrograph Showing Grain Boundary Precipitate in Specimens of Heat 187 of type 304 Stainless Steel, aged at 593°C (1100°F) for 22,622 hr. 40,000×

Fig. 5.24. Transmission Electron Micrograph Showing Grain Matrix Precipitate in Specimen of Heat 187 of Type 304 Stainless Steel, Aged at 593°C (1100°F) for 22,622 hr. 40,000×

The carbide sizes at the grain boundary and in the matrix were estimated to be 0.23 and 0.13 μm, respectively. The ORNL results indicated that the carbide size at the grain boundary was smaller, whereas in the matrix it was larger in comparison with the results of Etienne et al.[17] The larger size in the matrix could be understood, because of the 22,622-hr aging time for ORNL specimen, compared with the 10,000-hr treatment reported by Etienne et al. The small size of carbide at grain boundaries observed at ORNL is hard to explain, except that only a few particles were used to determine their size, and thus the present size may be rather approximate. Etienne et al.[17] also reported that aging in the temperature range 500 to 600°C (932–1112°F) gave rise to considerable carbide ($M_{23}C_6$) precipitate along the grain boundaries and in the matrix. Whereas, for

aging treatments between 650 and 800°C (1200–1472°F), the carbides chiefly precipitate along the grain boundaries. Thus, the present results are from aging treatments where carbides are expected in both the grain boundaries and the matrix, whereas results of Garofalo et al.[8] are from an aging treatment that apparently produces precipitate only at the grain boundaries. The difference observed in effects on creep properties due to aging for long times (1000–10,000 hr) at temperatures between 482 and 649°C (900–1200°F) in comparison with results obtained from material aged for short times (24 hr) at 816°C (1500°F), along with the microstructure results of Etienne et al.,[17] clearly suggests that knowledge to predict *long-time low-temperature* aging for a reactor operating service cannot be obtained from *short-time high-temperature* aging.

5.2.2.3.3 Microstructure. Excellent reviews[18-22] are available on creep failure modes of metals and alloys. The most common feature of the present literature is that it refers to two basic failure modes: transgranular and intergranular. The transgranular mode is suggested to occur at low temperatures and high strain rates, whereas intergranular fracture occurs at high temperatures and low strain rates. At elevated temperature during creep, intergranular fracture is commonly observed and is suggested to occur by grain boundary sliding. The transition from transgranular to intergranular fracture is associated with a noticeable loss of ductility. The intergranular fracture involves the nucleation and growth of grain boundary cracks and voids. Garofalo[20] in his review paper listed the following grain boundary locations for the nucleation of cracks and voids:

1. triple points of high-angle boundaries,
2. inclusions and precipitated particles,
3. grain-boundary ledges, and
4. junctions between sub-boundaries and grain-boundaries.

Kemsley[23] investigated the crack paths in fatigued copper and found that cracks not only nucleated along grain boundaries but also along striations and annealing twins. In a recent paper, Michel et al.[24] have shown the deformation induced crack formation at twin boundaries in type 304 stainless steel. They suggested that, since cracks form along the twin boundaries, they may behave in a manner similar to grain boundaries under proper conditions. The observations of Michel et al. were restricted

to type 304 stainless steel tested at 650°C (1200°F) in tensile and creep tests at deformation rates between 8.33×10^{-4} and 4.6×10^{-8}. Most of the micrographs presented in their paper show cracks at both grain and twin boundaries.

At ORNL, we have observed that aging at 649°C (1200°F) for 10,000 hr can produce a transition from grain to twin boundary cracks in specimens creep tested at 593°C (1100°F) and 30 ksi (207 MPa). Also the transition from grain to twin boundary cracks is rather complete in the sense that they were the primary cracks. The specimens used in the present observation were from heat 926 of type 304 stainless steel.

Typical micrographs showing the fracture end of annealed and aged creep specimens are presented in Fig. 5.25. Figure 5.26 shows similar micrographs for the end farthest from fracture. The most significant observation in Fig. 5.25 is that all cracks for the annealed specimen are along the grain boundaries, and fracture appears intergranular, whereas, for the aged specimen, creep cracking is limited, and whatever cracks are observed are mostly along the twin boundaries. The creep cavities in the annealed specimen are mostly round, whereas for the aged specimen they are wedge shaped along the twin boundaries.

In the area away from the fracture end, where creep deformation is uniform, creep cavities along the grain boundaries were observed in the annealed but not the aged specimen. The aged specimen showed very limited creep cavities, and, as seen in Fig. 5.26, the one observed is again along a twin boundary. For the annealed specimen the cavity orientation near the fracture end is rather random, whereas at the farther end from fracture, it is normal to and at 45° from the stress axis. For the aged specimen the major axes of the twin boundary cracks are mostly at an angle of 45° to the stress axis near the fracture end and at 90° remote from the fracture surface. Figure 5.27 shows an additional set of micrographs for the aged specimen, where an approximately 45° angle between twin cracks and the stress axis is clearly observed.

The comparison of grain shape in Figs. 5.25 through 5.27 shows a large amount of intragranular deformation for the aged specimen in comparison with the annealed specimen. The large rupture elongation, the

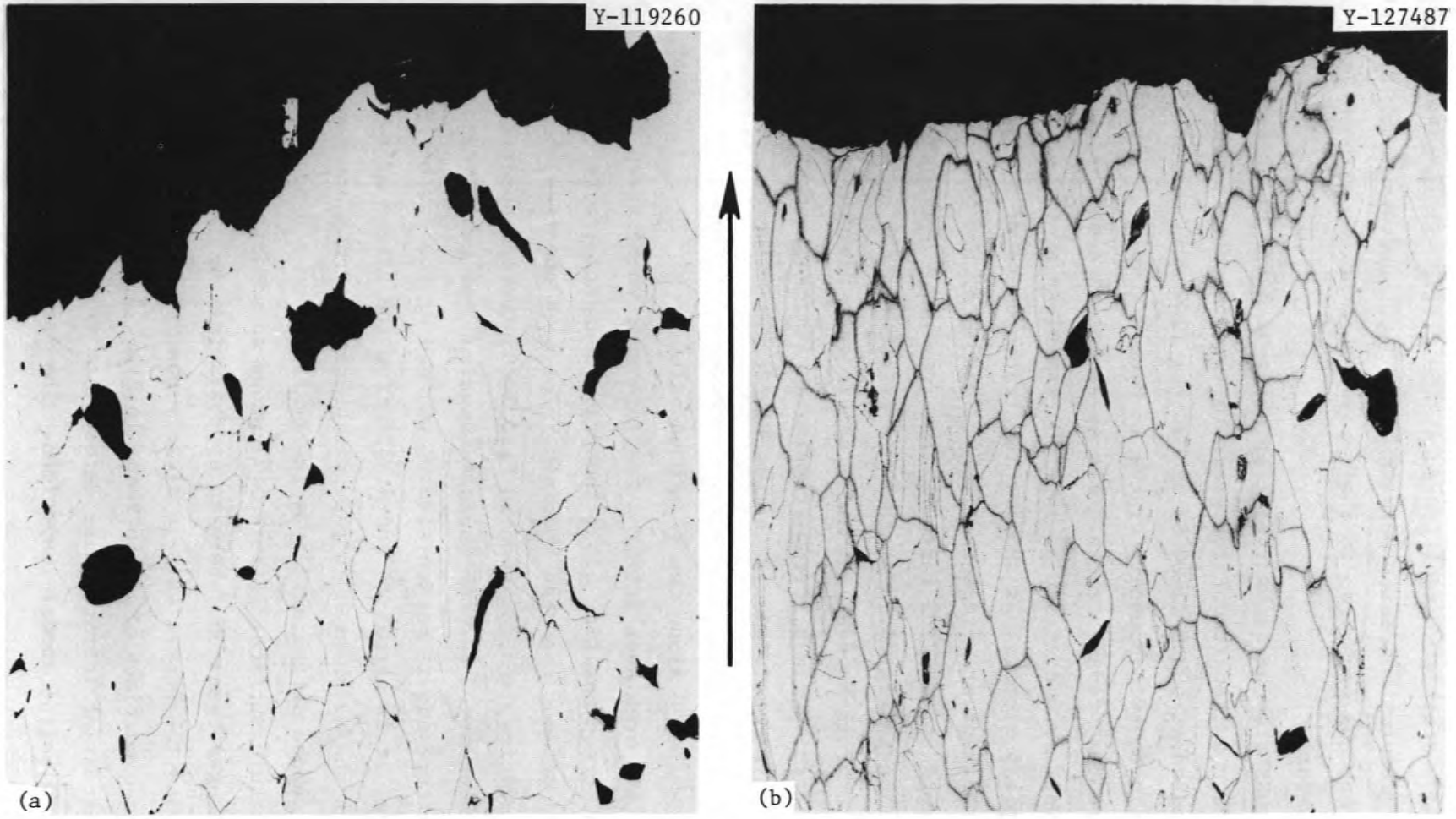

Fig. 5.25. Microstructure of the Fracture Ends of Creep Specimens of Heat 926 of Type 304 Stainless Steel Tested at 593°C (1100°F) and 30 ksi (207 MPa). 100×. Arrow indicates direction of applied stress. (a) Annealed and creep tested. (b) Aged at 649°C (1200°F) for 10,000 hr and creep tested.

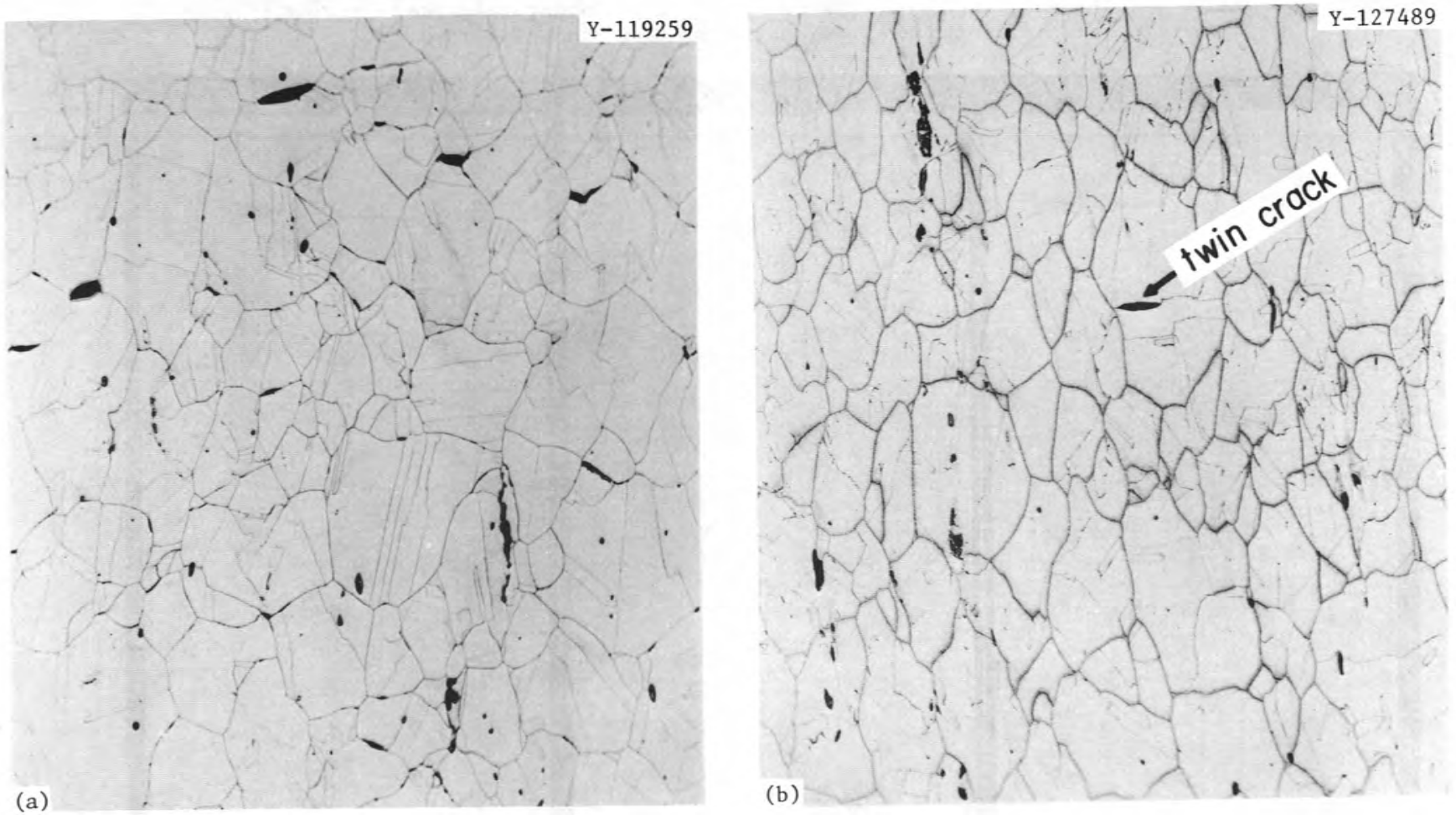

Fig. 5.26. Microstructure of the End Away from the Fractures in Creep Specimens of Heat 926 of Type 304 Stainless Steel Tested at 593°C (1100°F) and 30 ksi (207 MPa). 100×. Arrow indicates direction of applied stress. (a) Annealed and creep tested. (b) Aged at 649°C (1200°F) for 10,000 hr and creep tested.

Fig. 5.27. Microstructure Showing Extensive Twin Boundary Cracking in a Specimen Creep Tested at 593°C (1100°F) and 30 ksi (207 MPa) for Heat 926 of Type 304 Stainless Steel, Aged at 649°C (1200°F) for 10,000 hr. 100×. Arrow indicates direction of applied stress in all three views.

transgranular nature of the fracture, and the observation of no grain boundary cavities do again suggest that creep deformation in the aged specimen occurs primarily through the grain matrix.

Since the transition from grain to twin boundary cracking is observed on aging, it must be associated with the nature of precipitate formed during this process. A typical micrograph showing the precipitate in the aged specimen is shown in Fig. 5.28. The grain boundaries in the aged specimen are decorated with extensive precipitation. The matrix is relatively free of precipitate, and twin boundaries show some precipitation. Transmission electron microscopy showed that the aged material contained smaller and less dense precipitate particles within the grains than at the

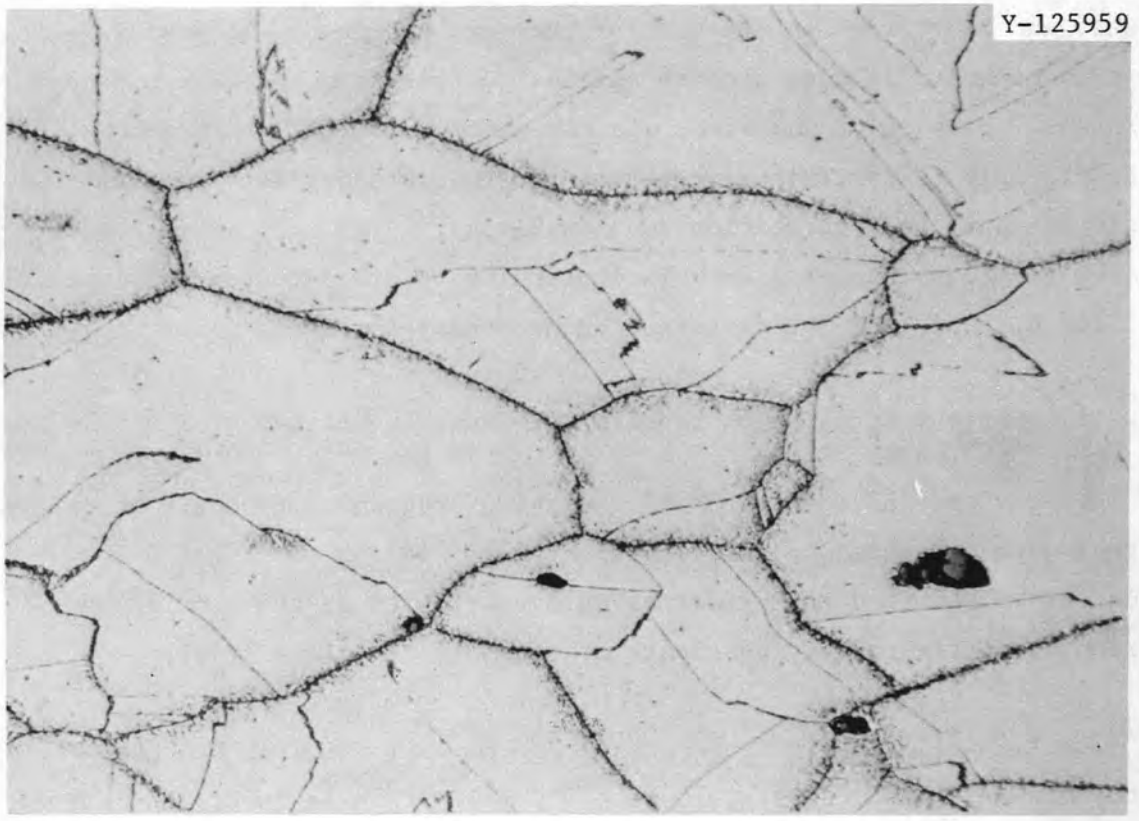

Fig. 5.28. Microstructure Showing Precipitation in Specimen Creep Tested at 593°C (1100°F) and 30 ksi (207 MPa) for Heat 926 of Type 304 Stainless Steel, Aged at 649°C (1200°F) for 10,000 hr. 500×

large-angle and twin boundaries. Precipitate particles were larger and denser at large-angle grain boundaries than at twin boundaries.

The following are some effects of aging on the microstructure and how they may explain the transition from the grain to twin boundary cracking.

1. Thermal aging at 649°C (1200°F) produces extensive precipitation at the grain boundaries; see Fig. 5.28.

2. The precipitate particles either must have a high cohesion (because no grain boundary cracks are observed) or because of their size, morphology, and distribution they restrict intergranular flow (grain boundary sliding) and therefore promote intragranular deformation.

Thus, item 2 above can explain the observed intragranular deformation, which is consistent with the large rupture elongation, high minimum creep rate, and short time to rupture for the aged specimen. We postulate that a twin boundary sliding process similar to the grain boundary sliding process — because of the size, distribution, and cohesive strength of the precipitate particles located at the twin boundaries — results in twin boundary void nucleation (weakest link).

The microstructural work is continuing on creep-tested specimens of different heats and for different aging temperatures and times.

5.2.2.4 Effect of Aging on Tensile and Creep Properties of Type 316 Stainless Steel

The scope and the status of the aging program on type 316 stainless steel were presented in earlier reports.[14,15,25,26] During the last quarter we examined the effect of aging variables on the tensile and creep properties of various heats of type 316 stainless steel.

5.2.2.4.1 Tensile Properties. Figure 5.29 shows 0.2% offset yield strength at a test temperature of 593°C (1100°F) as a function of aging temperature for a fixed aging time of 4000 hr. All four heats of type 316 stainless steel in both as-received and reannealed condition show an increase in yield strength with increase in aging temperature. In Fig. 5.30 the 0.2% offset yield strength is plotted as a function of aging time for

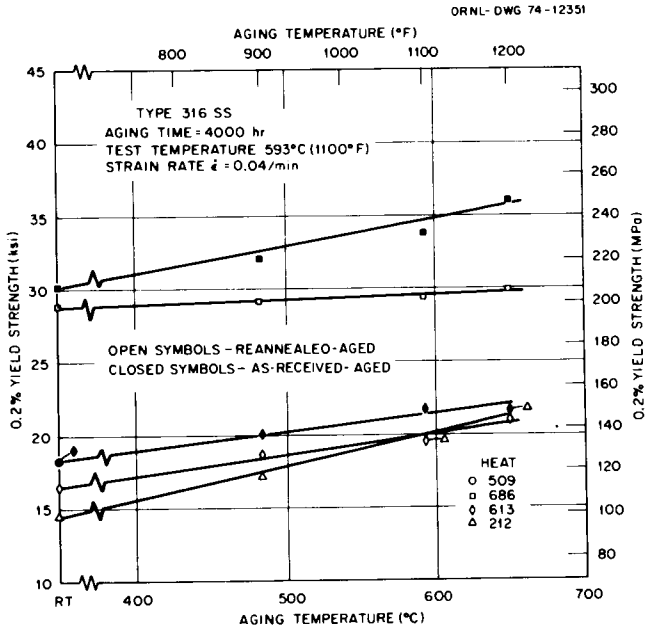

Fig. 5.29. Effect of Aging Temperature on 0.2% Offset Yield Strength of As-Received and Reannealed Type 316 Stainless Steels Aged for 4000 hr and Tested at 593°C (1100°F).

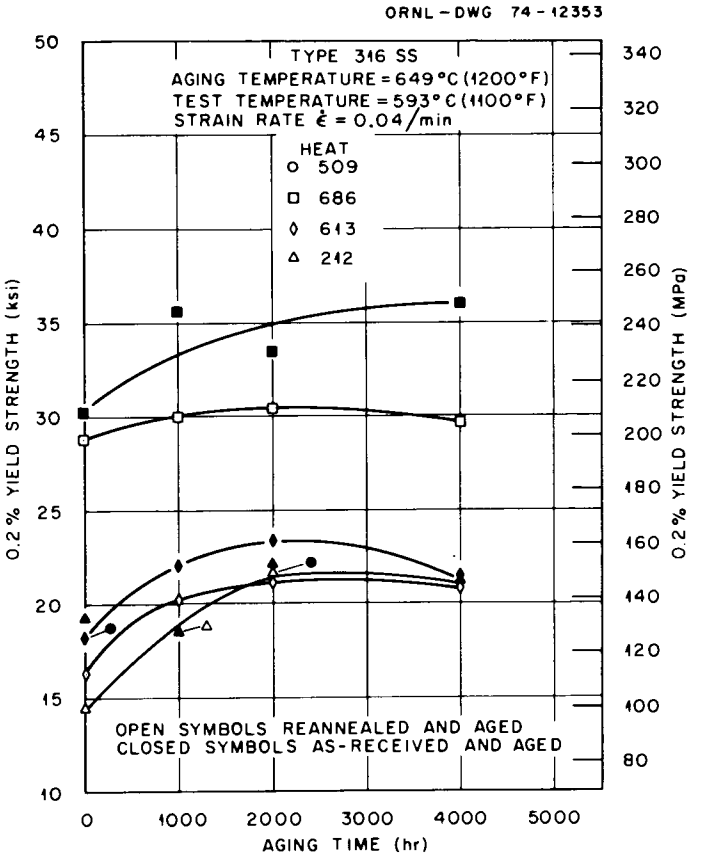

Fig. 5.30. Effect of Aging Time on 0.2% Offset Yield Strength of As-Received and Reannealed Type 316 Stainless Steel Aged at 649°C (1200°F) and Tested at 593°C (1100°F).

an aging temperature of 649°C (1200°F). The greatest increase in 0.2% yield strength occurs in the first 1000 hr of aging; the strength then increases at a decreasing rate.

The effect of aging temperature and time on the ultimate tensile strength is shown in Figs. 5.31 and 5.32, respectively. For all four heats the ultimate strength seems to remain unchanged for an aging temperature of 482°C (900°F) and shows a drop for 593 and 649°C (1100 and 1200°F). The drop in ultimate tensile strength at an aging temperature of 649°C (1200°F) is greatest in the first 1000 hr and then negligible for longer aging times. This is only known for aging times up to 4000 hr; data for 10,000 hr will become available for comparison during the next quarter.

The effect of aging temperature and time on uniform elongation at 593°C (1100°F) is shown in Figs. 5.33 and 5.34, respectively. Uniform elongation drops for all heats at aging temperatures of 482°C (900°F) and above, in contrast with 593°C (1100°F) and above for type 304 stainless steel (see Figs. 5.12 and 5.13). The greatest drop in uniform elongation for four heats is from 35–49% to 18–26% and occurs for an aging temperature of 649°C (1200°F). The decrease in uniform elongation at an aging temperature of 649°C (1200°F) is again greatest in the first 1000 hr and then diminishes with increasing aging time.

The uniform elongation data for unaged and aged type 316 stainless steel is compared with the minimum-expected value curve from the *Nuclear Systems Materials Handbook* in Fig. 5.35. The uniform elongation at room temperature and 593°C (1100°F) in the as-received and reannealed conditions for all four heats of type 316 stainless steel is above the minimum-expected value curve. Thermal aging, especially at 649°C (1200°F) for 4000 hr, brings the uniform elongation at both room temperature and 593°C (1100°F) below the minimum-expected value curve. The drop in uniform elongation at 593°C (1100°F) below the minimum-expected value curve occurs for two out of the four heats of type 316 stainless steel being investigated. Furthermore, it happens for the same heats on aging in both the as-received and reannealed conditions. The drop of uniform elongation below the minimum value curve is greater for the as-received and aged than the reannealed and aged condition.

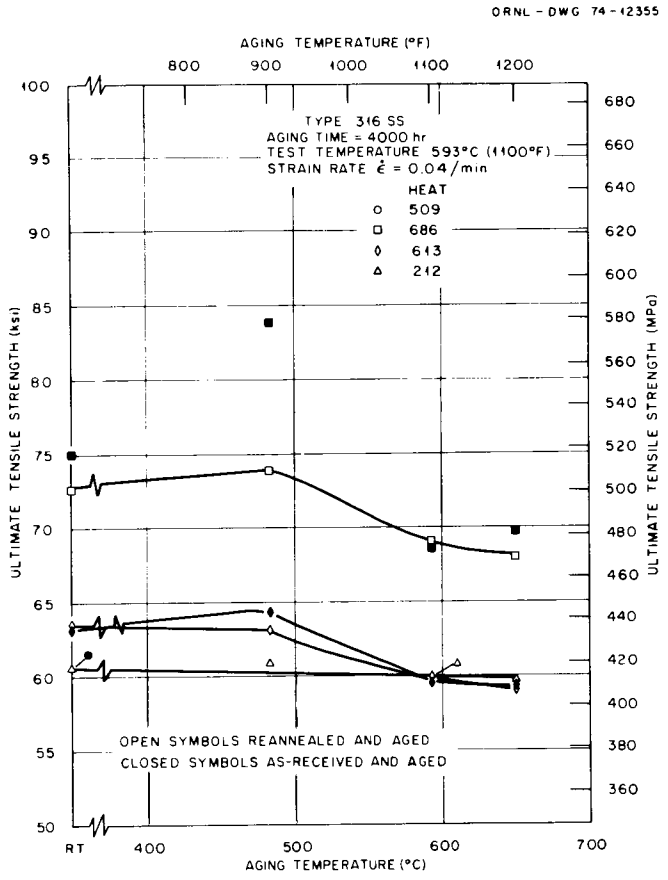

Fig. 5.31. Effect of Aging Temperature on the Ultimate Tensile Strength of As-Received and Reannealed Type 316 Stainless Steel Aged for 4000 hr and Tested at 593°C (1100°F).

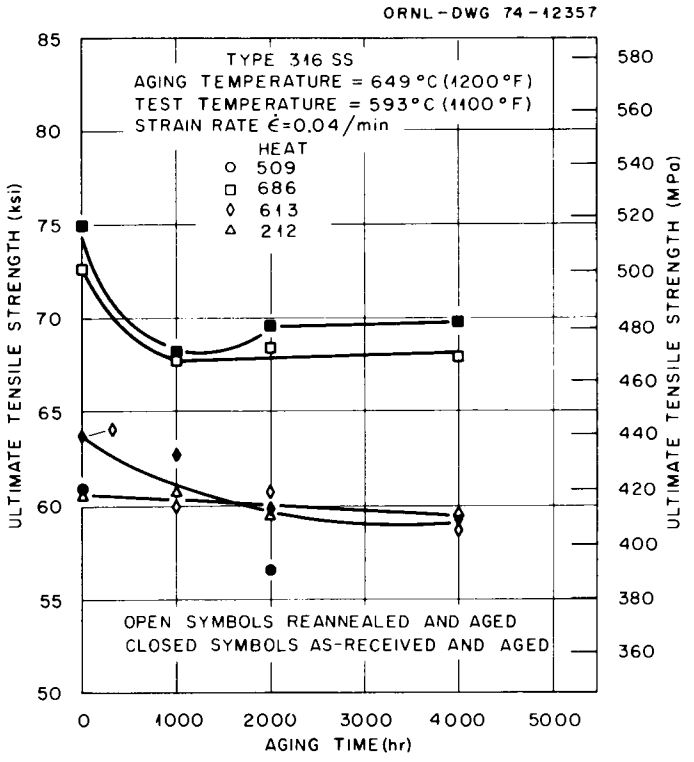

Fig. 5.32. Effect of Aging Time on the Ultimate Tensile Strength of As-Received and Reannealed Type 316 Stainless Steel Aged at 649°C (1200°F) and Tested at 593°C (1100°F).

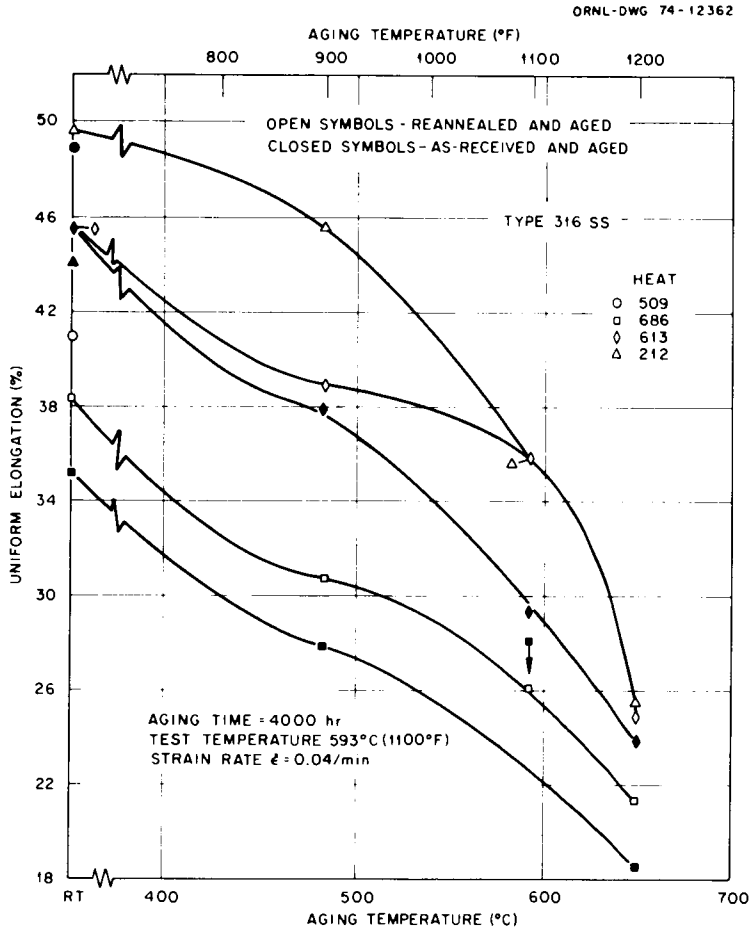

Fig. 5.33. Effect of Aging Temperature on Uniform Elongation of As-Received and Reannealed Type 316 Stainless Steel Aged for 4000 Hr and Tested at 593°C (1100°F).

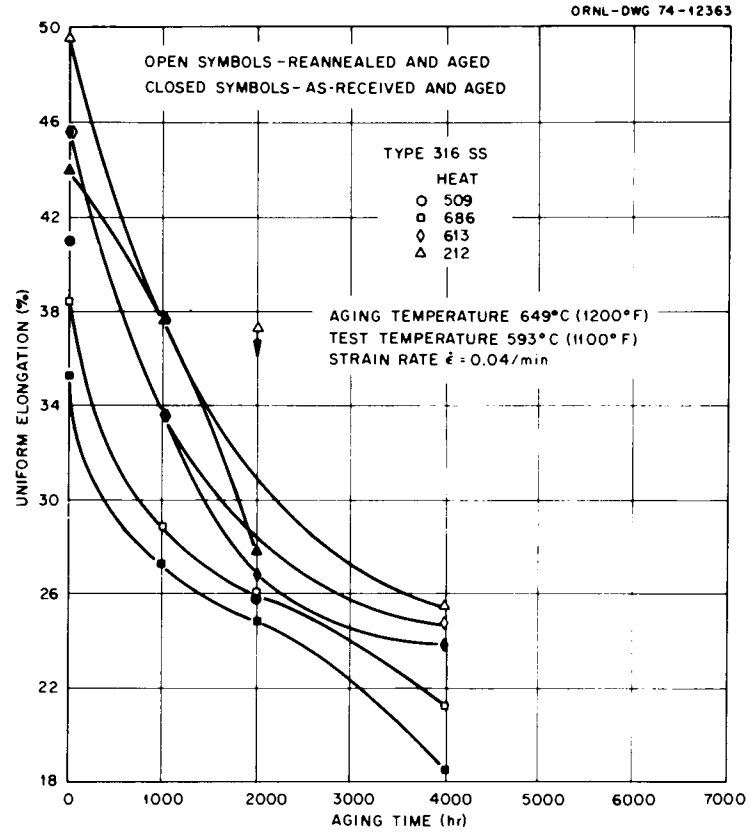

Fig. 5.34. Effect of Aging Time on Uniform Elongation of As-Received and Reannealed Type 316 Stainless Steel Aged at 649°C (1200°F) and Tested at 593°C (1100°F).

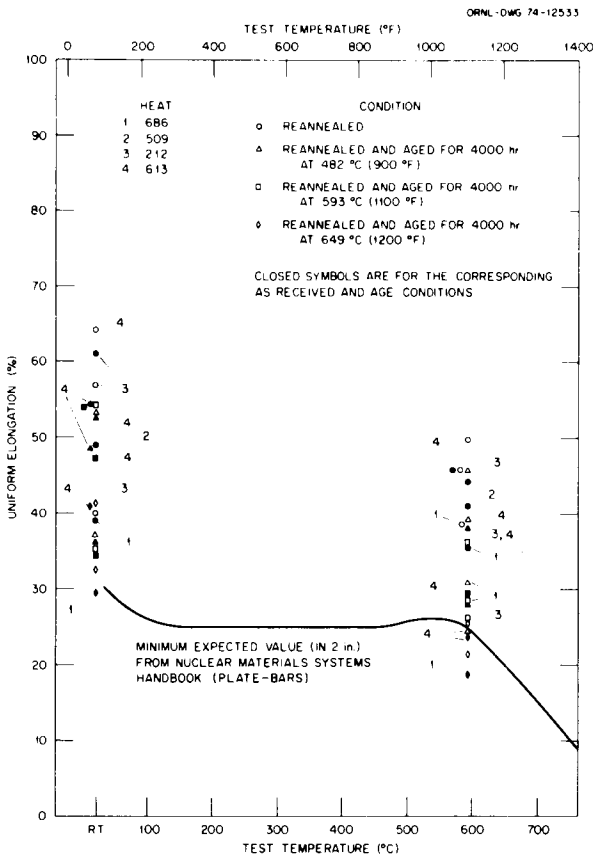

Fig. 5.35. Comparison of Uniform Elongation As-Received and Reannealed Type 316 Stainless Steel for Unaged of Aged Conditions with Minimum-Expected Values from the Handbook.

The effect of nitrogen content on uniform elongation at a test temperature of 593°C (1100°F) is shown in Fig. 5.36. For both the unaged and aged conditions, increasing the amount of nitrogen decreases the uniform elongation. For a similar carbon content, the drop in uniform elongation due to nitrogen for type 304 stainless steel (Fig. 5.19) is much less than for type 316.

The effect of aging temperature and time on total elongation is shown in Figs. 5.37 and 5.38, respectively. The total elongation for four heats of type 316 stainless steel changes from 46–54% to 29–37% for aging at 649°C (1200°F) for 4000 hr. The greatest decrease in total elongation for an aging temperature of 649°C (1200°F) occurs in the first 1000 hr, and further drop with aging time occurs at a decreasing rate. The changes in reduction of area as functions of aging temperature and time are similar to those observed for the total elongation and are

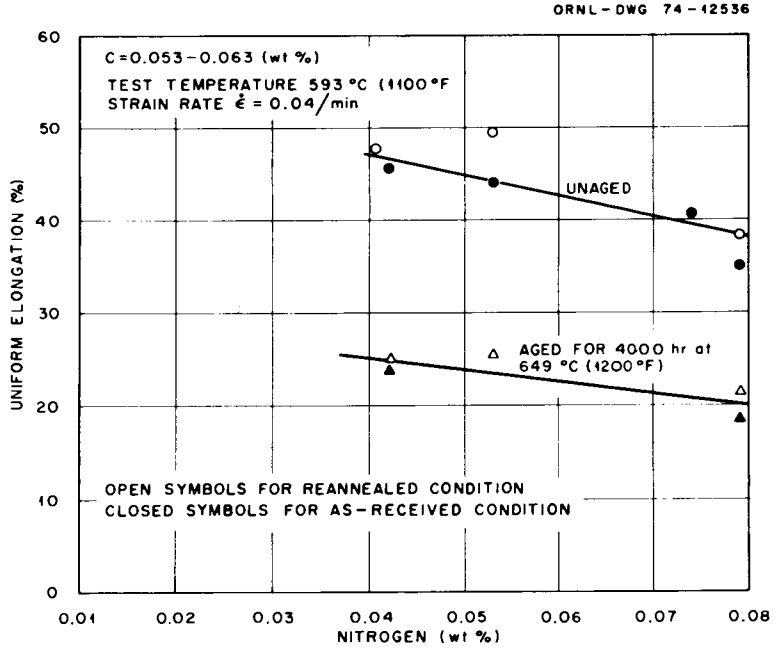

Fig. 5.36. Effect of Nitrogen on Uniform Elongation at 593°C (1100°F) of Various Heats of Type 316 Stainless Steel in Unaged and Aged Conditions.

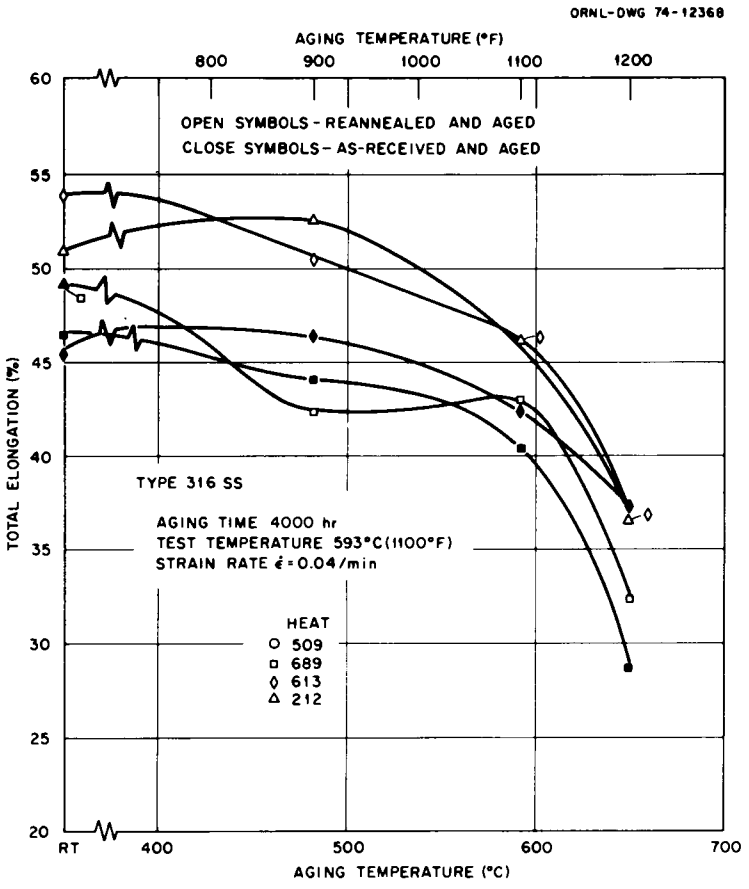

Fig. 5.37. Effect of Aging Temperature on Total Elongation of As-Received and Reannealed Type 316 Stainless Steel Aged for 4000 hr and Tested at 593°C (1100°F).

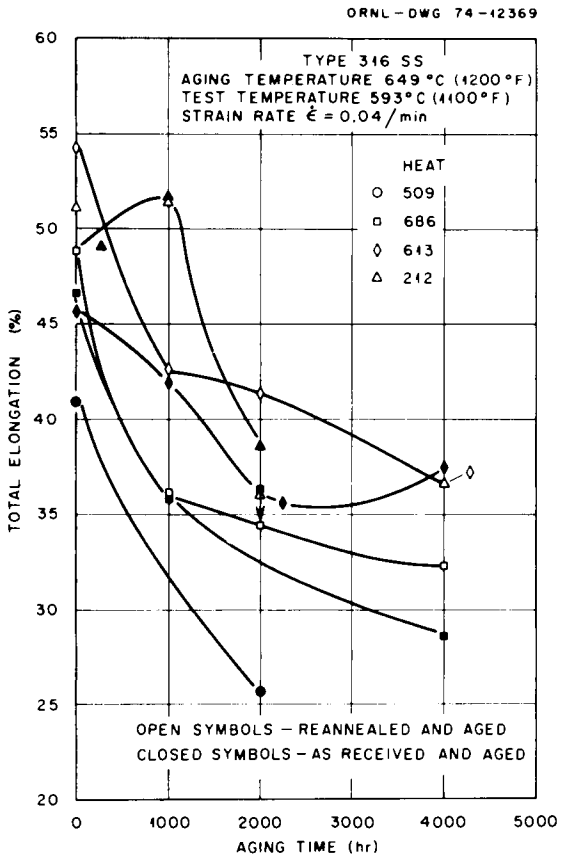

Fig. 5.38. Effect of Aging Time on Total Elongation of As-Received and Reannealed Type 316 Stainless Steel Aged at 649°C (1200°F) and Tested at 593°C (1100°F).

shown in Figs. 5.39 and 5.40. The reduction of area drops from 54–61% for the unaged condition to 45–50% for the aging treatment at 649°C (1200°F) for 4000 hr.

The results available to date clearly show that the aging treatment in the reactor operating temperature range, 482 to 649°C (900–1200°F), can decrease the uniform and total elongations of type 316 stainless steel by a large amount. The decrease in uniform elongation for two out of the four heats being investigated is so large that it brings the uniform elongation below the minimum-expected value curve.

5.2.2.4.2 Creep Properties. The limited data collected on aged type 316 stainless steel are summarized in Tables 5.9 through 5.11. The results of the present data show aging effects similar to those observed for type 304 stainless steel. Some general comments on the

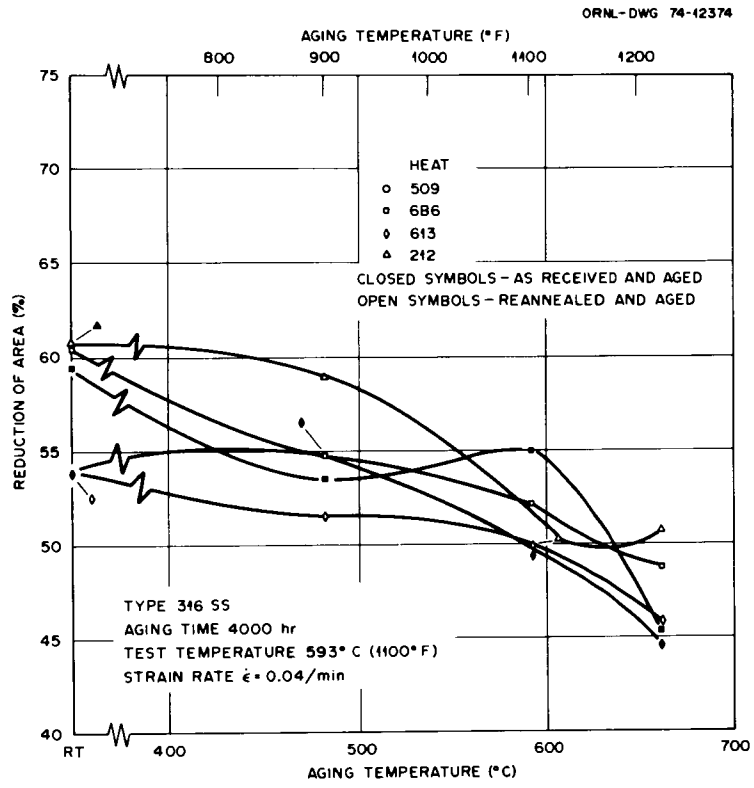

Fig. 5.39. Effect of Aging Temperature on Reduction of Area for As-Received and Reannealed Type 316 Stainless Steel Aged for 4000 hr and Tested at 593°C (1100°F).

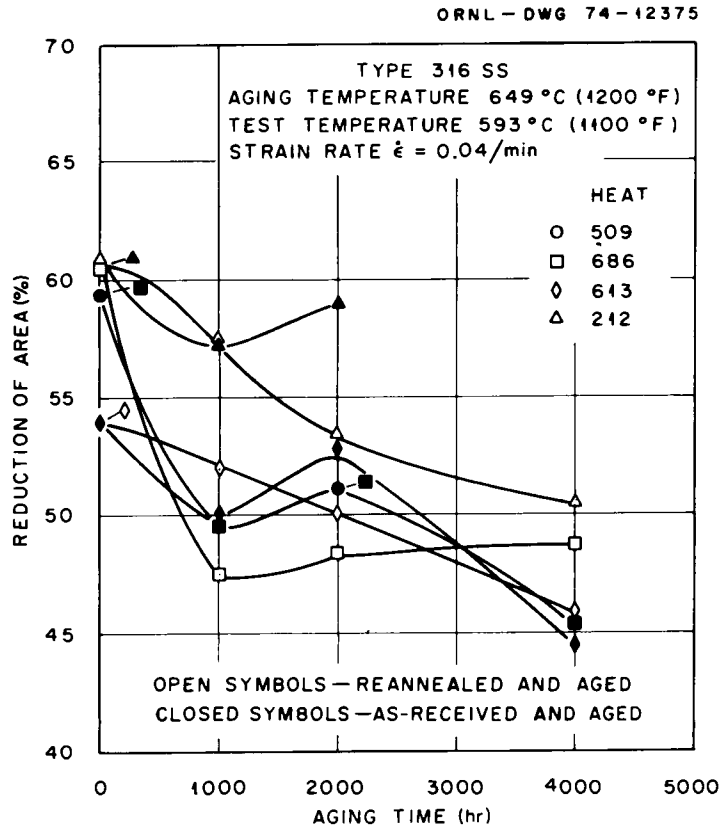

Fig. 5.40. Effect of Aging Time on Reduction of Area for As-Received and Reannealed Type 316 Stainless Steel Aged at 649°C (1200°F) and Tested at 593°C (1100°F).

Table 5.9. Creep[a] Properties of Aged Heats 212, 509, 613, and 686 of Type 316 Stainless Steel — Creep Rupture Data

Condition	Treatment			Stress ksi(MPa)	Stages (hr)		Minimum Creep Rate (%·hr^{-1})	Rupture Strain (%)	Reduction of Area (%)
	Time (hr)	Temperature (°C)	Temperature (°F)		Loading e_L	Rupture t_r	ε_{mcr}	ε_f	R_A
				Heat 212					
As-received				35(241)	5.5	883.7	1.33×10^{-2}	38.6	45.5
As-received[b]				35(241)	5.25	1831.3	6.10×10^{-3}	36.67	43.2
As-received				40(276)	9.12	163.1	6.75×10^{-2}	31.42	26.1
Reannealed	0.5	1065	1950	35(241)	7.97	1520.1	7.60×10^{-3}	33.27	38.3
Reannealed and aged	1000	649	1200	35(241)	4.69	1196.7	1.475×10^{-2}	50.29	57.47
Reannealed and aged	1000	649	1200	40(276)	6.72	257.0	7.51×10^{-2}	53.72	52.88
				Heat 509					
As-received				40(276)	9.37	186.0	3.225×10^{-2}	18.92	23.80
As-received and aged	2000	482	900	40(276)	8.48	177.9	4.125×10^{-2}	22.68	26.73
Reannealed	0.5	1065	1950	40(276)	10.95	142.0	4.60×10^{-2}	21.21	22.50
				Heat 613					
As-received				35(241)	5.90	465.4	7.96×10^{-3}	13.62	15.30
As-received[b]				35(241)	4.60	1244.5	3.4×10^{-3}	14.10	16.80
				Heat 686					
As-received				50(345)	5.16	531.4	1.075×10^{-3}	12.1	12.70
Reannealed and aged	4000	593	1100	50(345)	5.37	219.3	7.42×10^{-2}	41.57	50.79
Reannealed and aged	4000	649	1200	50(345)	4.05	158.4	1.36×10^{-1}	46.55	58.78

[a]All creep test were performed at a stress of 30 ksi (207 MPa) and a test temperature of 593°C (1100°F).

[b]Transverse specimens.

Table 5.10. Creep[a] Properties of Aged Heats 212, 509, 613, and 686 of Type 316 Stainless Steel at 593°C (1100°F) — Strain Measures

Condition	Treatment			Stress ksi(MPa)	Strain, %						Strain Ratio, %		Stable Creep Strain
	Time (hr)	Temperature (°C)	Temperature (°F)		End of Primary ε_1	End of Secondary		Creep Strain ε_{cs}	$\varepsilon_2 - \varepsilon_1$	$\varepsilon_{cs} - \varepsilon_2$	$\frac{\varepsilon_2 - \varepsilon_1}{\varepsilon_{cs}}$	$\frac{\varepsilon_{ss} - \varepsilon_2}{\varepsilon_{cs}}$	(%)
						Actual, ε_2	0.2% Offset, ε_{ss}						
							Heat 212						
As-received				35(241)	1.75	7.375	8.25	33.07	5.625	25.695	17.0	77.7	11.75
As-received[b]				35(241)	1.75	4.75	5.75	31.43	3.000	26.680	9.54	84.9	11.17
As-received				40(276)	2.375	7.125	8.25	22.3	4.75	15.175	21.30	68.10	11.01
Reannealed	0.5	1065	1950	35(241)	2.00	4.875	5.50	25.30	28.75	20.325	11.36	80.73	11.55
Reannealed and aged	1000	649	1200	35(241)	1.75	6.00	9.00	45.56	4.25	39.56	9.32	86.80	17.44
Reannealed and aged	1000	649	1200	40(276)	1.75	8.25	9.75	47.03	6.50	38.78	13.82	82.45	19.30
							Heat 509						
As-received				40(276)	0.450	4.40	5.35	9.55	3.95	5.15	41.4	53.9	6.00
As-received and aged	2000	482	900	40(276)	2.70	5.40	6.55	14.15	2.70	8.75	19.08	61.84	7.34
Reannealed	0.5	1065	1950	40(276)	2.20	4.70	5.50	10.26	2.50	5.56	24.40	54.20	6.53
							Heat 613						
As-received				35(241)	1.40	2.505	3.35	7.72	1.105	5.215	14.31	67.55	3.70
As-received[b]				35(241)	1.10	2.400	3.05	9.50	1.30	7.10	13.68	74.74	4.23
							Heat 686						
As-received				50(345)	0.40	0.550	0.825	6.9	0.150	6.35	2.17	92.10	0.614
Reannealed and aged	4000	593	1100	50(345)	5.50	15.0	17.00	36.15	9.50	21.15	26.3	58.51	16.272
Reannealed and aged	4000	649	1200	50(345)	2.50	12.75	14.50	42.46	10.25	29.71	24.14	70.00	21.54

[a]Unless otherwise noted, all tests were on longitudinal specimens.

[b]Transverse Specimens.

Table 5.11. Creep[a] Properties of Aged Heats 212, 509, 613, and 686 of Type 316 Stainless Steel at 593°C (1100°F) — Time Values

Condition	Treatment			Stress ksi(MPa)	Time, hr			Duration, hr		Time Ratio, %	
	Time (hr)	Temperature (°C)	Temperature (°F)		End of Primary t_1	End of Secondary		Third Stage $t_r - t_2$	Second Stage $t_2 - t_1$	$\frac{t_2 - t_1}{t_r}$	$\frac{t_r - t_2}{t_r}$
						Actual, t_2	0.2% Offset, t_{ss}				
					Heat 212						
As-received				35(241)	75.0	490.0	530.0	393.7	415	47.0	44.6
As-received[b]				35(241)	140.0	680.0	770.0	1151.3	540	29.5	62.87
As-received				40(276)	36.5	96.0	109.0	67.1	59.5	36.5	41.14
Reannealed	0.5	1065	1950	35(241)	140.00	525.0	580.0	995.1	385.0	25.3	65.46
Reannealed and aged	1000	649	1200	35(241)	50.0	335.0	520.0	861.7	285.0	23.8	72.00
Reannealed and aged	1000	649	1200	40(276)	10.0	95.0	112.5	162.0	85.0	33.1	63.0
					Heat 509						
As-received				40(276)	8.00	130	153.0	56.00	122.0	65.60	30.1
As-received and aged	2000	482	900	40(276)	35.0	100.0	124.0	77.9	65.00	36.53	43.8
Reannealed	0.5	1065	1950	40(276)	39.0	100.0	116.0	42.0	61.00	42.96	29.60
As-received				35(241)	130.0	271.25	347.5	194.15	141.25	30.35	41.72
As-received[b]				35(241)	230.0	600.0	735.0	649.5	370.0	29.73	51.79
					Heat 686						
As-received				50(345)	45.0	165.0	235.0	365.4	120.0	22.62	68.90
Reannealed and aged	4000	593	1100	50(345)	28.75	156.25	180.0	63.05	127.5	58.14	28.75
Reannealed and aged	4000	649	1200	50(345)	9.0	84.0	95.0	74.40	75.0	47.35	46.97

[a]Unless otherwise noted, all tests were on longitudinal specimens.

[b]Transverse specimens.

effect of aging on creep properties of type 316 stainless steel are as follows:

1. Minimum creep rate increases with decrease in time to rupture for all heats in both as-received and reannealed conditions.

2. Loading strain decreases on aging for all heats.

3. Strain in all stages (first, second, and third) increases on aging for all heats. Thereby, total elongation at rupture and reduction of area also increase.

4. The duration of the second and third stages decreases on aging for all heats.

The comparison of ORNL results on the aged specimens with those of Garofalo et al.[8] shows a contrast in that, while the present results show a decrease in time to rupture for most of the heats, Garofalo's results show an increase. The major difference between the ORNL aging treatment and the Garofalo et al. pretreatment is that they used a higher temperature, 816°C (1500°F), and shorter time, 24 hr, whereas we used a lower temperage range, 482 to 649°C (900–1200°F), and longer times, 1000 to 4000 hr. More results will be presented and discussed next quarter.

5.2.3 Materials Behavior in Support of Development and Evaluation of Failure Criteria for Materials — M. K. Booker

The problem of the prediction of elevated-temperature service failure of materials is two-fold. First, for practical design applications, one does not seek to predict failure itself, but to anticipate the useful service life of a component. Instabilities that develop before failure could end this useful life considerably before actual failure (fracture or collapse). However, the criteria for useful or stable life are many, and it is unclear which is the best to use. Second, even if the proper failure criteria are identified, one must be able to predict their occurrence at times far exceeding the range of actual test data. The treatment of creep and creep-rupture data illustrates these problems well.

The most common method for correlating and extrapolating creep and creep-rupture data has involved the use of so-called "time-temperature parameters."[3,27] Literally dozens of parameters have developed since

Larson and Miller[28] first introduced the concept, and the selection of the best parameter to use in a given case can be a bewildering task. Most of the parameters are based on assumptions (such as the appearance of isostress lines) that are overly difficult to verify. Moreover, while many data sets do not exactly fit the assumptions of any one parameter, many different computer-optimized parameters can fit the same data set. Calculation of parameter constants by least squares methods forces any reasonable parameter to fit any consistent data set fairly well in the range of experimental data. However, to yield reasonable extrapolations, the parametric form must be consistent with the behavior of the material under consideration. Still, to achieve consistent results, it is usually necessary to calculate parameter constants by computerized optimization techniques. However, this sort of analysis requires the assumption of an analytical form for the master curve. While simple polynomials usually suffice, this assumption still introduces an additional complication. Also, of course, if a material develops long-time instabilities at times beyond the range of actual data, it is difficult or impossible for any parameter to give correct predictions. Thus, it is not surprising that the entire field of parametric analysis of creep data is undergoing examination.

In an attempt to unify this field of analysis, ASTM and ASME have formed a joint task group chaired by R. M. Goldhoff to review the situation.[29] At present, the leading candidate to become a standardized method of analysis is the "minimum commitment method" (MCM), first introduced by Manson.[3] In conjunction with the ASTM-ASME parametric task group, the MCM has been applied to various sets of data at ORNL and other sites to assess its usefulness and applicability in the correlation and extrapolation of creep data. The analysis has been done with the MEGA computer program.[30]

The MCM has been applied to the analysis of rupture time and minimum creep rate for the ORNL data for 1-in. plate of heat 9T2796 of type 304 stainless steel[31] and the 2-in.plate of this heat.[32] In addition it has been applied[33] to the time to tertiary creep data for 2 1/4 Cr-1 Mo collected at ORNL for use in the generation of correlations for the *Nuclear Systems Materials Handbook*. Table 5.12 presents an

Table 5.12. Comparison of Various Correlation Methods for Type 304 Stainless Steel

	Number of Data Points Used	Optimized Constants[a]				Sum of Squared Residuals			
		MCM (A)	O-S-D (Q)	M-S (D)	L-M (C)	MCM	O-S-D	M-S	L-M
Rupture Life									
Heat 9T2796 1-in. plate	58	−0.05	1.874×10^4	−0.02094	18.054	1.013	0.784	1.636	1.034
Heat 9T2796 2-in. plate	20	0.15	1.885	−0.02324	19.615	0.0642	0.264	0.289	0.162
Heat 55697 3/8-in. rod	44	NA	1.716	NA	18.035	NA	0.879	NA	1.087
Minimum Creep Rate									
Heat 9T2796 1-in. plate	58	0.0	−2.34	0.02623	−24.359	0.975	1.780	5.432	2.805
Heat 9T2796 2-in. plate	20	0.10	−3.01	0.03695	−32.822	0.0940	0.427	0.647	0.494
Heat 55697 3/8-in. rod	44	NA	−2.33	NA	−26.097	NA	1.136	NA	1.162

[a]Constants are for these treatments: minimum commitment method, Orr-Sherby-Dorn, Manson-Succop, Larson-Miller; NA = not available at this time.

analysis of the effectiveness of the MCM in comparison with some standard time-temperature parameters. Figure 5.41 shows a master curve for the MCM stress station function; particular results will be discussed in context. In general, the method yields reasonable and consistent results, including

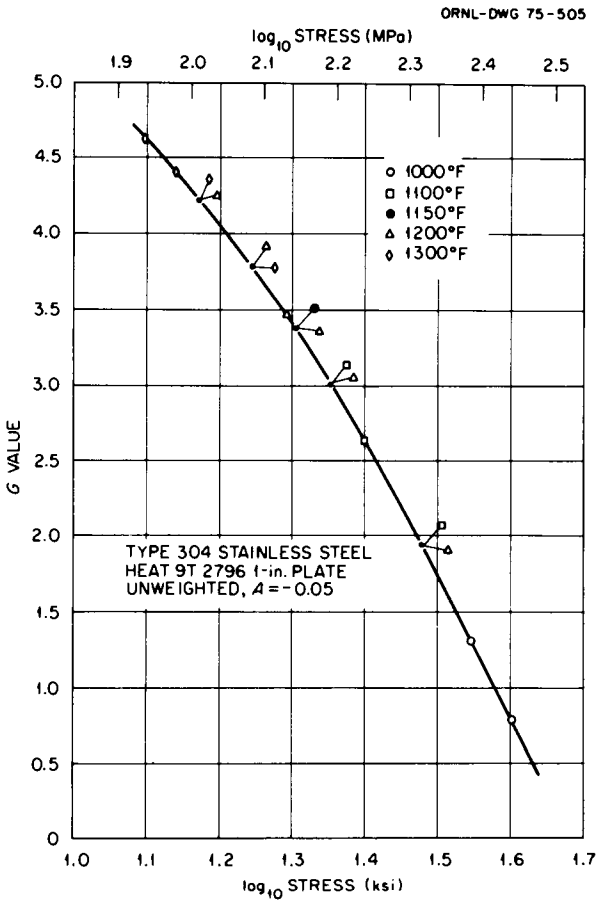

Fig. 5.41. MCM Stress Function Master Curve (Rupture Time).

extrapolations in time. However, in the analysis of the 2 1/4 Cr-1 Mo data, extrapolations in temperature are desired.[33] In this case, the isothermals for the extrapolated temperatures were unreasonable. In general, the MCM — as implemented by the MEGA computer program using a model of the form

$$\log H + (1 + A \log H)P(T) = G(\sigma) \ , \qquad (2)$$

where H = time or reciprocal creep rate,

A = adjustable constant,

P = temperature (°F) station function,

G = stress (ksi) station function —

seems to be a valid method of analysis, although acceptance of the method as a standard practice is not indicated by these results. Also, the method is still somewhat clouded by several unresolved questions. These include (1) What is the best method to choose an optimum A value? (2) Is the model too flexible, considering the generally smooth and consistent nature of the isothermals to be predicted? (3) What are the advantages and disadvantages of using faired rather than raw data? (4) What are the specific limitations to the application of the method?

By use of the MCM as well as some common time-temperature parameters, various creep failure criteria have been evaluated for several sets of data for type 304 stainless steel in a continuation of an effort reported previously.[34] These criteria include time to rupture, time to tertiary creep, rupture strength, and various strain limits. Data analyzed include the 1- and 2-in. (25- and 51-mm) plate of the ORNL reference heat (9T2796), and the HEDL data[7] for the 3/8-in. (9.5-mm) rod of heat 55697. Orr-Sherby-Dorn[35] and Manson-Succop[36] results for the 2-in. plate material have been reported previously,[34] while MCM results for the HEDL data are not yet available. Predicted results for rupture strengths are shown in Table 5.13. Figures 5.42 through 5.47 illustrate the results for rupture time and minimum creep rate.

Perhaps a more relevant design criterion than rupture time would be time to tertiary creep. Tertiary creep for ORNL data is usually defined by the 0.2% offset method, while tertiary creep for the HEDL data is defined by the first deviation from linear second-stage creep. There are advantages and disadvantages to both definitions. The first deviation from linearity might have the most physical significance, but, analogous to the proportional limit in tensile tests, it is somewhat difficult to determine with accuracy and consistency. Consistency, however, is vital to parametric analysis techniques. On the other hand, the 0.2% offset can be measured with more consistency, but is less conservative

Table 5.13. Creep-Rupture Strengths for Type 304 Stainless Steel

Temperature (°C)	Temperature (°F)	Prediction Method	Predicted Rupture Strength, ksi (MPa), for Rupture Time 10^2 hr	10^3 hr	10^4 hr	10^5 hr
			Heat 9T2796 1-in. (25-mm) Plate			
538	1000	MCM	42.4 (292)	32.7 (225)	24.6 (170)	17.5 (121)
		O-S-D	42.3 (292)	33.5 (231)	25.8 (178)	19.1 (132)
		M-S	42.0 (290)	31.3 (216)	23.0 (159)	16.7 (115)
593	1100	MCM	29.6 (204)	22.5 (155)	16.2 (112)	10.7 (74)
		O-S-D	29.8 (205)	22.5 (155)	16.4 (113)	11.5 (79)
		M-S	29.9 (206)	21.9 (151)	15.8 (109)	11.4 (79)
649	1200	MCM	21.1 (145)	15.3 (105)	10.3 (71)	6.6 (46)
		O-S-D	20.4 (141)	14.7 (101)	10.2 (70)	7.0 (48)
		M-S	20.7 (143)	15.0 (103)	10.7 (74)	7.6 (52)
704	1300	MCM	13.2(91)	9.0 (62)	5.9 (41)	NA[a]
		O-S-D	14.0 (97)	9.7 (67)	6.7 (46)	4.7 (32)
		M-S	14.2(98)	10.2 (70)	7.3 (50)	5.2 (36)
			Heat 9T2796 2-in. (51-mm) Plate			
538	1000	MCM	42.0 (290)	34.1 (235)	27.0 (186)	21.0 (145)
		O-S-D	42.0 (290)	33.7 (232)	25.7 (177)	18.4 (127)
		M-S	41.4 (285)	32.3 (223)	24.0 (165)	17.0 (117)
593	1100	MCM	29.5 (203)	22.0 (152)	16.4 (113)	12.3 (85)
		O-S-D	29.8 (205)	22.1 (152)	15.4 (106)	10.8 (74)
		M-S	30.0 (207)	21.8 (150)	15.4 (106)	10.9 (75)
649	1200	MCM	18.8 (130)	13.4 (92)	9.7 (67)	7.1 (49)
		O-S-D	19.8 (137)	13.7 (94)	9.7 (67)	7.2 (50)
		M-S	19.7 (136)	13.8 (95)	9.9 (68)	7.5 (52)
704	1300	MCM	13.3 (92)	9.3 (64)	6.5 (45)	NA
		O-S-D	13.0 (90)	9.2 (63)	6.7 (46)	5.6 (39)
		M-S	12.6 (87)	9.1 (63)	7.0 (48)	5.6 (39)
			Heat 55697 3/8-in. (9.5-mm) Rod			
538	1000	O-S-D	44.2 (305)	34.6 (239)	26.3 (181)	19.1 (132)
593	1100	O-S-D	31.6 (218)	23.7 (163)	16.9 (117)	11.2 (77)
649	1200	O-S-D	22.2 (153)	15.6 (108)	10.2 (70)	5.7 (39)

[a]NA = not available at this time.

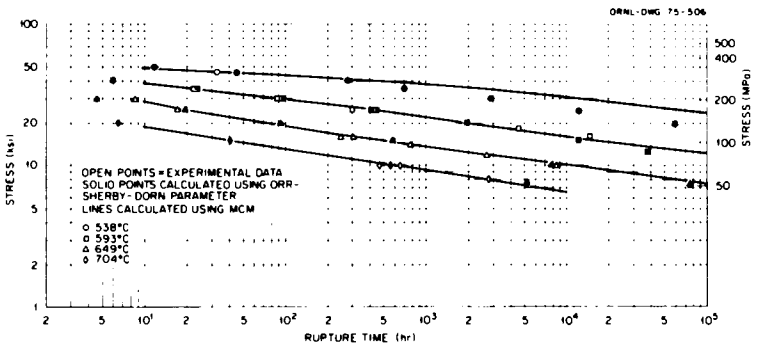

Fig. 5.42. Stress-Rupture Isothermals for Type 304 Stainless Steel Heat 9T2796 2-in. Plate, Annealed.

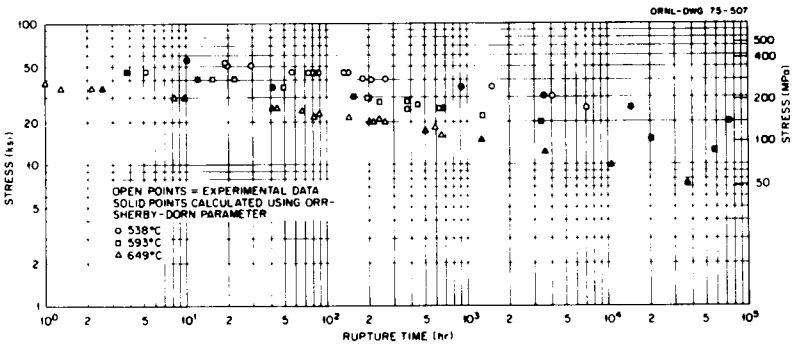

Fig. 5.43. Stress-Rupture Isothermals for Type 304 Stainless Steel Heat 55697, Annealed, HEDL 3/8-in. Rod Data.

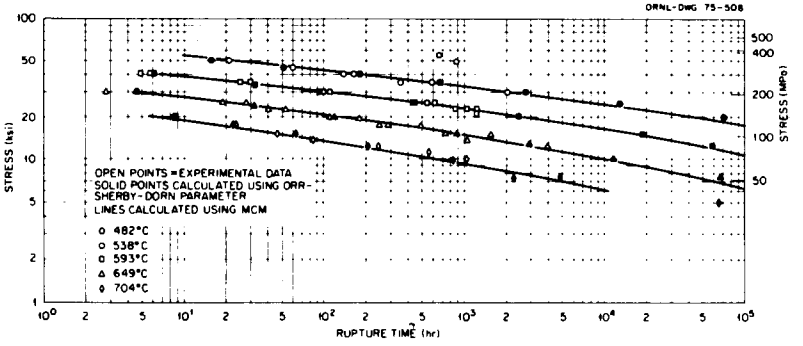

Fig. 5.44. Stress-Rupture Isothermals for Type 304 Stainless Steel Heat 9T2796 1-in. Plate.

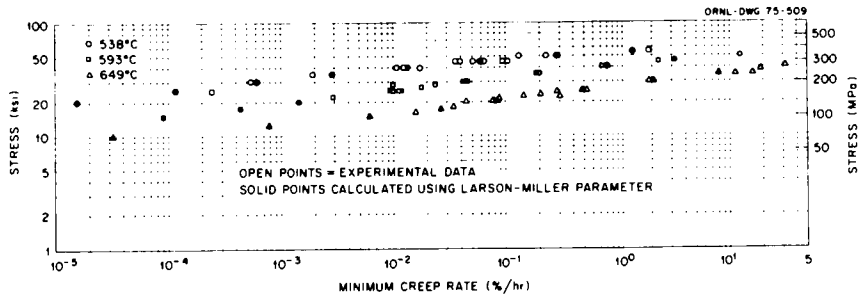

Fig. 5.45. Stress Versus Minimum Creep Rate for Type 304 Stainless Steel Heat 55697, Annealed, HEDL 3/8-in. Rod Data.

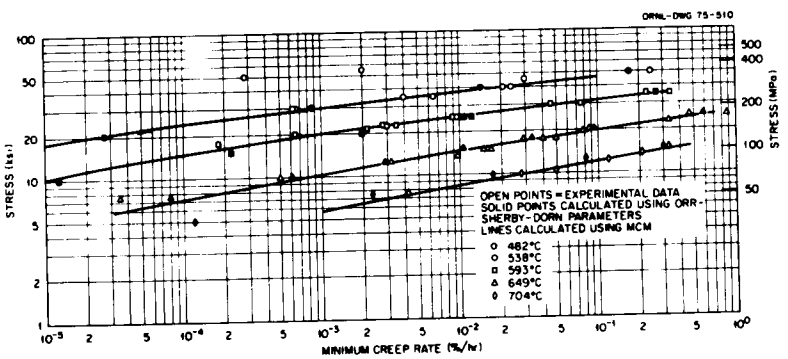

Fig. 5.46. Stress Versus Minimum Creep Rate Isothermals for Type 304 Stainless Steel Heat 9T2796 1-in. Plate.

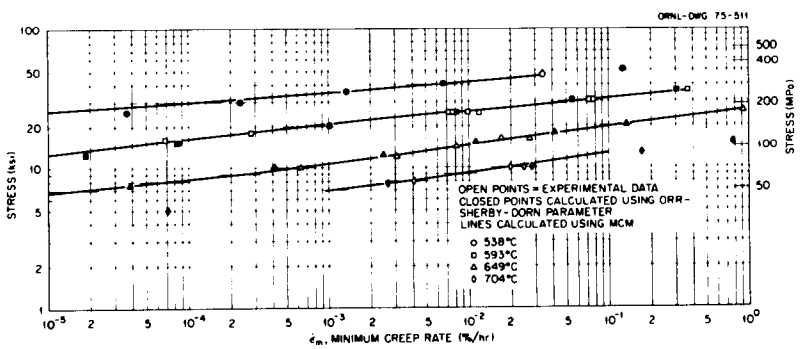

Fig. 5.47. Stress Versus Minimum Creep Rate Isothermals for Type 304 Stainless Steel Heat 9T2796 2-in. Plate.

and may have less meaning than the first deviation from linearity. Moreover, in some cases a specimen might undergo less than 0.2% tertiary creep, making the offset a null quantity. Still, in most cases the advantage of the consistency in offset measurements at least counterbalances the disadvantages, expecially for purposes of parametric analysis.

The most confusing and difficult to analyze (yet one of the most useful) of all failure criteria is the problem of strain limits. Parametric analysis of strain limits has been described eariler.[34] The correlations for time to rupture (t_r), time to tertiary creep (t_3), minimum creep rate ($\dot{e}_m$), and average creep rate to tertiary creep ($\dot{e}_3$) —

$\dot{e}_3$ = creep strain to tertiary creep/time to tertiary creep —

may be used to develop correlations for the quantities $e_s = \dot{e}_m t_r$ and $e_3 = \dot{e}_3 t_3$. Of course, e_3 is simply the strain to tertiary creep, while e_s has been called[32] the "stable creep strain." Strain limit predictions are shown in Figs. 5.48 through 5.52.

Whether or not the term "stable creep strain" is appropriate to describe the quantity e_s is open to question. Figure 5.53 illustrates the relationship of e_s to the creep curve. Clearly there is no visible reason why e_s should physically correspond to any sort of stability point. It does, however, correspond to the strain that would be reached if creep proceeded in second stage or "stable" creep throughout the life. A more appropriate name for the quantity e_s might be "plasticity resource" as first used by Ivanova.[37] On the other hand, the onset of tertiary creep is immediately suggested as an instability point. The exact relationship between e_s and e_3 is somewhat obscure. Clearly $\dot{e}_m < \dot{e}_3$ for classical creep curves, but $t_r > t_3$, leaving no immediate mathematical interpretation for this relationship. From Fig. 5.53 one can surmise that the correlation between e_s and e_3 depends on the primary creep behavior of a given material. If e_t is the transient primary creep strain,

$$\dot{e}_m = \frac{e_3 - e_t}{t_3} = \dot{e}_3 - \frac{e_t}{t_3} , \qquad (4)$$

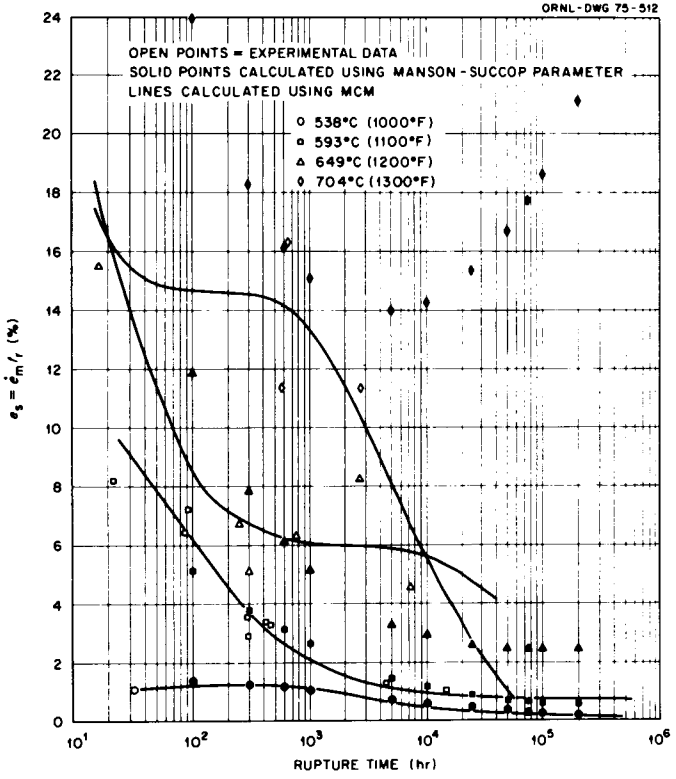

Fig. 5.48. Ductility Calculations for Type 304 Stainless Steel Heat 9T2796 2-in. Plate.

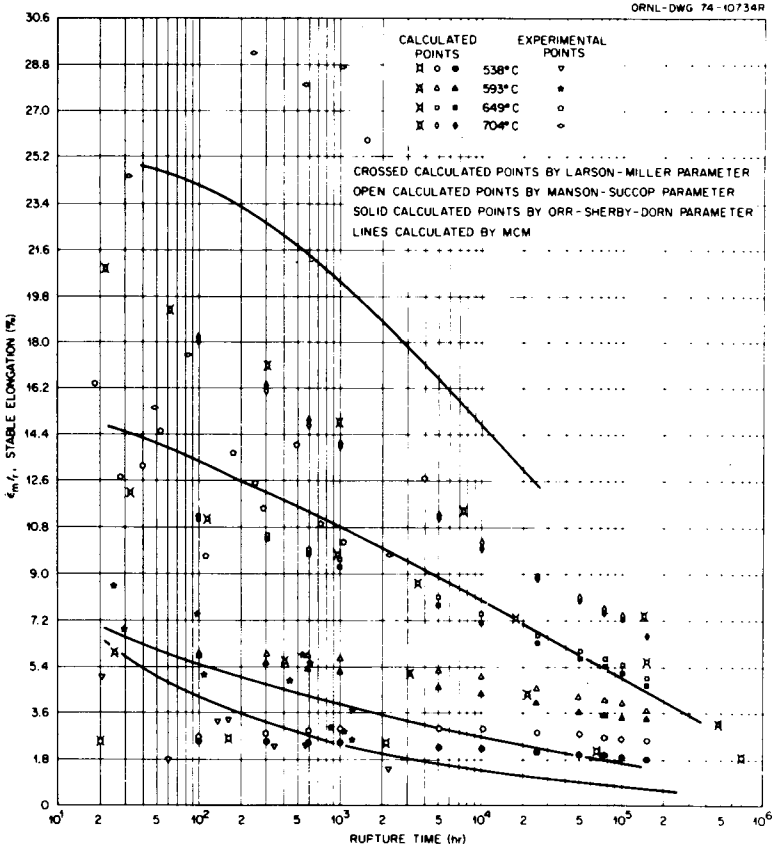

Fig. 5.49. Ductility Calculations for Type 304 Stainless Steel Heat 9T2796 1-in. Plate.

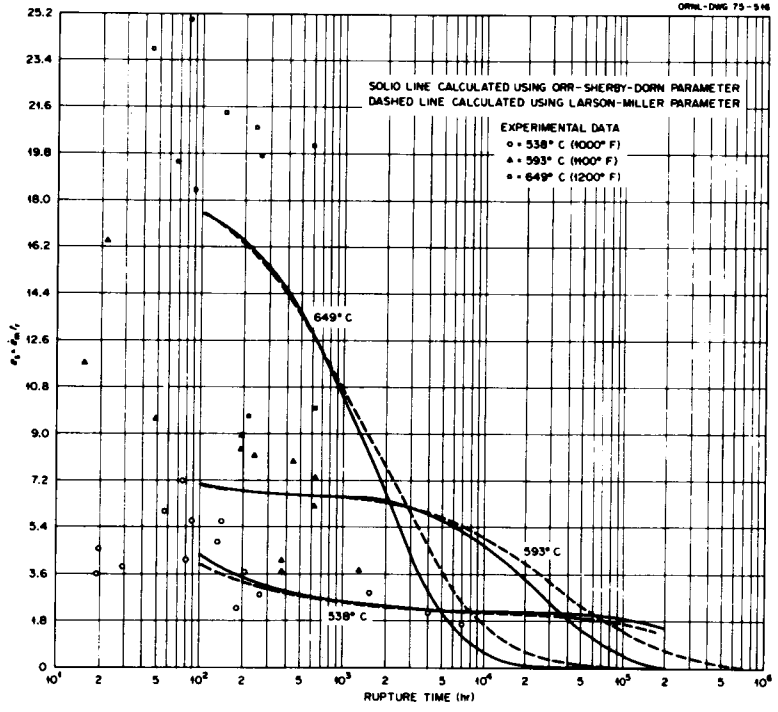

Fig. 5.50. Ductility Calculations for Type 304 Stainless Steel Heat 55697 3/8-in. Rod (HEDL Data).

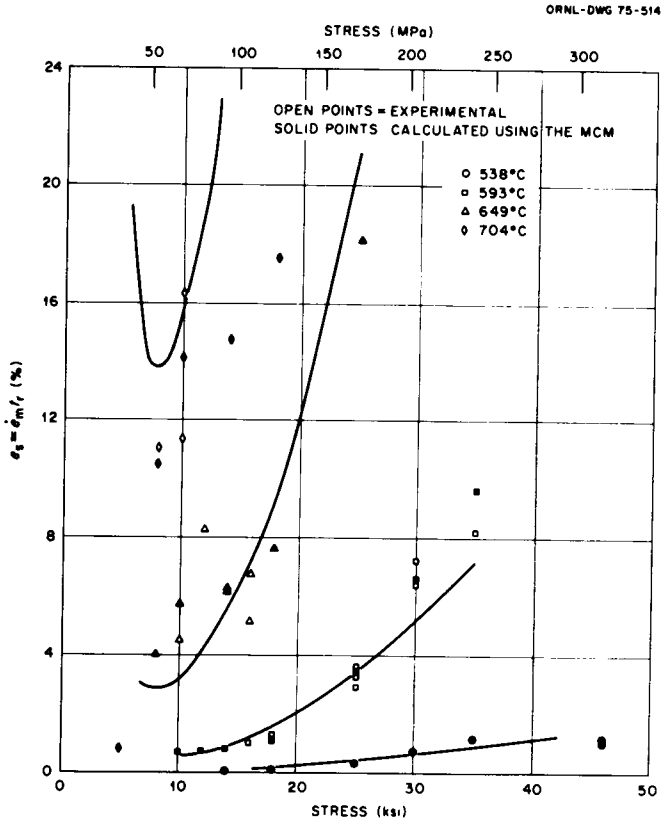

Fig. 5.51. Ductility Calculations for Type 304 Stainless Steel Heat 9T2796 2-in. Plate

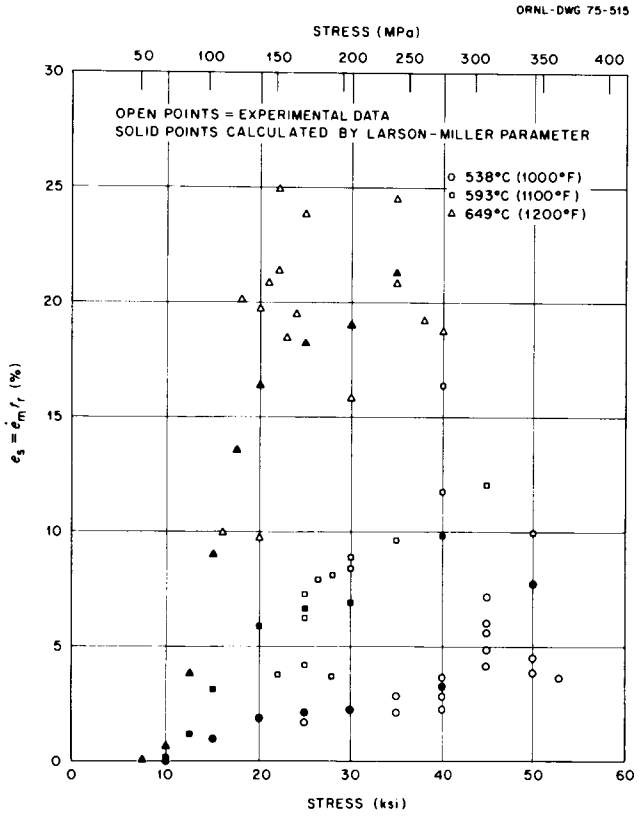

Fig. 5.52. Ductility Calculations for Type 304 Stainless Steel Heat 55697 3/8-in. Rod (HEDL Data).

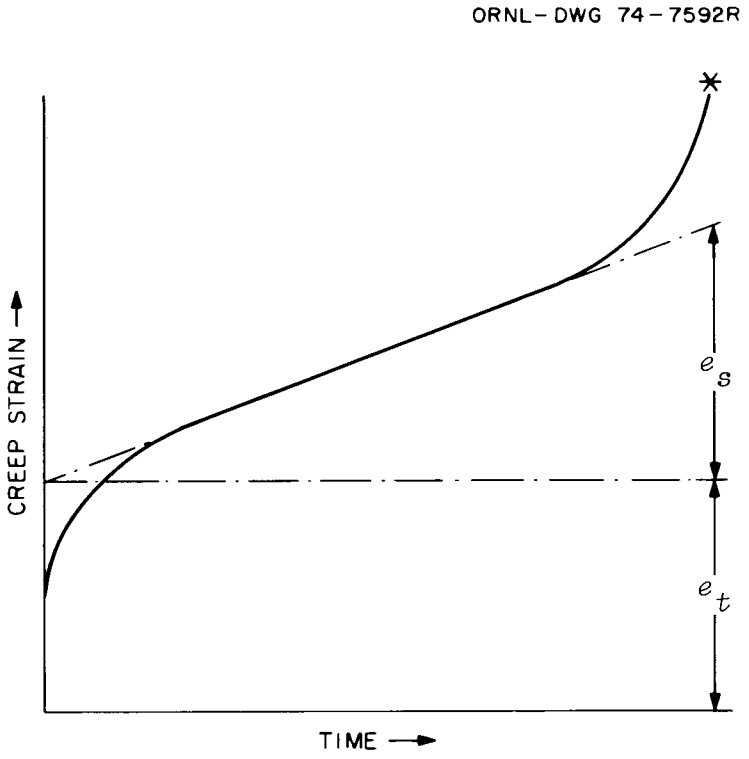

Fig. 5.53. Definition of the Quantity e_s.

so that

$$e_s = t_r \dot{e}_3 - \frac{t_r}{t_3} e_t \ , \tag{5}$$

$$e_s = \frac{t_r}{t_3} e_3 - \frac{t_r}{t_3} e_t \ , \tag{6}$$

$$e_s = \frac{t_r}{t_3} \left(e_3 - e_t \right) \ . \tag{7}$$

A further evaluation of this relationship can be obtained by examination of the quantity t_r/t_3. The simplest relationship is that proposed by Leyde and Rowe,[38] where

$$t_3 = F_s t_r \ , \tag{8}$$

$$\frac{t_3}{t_r} = F_s \ , \tag{9}$$

where F_s is a function of temperature only. Thus, using this criterion,

$$e_s = (e_3 - e_t)/F_s \ . \tag{10}$$

Actually, however, for types 304 and 316 stainless steel, a relationship of the form

$$t_3 = A t_r^{\beta} \ , \tag{11}$$

where A and β are constants independent of stress and temperature, has been found[9] to be applicable. Using this relationship

$$\frac{t_r}{t_3} = \frac{1}{A} t_r^{1-\beta} \ , \tag{12}$$

so that

$$e_s = \frac{1}{A} t_r^{1-\beta} \left(e_3 - e_t \right) . \qquad (13)$$

Thus, e_s and e_3 can be related if t_r and e_t are known.

The major advantage to using e_s as a failure criterion is simply that it can be calculated from available data. That it is independent of stress and temperature, as previously suggested,[39] does not appear to be the case with the present data for type 304 stainless steel. Still, a quantity is useful for prediction purposes only if its values can be determined. The quantities minimum creep rate and rupture life, used to calculate e_s, are often reported in the literature. On the other hand, the quantities time to the onset of tertiary creep and especially strain to the onset of tertiary creep are far less often reported.

Analysis of the results obtained for strain limits extrapolations is complicated somewhat by the nature of the experimental ductility data. As shown in Figs. 5.42 through 5.47, individual quantities such as t_r and $\dot{e}_m$, which make up the strain limits criteria, are correlated well by all methods of analysis used for all data sets investigated. However, Figs. 5.42 and 5.47 show that the set of data on the 2-in. plate of heat 9T2796 is somewhat sparse, containing only 1 point at 538°C (1000°F) and only 3 points at 704°C (1300°F).

Figures 5.48 and 5.51 present correlations of e_s with rupture time and stress for the 2-in. plate. Although only the 593°C (1100°F) raw data are really very consistent, the correlations in all cases are reasonable representations and can certainly be used at least as estimated values. Interestingly, while the results from different time-temperature parameters are quite similar, the MCM results appear from a visual analysis to give better and more realistic correlations. [For example, the curves calculated with parameters exhibit minima at 704°C (1300°F)]. Again, however, this data set is quite small.

Only Orr-Sherby-Dorn and Larson-Miller parameter results have been obtained for the HEDL heat 55697 data (Figs. 5.50 and 5.52). Again, the scatter is considerable, but the calculated values fall in the same range

as the experimental values. The crossovers seen in the curves of e_s vs t_r (Fig. 5.50) are perhaps not realistic, but the data for this material contain very few points with $t_r > 1000$ hr and none with $t_r > 10{,}000$ hr. Thus, extrapolation to $t_r \approx 10^5$ hr with these data is quite difficult.

Results for the 1-in. plate have been discussed previously.[34] Figure 5.49 compares earlier results with recent results, using the Larson-Miller parameter and the MCM. Again, all parameters yield similar results. In this case, MCM results are somewhat similar also, possibly because more data were taken under more conditions than in other data sets. Again, however, MCM appears perhaps a bit better than parametric results.

Minimum commitment method and Manson-Succop results for heat 55697, as well as results for e_3 for heat 55697 and the 2-in. plate of heat 9T2796, will be available soon as the effort to obtain meaningful extrapolations of strain limit criteria continues. In addition, correlations of total engineering creep strain will be investigated using the relationship

$$e_T = \dot{e}_r t_r \ , \tag{14}$$

where t_r = rupture time (hr) and $\dot{e}_r$ = average creep rate to rupture (%/hr), defined by

$$\dot{e}_r = \text{creep-rupture elongation/rupture time} \ . \tag{15}$$

This definition, of course, does not include load elongation. More meaningful than e_T is the quantity ε_T, the true rupture ductility, defined by

$$\varepsilon_T = 100 \ \ln \frac{100}{100 - \text{RA}} \ , \tag{16}$$

which may be correlated by parametric methods in the same manner as e_T, such as using

$$\varepsilon_T = \dot{\varepsilon}_r t_r \ , \tag{17}$$

where t_r = rupture time (hr), $\dot{\varepsilon}_r$ = average true strain rate to rupture (%/hr) defined by

$$\dot{\varepsilon}_r = \text{true rupture ductility/rupture time} . \quad (18)$$

This definition does include load elongation.

While having a good deal of physical significance, ε_T is still a measure of actual failure rather than of uniform deformation. Thus, criteria such as the true strain to tertiary creep (ε_3) might be useful. The true strain at the onset of tertiary creep is given by the expression

$$\varepsilon_3(\%) = 100 \ln(1 + e_3) , \quad (19)$$

where e_3 = engineering strain to onset of tertiary creep. The quantity e_s, on the other hand, has no clear physical meaning in terms of true strain. (However, one can define $\varepsilon_s = \dot{\varepsilon}_m t_r$, where $\dot{\varepsilon}_m$ = true minimum creep rate, defined by $\dot{\varepsilon}_m = (\varepsilon_3 - \varepsilon_t)/t_3$, where ε_3 = true strain to the onset of tertiary creep, and ε_t = true transient primary creep strain intercept.)

Much work remains to be done in the area of strain limits analysis, and the effort both to identify relevant failure criteria and to develop viable methods of analysis is continuing.

5.2.4. Mechanical Property Characterization of Type 316 Stainless Steel Reference Heat

5.2.4.1 Procurement of Type 316 Stainless Steel Reference Heat — R. J. Beaver

All items except the 16- and 28-in.-diam (406- and 711-mm) pipe have been received. The forgings produced at Republic Steel were formed into forged rings at Carlton Forge preparatory to production of the 16- and 28-in.-diam pipe at Rollmet. Delivery of these last two items has been scheduled for February. The certifications of the items produced by Republic Steel have been received and are in the process of being reviewed for acceptance.

5.2.5 Structural Materials Information Center — M. K. Booker and C. O. Stevens

The operation and ongoing development of a computerized system for the acquisition, analysis, storage, and retrieval of mechanical properties data are continuing. The Automatic Data Acquisition System (ADAS), a computerized system for the acquisition of creep data, is now in operation. The operation and expansion of the Mechanical Properties Data Storage and Retrieval System (DSRS) are continuing, including initial input of data into a new supplemental data base for data from sources other than ORNL These systems, along with the Structural Materials Information Center (SMIC), form a complete computerized mechanism for the management of mechanical properties data.

Several hardware problems discovered in initial experimental operation of ADAS have been corrected, and the system is now operating smoothly. essentials of this operation have been described earlier.[40] Future development of the system will include increased flexibility in methods of displaying test results, general software advancements, and expansion of current operations.

As described earlier,[40] DSRS consists of two separate data bases, one for data from tests conducted at ORNL, and the other for supplemental data from other sources. The ORNL data base now contains the results from over 2300 mechanical property tests, including tensile, creep, impact, slow-bend, and relaxation tests. Input of data to the supplemental data base began this quarter, with the results from 256 tensile and fatigue tests now on file. These tests may be sorted, checked, and retrieved by the ORLOOK[41,42] computer program, may be displayed by various auxiliary output programs, and are available for immediate access at any time.

Quick access to DSRS is accomplished by direct teletype communication with the ORNL IBM 360 computers through programs TSO and ORLOOK.[42] This access provides for searching, sorting, and checking of data and isolation of any subset of the entire data base on the basis of any of the two-letter identifiers described in the *DSRS Thesaurus*. In addition, the information stored under any of the identifiers in any test or subset of tests may be directly displayed at the teletype, or such output may be diverted to the line printer in the ORNL computer center, if desired. Alternately, any

subset isolated by ORLOOK may be labelled so as to be accessible by auxiliary programs run from card decks, etc. A program[43] to access such subsets and generate plots of data contained in the various identifiers of the subsets was described earlier.[44] In addition, a new program,[45] ADTABLE, has been added during this quarter. It allows tabular output of DSRS data, including background information as well as actual numerical test data (See Fig. 5.54). Numerical data may be output in any specified FORTRAN-like format (E, real, or integer). Columns may be specified to be of any width, with any input heading; and tables may be generated up to two standard computer paper pages wide (132 spaces wide each). At present, these two programs are the only auxiliary access programs available. However, other output programs — numerical, statistical, etc. — could be easily added. In fact, once data are stored on DSRS in computer machine formats, any program in the program library could be made to operate on them.

In addition to the mechanism for accessing data stored on DSRS, the TENSIS program[40,46] for analysis of raw tensile data and subsequent input of such data to DSRS has been expanded. TENSIS can now generate plots of engineering stress-strain curves, true stress-strain curves, and log-log plots of true stress versus true plastic strain (for analysis of strain-hardening exponents), as well as tables of test summary characteristics and punched cards for input to DSRS.

The important problem of standardization of data to be stored in DSRS is being dealt with by an extensive set of system documentation. Definitions of all identifiers used to label information stored in DSRS have been compiled in the *DSRS Thesaurus*. In addition, a draft of a manual of standard procedures for determination of DSRS identifiers from mechanical properties test outputs has been completed and is now being reviewed. To complete the system documentation, a new, comprehensive DSRS users' guide is also being developed.

The data handling capabilities of DSRS provide a powerful tool for the generation of mathematical models for data, and for the development of relationships among data useful in design applications, such as those to be contained in the *Nuclear Systems Materials Handbook*. Thus, it is natural to carry the computerized data management system one step further to

TABULATION OF TENSILE DATA FOR 2.25% CR, 1% MO ALLOY

TEST NO.	HEAT NO.	HEAT TREATMENT	TEMPERATURE (DEG C)	STRAIN RATE (%/MIN)	TENSILE STRENGTH (PSI)	FRACTURE STRESS (PSI)	UNIFORM ELONGATION (%)	TOTAL ELONGATION (%)
11201	20017	ANN/1.0/927/FC@50 PER HR	25.	2.0000E+00	75900.	62500.	11.30	18.00
11394	20017	ANN/1.0/927/FC@50 PER HR	565.	2.0000E+00	55700.	26500.	8.20	37.40
11397	20017	ANN/1.0/927/FC@50 PER HR	204.	2.0000E+00	69600.	57500.	7.20	15.90
11404	20017	ANN/1.0/927/FC@50 PER HR	371.	2.0000E+00	82800.	67400.	12.40	14.70
11405	20017	ANN/1.0/927/FC@50 PER HR	454.	2.0000E+00	79600.	53200.	10.90	14.00
11406	20017	ANN/1.0/927/FC@50 PER HR	510.	2.0000E+00	76800.	47100.	13.80	17.60
12033	20017	ANN	316.	4.0000E+00	69789.	48619.	9.20	18.72
12036	20017	ANN	204.	4.4000E+00	63813.	40000.	12.24	25.28
12037	20017	ANN.	93.	4.0000E+00	68292.	41728.	12.64	27.76
12038	20017	ANN	26.	4.0000E+00	74060.	44233.	12.78	28.51
12039	20017	ANN	510.	4.0000E+00	59601.	28773.	8.20	25.96
12040	20017	ANN	565.	4.4000E+00	49469.	16219.	8.28	33.60
12080	20017	ANN	371.	4.0000E+00	73542.	51948.	10.12	19.36
12099	20017	ANN	371.	4.0000E-01	73514.	48295.	10.32	21.48
12100	20017	ANN	454.	4.0000E-01	67173.	35622.	8.46	22.56
12101	20017	ANN	510.	4.0000E-01	57828.	21305.	8.16	29.52
12102	20017	ANN	566.	4.0000E-01	41075.	6145.	6.08	36.24
12113	20017	ANN	510.	4.0000E-02	50969.	7079.	6.69	31.38
12114	20017	ANN	566.	4.0000E-02	32968.	2427.	3.89	52.65
12177	20017	ANN	454.	4.0000E+00	67276.	38618.	10.00	22.50

(NEXT PAGE)

Fig. 5.54. Sample Output from the ADPLØT Computer Program.

contain these relationships as well as the actual raw data. This step is accomplished by SMIC, which is intended to become the computerized version of Volume I of the *NSM Handbook*. SMIC will allow quick teletype access to handbook information, which will be kept current through the efficiency of computerized updating procedures. ADAS, DSRS, and SMIC would then provide a complete path of computerized data management from collection of data by the test engineer, through data analysis and development of correlations and mathematical models, to eventual use of generated relationships by the designer.

5.3 MECHANICAL AND METALLURGICAL BEHAVIOR OF WELDMENTS FOR LMFBR — P. Patriarca, G. M. Slaughter, W. R. Martin, and C. R. Brinkman

5.3.1 Creep of Type 308 CRE Stainless Steel Welds in the Transverse-to-the-Weld Direction at 593°C — R. T. King and E. Bolling

The long-time creep and creep-rupture properties of type 308 stainless steel welds with controlled residual elements (CRE) are under investigation. These welds are prototypic of the longitudinal seam and girth welds of the FFTF vessel. We have previously reported the materials that were used to fabricate these welds;[47] they included two of the same heats of base metal and several of the batches of electrodes that were used in the FFTF vessel.

We have previously reported the method of preparation and creep testing of specimens with 0.25-in. (6.35-mm)-diam by 1.25-in. (31.7-mm)-long gage sections.[48,49] Figure 5.55 shows the orientation and location of longitudinal all-weld-metal specimens from three depths within the weld: L1, L2, and L3. Creep and creep-rupture data have previously been reported for these specimens.[50]

Further, transverse-to-the-weld specimens of the T1, T2, and T3 types were also prepared with 0.25-in. (6.35-mm)-diam by 1.25-in. (31.7-mm)-long gage sections (see Figs. 5.55 and 5.56). These specimens were creep tested at 593°C by the same methods used to test the longitudinal specimens. Because the width of the weld is about 0.7 in. (17.5 mm) in the T1 and T2 positions, and from 0.4 to 0.5 in. (10–12 mm) in the T3 position, these specimens contained both weld metal and base metal from the heat-affected

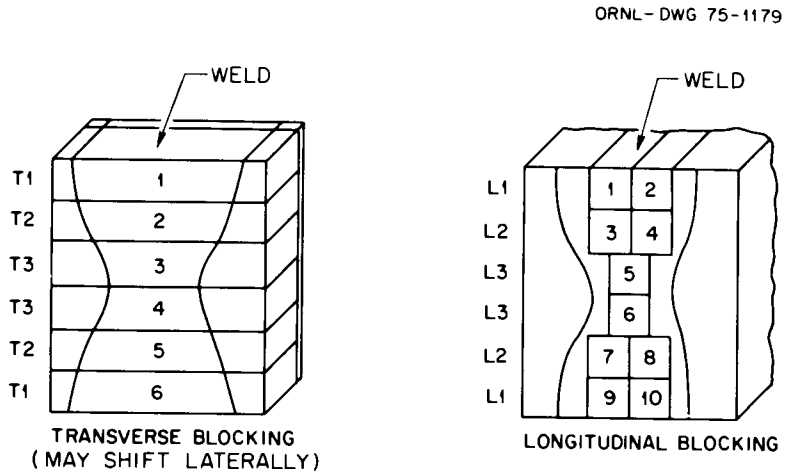

Fig. 5.55. FFTF Weld Test Matrix Specimen Layout.

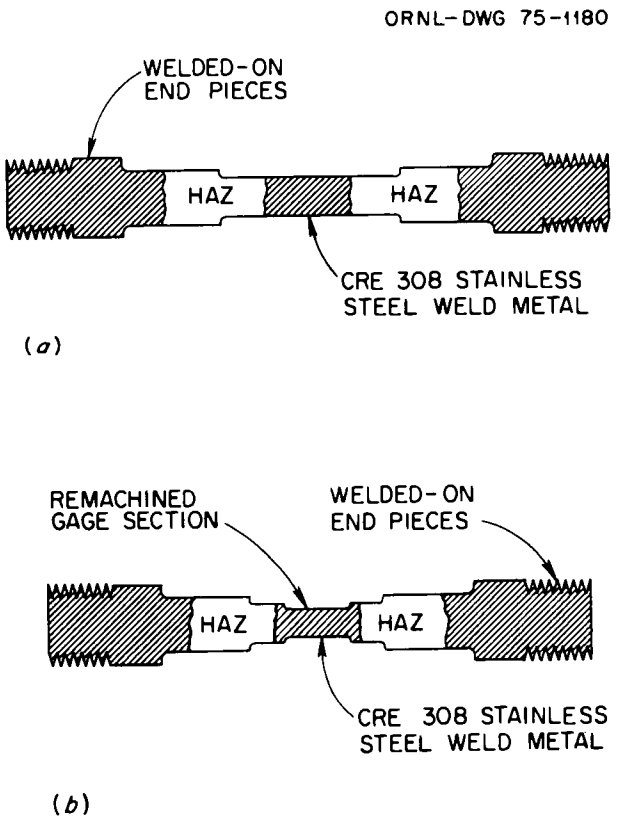

Fig. 5.56. Schematic Drawing of T1, T2, and T3 Specimens Showing Weld Metal, Heat-Affected Zone, and Remachined Gage Section.

zone. The creep and creep-rupture properties of these specimens are given in Table 5.14. These specimens always failed in the base metal beneath the indentations made in the gage section by the extensometers used in testing.

To obtain creep and creep-rupture data for weld metal only, several transverse specimens were remachined to smaller, all-weld-metal gage sections. The locations of the fusion lines were determined by macroetching surfaces that were later removed during machining. The gage sections machined in the T1 and T2 specimens were 0.15 in. in diameter by 0.74 in. long (3.8 × 18.9 mm), while those in the T3 specimens were 0.15 in. in diameter by 0.39 in. long (3.8 × 10 mm) (see Fig. 5.56). These specimens were tested as before, except that the extensometer indentations were outside the remachined gage area. The results of these tests are also given in Table 5.14.

Some care is needed in the interpretation of the results of Table 5.14. For specimens containing both weld metal and base metal in the gage length, the obvious heterogeneity of the gage section can lead to nonuniform straining along the gage. The overall strains measured by the extensometer are therefore not necessarily representative of the local strains in any particular region of the gage section. (We previously demonstrated[51] that the yield strength of the base metal increases by approximately a factor of 2 in going from the virgin base metal toward the fusion line; this observation agrees with transmission electron microscopy observations showing dislocation line density increasing over the same region.[52] In addition, the specimens that were remachined to have all-weld-metal gage lengths share another characteristic with the standard specimens that complicates interpretation of results, the anisotropic deformation behavior of the weld metal. This behavior has been observed in the elastic and plastic strain ranges, and has been observed to affect the deformation of whole weld cross sections.[53] Because the principal directions of anisotropy vary with the orientation of the local substructure within the weld, large variations in local strains within the weld metal occur.

Despite these differences in behavior, several useful observations can be made from the data given in Table 5.14. The measured creep strains before the onset of tertiary creep for specimens that contained base

Table 5.14. Creep Behavior of Type 308 CRE Stainless Steel Weld Metal at 593°C (1100°F)

Specimen	Specimen Type	Stress		Strain, %							Strain Rate, %/hr			Reduction of Area (%)	Rupture Time, t_r (hr)	t_{III}/t_r [a]
				Loading ε_L	$\varepsilon_{Stage\ I}$	$\varepsilon_{Stage\ II}$		$\varepsilon_{Stage\ III}$		Rupture ε_r	$\dot{\varepsilon}_{Stage\ II}$		ε_r/t_r			
		(ksi)	(MPa)			Real	Offset	Real	Offset		Real	Offset				
1.25-in.-diam (31.7-mm) Gage Specimens, Weld and Base Metal																
43-21	T1	33	227	0.68	1.57	2.32	2.57	4.10	3.85	7.10	0.00277	0.00311	0.01557	8.6	455.8	
43-33	T1	35	241	1.59						>7.12					642.8	0.823
43-34[a]	T2	33	227	0.13						>2.15					>1171	
43-37[a]	T2	35	241	0.54						>3.18					>907	
43-23	T3	33	227	0.15	0.5	0.25	0.70	4.74	4.55	5.4	0.00027	0.00040	2.90073	7.92	1861.6	0.752
43-24	T3	33	241	0.24	0.30	0.46	0.82	5.8	5.4	6.7	0.0003	0.0001	0.0087	5.9	771.7	0.99
43-36	T3	35	241	0.35	0.25	0.65	1.10	5.0	4.45	5.9	0.0092	0.00117	7.3888	1.2	798.5	0.501
Remachined Gage Section, Weld Metal Only																
43-32	T1	35	241	1.30	2.20	4.50	5.20	10.0	9.20	15.8	0.00584	0.00650	0.014748	42.5	1071.3	0.495
43-26	T1	37	255	1.50	3.87	7.65	9.15	11.45	10.10	20.6	0.07692	0.07708	0.16586	48.5	124.2	0.604
43-31[a]	T2	35	241	0.30											>1074.4	
43-25	T2	37	255	0.80	0.60	2.00	2.70	11.90	11.20	14.7	0.00321	0.00356	0.015402	42.0	954.4	0.524
43-30[a]	T3	35	241	0.23											>1050	
43-35	T3	37	255	0.60	0.70	1.60	2.30	12.0	11.30	14.2	0.01466	0.01657	0.058556	43.8	242.5	0.350
43-29	T3	37	255	0.25	0.35	0.90	1.60	6.55	5.85	7.7	0.00674	0.00683	0.030677	33.4	251	0.446

[a]Test still in progress.

metal were in the 1 to 4% range, while these for weld metal only were 2.5 and 3.9% for T3 level (root-pass region) specimens, and 3.3 to 13% for T1 and T2 specimens. The total strains for specimens containing base metal (which always fractured beneath the extensometer indentations in the base metal region) were between 5.4 and 7.1%. Reductions of area were less than 10%. Two creep-rupture tests have been completed on as-received base metal plate from the same heat (300380) as part of the heat-to-heat variation program.[54] One specimen strained 2.9% on loading and 2.7% in creep; the other specimen strained 4.1% on loading and 8.5% in creep. Our results for heat-affected zone base metal plus weld metal specimens are not inconsistent with these data. Other observations on strains will be reserved until the testing is completed and metallographic studies are made on the fractured specimens.

There are five types of creep-rupture data among which comparisons may be made:

1. data for longitudinal all-weld-metal specimens;[50]
2. data for transverse all-weld-metal specimens with remachined gage lengths;
3. data for transverse specimens containing weld metal and base metal (since these ruptures occurred in the base metal where the gage section had been damaged by the extensometer, they are not necessarily indicative of heat-effected zone metal properties);
4. data from specimens (buttonhead) that had gage sections parallel to the welding direction[55] (these data showed a tendency for rupture times of *base metal* from heat 600414 to increase as specimens were removed from locations that were progressivly closer to the fusion line. However, the buttonhead all-weld-metal specimens exhibited much shorter rupture times than any base metal specimens, in agreement with the data from the larger gage section specimens of item 1);
5. data for as-received base metal specimens from the ORNL heat-to-heat variation program.

In Fig. 5.57, several important comparisons are made:

1. The data for T1, T2, and T3 all-weld-metal specimens that have ruptured indicate that the rupture times for transverse specimens from

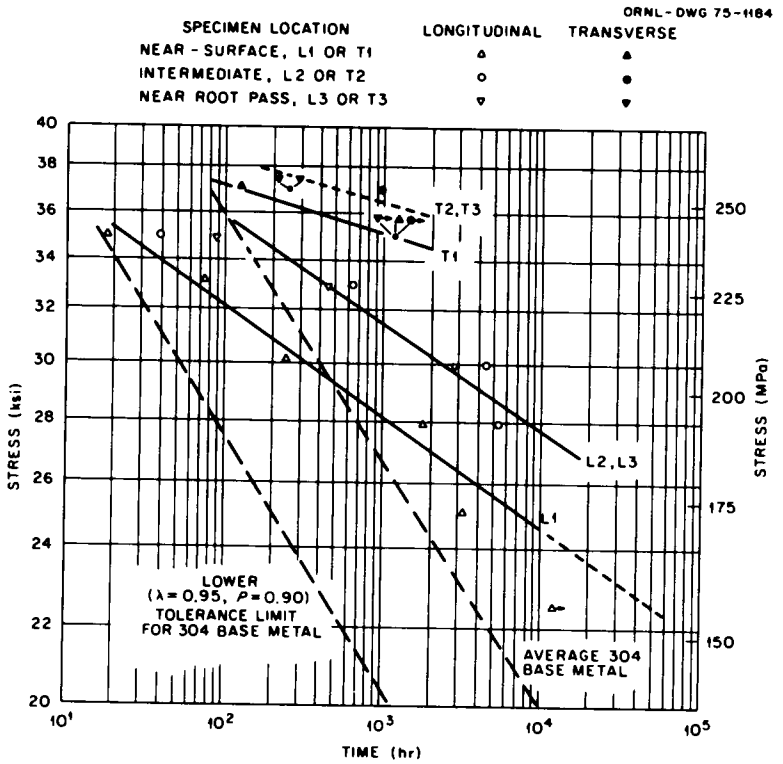

Fig 5.57. Comparison of Creep-Rupture Times of Longitudinal Versus Transverse All-Weld-Metal Specimens of Type 308 CRE Stainless Steel Weld Metal at 593°C (1100°F).

the surface region (T1) are shorter than these for intermediate (T2) and root pass region (T3) specimens at the stress levels explored.

2. Transverse all-weld-metal specimens have longer rupture times than longitudinal all-weld-metal specimens.

3. Average and (λ = 0.95, P = 0.90) lower tolerance limits[56] for type 304 stainless steel base metal at 593°C are shown. The rupture times for weld metal exceed the lower tolerance limit for base metal at all stress levels that were explored. However, data for longitudinal specimens approach the lower tolerance level at high stresses. At the lower stresses that were explored, weld metal rupture times exceed the average for base metal by amounts that increase with decreasing stress.

From Fig. 5.58, the following comparisons can be made:

4. The rupture times for transverse, all-weld-metal specimens tend to be greater than those for transverse weldment specimens that failed in the base metal.

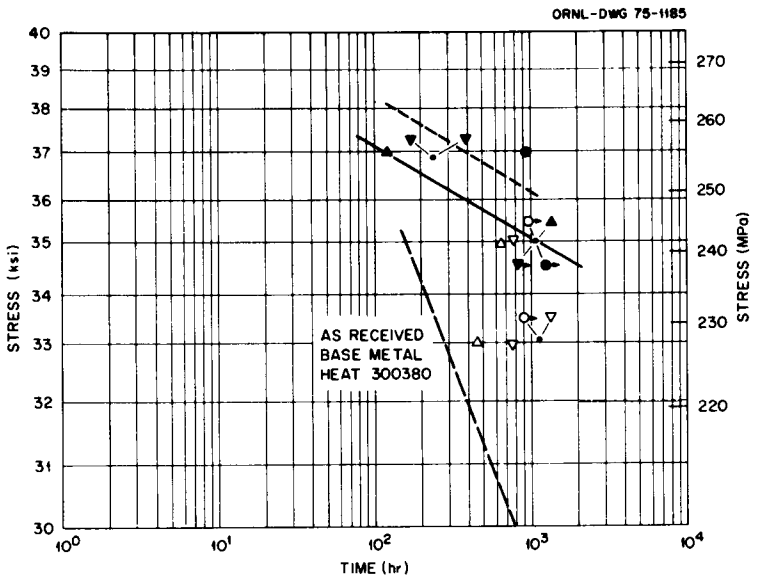

Fig. 5.58. Comparison of Creep-Rupture Times of All-Weld-Metal Versus Weld-Plus-Base-Metal Transverse Specimens with Type 308 CRE Stainless Steel Weld Metal at 593°C (1100°F).

5. The rupture times for transverse weldment specimens that failed in the heat-affected zone exceed those for as-received base metal. This is in agreement with earlier results.[55]

5.3.2 Studies of Strain Distribution in Weldments — B. R. Dewey, R. T. King, and R. G. Berggren

A whole-weld-cross-section specimen of type 304 stainless steel with a multipass weld of type 308 filler with controlled residual elements, has been tensile tested in the elastic strain range at room temperature. The 10 × 2.38 × 0.25 in. (254 × 60.3 × 6.3 mm) gage section was strain gaged to demonstrate the nonhomogeneity and elastic anisotropy present in the weldment for a uniaxial tensile stress (see Fig. 5.59). In Fig. 5.60, the front and rear views of the 0-45-90° strain gage rosettes are shown as installed.

A straightforward means of identifying elastic anisotropy is to observe the deviation of the principal directions of the measured strains from the applied stress axis. In the present test, the specimen has been subjected to a uniaxial load.

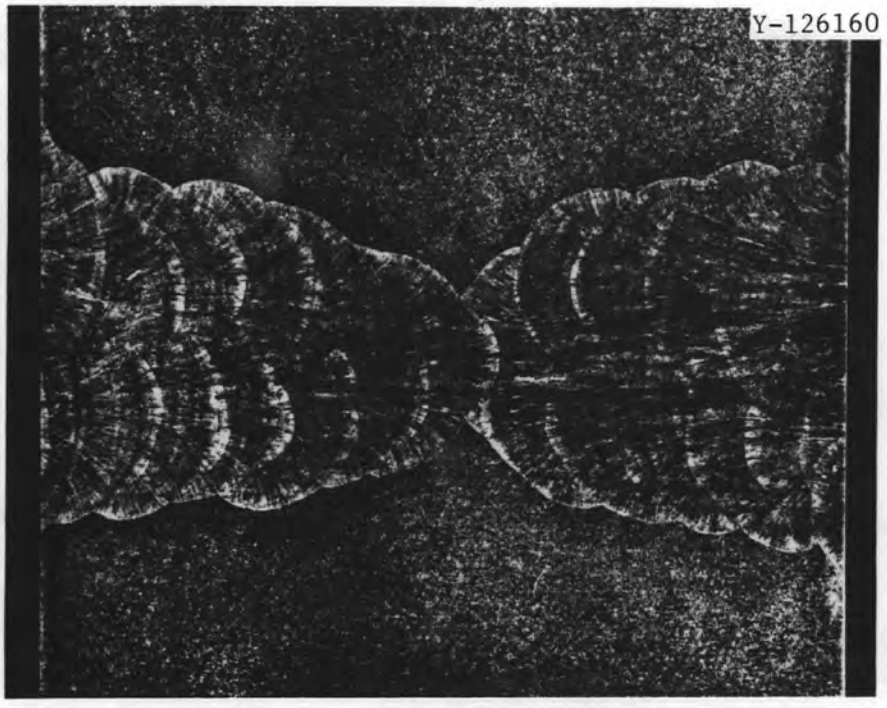

Fig. 5.59. Weldment Studied, Showing Interpass Boundaries and Oriented Substructure of Weld Metal. Base metal is type 304 stainless steel and filler is type 308 with controlled residual elements.

From the theory of elasticity, the results for a 0-45-90° rosette can be analyzed to determine θ_a, the direction of the maximum strain as referred to the direction of the uniaxial loading:

$$\theta_a = \frac{1}{2} \tan^{-1} \frac{\varepsilon_a - 2\varepsilon_b + \varepsilon_c}{\varepsilon_a - \varepsilon_c} , \tag{19}$$

where ε_a is the measured strain in the direction of loading, ε_b is the strain at 45°, ε_c is the strain at 90°, and the positive θ direction is clockwise.

The apparent Poisson's ratio is defined as

$$\mu = -\varepsilon_{max}/\varepsilon_{min} , \tag{20}$$

where ε_{max} and ε_{min} are the components of principal strain. With reference to Eq. (19), we may also define a normalized maximum principal strain as

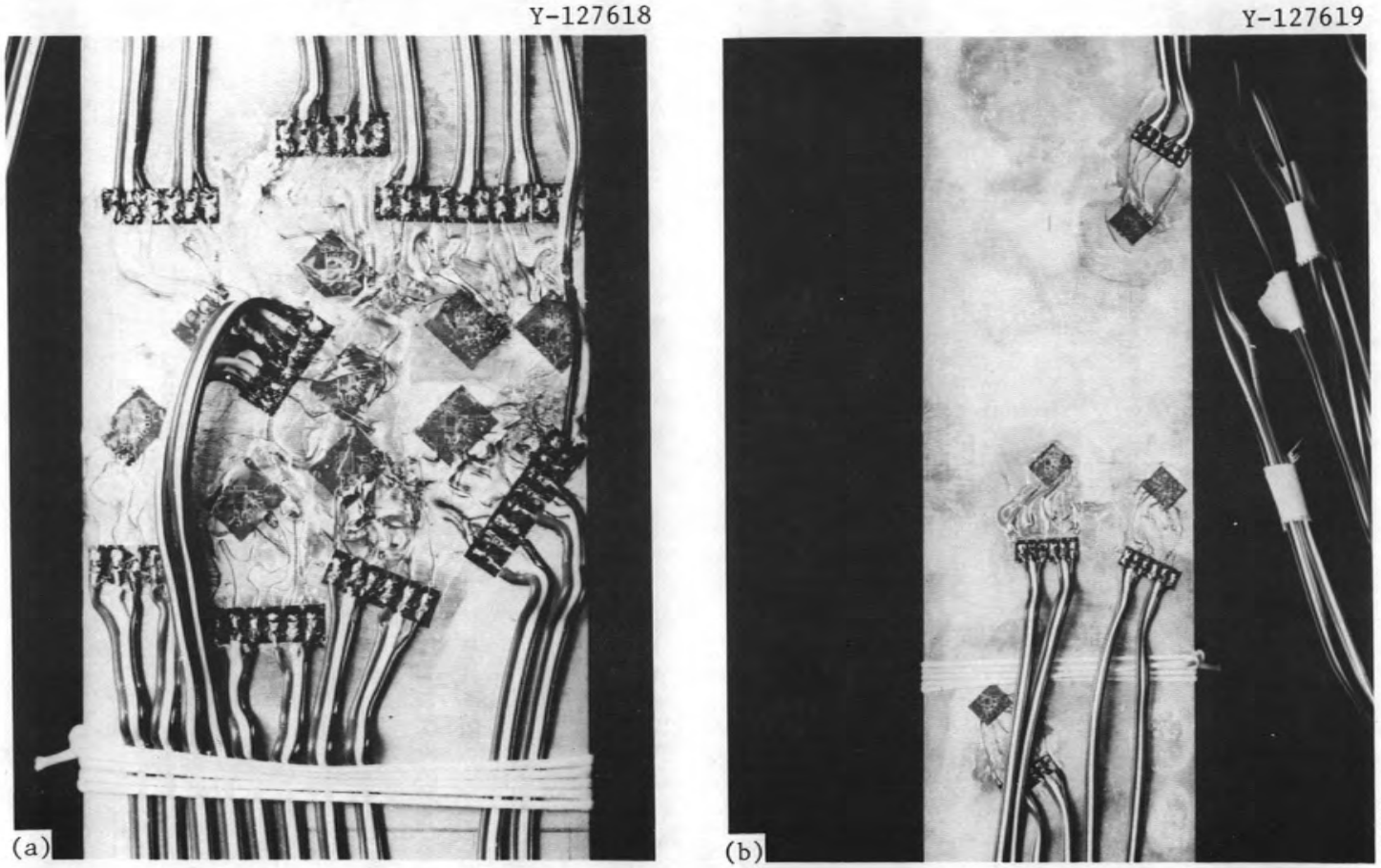

Fig. 5.60. Rosettes (0-45-90°) Installed on Weldment. (a) Front view. (b) Rear view.

$$\bar{\varepsilon}_{max} = \frac{1}{\varepsilon_R}\left[\frac{\varepsilon_a + \varepsilon_b}{2} + \frac{\varepsilon_a - 2\varepsilon_b + \varepsilon_c}{2}\cos(2\theta_a)\right], \qquad (21)$$

where ε_R is a reference strain, taken here as the maximum principal strain in the base metal (measured by one gage).

In Table 5.15 the above quantities are tabulated for the 13 strain gages shown in Fig. 5.60. The values tabulated represent mean values from six different loads. The maximum standard deviation in any of the principal directions is 0.18°.

Table 5.15. Results from Strain Gaged Weld Specimens Used to Demonstrate Elastic Anisotropy

Gage	Location	Direction of Principal Strain, deg	Apparent Poisson's Ratio	Normalized Maximum Principal Strain
1	Weld metal, right edge, top	8.4	0.34	0.93
2	HAZ, right central, top	0.8	0.28	0.83
3	HAZ, center, top	a	0.29	0.88
4	Weld metal, left central, top	a	a	0.90
5	Weld metal, center	−3.1	0.16	1.00
6	Weld metal, right central, bottom	−3.5	0.34	1.02
7	HAZ, center, bottom	2.0	0.30	0.86
8	Weld metal, left central, bottom	4.3	0.35	1.02
9	Weld metal, left edge, bottom	3.9	0.45	0.96
10	Base metal, left, top (back)	a	a	a
11	Back of No. 9	1.8	0.28	0.99
12	Back of No. 5	−5.0	0.27	1.05
13	Base metal, right, bottom (back)	1.4	0.27	(1.00)

[a]Failure of one channel precluded determination of principal direction and/or Poisson's ratio.

The results in Table 5.15 clearly show that elastic anisotropy and nonhomogeneity are present. While values of the apparent Poisson's ratio

in the base metal and the heat-affected zone are within the range normally expected (0.25–0.30), the values of apparent Poisson's ratio in the weld metal vary considerably. Since the strain gages happen to have been mounted at locations on the weld metal where the dendritic substructure is generally perpendicular to the tensile axis (gage length), it is difficult to distinguish in the directions of principal strain the contribution due to anisotropy from that due to misalignment in gage mounting. However, the 8.4° for gage 1 is too large to be due to misalignment. The normalized maximum principal strain demonstrates a combination of nonhomogeneity and anisotropy, wherein values smaller than unity indicate a stiffer-than-base-metal region, while those greater than unity indicate a less stiff region.

These tests will continue with an annealed specimen considered next. At the same time, the strain gage results are being used for comparison with a finite-element computer code, which has assumed anisotropic and nonuniform material properties for the weldment. Ultrasonic determinations of the dynamic elastic constants of the weld metal and base metal are in progress to provide independent measures of the degree of anisotropy of weld metal and constants needed for numerical analysis of weld deformation.

5.3.3 Comparison of the Creep-Rupture Behavior of Type 308 CRE Stainless Steel Welds Made with Electrodes Supplied by Various Commercial Vendors — D. P. Edmonds, R. T. King, and E. Bolling

Previous work[57–60] has demonstrated that the addition of small amounts of B, P, and Ti to the coatings of type 308 stainless steel shielded metal-arc (SMA) electrodes results in improved creep strength and long-time creep ductility. These observations had been made only for electrodes produced by Combustion Engineering of Chattanooga, Tennessee. To determine if the improvement afforded by the CRE composition could be reproduced by other electrode manufacturers, several commercial vendors were invited to supply similar electrodes for welding trials and subsequent evaluation of creep behavior. Evaluation and testing of weld deposits made from Airco and Arcos electrodes have now been completed, and work on welds made with McKay electrodes is in progress.

All the test welds were made in 12-mm-thick type 304 stainless steel plate, using a 75°-included-angle V-groove joint geometry. The welding conditions were about 28 V DCRP (direct current, reverse polarity), and 150 A current. The electrode sizes are given in Table 5.16. Sections taken normal to the welding direction were cut, mounted, and polished for metallographic examination. Ferrite numbers were measured on these sections with a Magne-Gage. Typical microstructures near the center of the welds are shown in Fig. 5.61. The chemical compositions of the deposits were obtained by spectrographic analyses, and they are given together with the desired ranges in Table 5.17. Ferrite numbers calculated for these compositions are compared with the measured values in Table 5.16.

Table 5.16. Experimental Type 308 CRE Shielded Metal-Arc Electrodes and Ferrite Levels of Welds

Vendor	Weld	Electrode Diameter		Ferrite Number	
		(in.)	(mm)	Calculated[a]	Measured[b]
Combustion Engineering	V-19,20	5/32	4.0	6.8	5.4
Airco	V-59,60	1/8	3.2	4.5	3.4
Arcos	V-63,64	5/32	4.0	6.0	8.4
McKay	V-136,137	1/8	3.2	7.5	7.0

[a]Calculated from DeLong Constitution Diagram.

[b]Average, measured with Magne Gage.

All-weld-metal buttonhead specimens with a 0.13-in.-diam by 1.13-in.-long (3.2-mm by 28.6-mm) gage section parallel to the welding direction were machined from each test weld. The center of each specimen coincided with the middle of the weld at a distance about 0.2 in. (5 mm) below the top of the weld. These specimens were creep tested in air at 650°C (1202°F) at stress levels intended to produce rupture times ranging from a few hours to several thousand hours. The loads were applied gradually by mechanical and/or hydraulic devices. Extensometers mounted on the grips were used to

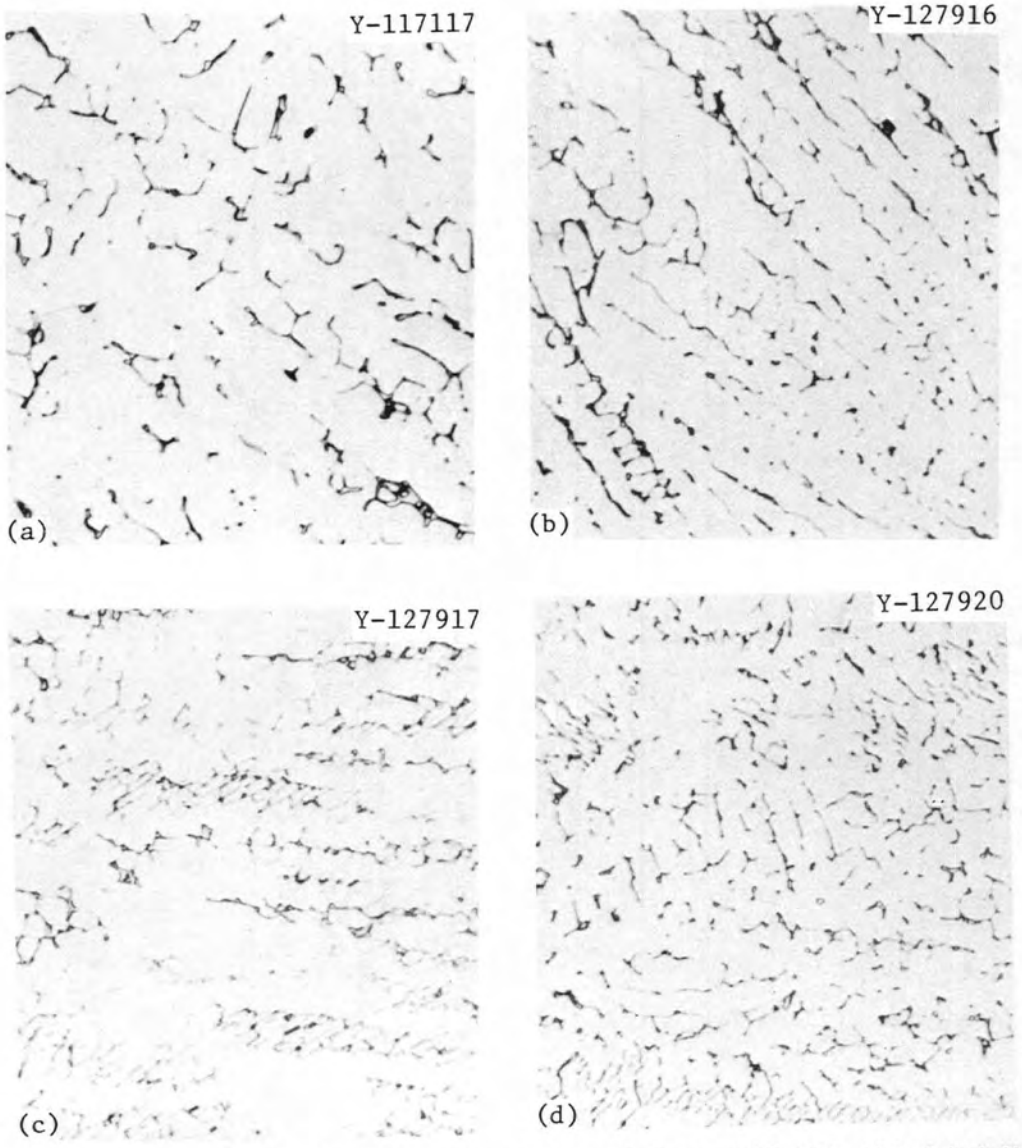

Fig. 5.61. Typical Microstructures of Type 308 CRE Shielded Metal-Arc Welds Made with Electrodes from Various Vendors. 500×. (a) Combustion Engineering weldment (V19,20). (b) Airco weldment (V-59,60). (c) Arcos weldment (V-63,64). (d) McKay weldment (V-136,137).

Table 5.17. Chemical Analysis of Experimental SMA Type 308 CRE Welds

Vendor	Content, %												
	Si	S	P	C	Mn	Cr	Ni	Mo	Co	Cu	B	Ti	N
Desired Range	0.37–0.60	0.004–0.016	0.040–0.044	0.060–0.068	1.76–1.95	19.48–20.10	9.48–10.14	0.06–0.27	0.03–0.17	0.04–0.18	0.007	0.05–0.07	0.030–0.048
Combustion Engineering	0.52	0.006	0.041	0.056	1.75	19.41	9.15	0.08	0.15	0.04	0.007	0.06	0.055
Airco	0.49	0.011	0.041	0.066	1.93	19.63	10.00	0.18	0.07	0.13	0.007	0.05	
Arcos	0.52	0.011	0.040	0.066	1.85	19.97	9.86	0.43	0.24	0.29	0.007	0.02	0.058
McKay	0.48		0.040	0.067	2.05	20.69	10.12	0.28		0.20	0.006	0.06	0.065

monitor creep strains to within ±1%, while total elongations were measured directly by fitting the fractured specimens together. Reductions of area were calculated by approximating the fracture surface projection as an ellipse. We report only rupture data here. Metallographic examinations of the fractures are in progress, but visual examination revealed no evidence of substructural boundary separations commonly associated[60] with low-ductility failures in austenitic steel weld metal.

The creep-rupture times for the type 308 CRE stainless steel welds made with electrodes supplied by different vendors are compared in Fig. 5.62 in terms of the Larson-Miller parameter $(T + 460)(20 + \log_{10} t_r)$ (T is temperature in degrees Fahrenheit and t_r is rupture time in hours). There is no important difference between the rupture times for welds made with Combustion Engineering, Arcos, or Airco electrodes. Appropriate statistical evaluations will be provided later.

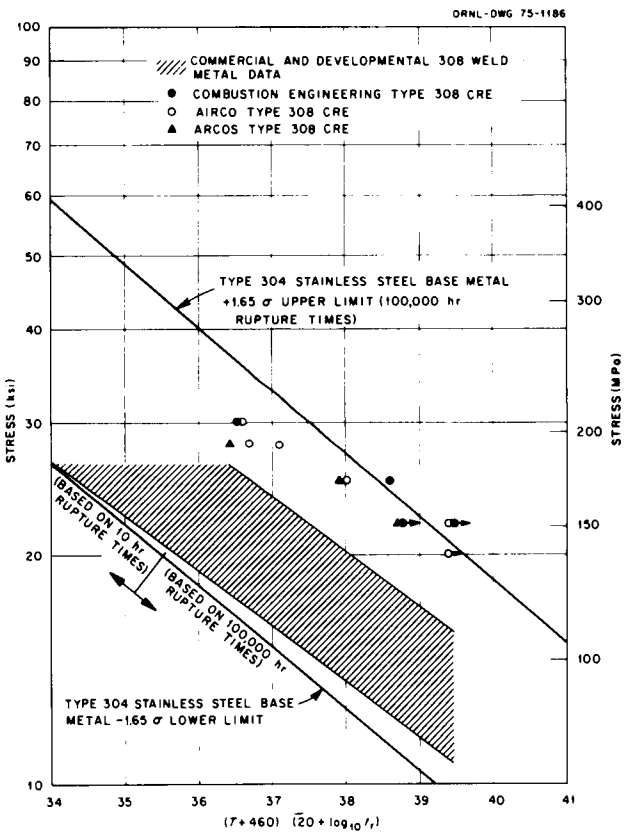

Fig. 5.62. Stress Rupture of CRE Type 308 Stainless Steel SMA Weld Metal.

We have previously shown approximate upper and lower limits for the stress-rupture behavior of type 304 stainless steel base metal,[58] based on Blackburn's analysis[61] of base metal data. The rupture times at 650°C for CRE weld metal tend to be above the average for type 304 stainless steel base metals, and some long-time values exceed the +1.65 standard deviation (σ) limit for type 304 stainless steel base metal (Fig. 5.62). Some rupture times are greater than 5000 hr. The CRE weld metal is also stronger than conventional type 308 stainless steel weld metal according to available data that have been discussed before.[58]

The total elongations and reductions of area for the test welds are shown in Figs. 5.63 and 5.64, respectively. The smallest total elongation observed for type 308 CRE weld metal was 9.5%, and the reductions of area all exceeded 40%. There is no trend for either of these measures of ductility to decrease with increasing rupture time for the CRE welds as

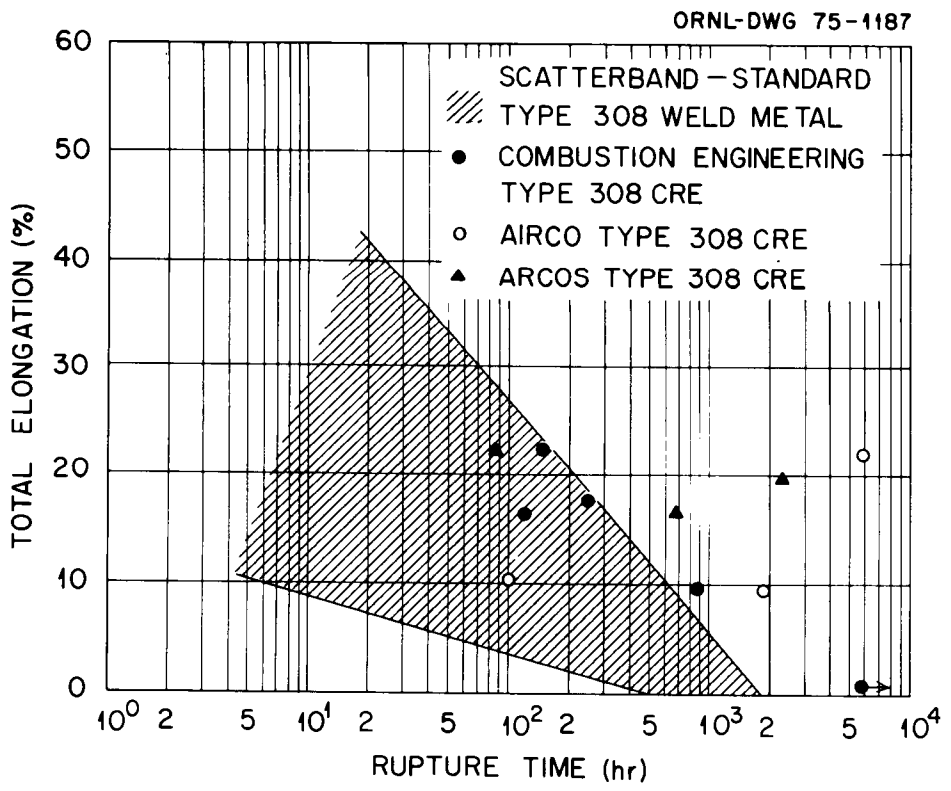

Fig. 5.63. Effects of Controlled Residual Elements on the Stress-Rupture Properties of Type 308 Shielded Metal Arc Welds at 649°C (1200°F).

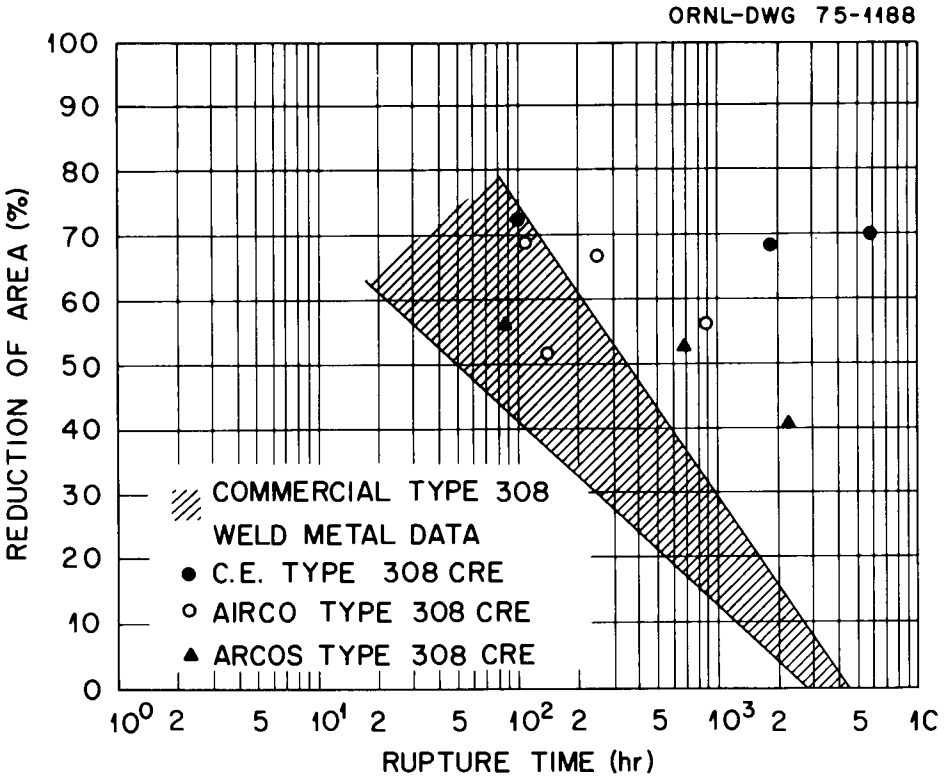

Fig. 5.64. Effects of Controlled Residual Elements on the Stress-Rupture Properties of Type 308 Shielded Metal Arc Welds at 1200°F.

a group. However, a test in excess of 1000 hr for the weld made with the Airco electrodes is required to establish the long-time total elongation behavior of this weld. Literature[58] and unpublished ORNL data for standard type 308 stainless steel weld metal show total elongations and reductions of area decreasing with time and approaching zero in less than 10,000 hr.

5.4 MECHANICAL PROPERTIES OF STEAM GENERATOR AND HEAT EXCHANGER MATERIALS — C. R. Brinkman

Extensive mechanical properties studies are under way on 2 1/4 Cr-1 Mo low-alloy steel. These include tensile, creep, fatigue, and heat-to-heat variations. A number of correlations, with their tolerance limits, have also been made for inclusion in the *Nuclear Systems Materials Handbook*. A small study is also under way to determine the properties of weld-overlaid stainless steel for intermediate heat exchanger applications.

5.4.1 High-Strain-Rate Tensile Properties of Annealed 2 1/4 Cr-1 Mo Steel — R. L. Klueh

As part of the safety analyses for the steam generator of the LMFBR demonstration plant, high-strain-rate elevated-temperature tensile properties of annealed 2 1/4 Cr-1 Mo steel are required. We have determined such properties over the range 0.16 to 144/sec (9.6 to 8640/min) at 25, 454, 510, and 566°C (77, 850, 950, and 1050°F); tests are also to be conducted at the same strain rates and 204 and 371°C (400 and 700°F). With the completion of these tests and those previously completed,[62] we will be able to describe the static tensile behavior of annealed 2 1/4 Cr-1 Mo steel over the temperature range 25 to 566°C and the strain rate range 3.33×10^{-6} to 144/sec (0.0002 to 8600/min).

The tensile tests were made on heat 20017 in the annealed condition on an MTS electrohydraulic, servocontrolled test machine. For all strain-rate tests, load versus piston displacement was photographically recorded by use of the X-Y mode of an oscilloscope. Piston displacement was determined by an LVDT-type transducer. Load for the low-rate tests (0.16 and 1.6/sec) was determined by the use of a strain gage load cell; a high-response piezoelectric load cell was used during the high-rate tests. The machine was operated at constant crosshead velocity, and the strain rates were determined from the crosshead velocity and the initial gage length.

The results of these tests are shown in Table 5.18, and in Figs. 5.65 through 5.69 the 0.2% yield stress, ultimate tensile strength, fracture stress, elongation, and reduction of area are shown as functions of strain rate.

The effect of strain rate on strength is greatest at room temperature, where both the yield strength and ultimate tensile strength show significant increases with increasing strain rate. On the other hand, at the elevated temperatures the changes in strength are somewhat more subtle. Yield strength is little affected by the strain rate, while the ultimate tensile strength appears to go through a minimum. The strain rate at which the apparent minimum occurs decreases with increasing temperature (Fig. 5.65). The minimum for the 566°C tests occurs at $\lesssim$0.1/sec, and thereafter the ultimate tensile strength increases with increasing

Table 5.18. High-Strain-Rate Tensile Properties of Annealed 2 1/4 Cr-1 Mo Steel

Strain Rate (sec^{-1})	Strength, ksi (MPa)			Elongation (%)	Reduction of Area (%)
	0.2% Yield	Ultimate Tensile	Fracture		
		25°C (77°F)			
0.16	46.0 (317)	76.6 (528)	38 (260)	35[a]	68
0.16	47.0 (324)	79.0 (545)	40 (280)	33[a]	68
1.6	47.6 (328)	82.0 (565)	45 (310)	36	67
1.6	47.9 (330)	80.2 (553)	48 (330)	33[a]	67
16		88.0 (607)	49 (340)	36[a]	68
16		88.4 (610)	50 (340)	36[a]	67
16	56.2 (387)	87.2 (601)	48 (330)	36	67
144		97.0 (669)			70
144		98.4 (678)	61 (420)	37	72
144				34	67
144	72.0 (496)	100 (689)	56 (390)	35	71
144	71.0 (490)	104 (717)	60 (410)	35	69
		454°C (850°F)			
0.16	34.0 (234)	68.6 (473)	38 (260)	23	59
0.16	32.0 (221)	67.6 (466)	44 (300)	24	61
1.6	36.0 (248)	65.4 (451)	47 (320)	22	62
16	29.8 (205)	62.4 (430)	42 (290)	22	65
16	32.2 (222)	63.6 (439)	43 (300)	20	63
144	32.0 (221)	63.0 (434)	42 (290)	22	70
144	34.0 (234)	68.6 (473)	46 (320)	23	66
		510°C (950°F)[5]			
0.16	33.0 (228)	63.6 (439)	33 (230)	26	71
0.16	30.8 (212)	64.2 (443)	34 (230)	26	68
1.6	34.3 (237)	68.6 (473)	44 (300)	24	61
1.6	34.0 (234)	67.0 (462)	44 (300)	25	62
16	30.6 (211)	63.6 (439)	44 (300)	21	63
16	30.0 (207)	66.2 (456)	47 (320)	21	60
144				20	65
144	32.0 (221)	70.0 (483)	48 (330)	21	65
		566°C (1050°F)			
0.16	31.6 (218)	55.4 (382)	26 (180)	29	78
0.16	30.4 (210)	58.4 (403)	26 (180)	26	76
1.6	34.3 (237)	60.4 (416)	30 (210)	28	73
1.6	34.2 (236)	63.4 (437)	31 (210)	28	72
16	32.0 (221)	63.0 (434)	39 (270)	26	68
16	30.6 (211)	66.0 (455)	42 (290)	24	62
144	30.4 (210)	68.6 (473)	49 (340)	23	61
144	33.6 (232)	72.0 (496)	50 (340)	22	58

[a]Determined from crosshead velocity; all other elongation measurements were made from 1-in. gage marks on specimen gage section.

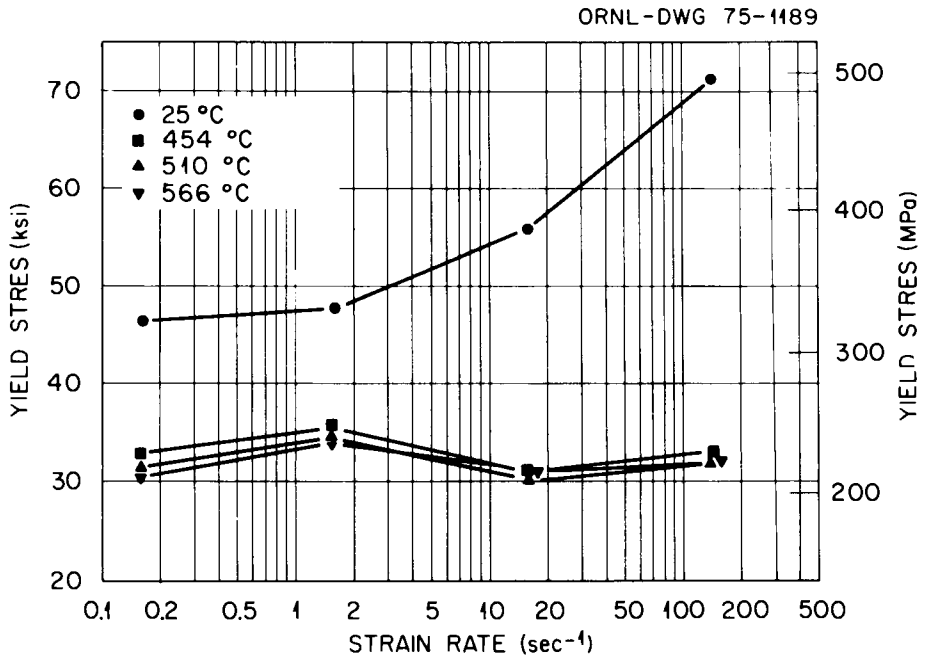

Fig. 5.65. Yield Strength of Annealed 2 1/4 Cr-1 Mo Steel as a Function of Strain Rate.

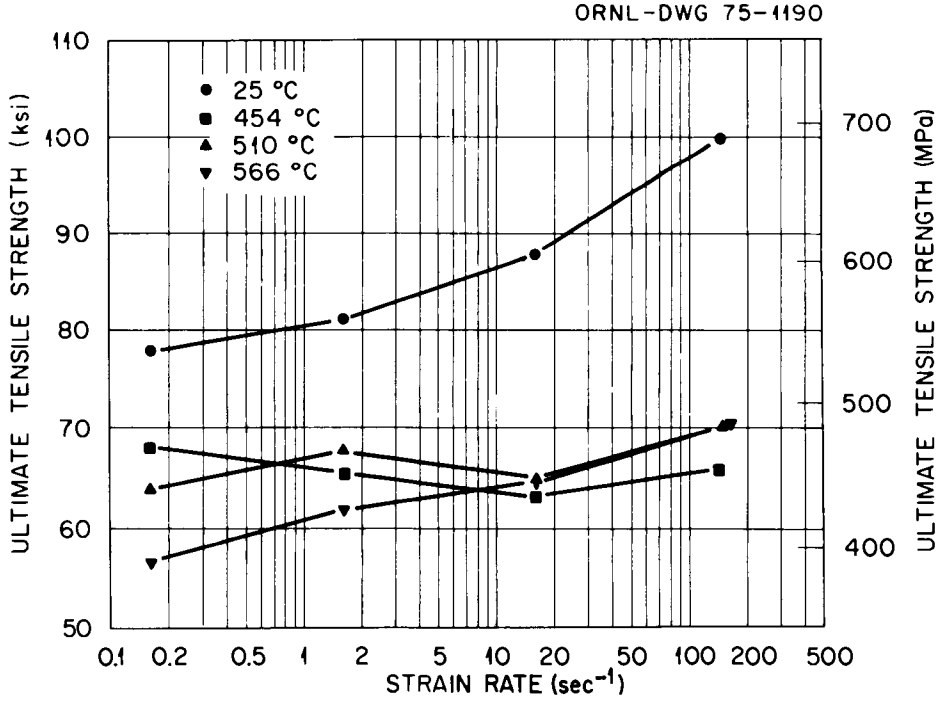

Fig. 5.66. Ultimate Tensile Strength of Annealed 2 1/4 Cr-1 Mo Steel as a Function of Strain Rate.

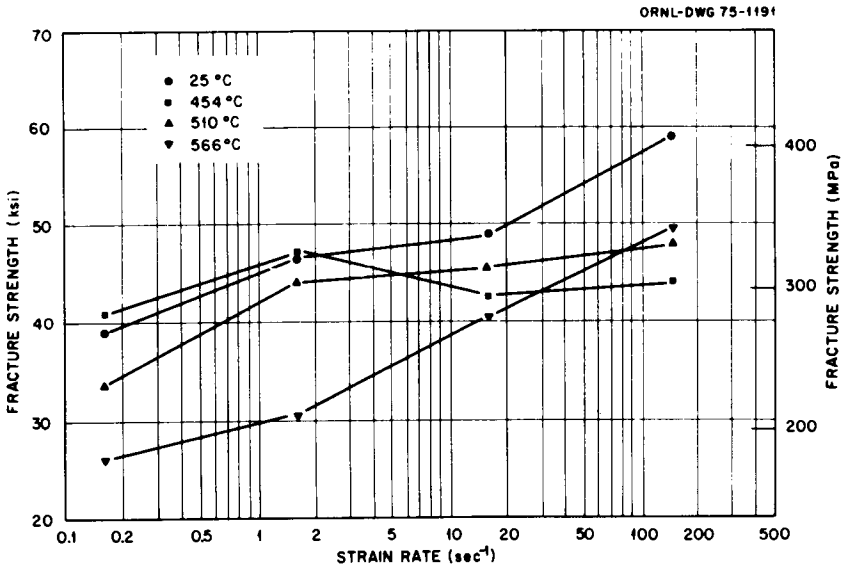

Fig. 5.67. Fracture Stress of Annealed 2 1/4 Cr-1 Mo Steel as a Function of Strain Rate.

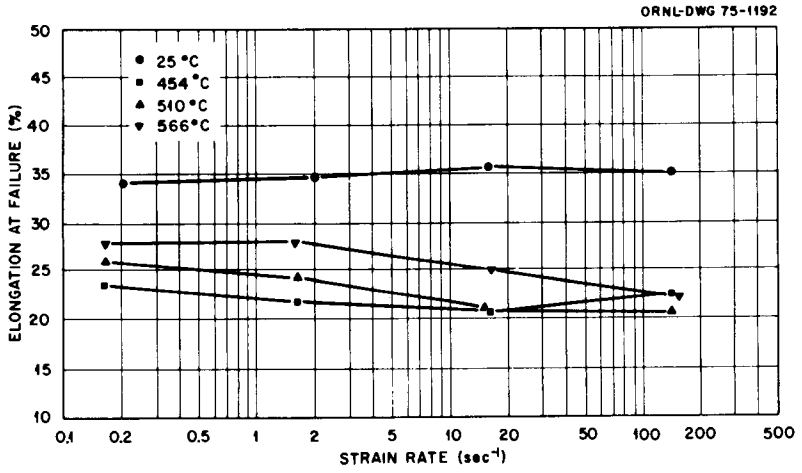

Fig. 5.68. Total Elongation of Annealed 2 1/4 Cr-1 Mo Steel as a Function of Strain Rate.

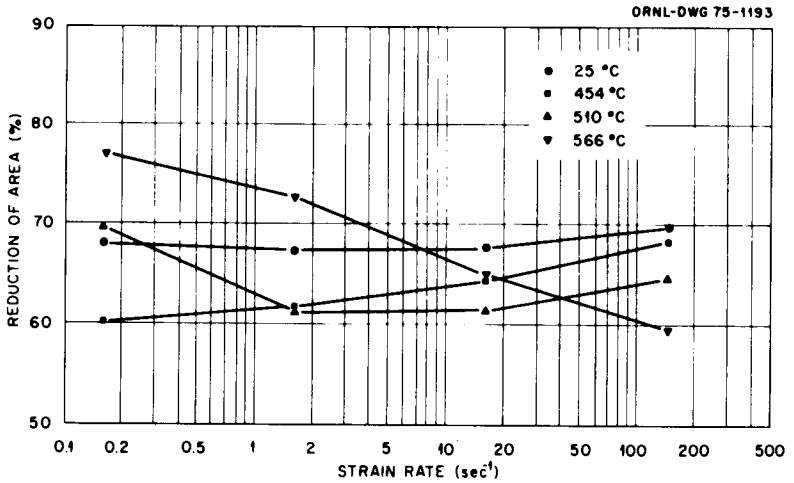

Fig. 5.69. Reduction of Area of Annealed 2 1/4 Cr-1 Mo Steel as a Function of Strain Rate.

strain rate. The minimum for the 454 and 510°C tests, though less pronounced, occur at higher strain rates.

The room-temperature ductility (elongation and reduction of area) appears little affected by strain rate. As was the case for the ultimate tensile strength, the ductility at elevated temperatures also appears to go through a minimum (Figs. 5.68 and 5.69); this is most clearly seen in the reduction of area (Fig. 5.69). However, although the strain rate of the ultimate tensile strength minimum decreased with increasing temperature, the strain rate of the ductility minimum increased with increasing temperature. That is, the minimum for 566°C (1050°F) occurs at a higher strain rate than the minimum at 510°C (950°F), which is higher than the minimum at 454°C (850°F).

During the next quarter the tests at 204 and 371°C (400 and 700°F) will be completed.

5.4.2 Heat-to-Heat Variation of 2 1/4 Cr-1 Mo Steel — R. L. Klueh

As part of our heat-to-heat variation study, we are looking at forgings produced by different techniques. We have obtained two small sections of forgings manufactured by the vacuum arc remelt (VAR) process, one produced by the Jorgensen Company, the other by the Coulter Company; we have also obtained a small section manufactured by the electroslag

remelt (ESR) process (trade name is Lukens Lectrefine) by Lukens Steel Corporation. During this past quarter, we made tensile tests on specimens taken from these three forgings.

The chemical analyses for the three forgings are given in Table 5.19. The two VAR forgings show few major differences, although the copper and oxygen contents are considerably lower in the Coulter forging (the copper for the Coulter forging is also considerably below that for the ESR forging, while the oxygen concentration is similar). The main differences between the ESR and VAR forgings appear to be the silicon, sulfur, and carbon.

Table 5.19. Composition of 2 1/4 Cr-1 Mo Steel Forgings Produced by the VAR and ESR Processes

Element	Content, %		
	Jorgensen VAR	Coulter VAR	Lukens ESR
Si	0.31	0.37	0.18
S	0.025	0.032	0.006
P	0.006	0.009	0.010
Mn	0.50	0.37	0.45
C	0.10	0.097	0.13
Cr	2.33	2.24	2.32
Ni	0.11	0.07	0.15
Mo	0.90	1.02	0.97
O	0.12	0.006	0.008
N	0.011	0.011	0.010
Cu	0.21	0.03	0.23
Al	0.006	0.018	0.013
V	0.025	0.013	0.009

Inclusion studies were previously conducted,[63] and we concluded that the Jorgensen (VAR) billet (1) exhibited the most inclusions per

field of view, and (2) contained the largest inclusions, including large globular, multiphase inclusions that are larger than any inclusions recorded on ASTM charts. In all the observations, the Coulter (VAR) and Lukens (ESR) samples contained smaller and more sparsely distributed inclusions.

Before test, the tensile specimens were given an identical isothermal anneal: 1 hr at 927°C (1700°F), furnace cooled to 704°C (1300°F), held at 704°C for 2 hr, then furnace cooled to room temperature. In the future, specimens will also be tested in the as-received condition.

Figures 5.70, 5.71, and 5.72 show photomicrographs of the Jorgensen (VAR), Coulter (VAR), and Lukens (ESR) forgings after the isothermal anneal; Table 5.20 gives ferrite grain size numbers and microhardness values. The microstructures of the Coulter (VAR) and Lukens (ESR) forgings are seen to be quite similar. These two materials contain about 25% pearlite, the balance ferrite. The ferrite contains a very fine matrix precipitate, and the ferrite grain boundaries are outlined by a fine precipitate. The Jorgensen forging, on the other hand, appeared to have less of the fine pearlite and contained two types of ferrite.

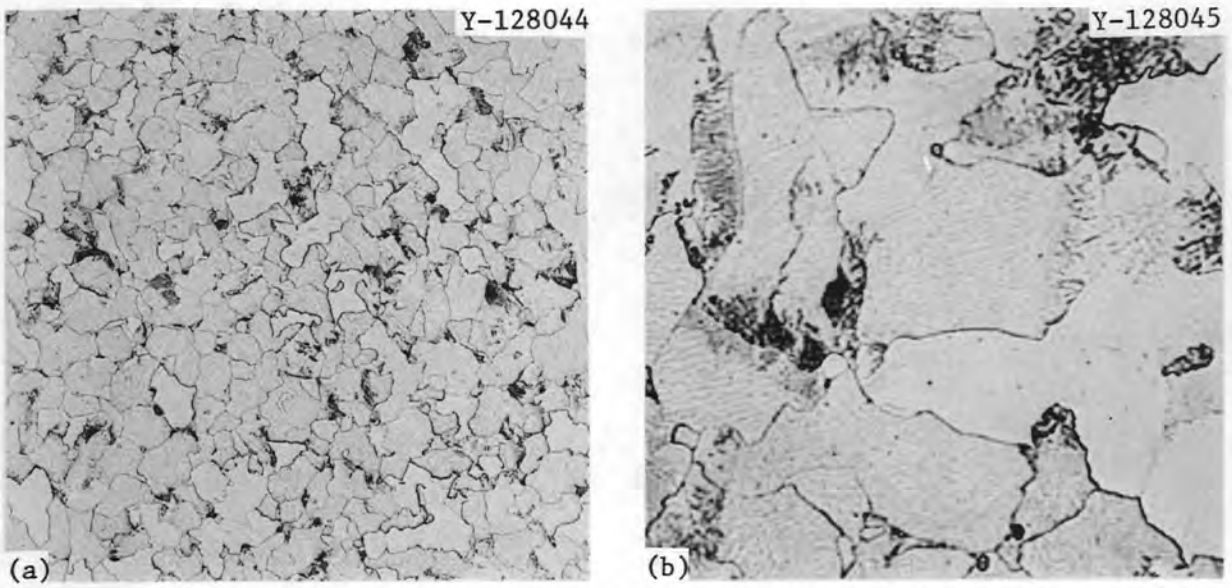

Fig. 5.70. Microstructure of Isothermally Annealed 2 1/4 Cr-1 Mo Steel of the Jorgensen VAR Forging. (a) 100×. (b) 500×.

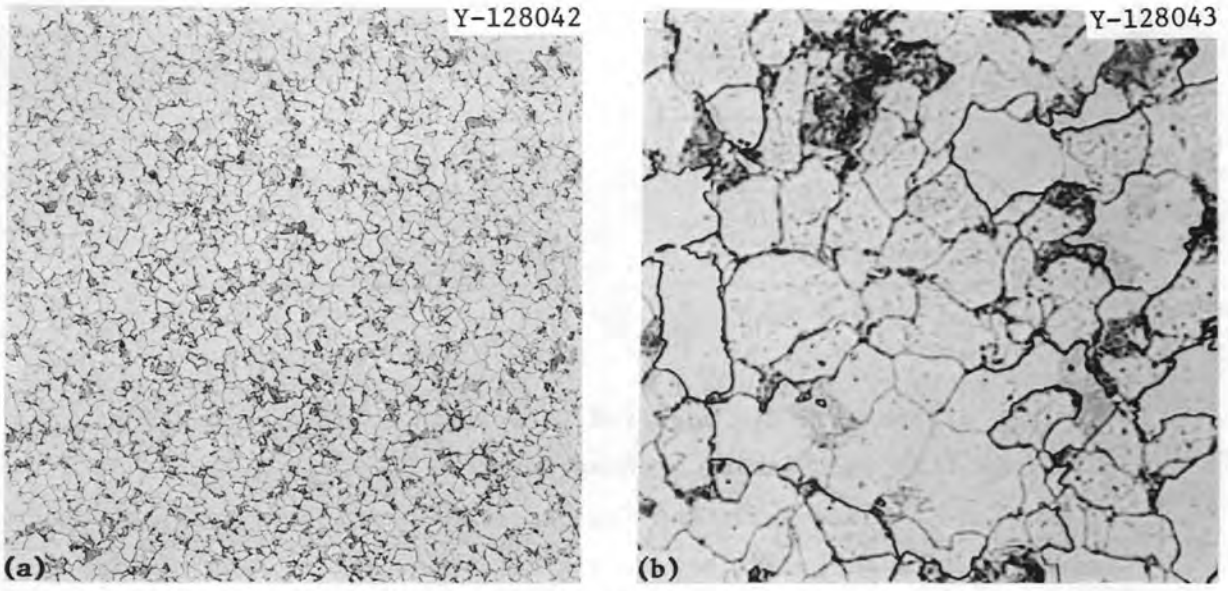

Fig. 5.71. Microstructure of Isothermally Annealed 2 1/4 Cr-1 Mo Steel of the Coulter VAR Forging. (a) 100×. (b) 500×.

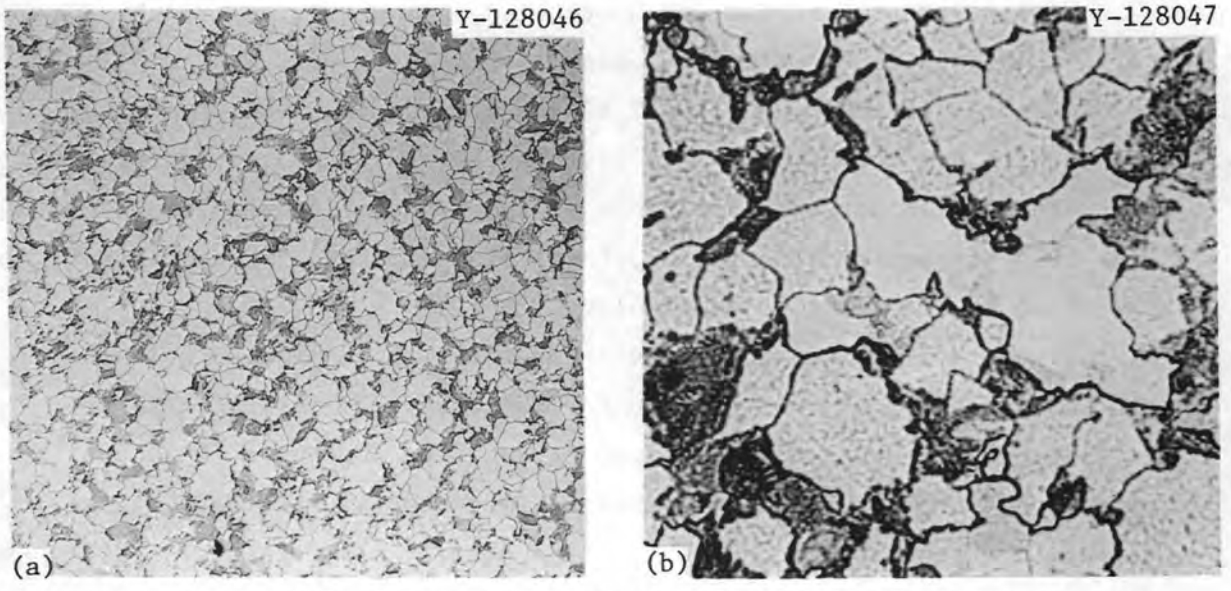

Fig. 5.72. Microstructure of Isothermally Annealed 2 1/4 Cr-1 Mo Steel of the Lukens ESR Forging. (a) 100×. (b) 500×.

Table 5.20. Microhardnesses and ASTM Grain Size Numbers for the Three Isothermally Annealed 2 1/4 Cr-1 Mo Steel Forgings

Forging	Microhardness (DPH)[a]	Grain Size (ASTM)
Jorgensen (VAR)	148	6
Coulter (VAR)	133	8
Lukens (VAR)	136	8

[a] 1 kg load.

The darker etching ferrite appeared to contain a higher density of fine precipitate than the lighter etching ferrite.

As seen in Table 5.20, the Coulter (VAR) and Lukens forgings had the same grain sizes, and the grain sizes were smaller (larger ASTM grain size number) than the grain size of the Jorgensen (VAR). Likewise, the Coulter and Lukens forgings had similar microhardnesses, which were somewhat less than that of the Jorgensen forging.

Tensile tests were made on buttonhead specimens at a crosshead speed of 0.05 in./min (1.27 mm/min) (nominal strain rate of 0.0444/min) at 25, 204, 371, 454, 510, and 566°C (75, 400, 700, 850, 950, and 1050°F). The results are shown in Table 5.21. In Fig. 5.73 the yield stress and ultimate tensile strength are shown as functions of temperature, and in Fig. 5.74 the uniform elongation, total elongation, and reduction of area are shown as functions of temperature.

Figure 5.73 shows that the strength properties — both yield stress and tensile strength — of the Coulter (VAR) and the Lukens (ESR) are similar over the entire temperature range. The Jorgensen (VAR), on the other hand, shows a slightly higher ultimate tensile strength at the low temperatures and approaches that of the other two forgings at the highest temperatures, while the yield stress shows just the opposite behavior: it is similar at the low temperatures and deviates at the highest temperatures. The ductility, especially the uniform and total elongation, is comparable for all three forgings.

Table 5.21. Tensile Properties of Isothermally Annealed 2 1/4 Cr-1 Mo Steel Forgings

Test Temperature		Strength, ksi (MPa)		Elongation, %		Reduction of Area
(°C)	(°F)	Yield	Ultimate Tensile	Uniform	Total	(%)
			Jorgensen (VAR)			
25	75	39.6 (273)	73.0 (503)	12.2	20.2	70.8
204	400	32.3 (223)	60.5 (417)	10.0	17.2	65.2
371	700	30.3 (209)	67.4 (465)	9.0	14.8	58.0
454	850	30.4 (210)	62.6 (432)	9.2	17.6	56.1
510	950	29.3 (202)	56.0 (386)	8.8	17.4	63.0
566	1050	27.7 (191)	45.2 (312)	7.5	26.0	72.2
			Coulter (VAR)			
25	75	41.9 (289)	67.7 (467)	14.6	25.6	66.7
204	400	33.2 (229)	57.5 (396)	13.5	20.7	62.6
371	700	28.9 (199)	63.2 (436)	9.5	15.2	57.4
454	850	25.2 (174)	59.3 (409)	9.8	18.7	65.6
510	950	24.0 (166)	53.1 (366)	9.6	20.6	76.1
566	1050	23.3 (161)	45.0 (310)	9.7	27.3	74.5
			Lukens (ESR)			
25	75	40.0 (276)	66.9 (461)	15.2	25.6	75.5
204	400	31.4 (217)	56.5 (390)	10.9	19.6	74.6
371	700	28.1 (200)	60.7 (419)	8.1	15.1	67.8
454	850	24.6 (170)	58.9 (406)	9.2	16.8	65.0
510	950	24.3 (168)	53.7 (370)	10.1	18.6	70.6
566	1050	23.1 (159)	45.2 (312)	10.2	29.6	78.5

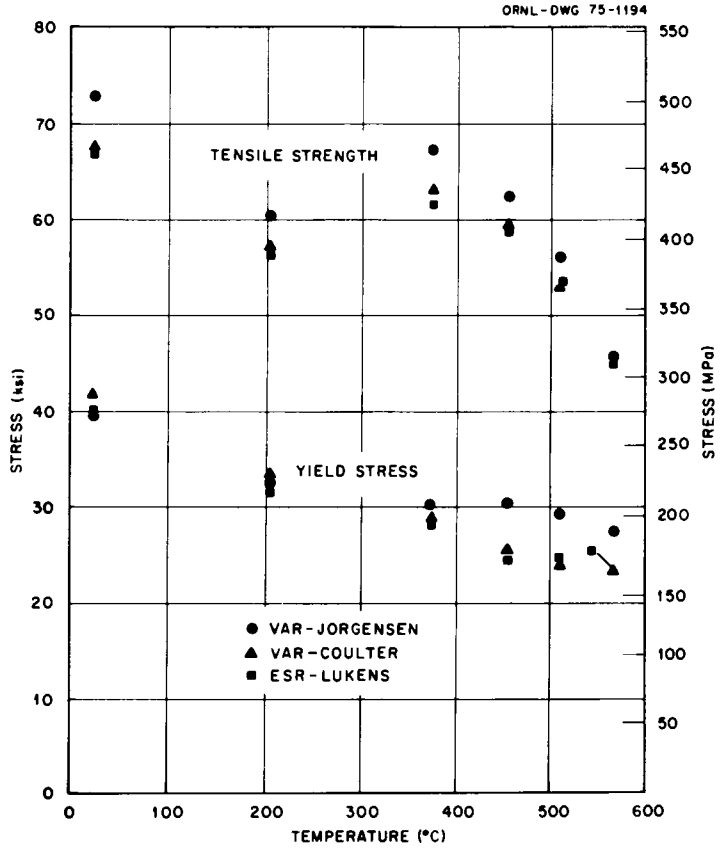

Fig. 5.73. The Yield Stress and Ultimate Tensile Strength as Functions of Temperature for the Jorgensen VAR, Coulter VAR, and Lukens ESR 2 1/4 Cr-1 Mo Steel Forgings, After an Identical Isothermal Anneal.

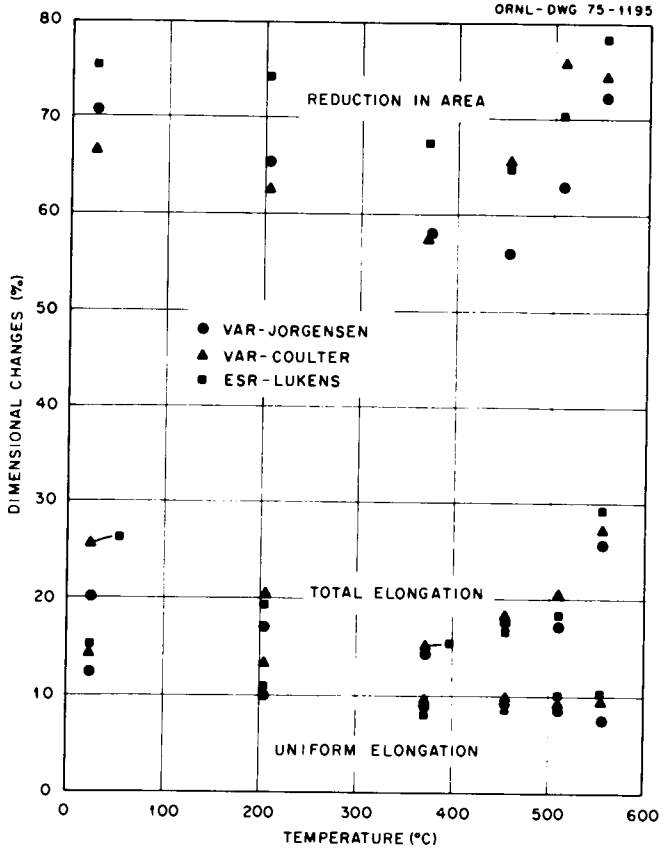

Fig. 5.74. The Uniform Elongation, Total Elongation, and Reduction of Area as Functions of Temperature for the Jorgensen VAR, Coulter VAR, and Lukens ESR 2 1/4 Cr-1 Mo Steel Forgings After an Identical Isothermal Anneal.

In summary, the differences in the tensile properties for the three forgings appear to be minor. In all cases, the properties fall near the center of the scatter band for commercial annealed material as given by Smith[64] in his compilation of elevated-temperature properties of 2 1/4 Cr-1 Mo steel. At present it is not possible to explain the small strength advantage that was noted for the Jorgensen (VAR) forging. From a chemical composition viewpoint (Table 5.19) the only major difference between the Jorgensen (VAR) and the other two forgings appears to be the oxygen content. The Jorgensen forging contains about 20 times as much oxygen. However, much of this oxygen is probably accounted for by the much higher inclusion content for this forging.[63]

5.4.3 Effect of Sodium on Mechanical Properties of 2 1/4 Cr-1 Mo Steel — R. L. Klueh and J. M. Leitnaker

We previously reported on the optical[65] and electron[66] microscopy of 2 1/4 Cr-1 Mo steel specimens that had been decarburized in sodium for 26,500 hr at 566°C and others that had been simultaneously aged in helium; annealed starting material was also examined. During this quarter, we serially sectioned a decarburized specimen to determine if a carbon gradient was present and attempted to identify the carbides in each type of sample.

To determine if there was a carbon gradient in the sodium-exposed specimens, successive 0.006-in.-thick (0.15 mm) layers were removed and analyzed. Since oxygen may have been involved in the surface penetrations previously shown,[65] approximately 0.003 in. (80 μm) from the specimen surface was also analyzed for oxygen and the result compared with 0.006-in.-thick cuts from the interior. The results of the carbon and oxygen determinations are given in Table 5.22.

The trend of the carbon results indicates that the carbon concentration increases slightly as the center of the specimen is approached. The oxygen results show a definite increase in the amount of oxygen in the surface region over that in the remainder of the specimen.

To determine the type of carbides and carbide gradients developed during decarburization and thermal aging, the carbides were electrolytically extracted in an HCl-methanol solution; that is, the ferrite

Table 5.22. Carbon and Oxygen Concentrations as Functions of Distance Across the Sodium-Exposed Specimen

Distance From One Edge[a]		Concentration, ppm	
(in.)	(mm)	Carbon	Oxygen
0–6 × 10^{-3}	0–0.15	695	
6–12	0.15–0.31	685	
12–18	0.31–0.46	725	
18–24	0.46–0.61	760	
24–30	0.61–0.76	775	
30–36	0.76–0.91	755	
36–42	0.91–1.07	740	
42–48	1.07–1.22		200
48–54	1.22–1.37		195
54–60	1.37–1.52		230
60–63	1.52–1.60		>5000

[a]Successive 0.006-in. (0.15-mm) layers of the cross section were removed; the specimen was 0.063 in. (1.6 mm) thick.

solid solution was dissolved, leaving the carbides. After extraction, the solutions were centrifuged to separate the carbides, and the separated carbide was weighed. The extracted carbides were identified by x-ray diffraction. To estimate the amount of alloying elements that remained in the α-iron solid solution (and by difference the amount in the carbides), the supernate was analyzed for Fe, Cr, Mo, and Si.

Carbides were extracted from pieces of 2 1/4 Cr-1 Mo steel in the annealed (starting material), helium-exposed, and sodium-exposed conditions. The first two specimens were totally dissolved, while the latter was dissolved in stages. In all cases, the supernate from the extraction was analyzed for chromium, molybdenum, and silicon to determine the amount of these elements that remained in the ferrite solid solution. The results are given in Table 5.23. Selected extracted precipitates were analyzed by x-ray diffraction, and these results are given in Table 5.24.

On a weight basis, the sodium-exposed specimen contained about 60% of the amount of precipitate contained by the thermally aged specimens. When the carbides extracted from these respective specimens were

Table 5.23. Summary of Analytical Chemistry Results from Carbide Extractions

Amount of Specimen Dissolved,[a] (%)	Specimen History	Amount of Precipitate in Steel (wt %)	Amount of Element in Solid Solution,[b] wt %		
			Cr	Mo	Si
100	Annealed[c]	1.41	1.77	0.69	0.17
100	He-exposed, aged	2.29	1.54	0.22	0.12
1.8[d]	Na-exposed	2.9[e]	1.0	0.42	0.13
6.4	Na-exposed	1.31[f]	1.87	0.32	
4.4	Na-exposed	1.29[f]	1.98	0.29	0.16
5.7	Na-exposed	1.32[f]	2.05	0.31	0.16
40	Na-exposed	1.55[f]	2.09	0.28	0.14
11.8	Na-exposed	1.57[f]	1.97	0.25	0.16

[a]Original specimen was 1.12 × 0.5 × 0.063 in. (28 × 13 × 1.6 mm).

[b]Determined by analyzing the supernate; material originally contained 2.22% Cr, 0.95% Mo, and 0.21% Si (by weight).

[c]To simulate starting material.

[d]Specimen dissolved in stages.

[e]Much of this precipitate is oxide.

[f]Precipitate analyzed by x-ray diffraction; see Table 5.24.

analyzed by x-ray diffraction, there was also a difference in the relative amounts of the respective carbides present. Both the helium- and sodium-exposed specimens contained M_6C and $M_{23}C_6$. The sodium-exposed specimen that contained less carbon contained proportionately more M_6C.

The amount of carbide extracted from the specimen annealed to simulate the starting microstructure was less than that of the aged specimen. This occurred for two reasons: first, precipitation was not completed during the initial heat treatment; secondly, the precipitates that evolve during aging increase the metal-to-carbon ratio. For the "annealed" specimen, the major portion of the extracted precipitate was $M_{23}C_6$ and M_3C, with lesser amounts of M_6C. Though the characteristic morphology of Mo_2C was detected by transmission electron microscopy, it was not identified by x-ray diffraction analysis, indicating that it was probably present in minor amounts.

Table 5.24. Summary of X-Ray Diffraction Identification of Carbides

Sample Identification	Carbide in Total Precipitate, mole %		
	$M_{23}C_6$	M_6C	M_3C
Annealed Starting Material[a]	present[a]	present[a]	present[a]
Helium-exposed[b]	51	49	
Sodium-exposed			
2nd Dissolution (1.31 wt % ppt)	10	90	
4th Dissolution (1.32 wt % ppt)	12	88	
6th Dissolution (1.57 wt % ppt)	19	81	

[a] It was not possible to determine the amounts of each carbide when three carbides were present; M_3C and $M_{23}C_6$ made up the bulk of the precipitate.

[b] The mole percents of $M_{23}C_6$ and M_6C were calculated on the basis of the unit cells $M_{92}C_{24}$ and $M_{96}C_{16}$, respectively.

The results in Tables 5.23 and 5.24 for the sodium-exposed specimen indicate that the amount of precipitate increases as the specimen center is approached. Although the first dissolution yielded an extremely large amount of precipitate, a large portion was an unidentified oxide phase. When this precipitate was examined by x-ray diffraction the relative amounts of M_6C and $M_{23}C_6$ appeared similar to those reported in Table 5.24 for the second and fourth dissolutions (an exact estimate was made difficult by the background caused by the oxide).

For the first four extractions, the amount of precipitate was quite constant at 1.3 wt %, as were the relative amounts of M_6C and $M_{23}C_6$. To speed up the process, the next extraction consumed 40% of the sample, and the amount of precipitate increased to 1.55%; the final extraction yielded 1.57%. As seen in Table 5.24, a definite change in the relative amounts of M_6C and $M_{23}C_6$ accompanied the change in the amount of carbides extracted: the amount of $M_{23}C_6$ almost doubled (from 11 to 19%), though M_6C still made up the major portion of the precipitate.

To determine what were the major elements (other than carbon) that made up the precipitate, one sample of the extracted carbides from the sodium-exposed specimen (third dissolution) was analyzed with the electron microprobe. Significant amounts of Fe, Cr, Mo, and Si were found. Because of specimen geometry, absolute concentrations could not be determined. Concentration ratios relative to iron were as follows:

$$Mo:Fe = 1.37;\ Cr:Fe = 0.31;\ Si:Fe = 0.13.$$

The results of these tests show that prolonged exposure of annealed 2 1/4 Cr-1 Mo steel at 566°C (1050°F) had a significant effect on the type and morphology of carbides present in the microstructure. Furthermore, when the decarburization process was superimposed on the thermal aging process, a slightly different sequence of events ensued. Both processes are expected to have a significant effect on the mechanical properties.

The results of the thermal aging studies at 566°C (1050°F) were similar to those of Hale[67] on annealed 2 1/4 Cr-1 Mo steel at 550 to 675°C (1022–1247°F). During aging, the amount of M_6C increased at the expense of the $M_{23}C_6$, M_3C, and Mo_2C. In aging studies on normalized-and-tempered and quenched-and-tempered 2 1/4 Cr-1 Mo steel, Baker and Nutting[68] observed a similar change of carbides, but implied that the equilibrium microstructure contains M_6C carbides in a ferrite matrix. However, they never reached this end-point; all specimens they examined contained $M_{23}C_6$, though the amount of this carbide continually decreased. Likewise, Hale's final microstructure also contained $M_{23}C_6$.

In a multicomponent system such as 2 1/4 Cr-1 Mo steel, more than one carbide species can exist at equilibrium. Thus, an equilibrium structure could contain both $M_{23}C_6$ and M_6C. Only with specimens aged beyond 26,500 hr will this question be resolved.

The results for the sodium-exposed specimen differ from those for the helium-aged specimen in two important respects. First, decarburization has lowered the total amount of carbon and carbide present after 26,500 hr. Second, decarburization has affected the relative amounts of the respective

carbides; that is, in the sodium-exposed specimen the ratio of M_6C to $M_{23}C_6$ was considerably greater than in the helium-exposed specimen. The important result, *vis-a-vis* a diffusion mechanism, however, is the two zones that contain different amounts of precipitate and different relative amounts of M_6C and $M_{23}C_6$. This result not only rules out the possibility of treating the problem as a single-phase diffusion process, but also rules out a simple diffusion-controlled moving boundary model.

The decarburization process is superimposed on the thermal aging process, and the kinetics of these two processes cannot be separated. When aging and decarburization begin, $M_{23}C_6$ and M_3C in the pearlite colonies are essentially the only carbides present, although Mo_2C is beginning to form in the proeutectoid ferrite.[67,68] The M_3C, Mo_2C, and much of the $M_{23}C_6$ are unstable; given enough time they will be replaced by M_6C. For whatever reason — less stability, favorable kinetics, or the the smaller amounts formed — the Mo_2C and M_3C are quickly replaced (essentially gone by 26,500 hr). Furthermore, the amount of carbide present in the center region of the sodium-exposed specimen, though greater than in the region near the surface, is less than that present in the helium-exposed specimen, an indication that decarburization has already (in less than 26,500 hr) affected the entire specimen.

From these limited observations, it appears that a kinetic diffusion model is, *at least*, one of a double moving boundary. That is, the first boundary moves through the specimen and lowers the amount of carbon and carbide; perhaps this moving boundary is accompanied by the decomposition and transformation of Mo_2C and M_3C. Although this boundary was not detected in our studies, its existence is indicated by the fact that the carbon and carbide concentrations of the specimen center have been reduced. This is followed by a second moving boundary that was detected in our experiments and differentiates the relative amounts of $M_{23}C_6$ and M_6C.

If the region near the surface with approximately 11% $M_{23}C_6$ is at equilibrium, then when this zone encompasses the entire specimen decarburization ceases. If this region is not at equilibrium, perhaps another moving boundary, not established by our studies, will move in.

In any event, our results, limited as they were by the lack of specimens between 0 and 26,500 hr, can only begin to suggest the complicated nature of the decarburization mechanism at 566°C.

Although these results are not directly applicable to an LMFBR steam generator that operates at a maximum temperature of 510°C (950°F), these specimens were exposed to sodium for a longer period of time and a lower temperature than in any previously reported results for 2 1/4 Cr-1 Mo steel. As such, these results should, assuming no mechanism change, offer the best estimate presently available as to the behavior of this material after prolonged periods of time (>100,000 hr) at 510°C.

It is of interest to speculate on the effect that decarburization and aging will have on the creep of 2 1/4 Cr-1 Mo steel. According to Irvine et al.,[69] possible creep-strengthening mechanisms in steel include: solid solution hardening, grain size, precipitation hardening involving coherent precipitates, and dispersion hardening involving noncoherent precipitates. Glen and Murray[70] have shown that for ferritic steels grain size has a negligible effect on creep strength. Baker and Nutting[68] have shown that Mo_2C has the largest effect on creep strength, probably because it initially forms coherently. As the Mo_2C is replaced by large globular particles of M_6C and $M_{23}C_6$, the strength will accordingly decrease. Since the dispersion strengthening afforded by such carbide particles is slight, their loss due to decarburization should only slightly lower the creep strength of the decarburized steel relative to the aged material that contains more such particles.

For long-time thermal and sodium exposures, the effect of precipitation on solid-solution strengthening may prove most important. As seen in Table 5.23, approximately 70 and 80% of the molybdenum has been removed from solid solution by precipitate formation in the sodium- and helium-exposed specimens, respectively; smaller percentages of chromium were removed. For binary iron alloys, Austin et al.[71] have shown that molybdenum is by far the most effective element in its ability to impart solid-solution strengthening (the effect of chromium above 0.75 wt % is minimal).

As a result of the above discussion, it would be expected that with prolonged thermal aging, the M_6C, which replaces the $M_{23}C_6$, coarsens, and its ability to dispersion strengthen the steel decreases. Simultaneously, the loss of molybdenum from the solid solution to the molybdenum-rich M_6C will further lower the creep strength, and in the extreme, the decarburized steel — or a low-carbon starting material — may eventually have a strength advantage.

5.4.4 Fatigue Behavior of 2 1/4 Cr-1 Mo Steel — C. R. Brinkman, M. K. Booker, and J. P. Strizak

Fatigue testing of 2 1/4 Cr-1 Mo steel in the annealed condition continued over the range room temperature to 538°C (1000°F). The objectives of this effort are to collect (1) sufficient continuous low- and high-cycle fatigue data to establish ASME design curves for this material, (2) sufficient hold time and frequency variation data to formulate creep-fatigue design rules, (3) adequate data covering the influence of material melting practice, heat treatment, and chemical or minor cold-work (heat-to-heat) variations, and (4) data covering other effects, such as aging, mean stress, environment, notch behavior, crack growth rates, and biaxiality. Considerable data have been collected in support of the first objective, and progress in this area will be discussed in detail in this report. Tests presently under way will fulfill the second objective, and results from these tests along with results from subcritical crack growth tests will be discussed in detail in subsequent quarterly progress reports.

Details concerning specific materials, heat treatments, specimen designs, and test methods have been discussed previously.[72] Results reported herein were obtained from three test laboratories: Mar-Test, Battelle Memorial Institute — Columbus, and Oak Ridge National Laboratory.

Additional strain- and load-controlled data were obtained by courtesy of General Atomic Company.[73] The chemical composition of the material tested in the GA program is compared with the ORNL heat (20017) in Table 5.25.

Tensile data obtained as a result of the GA effort, heats 1, 2, and 3, are compared with data obtained on the ORNL heat (heat 20017) in Fig. 5.75.

Table 5.25. Chemical Analysis of the 2 1/4 Cr-1 Mo Steel

Product Form	Heat	Chemical Composition, wt %								ASTM Grain Size
		C	Mn	Si	Cr	Mo	Ni	S	P	
Plate	20017	0.135	0.57	0.37	2.2	0.92	0.16	0.016	0.012	4–5
Pipe	1	0.145	0.53	0.40	2.18	0.94	0.30	0.019	0.014	7–8
Pipe	2	0.11	0.47	0.35	2.89	0.96	0.26	0.009	0.013	4–5
Pipe	3 (27479)	0.11	0.35	0.23	2.42	0.92	0.04	0.025	0.008	7–8

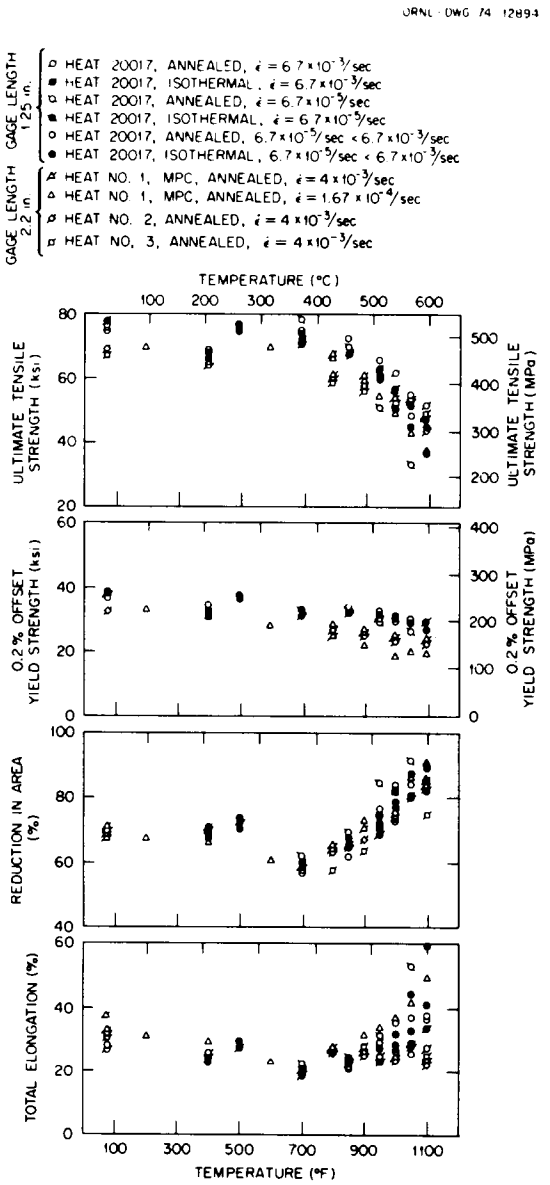

Fig. 5.75. Tensile Properties of 2 1/4 Cr-1 Mo Steels Tested. Gage lengths are 31.8 and 55.9 mm.

Generally, good agreement was found in comparing the tensile properties for the several heats and heat treatments reported in Fig. 5.75. Results of fatigue tests, both strain and load controlled, obtained from heat 20017 and the GA heats are compared in Figs. 5.76 through 5.79 with data obtained from the literature. The data are plotted as total strain range versus cycles to failure. Approximate strain range values for the load-controlled tests were determined from cyclic stress-strain curves or by simply dividing the stress range by the dynamic Young's modulus, for the high-cycle-to-failure tests. Converting stress ranges to strain

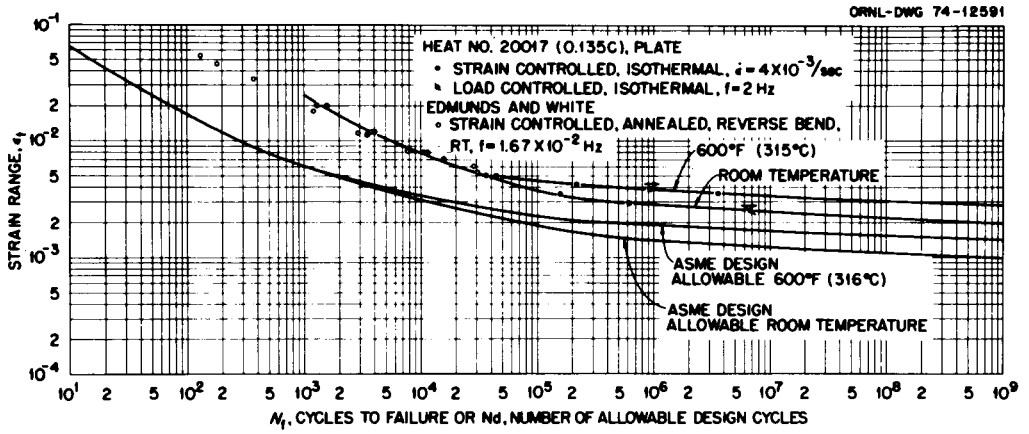

Fig. 5.76. Construction of Proposed ASME Code Allowable Fatigue Curves Based on Strain-Controlled Data at Room Temperature and 315°C (600°F) for 2 1/4 Cr-1 Mo steel isothermally annealed.

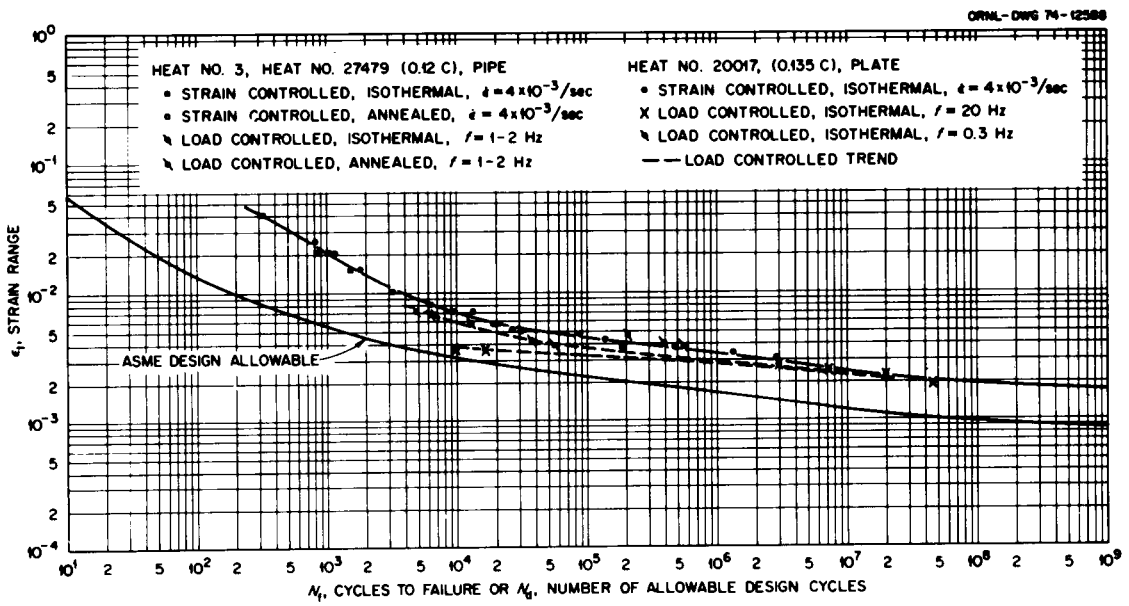

Fig. 5.77. Construction of Proposed ASME Code Allowable Fatigue Curve Based on Strain-Controlled Data at 427°C (800°F) for 2 1/4 Cr-1 Mo steel in the annealed and isothermally annealed conditions.

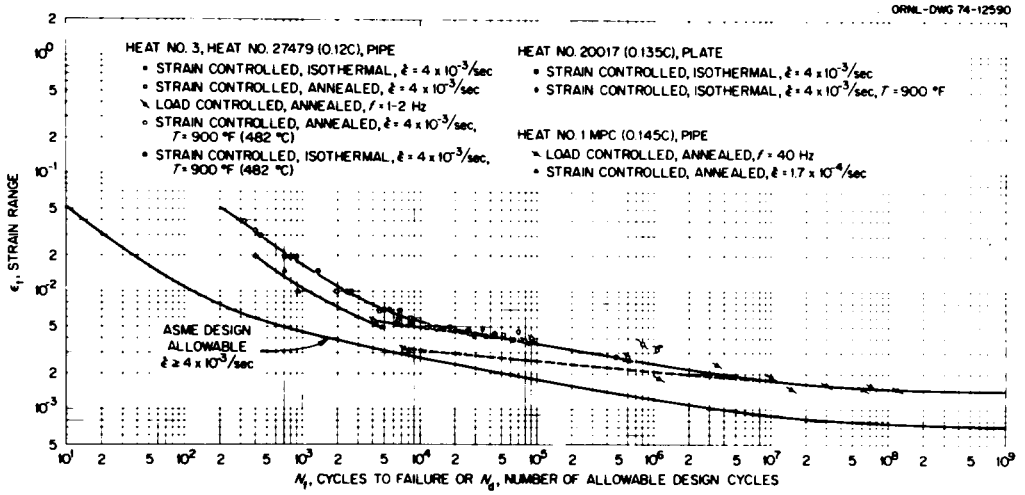

Fig. 5.78. Construction of Proposed ASME Code Allowable Fatigue Curve Based on Strain-Controlled Data at 482 to 538°C (900–1000°F) for 2 1/4 Cr-1 Mo steel in the annealed and isothermally annealed conditions.

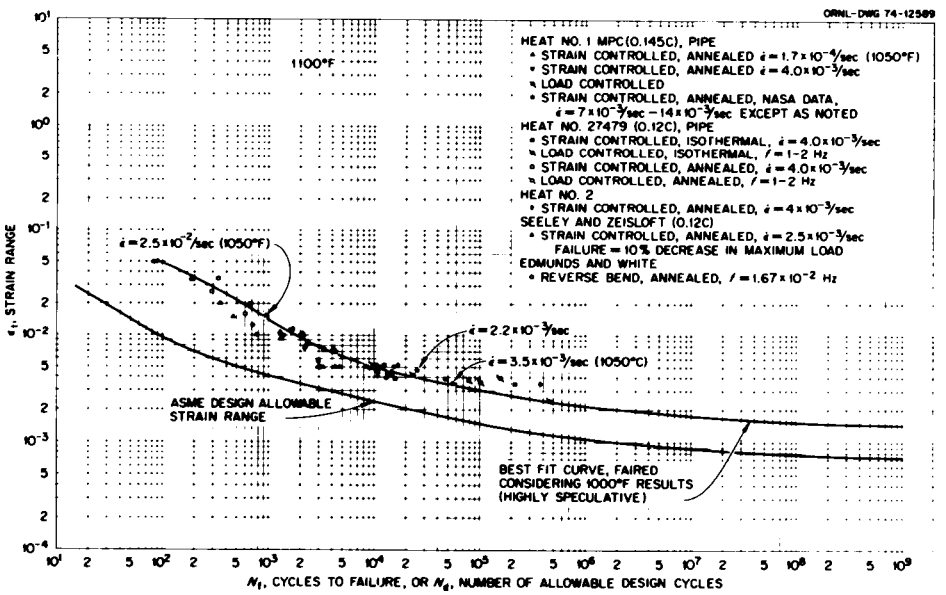

Fig. 5.79. Construction of Proposed ASME Code Allowable Fatigue Curve Based on Strain-Controlled Data at 593°C (1100°F) for 2 1/4 Cr-1 Mo steel in the annealed and isothermally annealed conditions.

ranges within the low-cycle range by these techniques is questionable because of the measureable amounts of plasticity[72] and for reasons that will be discussed. Graphically constructed best-fit lines were drawn through the strain-controlled data points and faired into the high-cycle load-controlled data in Figs. 5.77 and 5.78. From these plots, possible ASME design curves were constructed, using factors of safety of 2 on strain range or 20 on cycles to failure, depending upon which gave the most conservative results. These curves are shown in Figs. 5.76 through 5.78.

Additional testing of heat 20017 at 315°C (600°F) has continued to confirm the previously reported observation that in the high-cycle region at this temperature the fatigue behavior of this material is superior to that of room-temperature-tested material, as shown in Fig. 5.75. This has tentatively been attributed to the strain aging behavior, as shown by some of the tensile properties (ultimate tensile strength and ductility) in Fig. 5.75 over the temperature range of about 315 to 427°C (600–800°F). Additional fatigue testing at several different strain rates will be conducted in an effort to more fully define this temperature interval.

Comparing the strain-controlled cyclic lives of the annealed and isothermally annealed material, heat 3, in Figs. 5.77 and 5.78, we see that, based on existing data, little difference in lifetime is presently apparent from these heat treatment variations. However, differences in cyclic stress-strain behavior do occur, and variations in lifetimes are apparent when the materials are tested in load control. In Fig. 5.80, comparisons are made between the cyclic stress-strain curves for heat 20017 in the isothermally annealed condition and heat 3 in both the annealed and isothermally annealed conditions. Figure 5.80 shows that heat 3 material in the isothermally annealed condition cyclically hardens to higher values of stress than does the annealed material when subjected to strain-controlled loading. Thus in strain control higher loads were required to achieve the programmed strain range for the isothermally annealed material than for the same material in the annealed condition. Comparing the cyclic stress-strain response of the two heats in the isothermally annealed condition in Fig. 5.80 reveals that some heat-to-heat variations exist.

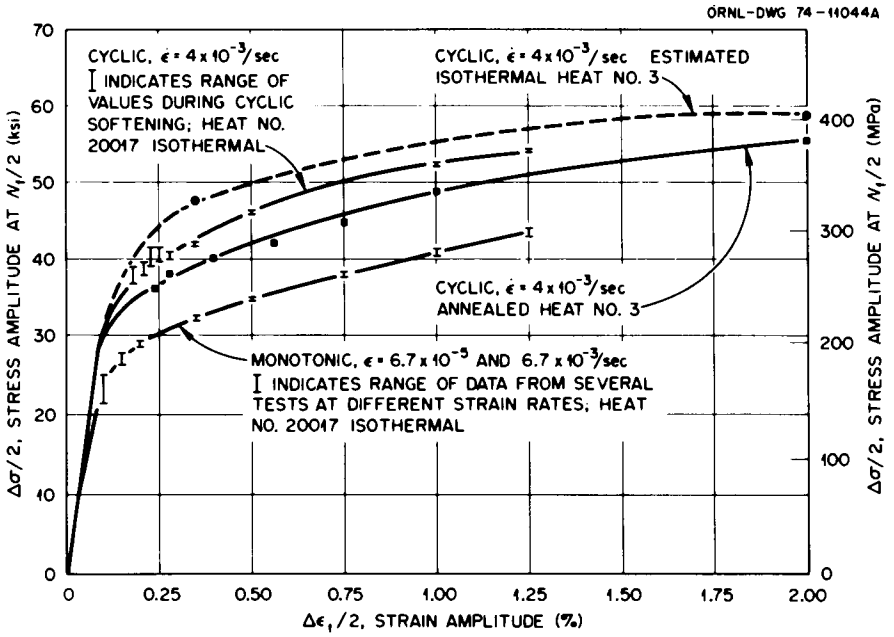

Fig. 5.80. Comparison of the Cyclic and Monotonic Stress-Strain Curves for 2 1/4 Cr-1 Mo Steel Isothermally Annealed and Annealed at 427°C (800°F).

Portions of the cyclic stress-strain curves for these materials were found to obey a simple expression of the form

$$\Delta\sigma/2 = A(\Delta\varepsilon_p/2)^n ,$$

where $\Delta\sigma/2$ and $\Delta\varepsilon_p/2$ are the stress amplitudes and plastic strain amplitudes, respectively, taken at half the cyclic life ($N_f/2$). The constants A and n depend on material, temperature, and strain rate. Isothermal plots of the data on log-log coordinates are shown in Fig. 5.81. Differences in cyclic stress-strain response between the annealed and isothermally annealed material are again apparent for heat 3 particularly at 593°C (1100°F).

It was previously stated that, from the available data, differences in the strain-controlled fatigue life of 2 1/4 Cr-1 Mo in the annealed or isothermally annealed condition appeared to be small in strain control However, in load control, over the temperature range 427 to 593°C (800–1100°F), from results of tests conducted on heat 3, material in the isothermally annealed condition clearly shows a superior fatigue resistance

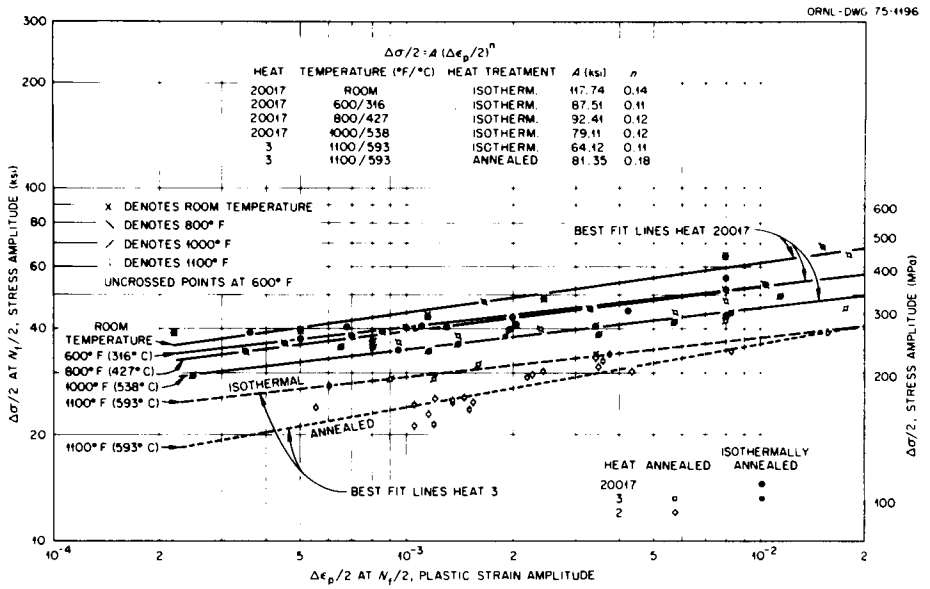

Fig. 5.81. Stress Amplitude as a Function of Plastic Strain Amplitude for Several Heats of 2 1/4 Cr-1 Mo Steel.

over that of the annealed material. This effect is shown for a single temperature, 427°C (800°F), in Fig. 5.82. The reason for the increased fatigue life of the isothermally annealed material in load control was attributed to the difference in cyclic hardening behavior. Figures 5.80

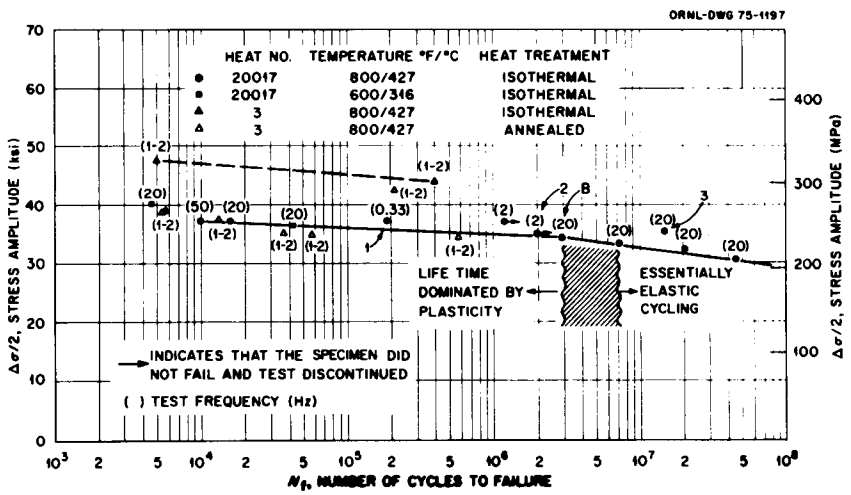

Fig. 5.82. Results of a Number of Load-Controlled Fatigue Tests Conducted on 2 1/4 Cr-1 Mo Steel in the Annealed and Isothermally Annealed Conditions. Region where cyclic lifetime was postulated to be influenced by plasticity variations is indicated for material in the isothermally annealed condition.

and 5.81 show that for a given stress the isothermally annealed material develops less plastic strain than does material in the annealed condition. It should also be mentioned that comparisons of behavior with respect to fatigue life for this material in the above heat treatments has only been possible for test conditions that allowed considerable amounts of plasticity (i.e., essentially low-cycle behavior). Figure 5.82 also illustrates why only the very high-cycle load-controlled data were used in formulating the design curves given in Figs. 5.77 and 5.78. That is, load control test results generated at stress levels high enough to induce considerable amounts of plasticity are complicated by a number of factors such as increased sensitivity to stress level, variable plastic strain history,[72] and possibly strain rate effects.

The strain histories developed during several of the load-controlled tests were monitored with extensometers and identified as tests 1 and 2 in Fig. 5.82. Strain ranges at the start of the test and after hardening (apparent stabilization) were recorded and are shown in Table 5.26. Figure 5.82 also indicates a break point (B) in the plot of stress amplitude versus cycles to failure at about 34 ksi (234 MPa), namely, bilinearity of the solid line. This stress level is roughly equal to a cyclic proportional limit, as indicated in Fig. 5.80 for the 427°C (800°F) test results. That is, above this stress level the results of load-controlled fatigue tests would be expected to be heavily dominated by the variable strain history typified by the results given above. The relatively high strain ranges at the start of a load-control test in

Table 5.26. Strain Ranges During Load-Controlled Tests

Test	Stress Amplitude		Strain Range, %	
	(ksi)	(MPa)	At Start	After Hardening
1	±37	255	0.57	0.33
2	±35	241	0.38	0.29
3	±35	241		0.26[a]

[a]Essentially elastic behavior after hardening.

comparison with the values after hardening would be expected to be particularly damaging since they would increase crack nucleation rates. For this reason one would expect that a good correlation between strain- and load-controlled test results is not possible above this stress level. The stress level indicated as an approximate proportional limit is not a unique value, since it could show variability resulting from strain rate, temperature, material condition, etc.; hence, a transition region is shown in Fig. 5.82. Hopefully, the above dialogue makes the point that extensometry must be used somewhat in load-controlled fatigue testing to determine the amount of plasticity present and its variability throughout a given test.

Curve fitting of the proposed ASME design curves given in Figs. 5.76 through 5.79 was attempted, and after some smoothing of the curves the following fourth-order polynomial equations were developed:

Room Temperature:
$$\ln \Delta\varepsilon_t = 2.2570503 \times 10^{-5}(\ln N_d)^4 - 1.7928118 \times 10^{-3}(\ln N_d)^3 + 5.8594084 \times 10^{-2}(\ln N_d)^2 - 0.93764977(\ln N_d) - 0.85908496$$

315°C (600°F):
$$\ln \Delta\varepsilon_t = 5.9002882 \times 10^{-6}(\ln N_d)^4 - 1.2723641 \times 10^{-3}(\ln N_d)^3 + 5.5791674 \times 10^{-2}(\ln N_d)^2 - 0.93906408(\ln N_d) - 0.84242872$$

427°C (800°F):
$$\ln \Delta\varepsilon_t = 7.1025782 \times 10^{-5}(\ln N_d)^4 - 4.2456055 \times 10^{-3}(\ln N_d)^3 + 9.8994513 \times 10^{-2}(\ln N_d)^2 - 1.1731638(\ln N_d) - 0.59251023$$

483–538°C (900–1000°F):
$$\ln \Delta\varepsilon_t = 1.2994144 \times 10^{-4}(\ln N_d)^4 - 6.851785 \times 10^{-3}(\ln N_d)^3 + 0.13744621(\ln N_d)^2 - 1.3912736(\ln N_d) - 0.36894722$$

593°C (1100°F):
$$\ln \Delta\varepsilon_t = 7.0069257 \times 10^{-5}(\ln N_d)^4 - 3.9097709 \times 10^{-3}(\ln N_d)^3 + 8.8212889 \times 10^{-2}(\ln N_d)^2 - 1.0594719(\ln N_d) - 1.2561289$$

The above equations are mathematically applicable over the range of: $10^2 \leq N_d \leq 5 \times 10^8$.

As was mentioned previously, fatigue hold time and strain rate tests are currently under way to formulate the required design creep-fatigue relationships. One of the techniques that will be used for correlating the data will be the method of strain range partitioning proposed by Manson et al.[74] The width of the fully reversed hysteresis loops or plastic strain range, $\Delta\varepsilon_p$, of tests conducted at a high enough strain rate to exclude creep damage is $\Delta\varepsilon_{pp}$. These values, along with plastic strain range values determined from hysteresis loops containing periods of relaxation (creep damage), are used in formulating the predictive equations used in damage summation. The $\Delta\varepsilon_{pp}$ values determined from the continuous cycling fatigue tests conducted to date are plotted as a function of cyclic life in Fig. 5.83. All data collected within the temperature range 427–593°C (800–1100°F) were included since creep can

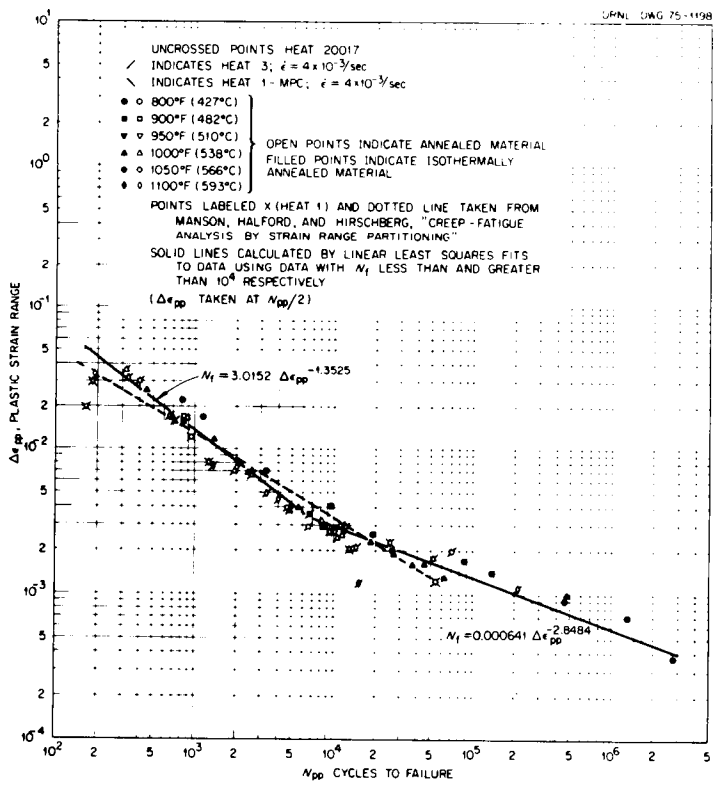

Fig. 5.83. Plastic Strain Range Versus Cycles to Failure for 2 1/4 Cr-1 Mo Steel.

occur over this interval. Best-fit lines were determined for only the data collected at strain rates greater than 2×10^{-3}/sec, and the results are compared with the best-fit line established by Manson et al.[74] for 593°C (1100°F). Good agreement is apparent in the low-cycle regime. However, the line established by Manson et al. does not reflect bilinearity due to cyclic softening at low strain ranges, as was found from the recent test results.[72]

5.4.5 Mechanical Properties Correlations of 2 1/4 Cr-1 Mo Steel for LMFBR Steam Generators — M. K. Booker and T. L. Hebble*

The effort to develop mechanical properties correlations of 2 1/4 Cr-1 Mo steel for input to the *Nuclear Systems Materials Handbook* (NSMH) continues. Volume I of the NSMH is to include actual results of correlations (i.e., mathematical models and corresponding tolerance limits). Volume II is to include backup information, including data base and methods of analysis. For both Volumes I and II we have completed and submitted documents for time to tertiary creep (0.2% offset), true fracture stress, and diamond pyramid hardness. In addition, correlations for Charpy impact energy and ductile-brittle transition temperature (DBTT) are now under way. All results are expressed in both English and SI units, but only the models in English (engineering) units will be presented here.

A model for time to tertiary creep was presented earlier.[75] This previous model described available data well but exhibited unreasonable results outside the range of data. However, for design applications, it is desirable to be able to estimate times to tertiary creep in the low-temperature low-stress region from available test data. Such extrapolations can, of course, be dangerous and misleading, but their use is essential. With these requirements in mind, a new model for time to tertiary creep has been developed. It (1) is consistent with existing data and (2) estimates reasonable and conservative results outside the range of data (see Fig. 5.84). These criteria have been met by a model of the form

---

*Mathematics Research Staff.

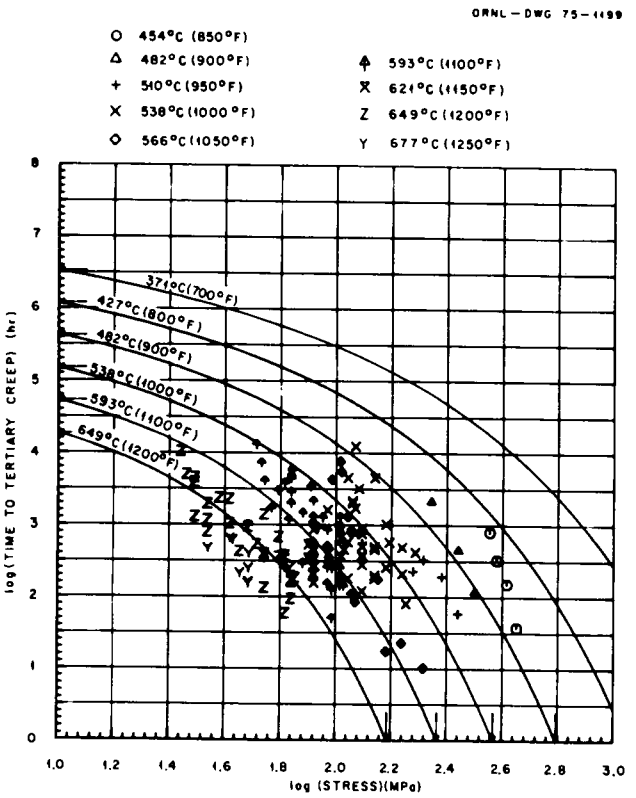

Fig. 5.84. Time to Tertiary Creep for 2 1/4 Cr-1 Mo Steel.

$$\widehat{\log t_3} = b_0 + b_1 \log \sigma + b_2 T + b_3 (10)^{(T \log \sigma / 1000)}$$

where $\widehat{\log t_3}$ = expected value of time to tertiary creep (hr)

σ = stress, ksi

T = temperature, degrees Rankine

$b_0 = 18.94 \pm 1.7$

$b_1 = -3.15 \pm 0.57$

$b_2 = -0.00805 \pm 0.00083$

$b_3 = -0.00370 \pm 0.0024$

Although this model yields "reasonable" results over a wide range of conditions, it is suggested that it be applied within the following bounds:

$$1160°R \leq T \leq 1560°R, \ \sigma < 40 \text{ ksi}, \text{ and } t_3 < 50{,}000 \text{ hr}.$$

To provide a check of the effectiveness of the above model, several "standard" models have been applied to the same data base. Table 5.27 illustrates the results of such comparisons among the above NSMH model; the Manson-Succop, Orr-Sherby-Dorn, and Larson-Miller time-temperature parameters; and the minimum commitment method.

The above model for time to tertiary creep serves both as a measure of useful service life and as a time limit on the previously reported[76] creep equation for 2 1/4 Cr-1 Mo steel. This latter equation is of the form

$$\varepsilon_c = t(A + Bt) + Ct \ ,$$

where ε_c = creep strain (%), t = time (hr), A,B,C = empirical constants. The equation contains a transient primary term and a steady-state secondary term, which continues in a straight line to infinite times. Clearly, this equation is valid only until tertiary creep begins. Thus, the model for time to tertiary creep provides the needed limit to the extrapolation of the creep equation.

The previously reported model for Bridgman-corrected true fracture stress[75] has remained unaltered. However, it is recognized that the properties of 2 1/4 Cr-1 Mo, which exhibits strain aging, might be somewhat dependent on strain rate.

Many of the properties of 2 1/4 Cr-1 Mo steel give indications that the material undergoes strain aging effects. These indications include: (1) the increase in high-cycle fatigue life seen[77] at 316°C (600°F), and (2) increases in yield strength and ultimate tensile strength, accompanied by decreases in ductility, between 316 and 427°C (600–800°F).

If strain aging effects are important, the tensile properties should be somewhat strain-rate dependent. Since such variations have been noted[78] (see Fig. 5.67 of this report), the previously reported model for Bridgman-corrected true fracture stress[75] has been examined for possible strain rate effects. However, no systematic trends have been found, and the previous model has been submitted unchanged.

Table 5.27. Time to Tertiary Creep for 2 1/4 Cr-1 Mo Steel Estimated by Various Models

Temperature (°F)	Stress (ksi)	Time, hr, to Tertiary Creep, Estimated According to				
		MCM	Manson-Succop	ORNL-NSMH	Orr-Sherby-Dorn	Larson-Miller
700	10	1,830,000,000,000,000	4,290,000	2,500,000	60,300,000	83,600,000
	20	802,000,000,000,000	234,000	242,000	3,220,000	1,810,000
	30	437,000,000,000,000	42,300	57,300	494,000	199,000
	40	268,000,000,000,000	13,300	19,400	125,000	45,900
800	10	347,000,000	562,000	380,000	2,100,000	2,650,000
	20	47,300,000	30,700	34,500	112,000	77,900
	30	10,900,000	5,540	7,500	17,200	10,200
	40	3,340,000	1,740	2,310	4,360	2,650
900	10	156,000	76,400	57,200	126,000	147,000
	20	11,900	4,180	4,740	6,730	5,590
	30	1,780	754	915	1,030	851
	40	388	237	244	262	243
1000	10	9,120	10,000	8,520	10,600	11,600
	20	560	548	624	568	552
	30	72	99	101	87	96
	40	14	31	22	22	30
1100	10	1,330	1,360	1,250	1,280	1,310
	20	71	74	77	68	76
	30	8	13	10	10	15
	40	1	4	1	3	5
	ΣR^2	23.85	24.58	24.48	24.56	
	ν		5	4	5	

The previously established correlation between room-temperature ultimate tensile strength and diamond pyramid hardness number has been revised. The new model, which has been submitted to the NSMH, is given by

$$\hat{H} = 5.4 + 2.14\tau \ ,$$

where $\hat{H}$ = expected value of diamond pyramid hardness number,

τ = room-temperature ultimate tensile strength (ksi).

In addition to the above correlations, the variations in Charpy impact energy with temperature for 2 1/4 Cr-1 Mo steel are being investigated. A model for this behavior would then permit an estimate of ductile-brittle transition temperature (DBTT). No data for the impact properties of annealed 2 1/4 Cr-1 Mo have been found in the literature. However, some such data have been obtained from ORNL[79] and from General Atomic Corporation (GA).[80] The ORNL data include sets on four different heat treatments of one heat, and two heat treatments of another heat of material. The GA data include one set on each of three heats of material. Thus, a total of nine sets of data is available.

All these nine sets of data display widely differing properties, making the description of general behavior with one model somewhat difficult. As a result, the nine data sets are currently being analyzed separately with a model of the form

$$Y = A\left[1 - e^{-B(T - C)^2}\right] \ ,$$

where Y = a function of impact fracture energy,

T = temperature, and

A, B, C = constants estimated from the data by method of least squares.

(A transformation of impact energy may be necessary to stabilize the variance.) Note that in this model the constant A corresponds to an upper shelf energy. The constant C corresponds to a temperature at which impact

energy is zero. This situation is of course a false one since impact energy is always positive. However, impact energy does approach very low values at low temperatures, and for practical purposes of fitting data may be considered to become zero as long as C is taken as the lower bound on the applicable temperature range of the model. Additional work will continue on the establishment of an acceptable model for Charpy impact energy.

5.4.6 Mechanical Properties of Weld-Overlaid Stainless Steel — R. L. Klueh

We previously reported[81–83] on the creep-rupture behavior of the type 304 stainless steel forging that had been overlaid with type 308 stainless steel weld metal. Tests were made at 482 and 593°C (900 and 1100°F). From the forging, specimens were taken from the axial, radial, and tangential orientations, and specimens from the overlay and from the forging immediately adjacent to the fusion line were taken in the radial and tangential orientations. We have now conducted tests at 538°C (1000°F) on all types of specimens and from each of various locations in the overlaid forging. The results are given in Tables 5.28, 5.29, and 5.30 for the forging, forging immediately adjacent to the fusion line, and overlay, respectively.

In Fig. 5.85 the results are shown for axial, radial, and tangential specimens taken from the forging; there appears to be no effect of orientation, either on the rupture life [Fig. 5.85(a)] or minimum creep rate [Fig. 5.85(b)]. Likewise, orientation does not affect the properties of the specimens taken near the interface (Fig. 5.86). For the type 308 stainless steel shown in Fig. 5.87, rupture life shows a slight orientation effect [Fig. 5.87(a)], but the minimum creep curve appears unaffected. In general, these results relative to orientation are similar to those previously found[81,82] at 593°C (1100°F).

We are presently testing axial composite specimens in creep rupture at 538°C (1000°F). These specimens, which were taken from across the fusion line, contain both weld metal and forging in the gage section. During the next quarter, these tests should be completed, and with the exception of a few continuing long-time tests, our experimental studies on the overlaid forging should be complete.

Table 5.28. Creep-Rupture Properties of Type 304 Stainless Steel Forging at 538°C (1000°F)

Stress (ksi)	Stress (MPa)	Rupture Life (hr)	Elongation (%)	Reduction of Area (%)	Minimum Creep Rate (%/hr)
		Axial Specimens			
60	414	50.0	33.7	28.2	0.33
58	400	83.6	31.9	29.1	0.03
55	379	193.3	27.0	24.5	0.0069
50	345	964.7	16.2	16.2	0.00129
48	331	a			
		Tangential Specimens			
58	400	119.5	26.4	22.4	0.0109
55	379	207.4	21.9	24.1	0.005
48	331	1197.1	14.9	16.8	0.002
		Radial Specimens			
58	400	105.5	30.6	21.3	0.00833
55	379	197.9	27.0	21.8	0.005
48	331	689.8	19.1	25.2	0.0018
48	331	a			

[a]Test in progress.

Table 5.29. Creep-Rupture Properties of Type 304 Stainless Steel Forging Adjacent to the Fusion Line at 538°C (1000°F)

Stress (ksi)	Stress (MPa)	Rupture Life (hr)	Elongation (%)	Reduction of Area (%)	Minimum Creep Rate (%/hr)
		Tangential Specimens			
60	414	82.7	29.1	27.7	0.033
57.5	397	192.6	16.2	15.9	0.0084
55	379	457.5	13.8	13.2	0.00463
53	365	738.8	12.9	11.4	0.00258
50	345	1136.0	10.1	8.9	0.00143
		Radial Specimens			
60	414	77.5	27.0	23.9	0.0279
55	379	383.4	15.4	14.6	0.00464
53	365	621.5	14.1	13.7	0.00263
50	345	1501.7			

Table 5.30. Creep-Rupture Properties of Type 308 Stainless Steel Weld Metal at 538°C (1000°F)

Stress (ksi)	Stress (MPa)	Rupture Life (hr)	Elongation (%)	Reduction of Area (%)	Minimum Creep Rate (%/hr)
		Tangential Specimens			
50	345	100.7	34.6	34.7	0.075
45	310	303.0	21.8	30.6	0.0332
40	276	1377.0	17.2	26.0	0.00487
		Radial Specimens			
55	379	8.5	24.0	35.8	0.203
50	345	48.5	24.8	39.2	0.08
45	310	263.0	26.2	34.7	0.044
40	276	1176.0	15.3	25.1	0.00487

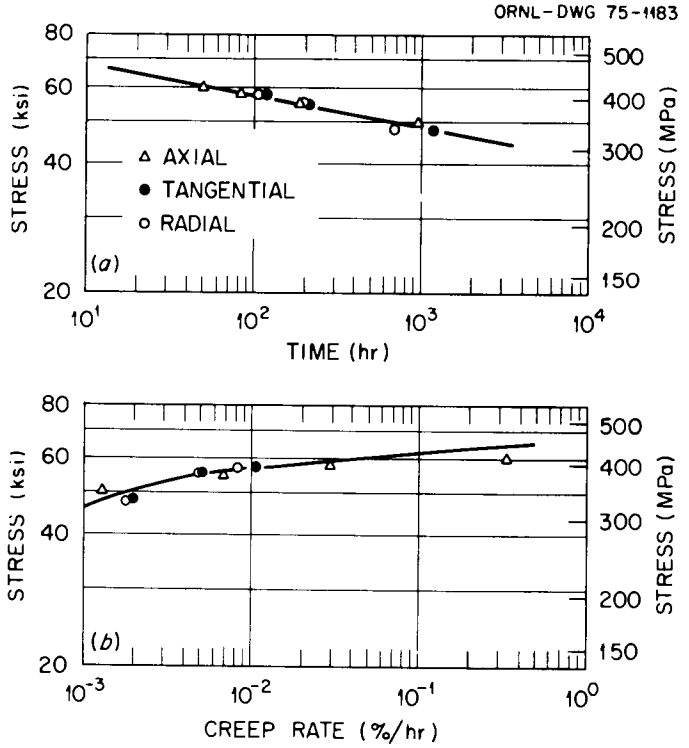

Fig. 5.85. Creep-Rupture Properties of Type 304 Stainless Steel Forging at 538°C (1000°F). (a) Rupture life. (b) Minimum creep rate.

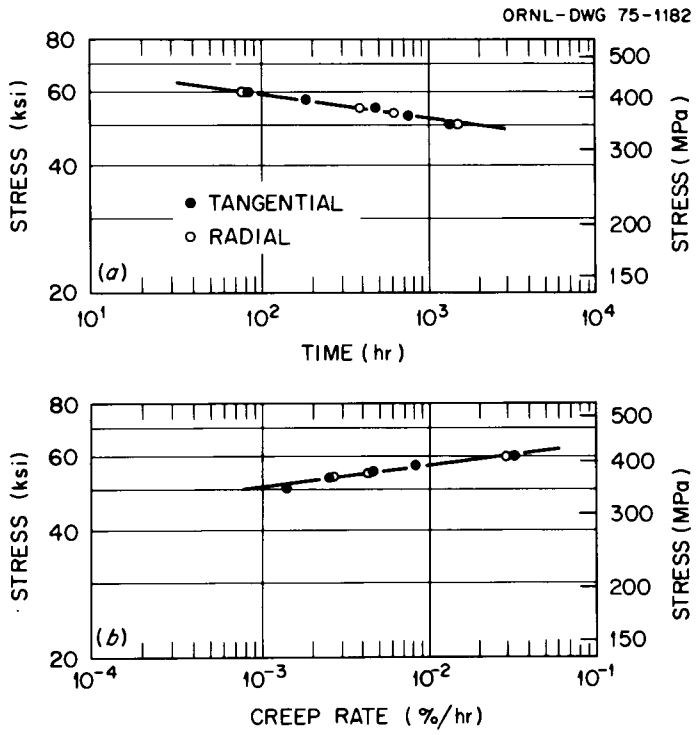

Fig. 5.86. Creep-Rupture Properties of Type 304 Stainless Steel Forging Adjacent to the Weld Overlay Fusion Line at 538°C (1000°F). (a) Rupture life. (b) Minimum creep rate.

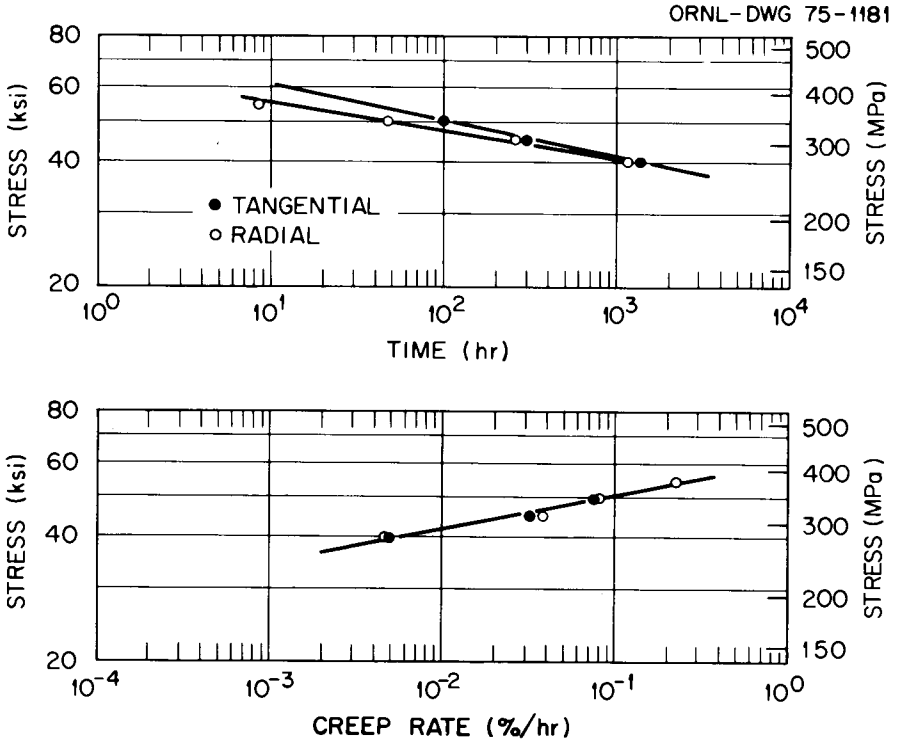

Fig. 5.87. Creep-Rupture Properties of Type 308 Stainless Steel Weld Overlay at 538°C (1000°F). (a) Rupture life. (b) Minimum creep rate.

5.5 HIGH-TEMPERATURE DESIGN — W. L. Greenstreet,* J. M. Corum,* and C. E. Pugh*

5.5.1 Exploratory Studies in Support of Structural Design Methods

5.5.1.1 Characterization of the Product Forms of the Reference Heat of Type 304 Stainless Steel — R. W. Swindeman and V. K. Sikka

Low-stress creep tests have been performed at 593°C (1100°F) on specimens machined from several product forms of the reference heat of type 304 stainless steel (heat 9T2796). Tests were at 15 and 12.5 ksi (103 and 86.2 MPa) and were continued for approximately 1000 hr. Creep curves for 15 ksi (103 MPa) are plotted in Fig. 5.88. Curves for 12.5 ksi (86.2 MPa) are shown in Fig. 5.89 and follow a pattern similar to the 15 ksi (103 MPa) curves.

Using creep data at 15 and 12.5 ksi (103 and 86.2 MPa), in addition to the high-stress creep data previously reported,[84] we hope to develop scale factors for normalizing the creep curves to account for product form variability. Hopefully, these factors can be used in conjunction with the creep law, being developed elsewhere,[85] to produce a fairly good representation for the creep behavior of each product form.

The status of the creep rupture tests for all product forms is given in Table 5.31. Depending on the results of our analysis, we may decide to repeat some of the tests that have been completed.

5.5.1.2 Creep Testing of 1-in. Plate of Type 304 Stainless Steel Heat 9T2796 — R. W. Swindeman

The evaluation of creep-rupture behavior is continuing on the 1-in. (25.4-mm) plate of the reference heat of type 304 stainless steel. The purposes for this effort are to characterize the material relative to other heats, to provide information for use in evaluating creep-fatigue data, and to form a basis on which to develop predictions of long-time strength and ductility. The results obtained by using several different time-temperature parameters to represent the minimum creep rate, time to tertiary creep, and time to rupture have been presented in earlier reports.[86,87]

---

*Reactor Division.

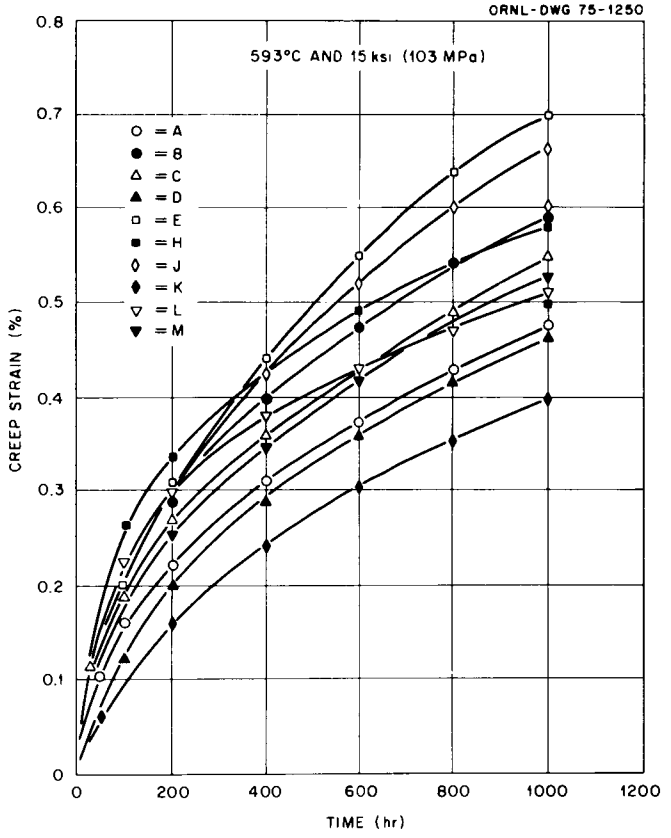

Fig. 5.88. Creep Curves for Different Product Forms (Designated by Letters as in Table 5.31) of Type 304 Stainless Steel (Heat 9T2796). All specimens were reannealed at 1093°C (2000°F) and tested at 15 ksi (103 MPa) and 593°C (1100°F).

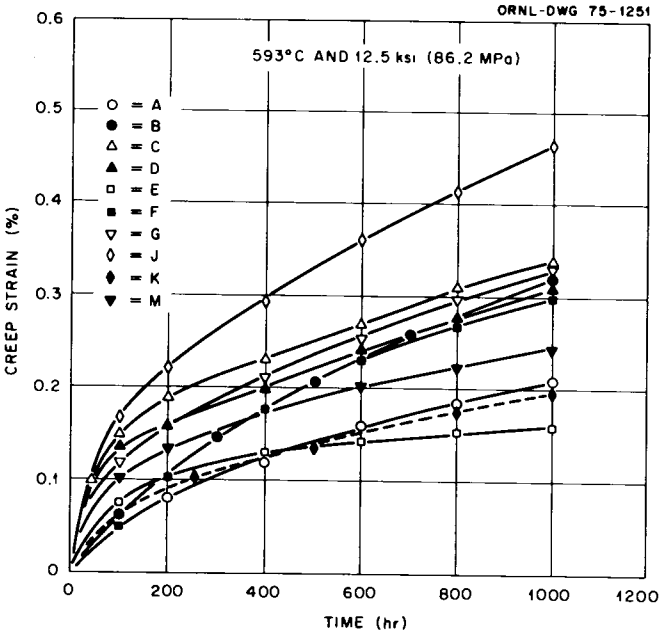

Fig. 5.89. Creep Curves for Different Product Forms (Designated by Letters as in Table 5.31) of Type 304 Stainless Steel (Heat 9T2796). All specimens were reannealed at 1093°C (2000°F) and tested at 12.5 ksi (86 MPa) and 593°C (1100°F). The curve labeled K was interpolated from data at 12 and 14 ksi (82.7 and 96.5 MPa).

Table 5.31. Status of Creep-Rupture Tests[a] on Different Product Forms of the Reference Heat of Type 304 Stainless Steel

Item	Form	Size[b] (in.)	Size[b] (mm)	Designation	Tests Completed
2	Plate	3/16	4.8	P	None
3	Plate	1/4	6.4	Q	None
4	Plate	3/8	9.5	L	(1), (2), (3), (4)
5	Plate	1/2	12.7	J	All
6	Plate	3/4	19	H	(1), (2), (3), (4)
7	Plate	1	25	M	All
8	Plate	2	51	K	All
10	Pipe	4 sched 160	102	B	All
11	Pipe	8 sched 80	203	A	All
15	Pipe	2 1/2 OD (CD)	64	D	All
51	Pipe	2 1/2 OD (HR)	64	C	All
17	Heads	24 ID	610		None
18	Bar	5/8 (HR)	16	R	(1), (2), (3)
19	Bar	1	25	T	(1), (2)
20	Bar	1 3/4	44	G	(1), (2), (3), (5)
21	Bar	1 7/8	48	F	(1), (2), (3), (5)
22	Bar	4 1/2	114	E	All
23	Bar	5/8 (CD)	16	S	(3)

[a]Tests at 593°C (1100°F) and (1) 35 ksi (241 MPa); (2) 30 ksi (207 MPa); (3) 25 ksi (172 MPa); (4) 15 ksi (103 MPa); (5) 12.5 ksi (86 MPa).

[b]CD = cold drawn; HR = hot rolled.

In this report we summarize the data on a strain-component basis. Following Ettenson and Manjoine,[88] the creep curves were divided into four strain components: plastic loading strains, transient strains, linear strains, and tertiary strains. These components are added in the sequence given above and plotted against the creep stress. Plots for eight temperatures are shown in Fig. 5.90.

At 482°C (900°F) the creep-rupture elongation is dominated by the plastic loading strain. The transient and linear creep components are quite small, and most of the time-dependent deformation is produced in

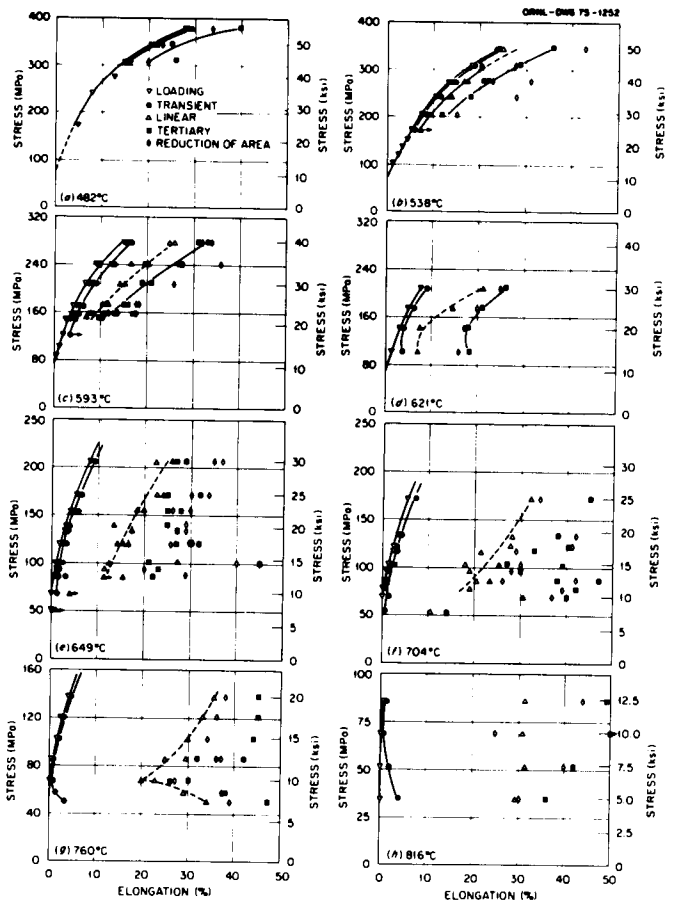

Fig. 5.90. Stress Versus Strain Component Diagrams for Type 304 Stainless Steel (Heat 9T2796).

the tertiary creep stage. As the testing temperature is increased, the creep stress is lowered, and, concomitantly, the plastic loading strains become less significant relative to the other strain components. The transient creep component, however, never constitutes a large portion of the creep-rupture elongation. It appears to be most significant at 593°C, where at the lowest stresses it approaches 20% of the rupture elongation. The linear creep component, on the other hand, becomes more significant as the temperature is increased and creep stress decreased. At 649°C (1200°F) and above, linear creep constitutes the largest component of the rupture elongation. Finally, the tertiary creep component is significant for most of the testing conditions, but the behavior is erratic with changing stress and temperature, and it is difficult to specify the general trend. The plastic loading strains, of course, may be

calculated from the model developed to represent the tensile curve for this material.[89] However, the calculation of the linear component requires a model for both the rupture life and the secondary creep rate since the linear component is defined to be the product of the two terms. Models for representing the creep rate and rupture life are being developed,[87] but the description of the stress and temperature dependencies of the primary creep component is still not available. This is not a major problem because the transient component is small relative to the rupture elongation. The transient component for this heat of material may be regarded at constant and near 1%, at least to a first approximation.

Although the transient creep component is not too important in developing a model for the "usable strain," it is essential to consider transient creep in developing a creep law to be used in the analysis of the results of tests on structures. Also important in this respect is the development of an understanding of how thermomechanical history influences the different components of creep. This is because most structures undergo stress and strain readjustments during testing, and most of the locations within the structure experience this varying thermomechanical history. The results of creep tests at 593°C (1100°F) on specimens precycled at room temperature are shown by the Ettenson-Manjoine plot in Fig. 5.91. Comparing Fig. 5.91 with Fig. 5.90(c) reveals that the precycling has slightly reduced the plastic loading and transient strain components. The linear strain component and rupture elongation, on the other hand, have been increased.

The Ettenson-Manjoine plot in Fig. 5.92 was obtained from tests on specimens prestrained in tension to 34,000 psi (234 MPa) at room temperature. The plastic loading and transient creep components at 593°C (1100°F) are generally less than those observed for reannealed material [Fig. 5.90(c)] and very close to values observed for precycled material (Fig. 5.91). The linear creep component and rupture elongation are extended, relative to reannealed material, in a way similar to the precycled material.

We reported[90] earlier that the 1-in. (25.4-mm) plate product form (Item 7) was not very sensitive to the reannealing temperature, but the

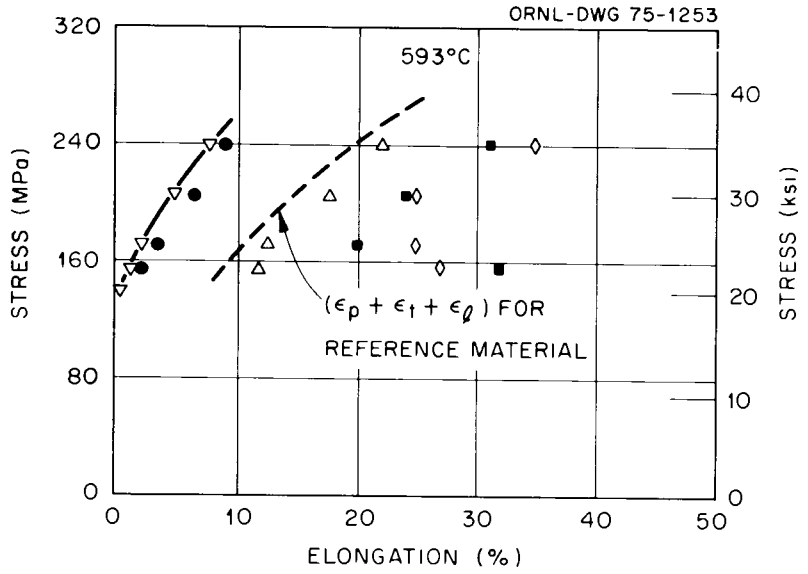

Fig. 5.91. Stress Versus Strain Component Diagram for Precycled Type 304 Stainless Steel (Heat 9T2796). Specimens were cycled at room temperature and 1% strain range to raise the yield strength to near 34 ksi (234 MPa). Curve for reference material is from Fig. 5.90(c), and point symbols are defined on Fig. 5.90.

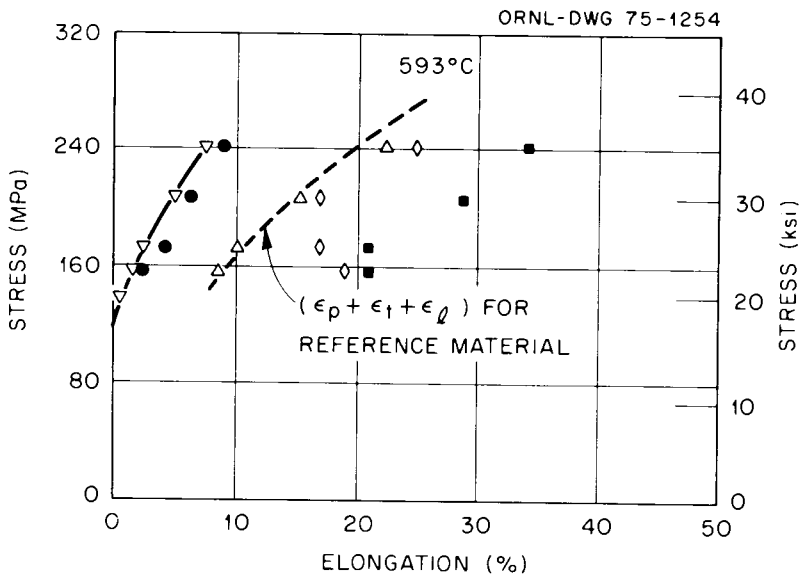

Fig. 5.92. Stress Versus Strain Component Diagram for Prestrained Type 304 Stainless Steel (Heat 9T2796). Specimens were strained at room temperature to raise the yield strength to near 34 ksi (234 MPa). Curve for reference material is from Fig. 5.90(c), and point symbols are defined on Fig. 5.90.

cooling rate after the annealing could be important. Water quenching small test bars increased the hardness, decreased the plastic loading strains, and had only slight influences on the creep curve. Furnace cooling, on the other hand, decreased the hardness slightly but greatly extended the rupture ductility. An Ettenson-Manjoine plot showing the strain components for 593°C (1100°F) illustrates this point. Comparison of Fig. 5.93 for the furnace-cooled material with Fig. 5.90(c) for the rapidly cooled material shows that the increase in the rupture strain develops primarily from an extension of the linear component. The rupture elongation is approximately doubled by the furnace cool. The reason for this is probably the same as that proposed by Garofalo[91] to explain the improvement in the creep life of type 316 stainless steel tested at

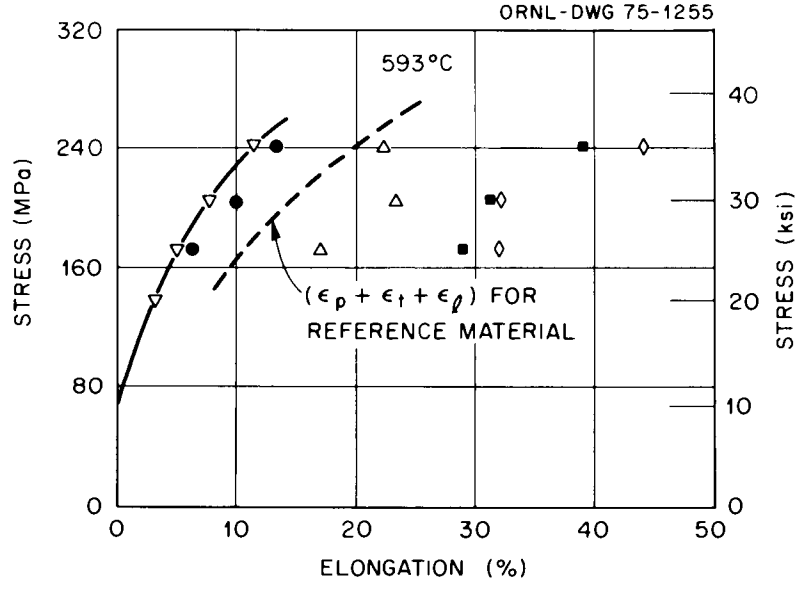

Fig. 5.93. Stress Versus Strain Component Diagram for Furnace-Cooled Type 304 Stainless Steel (Heat 9T2796). Specimens were cooled from 1093°C to room temperature over a period of 16 hr. Curve for reference material is from Fig. 5.90(c), and point symbols are defined on Fig. 5.90.

593°C (1100°F) after aging at 816°C (1500°F). This improvement is associated with the development of large carbide particles on grain boundaries. Although the linear strain component and rupture elongation have been extended by furnace cooling, the transient creep component and

minimum creep rate are about the same for furnace-cooled material as for conventionally cooled material. This suggests that it should be valid to use the mechanical behavior of conventionally cooled material in the analysis of test structures that have been slowly cooled. Extensive data regarding the influence of thermal aging on the mechanical behavior of type 304 stainless steel are being developed by Sikka and Brinkman;[92] this source shows that aging at 593°C and above often produces substantial increases in the creep rate as well as extensions in creep ductility.

5.5.1.3 Strain Cycling Tests on Type 304 Stainless Steel — R. W. Swindeman

Strain cycling tests were performed on two heats of type 304 stainless steel. The reference heat (heat 9T2796) was tested in the reannealed condition at several temperatures in the range from 427 to 649°C (800 to 1200°F). Emphasis was on testing at strain ranges of 1% or less.

Testing is still under way, especially at strain ranges below 0.4%. Eventually, we hope to develop a set of reference cyclic curves for temperatures in the range 427 to 649°C. These will be similar to the curves developed earlier[93] for 593°C (1100°F). It would be desirable to base the reference cyclic curves on a model that relates the cyclic stress range to cyclic strain range, cycle number, temperature, and strain rate. To this end, we are investigating the use of a "modified" Voce equation to represent the cyclic hardening rate. We assume that the cyclic stress range, $\Delta\sigma$, is related to the total accumulated strain, $\Sigma\varepsilon$, by the expression:

$$\Delta\sigma = (\Delta\sigma_i - \Delta\sigma_s)e^{-k_c\Sigma\varepsilon} + \Delta\sigma_s \ , \qquad (22)$$

where $\Delta\sigma_i$ is a constant related to the initial cyclic stress range, $\Delta\sigma_s$ is a constant related to the saturation stress range, and k_c is a constant that describes the rate of approach to $\Delta\sigma_s$. The constants can vary with cyclic strain range, temperature, and strain rate. The accumulated strain, of course, is given by the product $n\Delta\varepsilon$, where n is the cycle number and $\Delta\varepsilon$ is the strain range. In the temperature range from 427 to 538°C (800 to 1000°F), $\Delta\sigma_s$ is relatively insensitive to temperature at the

reference strain rate (0.005/min). The $\Delta\sigma_i$ values exhibit less dependence on $\Delta\varepsilon$ than the $\Delta\sigma_s$ values and fall slightly above the doubled monotonic curve. The dependence of $\Delta\sigma_i$ on temperature is also slight. Methods for evaluating k_c are being examined, but we have not decided on the best one. An example of a least squares fit by means of a computer is shown in Fig. 5.94 for a test at 482°C (900°F) and 1% strain range. As can be seen in the figure, the representation by the "modified" Voce relation is only an approximation to the real hardening behavior. In our current approach, for example, the constants are based on the use of the total strain range, $\Delta\varepsilon$, rather than the plastic strain range, $\Delta\varepsilon_p$. Further, it appears that the fit of the relation to the data could be improved if a fractional exponent is placed on the $\Sigma\varepsilon$ term. Data are insufficient to justify the use of such modifications at the present time. Liu,[94] however, uses the plastic strain for describing cyclic hardening in 2 1/4 Cr-1 Mo steel.

The modified Voce equation shows potential for representing the dependence of the cyclic stress range on accumulated strain. Further,

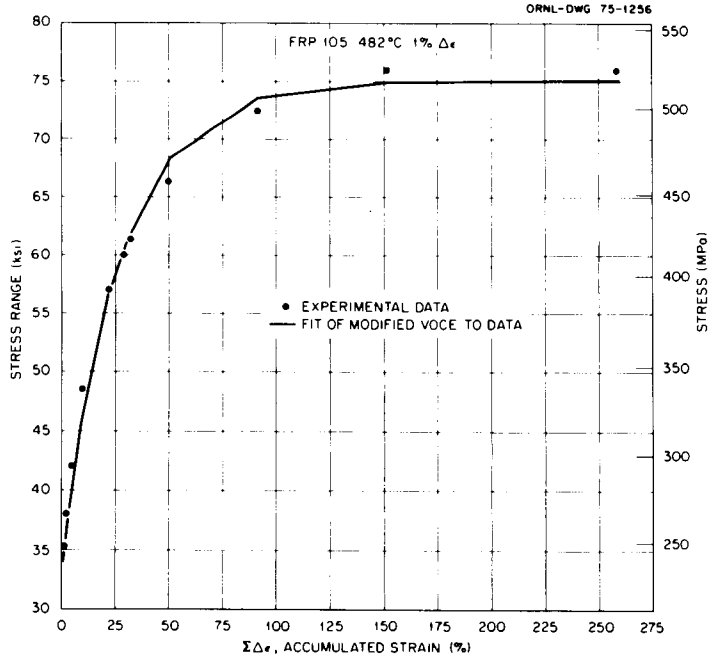

Fig. 5.94. Fit of a Modified Voce Relation to the Cyclic Hardening Behavior of Type 304 Stainless Steel (Heat 9T2796).

we can expect that, if the material is strained beyond the limits of the hysteresis loop, the subsequent tensile flow curve can be represented by the Voce model in its usual form. We remain interested, however, in developing an expression for the actual stress-strain behavior within the hysteresis loop. We are investigating the potential use of the Ludwigson[95] modification term. Ludwigson shows that, for monotonic tensile tests, the stress-strain behavior near the knee of the tensile curve is dominated by a term that has the form:

$$\sigma' = ae^{-k\varepsilon_p} , \tag{23}$$

where σ' is a stress component of the yield strength, which has the value a when yielding commences and decreases with increasing inelastic strain, ε_p, at a rate determined by the value of the constant k. This modification may be used in conjunction with the Voce equation in the following way: Consider the idealized test shown in Fig. 5.95. Suppose the material in

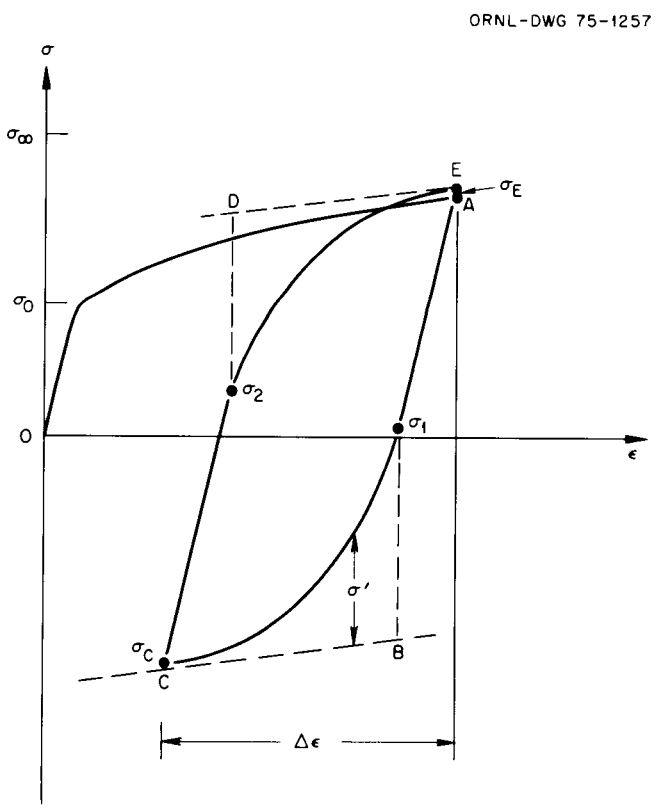

Fig. 5.95. Idealized Tensile Curve for Type 304 Stainless Steel.

the virgin condition shows Voce-type behavior. Then, the tensile curve should show abrupt yielding when the stress reaches σ_0. The flow curve would proceed along the solid line and approach the value σ_∞ according to the equation:

$$\sigma = (\sigma_0 - \sigma_\infty)e^{-\epsilon_p/\epsilon_c} + \sigma_\infty \ , \qquad (24)$$

where ϵ_c is a material constant. Suppose, however, that at point A on the curve a strain cycle is introduced over the strain range $\Delta\epsilon$. After elastic unloading and stress reversal, yielding might occur when the change in stress is less than, equal to, or greater than twice the initial yield stress, σ_0. At this point (σ_1), however, the yield curve departs dramatically from the bilinear behavior of virgin material and also at this point the Ludwigson modification becomes useful. Suppose the dashed curve B to C represents a portion of the Voce flow curve in compression. Then we assume that the stress difference between the actual hysteresis loop segment, σ_1 to σ_c, and the Voce curve, B to C, is given by the Ludwigson modification, Eq. (23). Similarly, the stress difference between the hysteresis segment (σ_2 to σ_E) and the segment D to E can be described by a relation such as Eq. (23). We have examined several hysteresis loops using either plastic or total strain in the argument of the exponential but have not decided which is the "best" approach. Figure 5.96 shows a hysteresis loop at 593°C (1100°F), and Fig. 5.97 shows a plot of log σ' vs ϵ' and ϵ_p, obtained from the hysteresis loop. Neither approach is perfect, but both provide fairly good approximations.

Some testing was performed at strain ranges comparable to $3S_m$ or $\pm 1.5S_m$. Hysteresis loops representative of four tests at room temperature are shown in Fig. 5.98. Two tests were performed on heat 8043813 and two on heat 9T2796. For each heat one specimen was in the mill-annealed condition (A 240) and one in the reannealed condition. Specimens were cycled from zero to approximately 0.2% strain, which is near the $3S_m$ value. All the specimens exhibited cyclic hardening and a gradual decay of the mean stress level. This development is indicated by the width and position of the 100th loop relative to the initial loop. Very little change

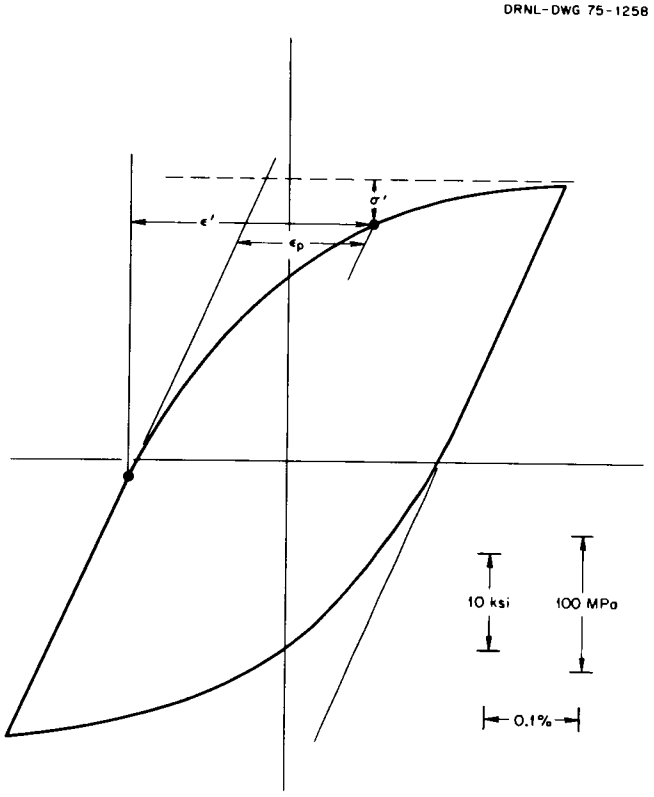

Fig. 5.96. Hysteresis Loop for Type 304 Stainless Steel (Heat 9T2796) at 593°C and 0.58% Δε. Construction shows how σ´, ε´, and ε_p are obtained.

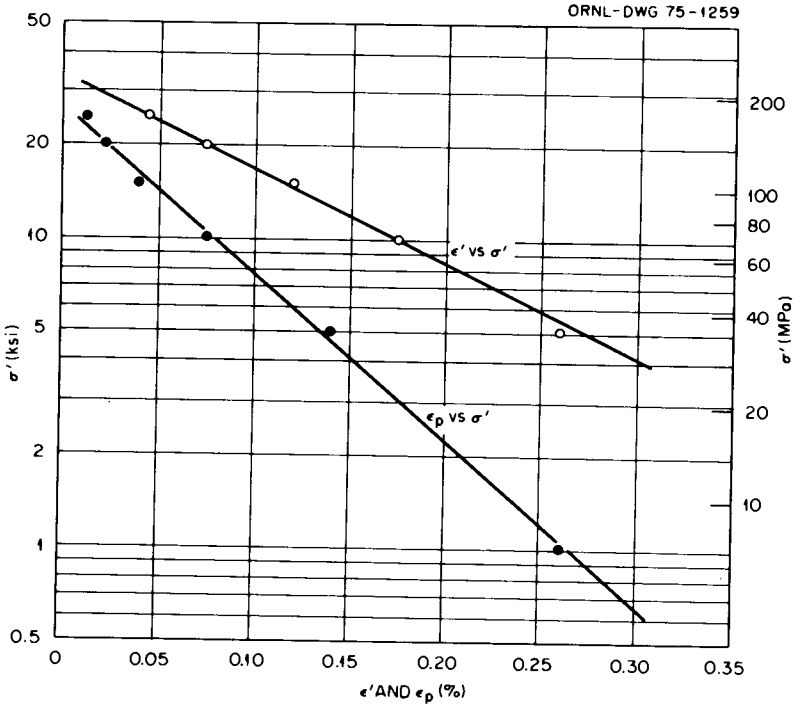

Fig. 5.97. Variation of σ´ with ε´ and ε_p Obtained from a Hysteresis Loop for Type 304 Stainless Steel (Heat 9T2796) at 593°C (1100°F) and 0.58% Δε.

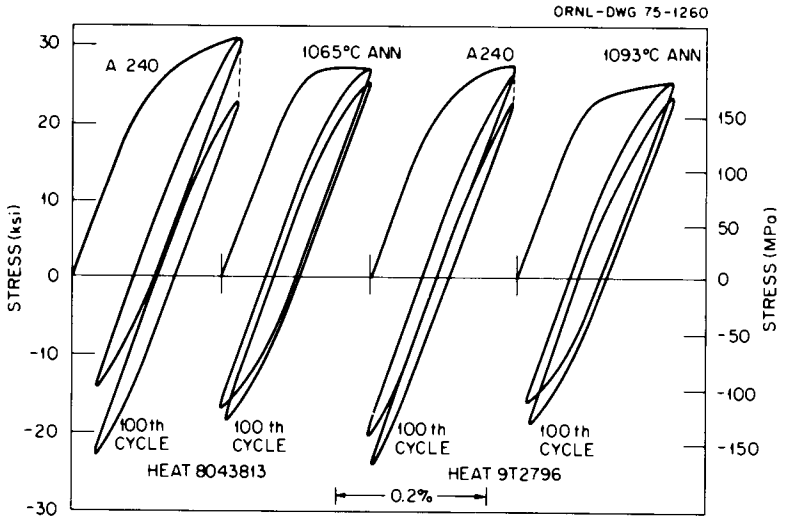

Fig. 5.98. Room-Temperature Hysteresis Loops for Type 304 Stainless Steel at Strain Ranges Near $3S_m$.

developed after the 100th cycle, however, and significant mean strains persisted for thousands of cycles. Additional tests were performed on heat 8043813 in the A 240 condition and heat 9T2796 in the reannealed condition. Room-temperature hysteresis loops for tests near $\pm 1.5S_m$ are shown in Fig. 5.99. Heat 8043813 exhibited slight hardening, then gradual weakening. Heat 9T2796 exhibited slight hardening and thereafter remained in a stable condition.

The results from tests at 427°C (800°F) are shown in Fig. 5.100. Initially, heat 8043813 was stronger than heat 9T2796, and it remained stronger for the duration of the tests (approximately 2000 cycles). Both heats exhibited significant strengthening, however, and were slowly approaching elastic behavior.

The results from tests at 593°C (1100°F) are shown in Fig. 5.101. Here again, heat 8043813 was initially stronger than heat 9T2796. It remained stronger for the duration of testing. Heat 9T2796 eventually developed greater strength at 593°C (1100°F) than at 427°C (800°F), while heat 8043813 achieved a strength at 593°C (1100°F) nearly equivalent to the strength at 427°C (800°F).

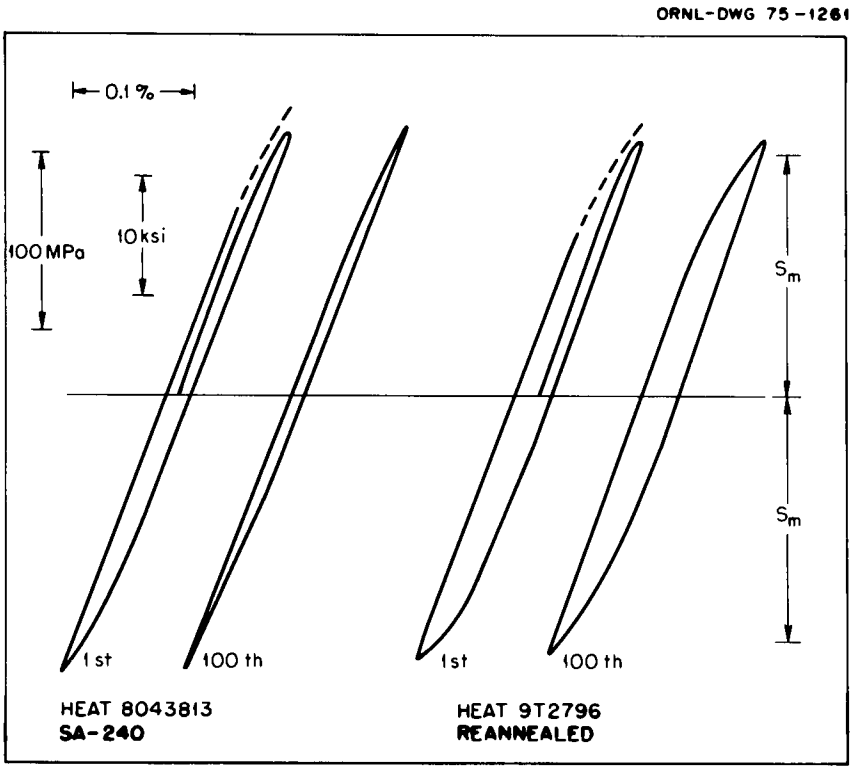

Fig. 5.99. Room-Temperature Hysteresis Loops for Type 304 Stainless Steel at Strains Near $\pm 1.5S_m$.

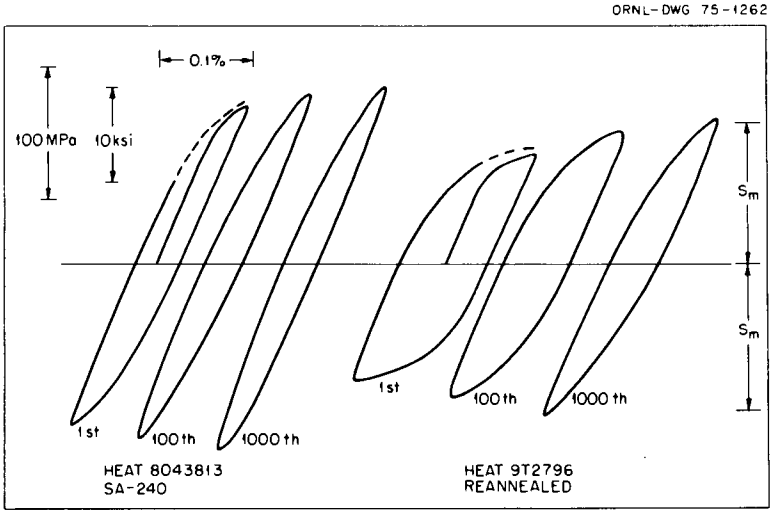

Fig. 5.100. Hysteresis Loops for Type 304 Stainless Steel at 427°C (800°F) and Strains Near $\pm 1.5S_m$

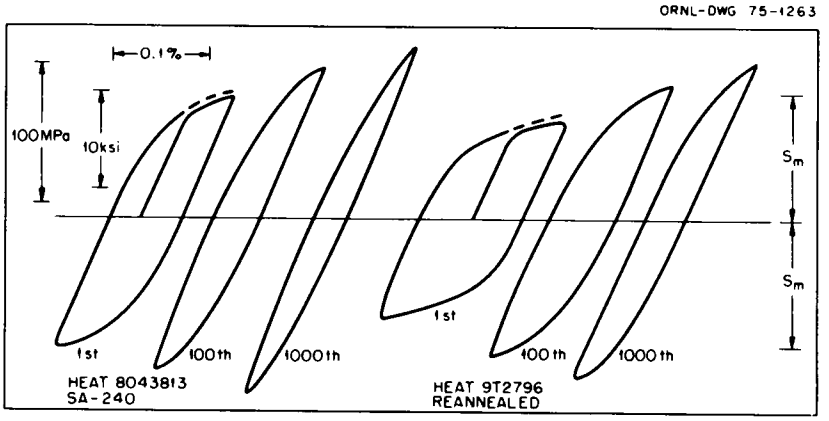

Fig. 5.101. Hysteresis Loops for Type 304 Stainless Steel at 593°C (1100°F) and Strains Near $\pm 1.5S_m$.

5.5.1.4 Tests on 2 1/4 Cr-1 Mo Steel — R. W. Swindeman and R. L. Klueh

Relaxation tests were performed on a ferritic alloy, 2 1/4 Cr-1 Mo steel, at 510°C (950°F). Several short-time tests and one long-time test were performed at starting stresses in the 18 to 26 ksi (124–172 MPa) range. Data are plotted in Fig. 5.102. The long-time test data suggest that the relaxation rate does not diminish very rapidly. The rate between 500 and 900 hr, for example, is almost constant and equivalent to a creep rate near 10^{-5} %/hr. In interpreting relaxation data for 2 1/4 Cr-1 Mo steel, however, one must consider the possibility of dimensional

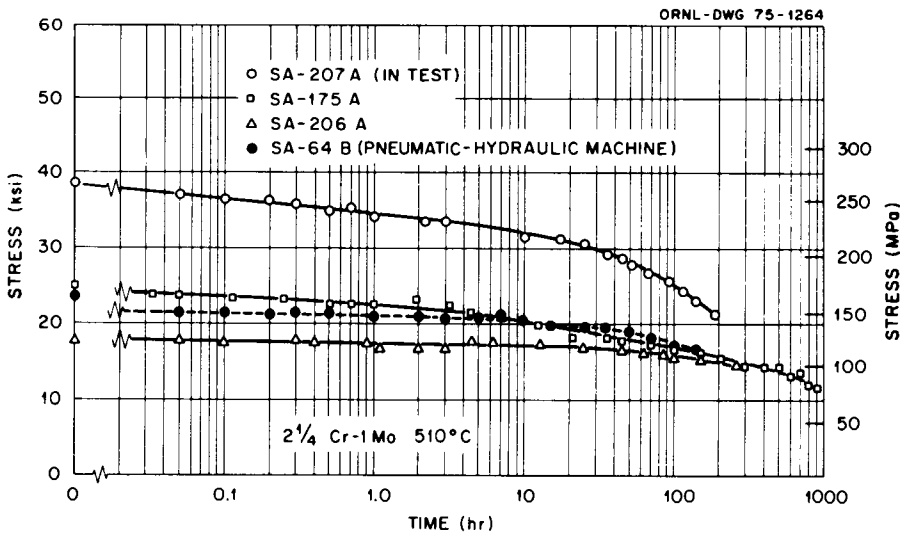

Fig. 5.102. Relaxation Curves for 2 1/4 Cr-1 Mo Steel at 510°C (950°F).

instability in the alloy. This could introduce a noncreep component of relaxation. We are developing a second relaxation testing system using a servo-controlled pneumatic-hydraulic machine. The response and stability of the system are quite satisfactory. However, the analysis of results from a 1000-hr test on 2 1/4 Cr-1 Mo steel at 510°C showed that the extensometer was too sloppy to provide a usable feedback signal, so we have a few more improvements to make.

A creep-plasticity test was performed to supplement data obtained by Jaske and Leis.[96] The results from the cyclic portions of the test are summarized in Fig. 5.103. Here the cyclic stress range is plotted against the cycle number. Hardening was observed during the first 20-cycle block, but, after interrupting the cycling by periods of creep at 18 ksi (124 MPa), loss in cyclic strength developed and strength never recovered. In regard to creep, the cycling did not produce hardening, as indicated in Fig. 5.104. Gradually, an exaggerated primary creep period developed,

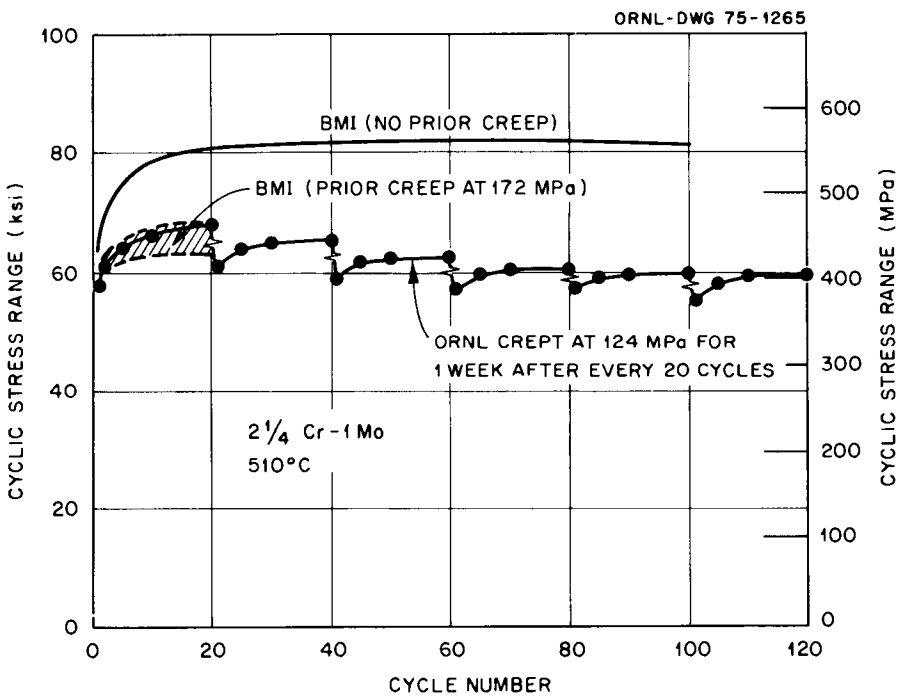

Fig. 5.103. Influence of Creep on the Cyclic Hardening Behavior for 2 1/4 Cr-1 Mo Steel at 510°C (950°F) and 0.4% Strain Range.

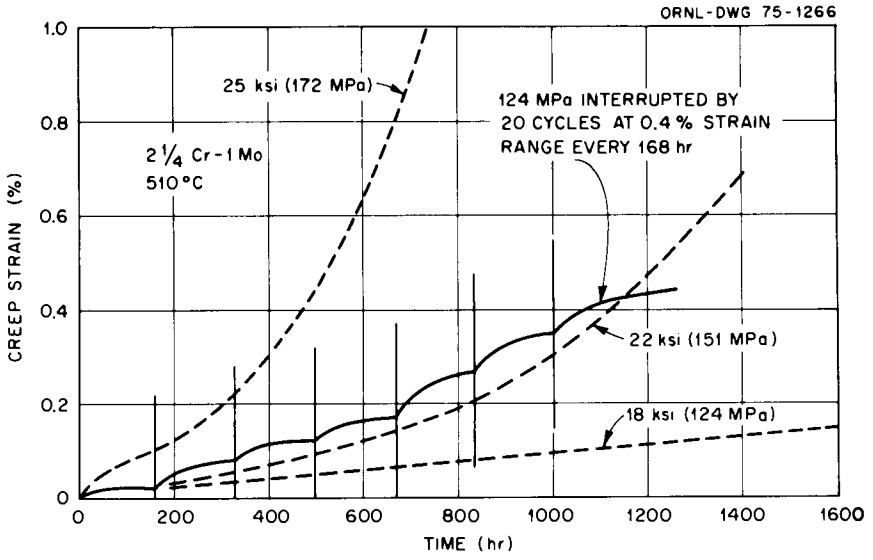

Fig. 5.104. Influence of Strain Cycling on the Creep Curve for 2 1/4 Cr-1 Mo Steel at 510°C (950°F).

and this produced an exaggerated creep rate. Thus, the resulting creep curve showed considerably more strain than would be expected from monotonic tests.

5.5.2 Investigations of Creep Failure Under Uniaxial and Multiaxial Conditions — C. C. Schultz — Babcock and Wilcox

The status of the constant-load uniaxial, step-load uniaxial, and interrupted uniaxial tests as of Sept. 30 is given in Tables 5.32 to 5.34 respectively, for type 304 stainless steel heat 9T2796 5/8-in. (16-mm) bar.

Figure 5.105 shows the creep strain–time results for test BWR-6 (19 ksi), which was the only constant-load uniaxial rupture occurring during this reporting period. Figure 5.106 shows the creep strain–time results for the constant-load uniaxial tests in progress: BWR-9 [18 ksi (124 MPa)], BWR-11 [17 ksi (117 MPa)], and BWR-7 [16 ksi (110 MPa)]. Note that test BWR-9 is well into tertiary creep.

The specimen in test BWLF-8 ruptured during this period, thus completing the initial series of step-load uniaxial tests (Table 5.33). The creep strain–time results for tests BWLF-7 and BWLF-8 are shown in Fig. 5.107. Although these two tests were subject to the same loading

Table 5.32. Status of Constant-Load, Uniaxial Rupture Tests — Type 304 Stainless Steel (Heat 9T2796), 593°C (1100°F)

Test No.	Specimen No.	Stress (ksi)	Total Strain Loading[a] (%)	Time to Secondary Creep (hr)	Minimum Creep Rate (%/hr)	Time to Tertiary Creep[b] (hr)	Intercept Creep Strain[c] (%)	Test Time[d] (hr)	Fracture Elongation[e] (%)	Reduction in Area (%)
BWC-1	7-15	30	4.7					187 R	19.0	30.5
BWR-1	7-1	30						138 R	21.5	32.9
BWC-2	2-22	28	5.8	40	0.016	195	0.50	227 R	13.0	20.4
BWR-2	2-1	28		40	0.022	230	0.65	368 R	16.5	29.0
BWR-13	7-13	28		60	0.023	215	0.88	276 R	16.5	18.9
BWC-9	7-25	28	3.8	85	0.021		1.16	415 R	18.3	25.2
BWC-3[f]	7-28	25	N.A.	80	0.0065	500	0.45	667 R	12.7	12.0
BWR-3	7-8	25		100	0.0079	585	0.71	948 R	17.0	23.2
BWC-4	2-28	22	3.7	175	0.0014	1,400	0.60	2130 R	10.7	13.7
BWR-4	7-7	22		160	0.0030	1,170	0.72	2026 R	12.5	16.6
BWC-5[g]	2-15	20						D		
BWC-5B	2-16	20	1.8	5000	0.000165	8,700	1.84	9584 R	10.5	12.0
BWR-5[h]	2-14	20						4842 D		
BWR-6	7-14	19		6000	0.000073	13,500	2.90	17547 R	9.5	12.6
BWR-9	7-11	18		7500	0.000036	18,000	2.40	18200 I		
BWR-11[i]	2-12	17						94 D		
BWR-11B	2-10	17						18300 I		
BWR-7	2-4	16						19000 I		
BWR-14	2-9	20	2.02	3200	0.00044	5,800	1.88	6868 R	8.5	13.1
BWC-10	7-18	20	1.52	4000	0.00021	8,000	2.30	7300 I		
BWR-15	2-3	20						1200 I		
BWC-11	2-19	20						1200 I		
BWC-13	7-19	25	2.62							
BWR-16	7-2	25	4.80							

[a] All specimens were step loaded at 1.87-ksi increments, except test BWC-5B, which was step loaded at 1.49-ksi increments. Loading curves on BWR series include load train displacements (thus not reported).

[b] Based on the 0.2% offset from the minimum rate line.

[c] Does not include the elastic and initial plastic components.

[d] R = rupture; D = discontinued; I = in test.

[e] Elongation over 3 in. in BWC series; over 2 in. in BWR series.

[f] Failure occurred near end of gage length.

[g] Temperature excursion to 704°C (1300°F) prior to loading; replaced by test BWC-5B.

[h] Temperature excursion to 749°C (1380°F) at 4842 hr; terminated.

[i] Temperature excursion to 704°C (1300°F) at 94 hr; replaced by test BWR-11B.

Table 5.33. Status of Step-Load Uniaxial Rupture Tests — Type 304 Stainless Steel (Heat 9T2796), 593°C (1100°F)

Test No.	Specimen No.	Stress (ksi)	Total Strain Loading (%)	Time at Load[a] (hr)		Life Fraction (%)	Fracture Elongation[b] (%)	Reduction in Area (%)
BWC-6	2-17	16	0.42	3,871		6		
		25		136		17		
		20		9,251		123		
				13,258	R	146	9.0	16.0
BWR-10	2-11	16		3,871		6		
		25		136		17		
		20		5,655		75		
				9,662	R	98	11.5	17.8
BWC-7	2-18	17	0.76	3,699		11		
		25		136		17		
		20		5,066		68		
				8,901	R	96	12.0	20.6
BWR-8	2-5	17		3,703		11		
		25		136		17		
		20		8,901		119		
				12,740	R	147	11.0	13.8
BWLF-5	2-25	20	2.06	503		7		
		25		198		25		
		20		5,246		70		
				5,947	R	102	12.5	17.0
BWC-8	7-16	18	1.78	5,071		25		
		25		136		17		
		20		5,420		72		
				10,627	R	114	8.0	15.5
BWR-12	7-12	18		4,897		24		
		25		136		17		
		20		3,996		53		
				9,029	R	94	11.5	17.2
BWLF-5B	2-21	21	2.62	500		10		
		25		200		25		
		21		1,236		25		
				1,936	R	60	10.3	15.9
BWLF-7	2-26	21	2.25	750		15		
		25		136		17		
		21		2,003		40		
				2,889	R	72	12.3	20.5
BWLF-9	7-24	21	2.21	1,014		20		
		25		136		17		
		21		1,816		36		
				2,966	R	73	18.0	16.5
BWLF-10	2-27	21	2.47	1,006		20		
		25		136		17		
		21		2,286		45		
				3,428	R	82	16.0	18.2
BWLF-8	7-23	21	1.60	750		15		
		25		136		17		
		21		3,711		74		
				4,597	R	106	12.3	15.4
BWLF-6	7-22	21	3.11	500		10		
		25		200		25		
		21		1,214		24		
				1,914	R	59	10.5	14.8

[a] R = rupture; D = discontinued; I = in test.

[b] Elongation over 3 in. in BWC series; over 2 in. in BWR series.

Table 5.34. Status of Interrupted Uniaxial Tests — Type 304 Stainless Steel (Heat 9T2796), 593°C (1100°F)[a]

Test No.	Specimen No.	Stress (ksi)	Time to Secondary Creep (hr)	Minimum Creep Rate (%/hr)	Time to Tertiary Creep[b] (hr)	Intercept Creep Strain[c] (%)	Test Time[d] (hr)	Fracture Elongation[e] (%)	Reduction in Area (%)
BWI-1	6-4	19.5	5600	0.00008	13000	3.3	12750 I		
BWI-2	6-5	19.5	5400	0.00010	13000	3.2	12750 I		
BWI-3	6-6	19.5	4800	0.00019	9000	3.2	11608 R	11.0	13.3
BWI-4	6-1	19.5					5900 I		
BWI-5	6-2	19.5					5900 I		
BWI-6	6-3	19.5					5900 I		

[a]All specimens were step-loaded at 1.87-ksi increments. Loading curves include load train displacements, thus are not reported.

[b]Based on the 0.2% offset from the minimum rate line.

[c]Intercept creep strain does not include the elastic and initial plastic components.

[d]R = rupture; D = discontinued; I = in test.

[e]Elongation over 2-in. gage length.

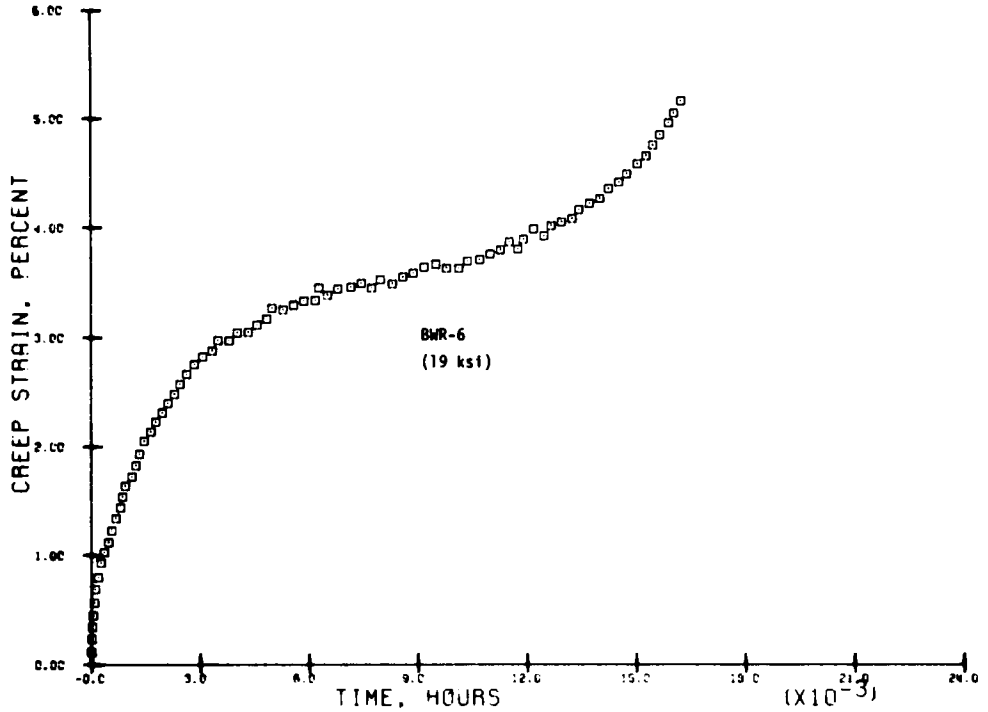

Fig. 5.105. Constant-Load Uniaxial Rupture Test. Loaded at 593°C (1100°F), type 304 stainless steel (heat 9T2796), 5/8-in. bar.

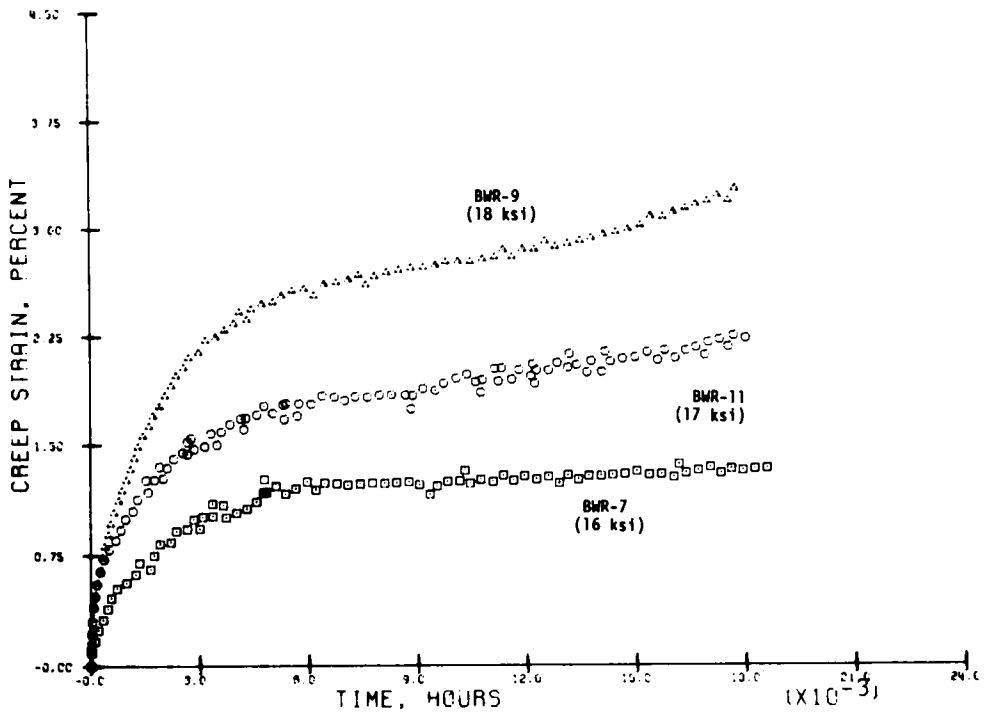

Fig. 5.106. Constant-Load Uniaxial Rupture Tests (In Progress). Loaded to 593°C (1100°F), type 304 stainless steel (heat 9T2796), 5/8-in. bar.

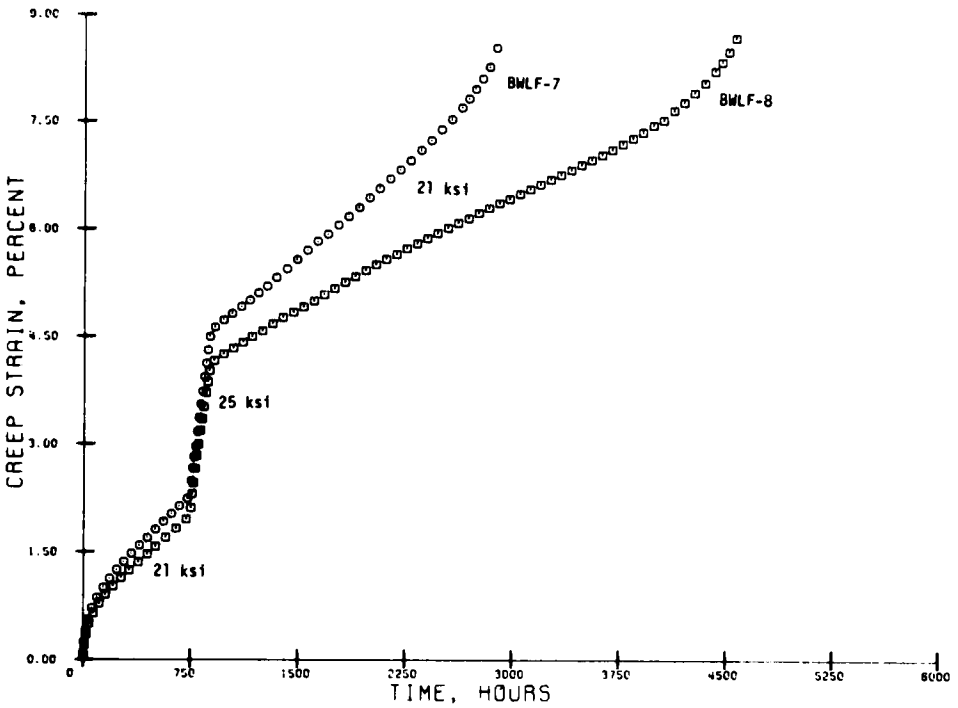

Fig. 5.107. Step-Load Uniaxial Rupture Tests at 593°C (1100°F) with Identical Loading Histories. Type 304 stainless steel (heat 9T2796), 5/8-in. bar.

history, the rupture time for BWLF-8 was 50% higher than that for BWLF-7. Similar differences in time to rupture occurred between step-load tests BWC-6 and BWR-10 and between BWC-7 and BWR-8. Step-load tests BWLF-5B through BWLF-10 represent duplicate experiments for three different load-time histories. The creep strain–time data for these six tests are compared in Fig. 5.108. Tests BWLF-5B and BWLF-6, which had extended periods of loading at 25 ksi (172 MPa), showed lower calculated life fractions than the other four tests. Another trend to be noted is that the fracture elongations for step-loaded specimens appear to correlate strongly with the time at initial load. Specifically, the specimens with the highest fracture elongations had the longest initial loading times (see Table 5.33). These preliminary observations are made with reservation because of the experience with grain size variability. For example, the two tests with the highest total creep strain (tests BWLF-7 and BWLF-8) also showed higher creep rates prior to the introduction of any load changes. It should also be noted that the shortest time test, BWLF-6, incurred the

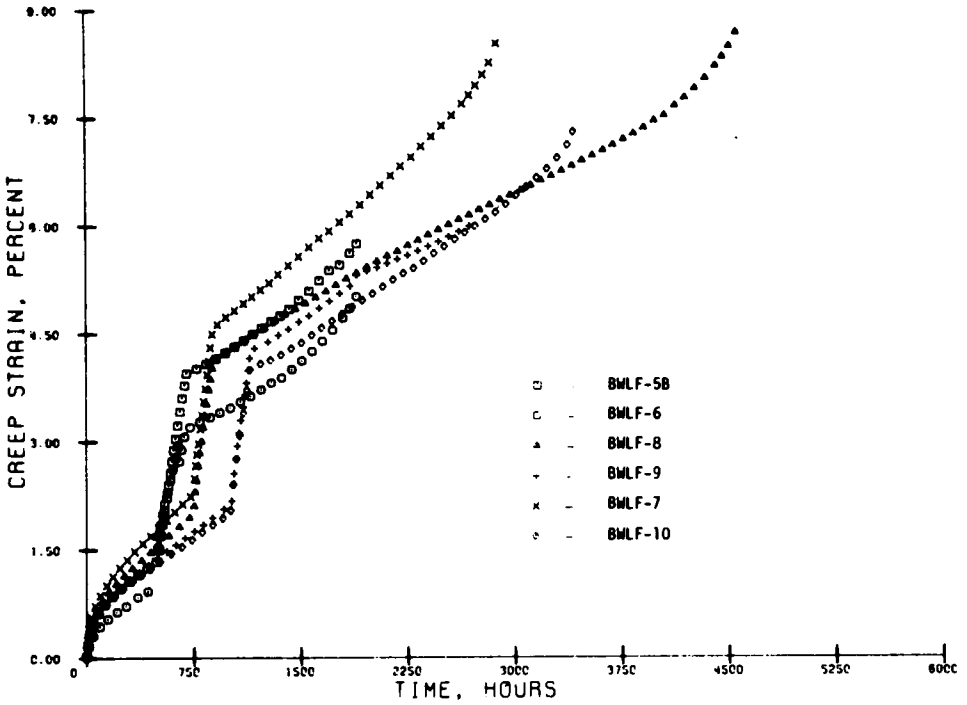

Fig. 5.108. Step-Loaded Uniaxial Rupture Tests at 593°C (1100°F). Loaded as shown in Table 5.33, type 304 stainless steel (heat 9T2796), 5/8-in. bar.

greatest strain on loading, while the longest, BWLF-8, incurred the least strain during loading.

The interrupted uniaxial tests are shown in Table 5.34; BWI-3 failed during this reporting period. Two other tests (BWI-1 and BWI-2) at the same stress level [19.5 ksi (134 MPa)] are still in progress and have already exceeded the expected rupture time of about 10,000 hr. The creep strain–time data for these three tests are shown in Fig. 5.109. Similar plots for the other three tests in Table 5.34 (BWI-4, BWI-5, and BWI-6) are shown in Fig. 5.110. These six tests are compared in Fig. 5.111 out to 6000 hr, which is the present limit of the three shortest time tests. If the relationship between creep rate and rupture time observed in Fig. 5.109 remains consistent, considerable variation in rupture times may also be expected for these tests.

Test BWC-10 [20 ksi (138 MPa)] continued as a part of B&W's investigation of the apparently different creep strain–time responses exhibited by the two types of testing machines and specimens. This test specimen has two

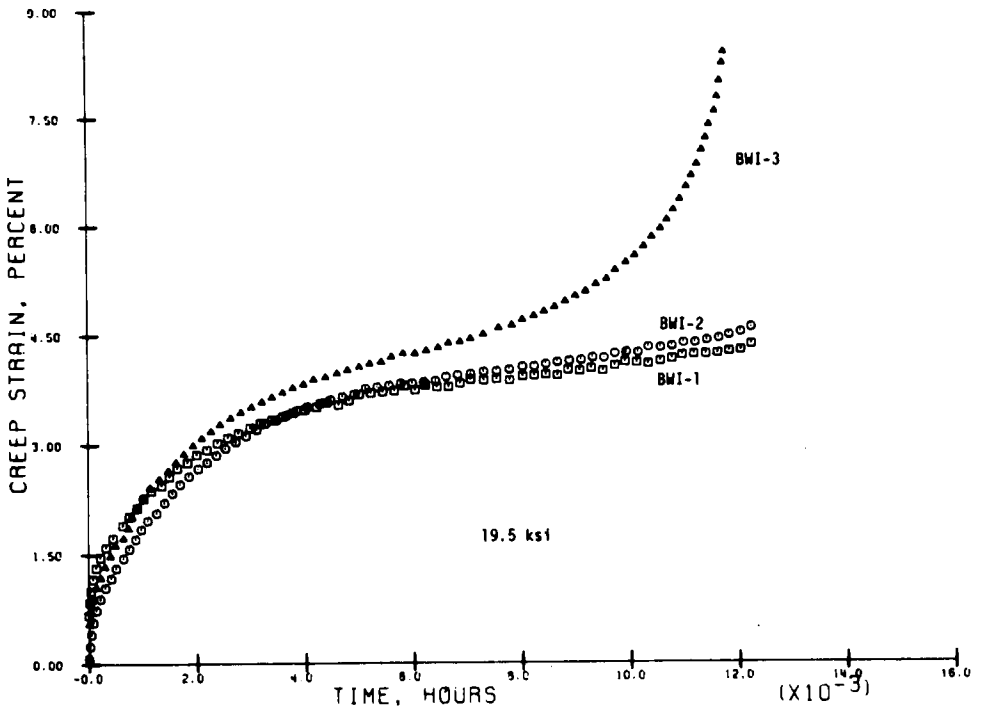

Fig. 5.109. Constant-Load Uniaxial Tests Scheduled for Subsequent Interruption and Destructive Examination. Loaded at 593°C (1100°F), type 304 stainless steel (heat 9T2796), 5/8-in. bar.

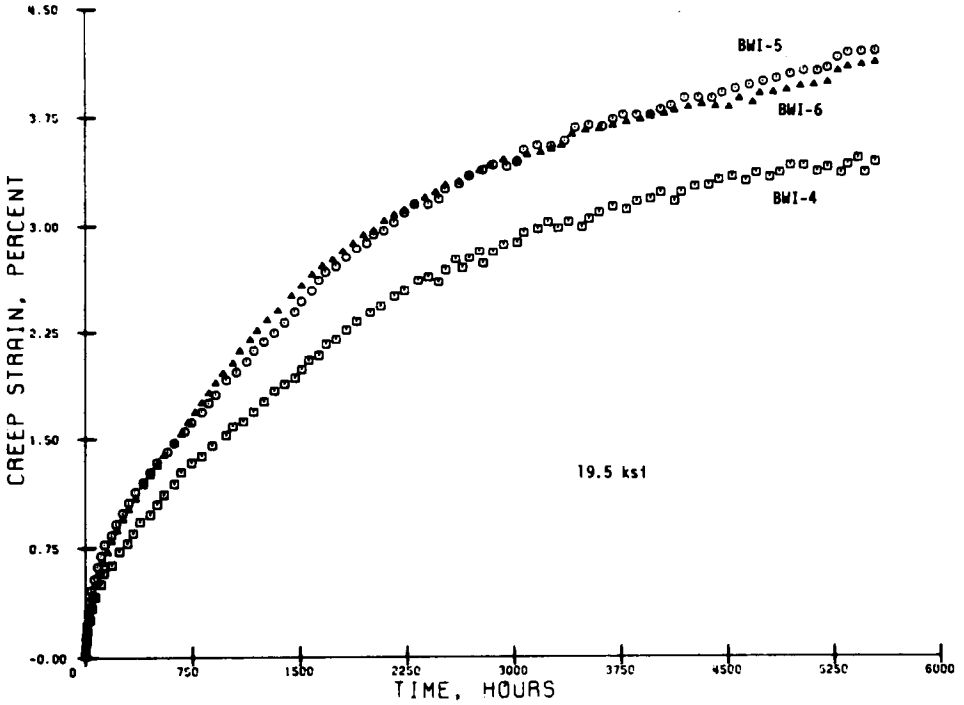

Fig. 5.110. Constant-Load Uniaxial Tests Scheduled for Subsequent Interruption and Destructive Examination. Loaded at 593°C (1100°F), type 304 stainless steel (heat 9T2796), 5/8-in. bar.

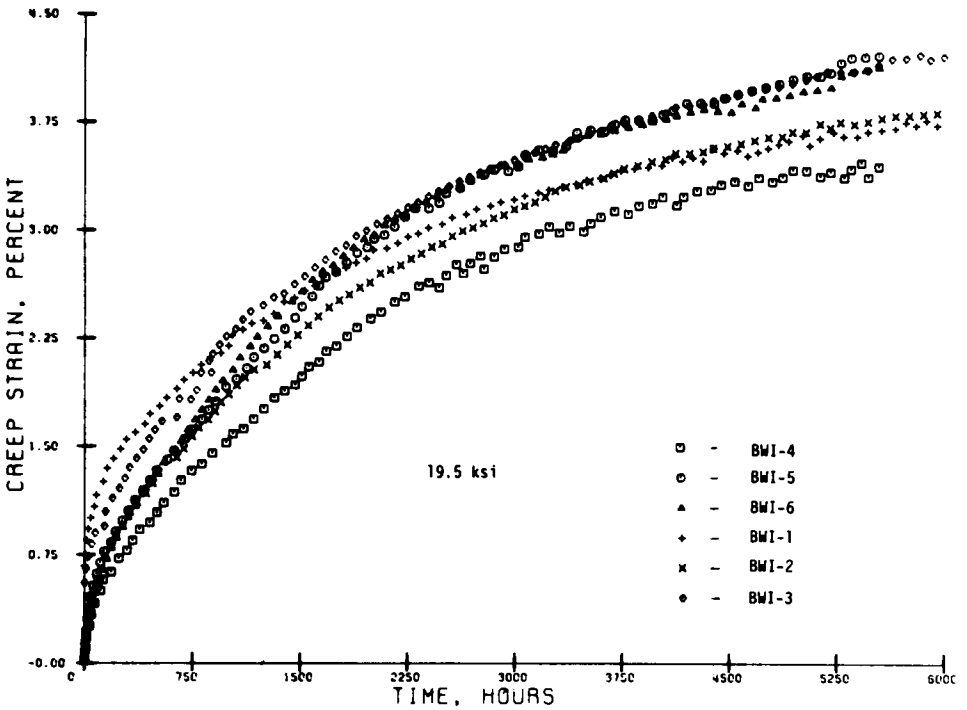

Fig. 5.111. Comparison of Six Identically Loaded Constant-Load Uniaxial Tests. Loaded to 19.5 ksi at 593°C (1100°F), type 304 stainless steel (heat 9T2796), 5/8-in. bar.

opposed extensometers over the full 3-in. (76-mm) gage length and two opposed extensometers over the center 2 in. (51-mm) of the gage length, as well as a dial gage monitoring the full load train motion. The purpose of the test was to determine if significant strain localization occurs prior to initiation of tertiary creep. The creep strain–time data for this test are shown in Fig. 5.112. As shown in the figure and discussed earlier,[97] no strain localization was apparent during the early stages of creep. The specimen is now in tertiary creep, and no localization of strain is yet apparent; however, at this time the teriary creep strain is minimal. The data of test BWC-10 are compared with those of previous tests at the same stress level in Fig. 5.113. Considerable differences are seen in the time-to-rupture values as well as in the strain-time responses.

In an effort to separate the potential effects of grain size variability and machine-specimen-type differences, B&W has initiated four constant-load uniaxial tests using specimens that were reannealed at 1093°C (2000°F)

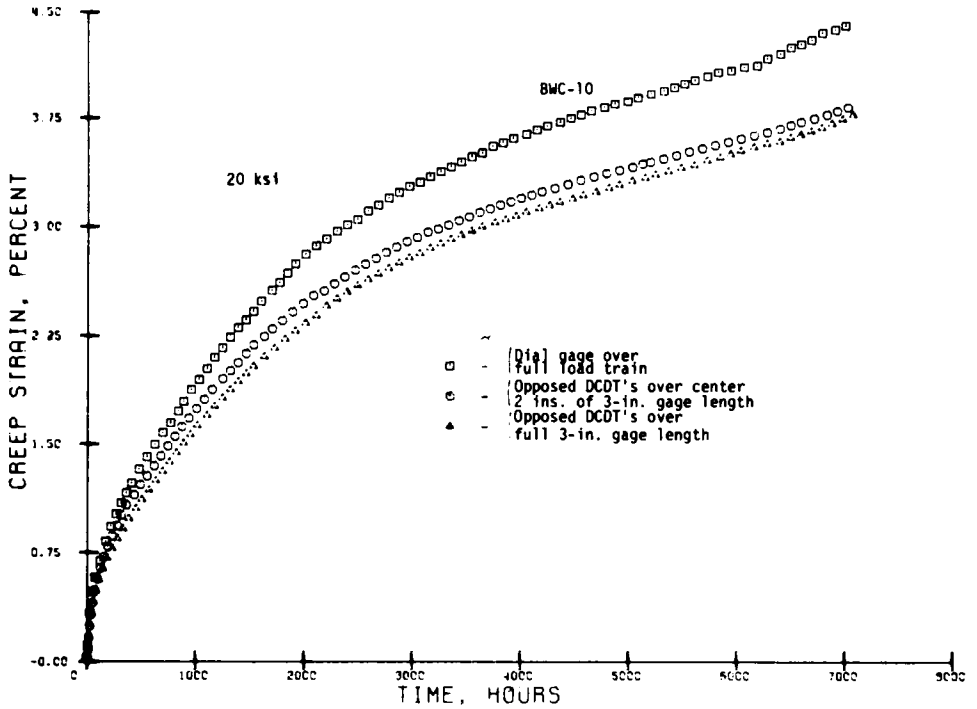

Fig. 5.112. Constant-Load Uniaxial Test to Evaluate Localization of Strain in 3-in. Button-Head Creep Machine Specimen. Loaded at 593°C (1100°F), type 304 stainless steel (heat 9T2796), 5/9-in. bar.

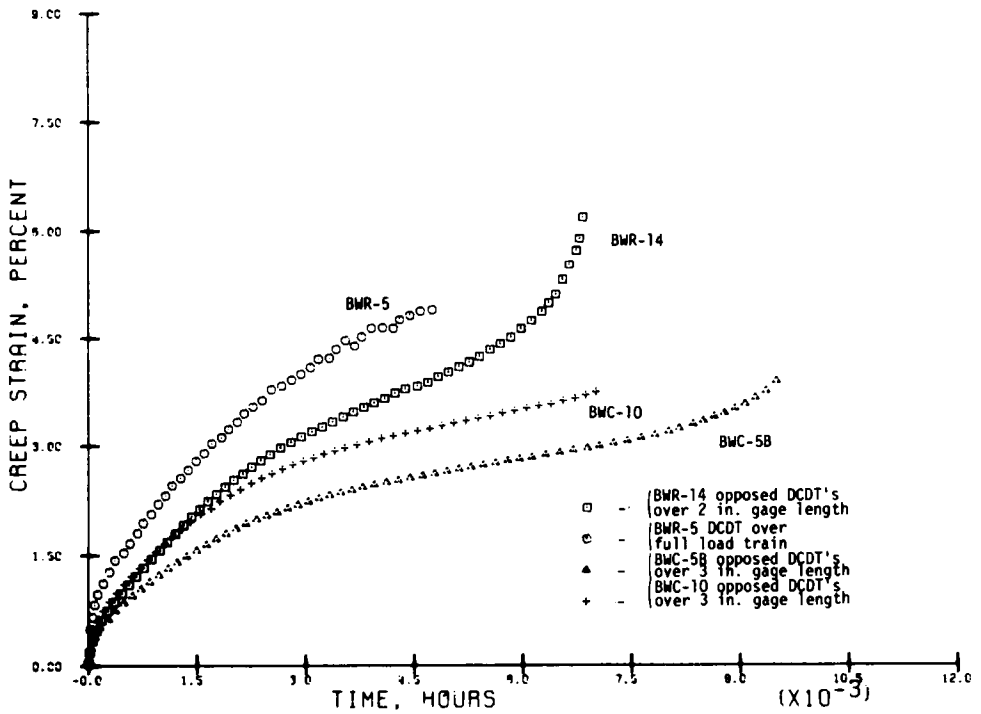

Fig. 5.113. Comparison of Uniaxial Tests All Loaded to 20 ksi at 593°C (1100°F), type 304 stainless steel (heat 9T2796), 5/8-in. bar.

for 60 min in addition to the usual 30 min. It is hoped that this additional anneal will eliminate any grain size variability, as previously described.[97] Two of these tests, BWC-11 and BWR-15, were loaded at 20 ksi (138 MPa) (see Table 5.32); the other two tests were loaded at 25 ksi (172 MPa). The creep strain–time data for tests BWC-11 and BWR-15 are shown in Fig. 5.114. At this point the data are inconclusive; no data are yet available for the two tests at 25 ksi.

Tubular test BWTR-3 was continued at the original equal biaxial tension of 21.85 ksi (150.7 MPa) after an interruption at 100 hr for specimen deformation measurements. However, the internal pressure began to drop after approximately 585 hr (total time under load). Visual examination of the specimen did not reveal any obvious perforations, and a subsequent helium leak test was inconclusive because of a rather profuse leak in the pressure inlet line to the specimen. The leak in the inlet line is presently assumed to be the result of mechanical damage incurred in handling the specimen. After new specimen deformation measurements are made, the inlet

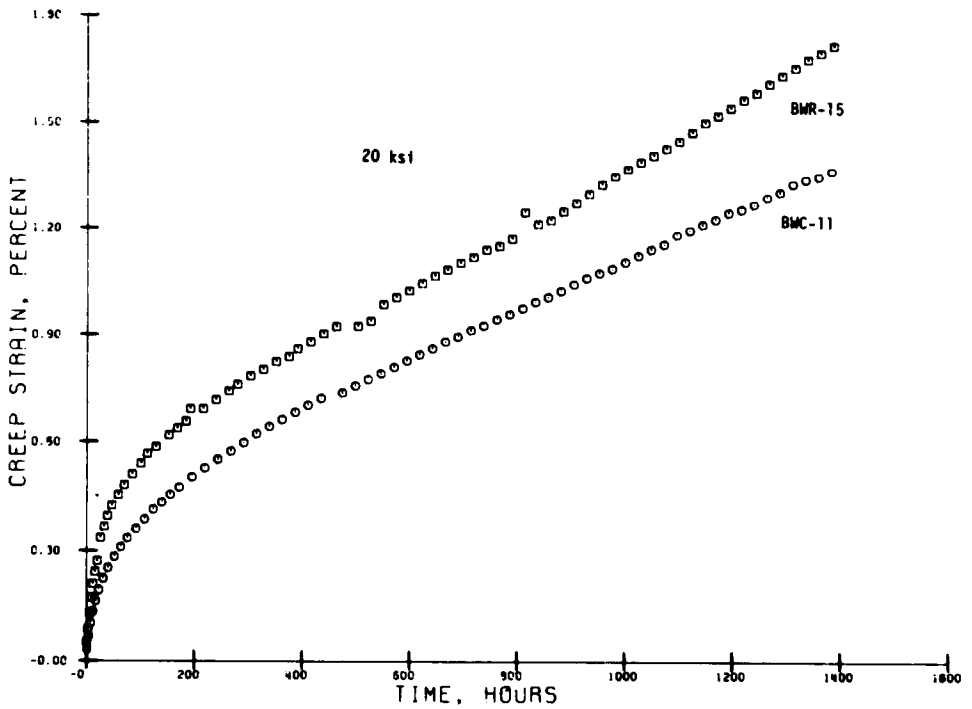

Fig. 5.114. Comparison of Tests Loaded at 593°C (1100°F). Reannealed at 1093°C (2000°F) for 90 min, type 304 stainless steel (heat 9T2796), 5/8-in. bar.

line will be replaced and the leak test repeated. Figure 5.115 shows the axial creep strain–time results for test BWTR-3 for the accumulated time under load. Figure 5.116 shows the circumferential strain at the midlength of the specimen, with each set of data representing the average of two opposed radial DCDT's. These radial DCDT's were not functional during the initial 100 hr of loading.

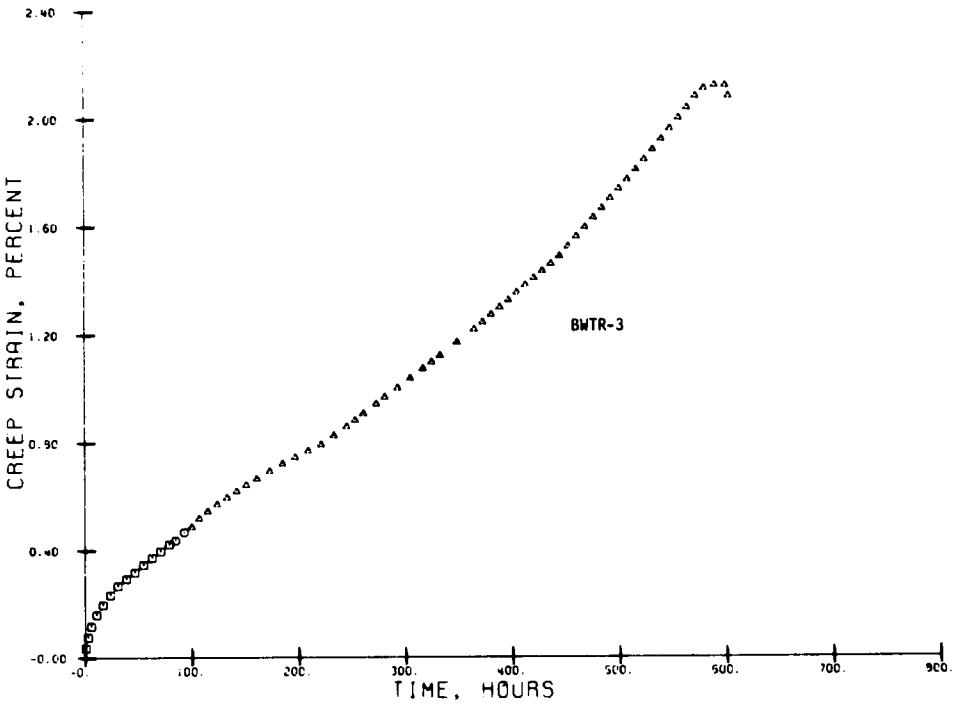

Fig. 5.115. Axial Creep Strain in Constant-Load Biaxial Rupture Test. Tubular specimen with internal pressure and axial load. Equal biaxial tension of 21.85 ksi (150.7 MPa) at 593°C (1100°F). Outside diameter of 1.50 in. and wall thickness of 0.075 in. Type 304 stainless steel (heat 9T2796), 2-in. bar.

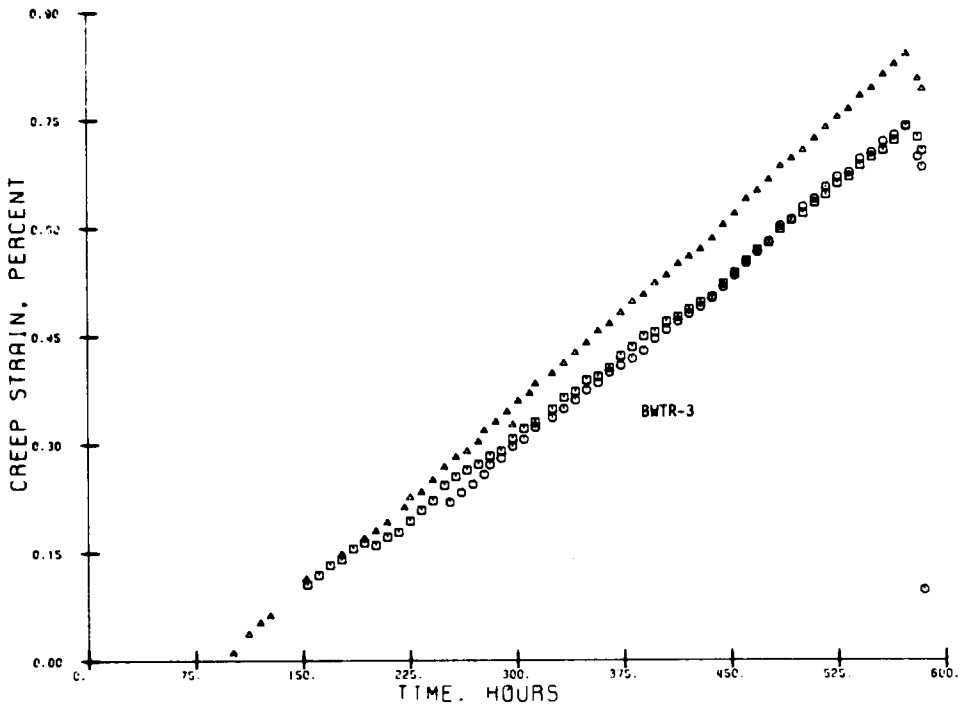

Fig. 5.116. Circumferential Creep Strain in Constant-Load Biaxial Rupture Test. Tubular specimen with internal pressure and additional axial load. Equal biaxial tension of 21.85 ksi (150.7 MPa) at 593°C (1100°F). Outside diameter of 1.50 in. and wall thickness of 0.075 in. Type 304 stainless steel (heat 9T2796), 2-in. bar.

5.6 MECHANICAL PROPERTIES OF HTGR STEAM GENERATOR AND PRIMARY CIRCUIT MATERIALS — P. L. Rittenhouse

The principal aims of this program are to (1) determine whether compatibility or property degradation problems are significant for alloys of current use in HTGR steam-cycle plants and (2) provide a compilation and analysis of materials design data for commercial HTGRs. As an integral part of accomplishing these objectives, mechanical property tests (i.e., tensile, creep, low-cycle fatigue, and subcritical crack growth) are being conducted on a number of materials at temperatures consistent with their service in the HTGR. Many of these tests are being run in helium and steam environments appropriate to HTGR operating conditions.

5.6.1 Materials

Recommendations for the purchase of a reference heat of Alloy 800 have been prepared and transmitted to the Atomic Energy Commission. The

proposed reference heat would meet present and future materials testing and development needs for both HTGR programs and the program on advanced LMFBR steam generator materials.

Stock for providing mechanical property specimens of Inconel 617 is currently being prepared from 4-in.-diam (0.1-m)bar. The bar has been extruded to 1 in. (25 mm) in diameter and will be rolled and swaged to a final size of 5/8 in. (16 mm) in diameter.

5.6.2 Tensile Testing — W. R. Corwin and A. B. Boatwright

The tensile tests on the three Babcock and Wilcox heats of 2 1/4 Cr-1 Mo steel tubing have been completed, and the yield and tensile data are shown in Table 5.35. Yield and tensile strengths for all three heats consistently fall below the expected values given for isothermally annealed 2 1/4 Cr-1 Mo in the *Nuclear Systems Materials Handbook*. However, they are within the statistically determined tolerance limits given in the same source.

Approximately 30 tests on Hastelloy X have been completed, and the data are currently being processed. A marked effect of strain rate has been noted at temperatures above 704°C (1300°F). The results of these tests will appear in the next quarterly report. Additionally, the tensile tests of Hastelloy S, now about half completed, will be reported.

5.6.3 Environmental Creep Testing — W. R. Corwin

The construction and installation of the ten environmental creep frames (five premix and five dynamic-mix frames as described previously[98]) have been completed. The only work remaining involves the elimination of seal-lubricant contamination within the environmental chambers.

The premix gas supply system is complete with the exception of a moisture injection device. Moisture injection is a recent design requirement necessitated by revised estimates of water levels in the primary coolant of the HTGR. The dynamic-mix supply system, including the moisture injection device, will be finished early in 1975.

The gas chromotograph for use in monitoring impurities in the helium environment is on line and functional. Construction of the oxygen potential

Table 5.35. Elevated-Temperature Tensile Data for 2 1/4 Cr-1 Mo Steel

Test	Heat	Temperature		Tensile Strength			
				0.2% Yield		Ultimate	
		(°C)	(°F)	(ksi)	(MPa)	(ksi)	(MPa)
14496	72768[a]	24	75	32.4	223	69.0	476
14497	72768	24	75	32.1	221	69.0	476
14159	72768	24	75	33.3	230	65.5	452
14162	72768	24	75	34.2	236	68.3	471
14498	36202[b]	24	75	36.2	250	73.5	507
14105	36202	24	75	37.3	257	73.1	504
14106	36202	24	75	36.7	253	72.8	502
14199	36202	24	75	32.7	225	72.7	501
14492	X-6216[b]	24	75	35.4	244	72.3	498
14493	X-6216	24	75	34.9	241	71.6	494
14494	X-6216	24	75	35.0	241	71.6	494
14495	X-6216	24	75	34.8	240	71.7	494
14152	72768	260	500	25.9	179	56.3	388
14153	72768	260	500	25.8	178	55.5	383
14154	36202	260	500	27.5	190	60.3	416
14155	36202	260	500	28.3	195	60.0	414
14151	X-6216	260	500	28.6	197	61.6	425
14111	X-6216	260	500	28.1	194	58.5	403
14066	72768	315	600	25.0	172	57.1	394
14068	72768	315	600	22.4	154	56.9	392
14071	36202	315	600	27.8	192	61.3	423
14073	36202	315	600	27.6	190	61.7	425
14158	X-6216	315	600	27.0	186	59.8	412
14501	X-6216	315	600	27.5	190	64.0	441
14502	72768	371	700	23.7	163	62.1	428
14070	72768	371	700	26.4	182	66.3	457
14086	36202	371	700	25.9	179	64.6	445
14503	36202	371	700	26.0	179	65.5	452
14067	X-6216	371	700	26.3	181	63.3	436
14069	X-6216	371	700	27.2	188	62.8	433
10489	72768	427	800	23.9	165	57.9	399
14091	72768	427	800	20.7	143	57.6	397
14505	72768	427	800	25.8	178	59.2	408
14504	36202	427	800	24.7	170	63.4	437
14094	36202	427	800	29.4	203	62.0	427
14075	X-6216	427	800	26.1	180	60.2	415
14088	X-6216	427	800	27.7	191	56.7	391
14092	72768	482	900	23.5	162	52.5	362
14093	72768	482	900	26.7	184	52.5	362
14506	72768	482	900	22.7	157	52.3	361
14095	36202	482	900	19.1	132	56.6	390
14096	36202	482	900	18.7	129	56.5	390
14087	X-6216	482	900	23.3	161	54.5	376
14097	X-6216	482	900	25.5	176	55.3	381
14101	72768	538	1000	21.1	145	44.1	304
14104	72768	538	1000	19.2	132	44.2	305
14109	36202	538	1000	23.1	159	47.3	326
14511	36202	538	1000	24.4	168	47.9	330
14098	X-6216	538	1000	23.6	163	48.2	332
14100	X-6216	538	1000	22.0	152	46.1	318
14102	72768	593	1100	16.8	116	34.7	239
17513	72768	593	1100	19.3	133	33.9	234
14512	36202	593	1100	19.7	136	36.8	254
14108	36202	593	1100	21.1	145	37.3	257
14097	X-6216	593	1100	19.7	136	36.2	250
14099	X-6216	593	1100	21.9	151	36.2	250

[a] Carbon content 0.10%.

[b] Carbon content 0.12%.

meter has also been completed, and installation should be complete in January 1975. The moisture analyzer is currently undergoing modifications to allow its use in the modified (wetter) environment. It should be functional in February 1975.

In summary, we currently have the capability for testing in "dry" helium as supplied by the premix system. However, some problems of contamination by the seal-lubricant are being experienced. Testing in the five premix systems will commence when this problem is solved, probably in February 1975.

Four creep tests, two on 2 1/4 Cr-1 Mo steel at 593°C (1100°F) and two on Hastelloy S at 704°C (1300°F), have been performed to date by use of the premix systems. These tests will be repeated later, however, because of initial system instabilities and the seal-lubricant problem.

5.6.4 Environmental Fatigue Testing — W. R. Corwin and J. P. Strizak

5.6.4.1 Subcritical Crack Growth in Helium

The mechanical portion of the test facility for crack growth studies is complete. The originally designed gas supply system (premix type) is installed and is currently being cleaned and leak checked. However, as with the environmental supply systems for the creep frames, a moisture injection system must be added.

The replacement for the faulty detector of the gas chromatograph has not yet been received but was reported to have been shipped in mid-December of 1974. Once it is obtained, the chromatograph should be on line and functional within a few weeks. The moisture analyzer is currently being calibrated and should be operative in mid-January 1975; the oxygen potential meter has been constructed and is being installed. Testing will begin in early January and will employ remote gas sampling techniques until the items noted above are completed.

5.6.4.2 Subcritical Crack Growth in Steam and Air

Testing of 2 1/4 Cr-1 Mo Steel in steam at 510°C (950°F) is continuing. The steam production system has been automated to allow continuous testing except during the periods required for optical reading

of crack length. Most of the system downtime is due to the time required for heating and cooling of the test chamber to allow optical readings of crack growth. Work is now in progress to reduce the number of optical readings by employing an electronic-potential crack follower. This device has been modified to permit its use in the test environment and is almost operational. Use of the electronic crack follower will substantially increase the availability (i.e., ratio of test time to total time) of the system.

A crack growth test of 2 1/4 Cr-1 Mo steel is also in progress in air at 510°C (950°F) with an R ratio (i.e., ratio of minimum to maximum stress) of 0.75. This is a higher R ratio than has been tested previously and was selected to expand the data base for this material. An additional machine for studying crack growth in air will be available early in January 1975.

5.6.4.3 Fatigue Life Testing

The MTS system has been installed and is operational. It is currently capable of load- or displacement-controlled testing in air. Work is continuing to allow its use in strain-controlled tests in simulated HTGR primary coolant helium. In this regard, connections are currently being made to the environmental supply and control system of the HTGR creep frames, and electronic modifications are in progress to permit axial strain control using a diametral extensometer. The system should be operational in environment in early 1975.

5.7 REFERENCES

1. H. E. McCoy, *Interim Report of Tensile and Creep Data for Type 304 Stainless Steel Plate (Reference Heat 9T2796, 2 in. Thick)*, ORNL-TM-4627 (October 1974).
2. R. W. Swindeman, *Mechanical Properties Test Data for Structural Materials Quart. Progr. Rep. Oct. 31, 1974*, ORNL-5103, pp. 242–43.
3. S. S. Manson, "Time-Temperature Parameters — A Re-Evaluation and Some New Approaches," pp. 1–113 in *Time-Temperature Parameters for Creep-Rupture Analysis, ASM Publ.* D8-100, American Society for Metals, Metals Park, Ohio, 1968.

4. G. V. Smith, *An Evaluation of the Yield, Tensile, Creep, and Rupture Properties of Wrought 304, 316, 321, and 347 Stainless Steels at Elevated Temperatures, ASTM DATA Ser. Publ.* DS 5-S2, American Society for Testing and Materials, Philadelphia, February 1969.
5. V. K. Sikka, E. Lee, and E. B. Patton, *Mechanical Properties Test Data for Structural Materials Quart. Progr. Rep. Oct. 31, 1974,* pp. 116–18.
6. A. J. Lovell, L. D. Blackburn, and J. J. Holmes, *Quarterly Progress Report Irradation Effects on Reactor Structural Materials, August–October 1970,* WHAN-FR-40-1, pp. 8.4–8.14.
7. L. D. Blackburn, Hanford Engineering Development Laboratory, private communication, November 1973.
8. F. Garofalo et al., "Creep and Creep-Rupture Relationship in an Austenitic Stainless Steel," *Trans. AIME* 221: 310–19 (1961).
9. V. K. Sikka, H. E. McCoy, M. K. Booker, and C. R. Brinkman, "Heat-to-Heat Variation in Creep Properties of Types 304 and 316 Stainless Steels," submitted for presentation at the 2nd National Congress on Pressure Vessels and Piping, 1975 ASME Summer Meeting, June 23–27, 1975.
10. T. M. Cullen and M. W. Davis, "Influence of Nitrogen on the Creep Rupture Properties of Type 316 Stainless Steel," pp. 60–78 in *Elevated Temperature Properties as Influenced by Nitrogen Additions to Type 304 and 316 Stainless Steels, Spec. Tech. Publ.* 522, American Society for Testing and Materials, Philadelphia, 1973.
11. V. K. Sikka, *Mechanical Properties Test Data for Structural Materials Quart. Progr. Rep. July 31, 1974,* ORNL-4998, pp. 155–63.
12. H. E. McCoy, *Mechanical Properties Test Data for Structural Materials Quart. Progr. Rep. Jan. 31, 1974,* ORNL-4948, pp. 204–10.
13. V. K. Sikka, *Mechanical Properties Test Data for Structural Materials Quart. Progr. Rep. Apr. 30, 1974,* ORNL-4963, pp. 84–103.
14. *Ibid., July 31, 1974,* ORNL-4998, pp. 132–63.
15. V. K. Sikka, E. Lee, and E. B. Patton, *Mechanical Properties Test Data for Structural Materials Quart. Progr. Rep. Oct. 31, 1974,* ORNL-5103, pp. 119–47.

16. W.J.M. Tegart, *Elements of Mechanical Metallurgy*, Macmillan, New York, 1966, pp. 23–24.

17. E. F. Etienne, W. Dortland, and H. B. Zeedijk, "On the Capability of Austenitic Steel to Withstand Cyclic Deformation During Service at Elevated Temperature," paper presented at International Conference on Creep and Fatigue in Elevated Temperature Applications, Philadelphia, September 1973 and Sheffield, UK, April 1974.

18. D. A. Woodford and R. M. Goldhoff, "An Approach to the Understanding of Brittle Behavior of Steel at Elevated Temperatures," *Mater. Sci. Eng.* 5: 303–24 (1969–70).

19. F. Garofalo, *Fundamentals of Creep and Creep-Rupture in Metals*, Macmillan, New York, 1965.

20. F. Garofalo, *Ductility*, American Society for Metals, Metals Park, Ohio, 1968, pp. 87–129.

21. C. Zener, *Elasticity and Inelasticity of Metals*, University of Chicago Press, Chicago, 1948.

22. D. McLean, "The Physics of High Temperature Creep in Metals," *Rep. Progr. Phys.* 29; Part I: 1–33 (1966).

23. D. S. Kemsley, "Crack Paths in Fatigued Copper," *J. Inst. Metals* 85: 420–21 (1956–57).

24. D. J. Michel, H. Nahm, and J. Moteff, "Deformation Induced Twin Boundary Crack Formation in Type 304 Stainless Steel," *Mater. Sci. Eng.* 11: 97–102 (1973).

25. H. E. McCoy, *Mechanical Properties Test Data for Structural Materials Quart. Progr. Rep. Jan. 31, 1974*, ORNL-4948, pp. 220–21.

26. V. K. Sikka, *Mechanical Properties Test Data for Structural Materials Quart. Progr. Rep. Apr. 30, 1974*, ORNL-4963, pp. 119–23.

27. J. B. Conway, *Stress-Rupture Parameters: Origin, Calculation, and Use*, Gordon and Breach, New York, 1969.

28. F. R. Larson and J. Miller, "A Time-Temperature Relationship for Rupture and Creep Stresses," *Trans. ASME* 74: 765–75 (1952).

29. R. M. Goldhoff, "Towards the Standardization of Time-Temperature Parameter Usage in Elevated Temperature Data Analysis," *J. Test. Evaluation* 2(5): 387 (September 1974).

30. S. S. Manson and C. R. Ensign, *A Specialized Model for Analysis of Creep-Rupture Data by the Minimum Commitment, Station Function Approach*, NASA-TM-X-52999 (1970).

31. R. W. Swindeman, *Mechanical Properties Test Data for Structural Materials Quart. Progr. Rep. Oct. 31, 1974*, ORNL-5103, pp. 241–50.

32. V. K. Sikka, *Mechanical Properties Test Data for Structural Materials Quart. Progr. Rep. Oct. 31, 1974*, ORNL-5103, pp. 109–16.

33. M. K. Booker and T. L. Hebble, *Mechanical Properties Test Data for Structural Materials Quart. Progr. Rep. Oct. 31, 1974*, ORNL-5103, pp. 232–34.

34. M. K. Booker, *Mechanical Properties Test Data for Structural Materials Quart. Progr. Rep. Oct. 31, 1974*, ORNL-5103, pp. 148–57.

35. R. L. Orr, O. D. Sherby, and J. E. Dorn, "Correlations of Rupture Data for Metals at Elevated Temperatures," *Trans. Amer. Soc. Metals* 46: 113 (1954).

36. S. S. Manson and G. Succop, "Stress-Rupture Properties of Inconel 700 and Correlation on the Basis of Several Time-Temperature Parameters," pp. 40–46 in *Symposium on Metallic Materials for Service at Temperatures Above 1600°F, ASTM Spec. Tech. Publ.* 174, American Society for Testing and Materials, Philadelphia, 1956.

37. V. S. Ivanova, *Zavodsk. Lab.* 1955(2) as cited by E. E. Underwood, "Interrelationships Among High-Temperature Strength and Ductility Criteria," pp. 6-49–6-57 in *Joint International Conference on Creep* (Held in London, Sept. 30–Oct. 4, 1963), Institution of Mechanical Engineers, London, 1963.

38. W. E. Leyda and J. P. Rowe, *A Study of Time for Departure from Secondary Creep for Eighteen Steels*, ASM Technical Report P9-6.1, American Society for Metals, Metals Park, Ohio, 1969.

39. R. K. Penny and D. L. Marriott, *Design for Creep*, McGraw-Hill, New York, 1971, pp. 173–81.

40. M. K. Booker and C. O. Stevens, *Mechanical Properties Test Data for Structural Materials Quart Progr. Rep. Oct. 31, 1974*, ORNL-5103, pp. 158–61.

41. V. A. Singletary, *An On-Line Conversational Retrieval System for Orchis Text-Orientated Data Bases User's Manual*, ORNL-4951 (April 1974).

42. J. W. Woods, *Mechanical Properties Test Data for Structural Materials Quart. Progr. Rep. Jan. 31, 1974*, ORNL-4948, pp. 226–30.

43. R. L. Stephenson, "ADPLOT," unpublished computer program.

44. M. K. Booker, *Mechanical Properties Test Data for Structural Materials Quart. Progr. Rep. Oct. 31, 1974*, ORNL-4998, pp. 168–72.

45. V. A. Singletary, "ADTABLE," unpublished computer program.

46. M. K. Booker and B.L.P. Booker, "TENSIS," unpublished computer program.

47. R. T. King and G. M. Goodwin, *Fuels and Materials Development Program Quart. Progr. Rep. Sept. 30, 1972*, ORNL-TM-4055, pp. 5.14–5.16.

48. R. T. King, R. E. Adams, and G. M. Goodwin, *Fuels and Materials Development Program Quart. Progr. Rep. Mar. 31, 1972*, ORNL-TM-3797, pp. 210–20.

49. R. T. King and G. M. Goodwin, *Fuels and Materials Development Program Quart. Progr. Rep. Dec. 31, 1971*, ORNL-3703, p. 209.

50. R. T. King and E. Bolling, *Mechanical Properties Test Data for Structural Materials Quart. Progr. Rep. Apr. 30, 1974*, ORNL-4963, pp. 140–43.

51. R. T. King, E. Bolling, and L. T. Ratcliff, *Mechanical Properties Test Data for Structural Materials Quart. Progr. Rep. July 31, 1974*, ORNL-4998, pp. 178–87.

52. J. O. Stiegler, R. T. King, and G. M. Goodwin, "Effect of Residual Elements on Fracture Characteristics and Creep Ductility of Type 308 Stainless Steel Weld Metal," accepted for publication in *Journal of Engineering Materials and Technology*.

53. R. G. Berggren and R. T. King, *Mechanical Properties Test Data for Structural Materials Quart. Progr. Rep. Apr. 30, 1974*, ORNL-4963, pp. 143–51.

54. V. K. Sikka, ORNL, private communication, January 1975.

55. R. T. King and E. Bolling, *Fuels and Materials Development Program Quart. Progr. Rep. Dec. 31, 1972*, ORNL-TM-4105, pp. 5.22–5.23.

56. D. O. Hobson and T. L. Hebble, *Mechanical Properties Test Data for Structural Materials Quart. Progr. Rep. Oct. 31, 1973*, ORNL-4936, pp. 111–18.

57. N. C. Binkley, G. M. Goodwin, and D. G. Harman, "Effects of Electrode Coverings on Elevated Temperature Properties of Austenitic Stainless Steel Weld Metal," *Weld. J. (Miami)* 52(7): 306-s–311-s (July 1973).

58. R. T. King, J. O. Stiegler, and G. M. Goodwin, *Creep Properties of a Type 308 Stainless Steel Pressure Vessel Weld with Controlled Residual Elements*, ORNL-TM-4131 (May 1973).

59. N. C. Binkley, R. G. Berggren, and G. M. Goodwin, "Effects of Slight Compositional Variations on Type E308 Electrode Deposits," *Weld. J. (Miami)* 53(2): 91-s–95-s (February 1974).

60. J. O. Stiegler, R. T. King, and G. M. Goodwin, "Effect of Composition on Fracture Characteristics and Creep Ductility of Type 308 Stainless Steel Weld Metal," paper presented at Materials Division, ASME Winter Annual Meeting, Detroit, Nov. 12–15, 1973, to be published in special American Society of Mechanical Engineers publication.

61. L. D. Blackburn, "Isochronous Stress-Strain Curves for Austenitic Stainless Steels," pp. 15–48 in *The Generation of Isochronous Stress-Strain Curves*, ed. by A. O. Schaefer, American Society of Mechanical Engineers, New York, 1972.

62. R. L. Klueh, *Fuels and Materials Development Program Quart. Progr. Rep. Mar. 31, 1974*, ORNL-TM-4620, pp. 33–35.

63. R. J. Beaver, B. C. Leslie, and G. M. Slaughter, *Fuels and Materials Development Program Quart. Progr. Rep. June 30, 1974*, pp. 29–39.

64. G. V. Smith, *Supplemental Report on the Elevated-Temperature Properties of Chromium-Molybdenum Steels (An Evaluation of 2 1/4 Cr-1 Mo Steel), ASTM Data Ser. Publ.* DS 6-S2, American Society for Testing and Materials, Philadelphia, March 1971.

65. R. L. Klueh, *Fuels and Materials Development Program Quart. Progr. Rep. June 30, 1974*, ORNL-TM-4688, pp. 50–55.

66. R. L. Klueh, *Mechanical Properties Test Data for Structural Materials Quart. Progr. Rep. Oct. 31, 1974*, ORNL-5103, pp. 219–21.

67. K. F. Hale, p. 650 in *Proc. 4th Intern. Conf. Electron Microscopy*, Vol. 1, Springer-Verlag, Berlin, 1960.

68. R. G. Baker and J. Nutting, *J. Iron Steel Inst.* 192: 257 (1957).

69. K. J. Irvine, J. D. Murray, and F. B. Pickering, "Structural Aspects of Creep-Resisting Steel," p. 246 in *Structural Processes in Creep*, Iron and Steel Institute, London, 1961.

70. J. Glen and J. D. Murray, p. 40 in *Steels for Reactor Pressure Circuits, ISI Spec. Rept.* 69, Iron and Steel Institute, London, 1961.

71. C. R. Austin, C. R. St. John, and R. W. Lindsay, *Trans. AIME* 162: 84 (1945).

72. C. R. Brinkman, J. R. Strizak, and C. O. Stevens, *Mechanical Properties Test Data for Structural Materials Quart. Progr. Rep. Oct. 31, 1974*, ORNL-5103, pp. 220–31.

73. Personal communications from Mr. R. Ellis, General Atomic Co., Oct. 15 and Nov. 15, 1974.

74. S. S. Manson, G. R. Halford, and M. H. Hirschberg, *Creep-Fatigue Analysis by Strain-Range Partitioning*, NASA-TM-X-67838, Lewis Research Center, 1971.

75. M. K. Booker and T. L. Hebble, *Mechanical Properties Test Data for Structural Materials Quart. Progr. Rep. Oct. 31, 1974*, ORNL-5103, pp. 232–34.

76. D. O. Hobson and T. L. Hebble, *Mechanical Properties Test Data for Structural Materials Quart. Progr. Rep. Oct. 31, 1974*, ORNL-5103, pp. 234–36.

77. C. R. Brinkman, M. K. Booker, J. P. Strizak, and W. R. Corwin, "Elevated-Temperature Fatigue Behavior of 2 1/4 Cr-1 Mo Steel," submitted to ASME for presentation and publication at the Second National Congress on Pressure Vessels and Piping, San Francisco, June 23–25, 1975.

78. R. L. Klueh, *Mechanical Properties Test Data for Structural Materials Quart. Progr. Rep. Oct. 31, 1974*, ORNL-5103, pp. 207–18.

79. D. A. Canonico and W. J. Stelzman, ORNL, private communication.

80. D. I. Roberts and J. R. Ellis, General Atomic Co., private communication.

81. R. L. Klueh, *Fuels and Materials Development Program Quart. Progr. Rep. Mar. 31, 1974*, ORNL-TM-4620, pp. 49–53.

82. R. L. Klueh, *Fuels and Materials Development Program Quart. Progr. Rep. June 30, 1974*, ORNL-TM-4688, pp. 68–74.

83. R. L. Klueh, *Mechanical Properties Test Data for Structural Materials Quart. Progr. Rep. Oct. 31, 1974*, ORNL-5103, pp. 236–40.

84. H. E. McCoy, *High-Temperature Structural Design Methods for LMFBR Components Progr. Rep. Dec. 31, 1973*, ORNL-4947, pp. 1–14.

85. C. E. Pugh, *High-Temperature Structural Design Methods for LMFBR Components Quart. Progr. Rep. Mar. 31, 1974*, ORNL-4977, pp. 37–57.

86. R. W. Swindeman and C. E. Pugh, *Creep Studies on Type 304 Stainless Steel (Heat 8043813) Under Constant and Varying Loads*, ORNL-TM-4427 (June 1974).

87. R. W. Swindeman, "Creep Testing" in *High Temperature Structural Design Methods for LMFBR Components Progr. Rep. June 30, 1974*, ORNL-5005, pp. 1–22.

88. N. G. Ettenson and M. Manjoine, *Mechanical Properties Test Data for Structural Materials Quart. Progr. Rep. Apr. 30, 1974*, ORNL-4963, pp. 201–19.

89. R. W. Swindeman, "Representation of the High-Temperature Tensile Behavior of Reannealed Type 304 Stainless Steel by the Voce Equation," ASME paper 74-WA/Mat-7 presented at the ASME Winter Annual Meeting, New York, Nov. 17–22, 1974.

90. R. W. Swindeman, "Variation of Short-Term Creep Properties with Annealing Conditions," *High-Temperature Structural Design Methods for LMFBR Components Progr. Rep. Oct. 1972 Through Mar. 1973*, ORNL-TM-4089 pp. 202–04.

91. F. Garofalo, *Fundamentals of Creep and Creep-Rupture in Metals*, Macmillan Company, New York, 1965, pp. 223–24.

92. V. K. Sikka and C. R. Brinkman, *Effect of Aging on Tensile and Creep Properties of Types 304 and 316 Stainless Steel*, report in preparation.

93. J. M. Corum, J. A. Clinard, and W. K. Sartong, "Cyclic Elastic-Plastic Analysis of Beam B6 and Comparisons with Test Results," *High-Temperature Structural Design Methods for LMFBR Components Progr. Rep. Oct. 1972 Through Mar. 1973*, ORNL-TM-4089, pp. 115–31.

94. K. C. Liu, Reactor Division, ORNL, private communication.

95. D. C. Ludwigson, "Modified Stress-Strain Relation for FCC Metals and Alloys," *Met. Trans.* 2: 2825–28 (1971).

96. C. E. Jaske and B. N. Leis, *Final Report on Cyclic Stress-Strain of 2 1/4 Cr-1 Mo Steel*, Battelle Columbus Laboratory Report ORNL-Sub-4004-1 (October 1974).

97. C. C. Schultz, "Investigations of Creep Failure Under Uniaxial and Multiaxial Conditions," *Mechanical Properties Test Data for Structural Materials Quart. Progr. Rep. June 30, 1974*, ORNL-5103, pp. 260–85.

98. W. R. Corwin, *Mechanical Properties Test Data for Structural Materials Quart. Progr. Rep. Oct. 31, 1974*, ORNL-5103, pp. 287–93.

6. WESTINGHOUSE ADVANCED REACTORS DIVISION

E. C. Bishop

6.1 INTRODUCTION

The program being performed at Westinghouse Advanced Reactors Division (ARD) is entitled "Validation of High Temperature Design Methods and Criteria" (189a No. 04165). Two of the tasks in this program are "Basic Specimen Testing" and "Tubular Specimen Testing." The objective of these tasks is to design and test specimens of increasing complexity to determine the inelastic behavior and strain tolerances of Types 304 and 316 stainless steel under complex stress distributions. This report covers the work performed during the period from August 31, 1974 to November 30, 1974.

6.2 BASIC SPECIMEN TESTING - N. J. Ettenson, M. Manjoine (Westinghouse Research Laboratories)

A variety of specimen designs have been selected for this task, as shown in Table 6.1 and Figure 6.1. Data obtained to date are presented in Table 6.2.

6.2.1 Uniaxially Loaded Specimen Models with Nonuniform Gage Section (304 SS, Heat 9T2796)

6.2.1.1 Test Piece Description

Types C and D test piece designs, as shown in Table 6.1, are used for this part of the test program.

6.2.1.2 Current Results

The test of circumferentially notched bar D6 was stopped at 4023 hours, which is near the estimated half-life. Fine cracks were observed in the oxide at the base of the notch. Half of the specimen, D6-1, will be sectioned to determine the extent of the crack in the base metal. The other half, D6-2, has not broken after a total of 7333 hours of testing, which is about double the rupture life of the unnotched base metal.

TABLE 6-1. MODEL TYPES

Specimens From Base Material[a]

Code Designation	Description[b]
A.	Plane Stress Specimen 1/3 x 2/3 x 3 in. (8.5 x 17 x 76.2 mm) gage section.
B.	Plate Specimen 1/3 x 10/3 x 3 in. (8.5 x 85 x 76.2 mm) gage section.
C.	Plate Specimen with Central Hole of 1/3 in. (8.5 mm) Diameter, 1/3 x 10/3 x 3 inc. (8.5 x 85 x 76.2 mm) plate section.
D.	Round Circumferentially Notched Specimen, Major Diameter = 0.96 in. (24.4 mm), Minor Diameter = 0.64 in. (16.2 mm), K_t = 4, Root Radius = 0.018 in. (0.46 mm), Two nearly identical notches in specimen.
E.	Plate Specimen in bending and tension, 1/3 x 10/3 x 2 in. (8.5 x 85 x 50.8 mm) plates section, eccentric load
F.	Designation generally refers to failure or fracture; therefore, it is not used to identify a type of model.
G.	Plane Strain Specimen 1/3 x 10/3 x 1 in. (8.5 x 85 x 25.4 mm) gage section. Ends constrained in transverse direction
H.	Biaxially Loaded Notched Plates, Wedge-opening-loaded Plates with 1/3 in. (8.5 mm) Diameter Notch.

Specimen With Welds

BTW - B-type plate specimen with transverse weld at mid-length of gage section.

BAW - B-type plate specimen with axial weld at center of gage section.

CTW - C-type specimen with hole through transverse weld.

CAW - C-type specimen with hole through axial weld.

DTW - D-type specimen with notch root in transverse weld.

DZTW - D-type specimen with notch root at weld fusion line of heat affected zone.

GTW - G-type specimen with transverse weld at mid-gage length.

GAW - G-type specimen with axial weld at center of gage section.

(a) Type 304 SS (HT9T2796) annealed at 2000°F.

(b) Reference Figure 3-1.

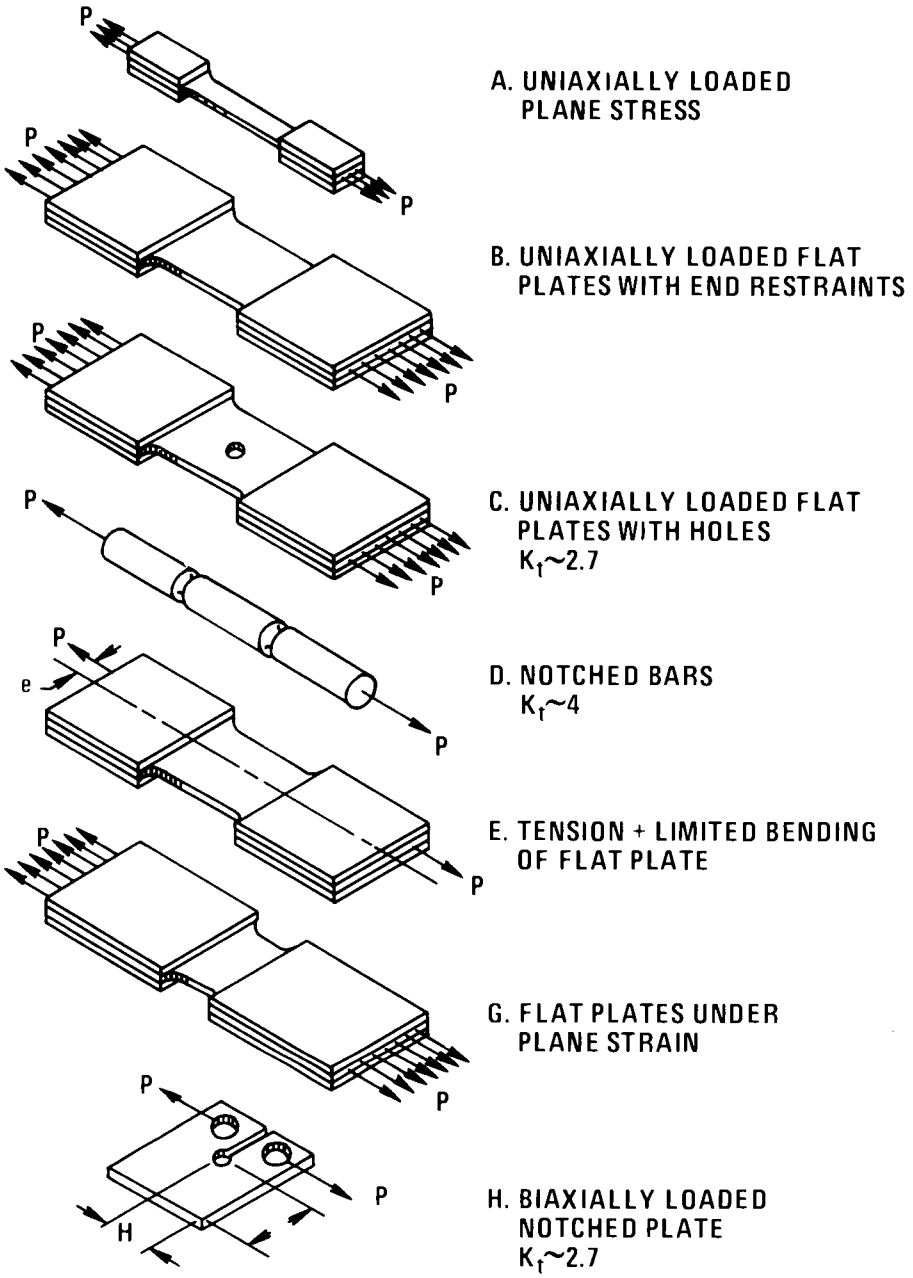

Figure 6.1 Basic Specimen Types

TABLE 6-2. SUMMARY OF CREEP DATA, TYPE 304 STAINLESS STEEL* AT 1100°F (593°C)

Test No. (Gage Section)	Loading Data: Stress (ksi)	Loading Data: Stress (MPa)	Loading Data: Plastic Strain (%)	Creep Data: Creep Rate (%/hr)	Creep Data: Increment Strain (%)	Creep Data: Increment Time (hr)	Creep Data: Accumulated Strain (%)	Creep Data: Accumulated Time (hr)	Creep Data: Permanent Strain (%)
A1	21.0	144.8	4.66	2.2×10^{-3}	1.10	303	1.10	303[a]	5.76
(1/3x2/3x3 in)				2.2×10^{-3}	0.89	403	1.99	706[a]	6.65
(8.5x17x76.2mm)					1.48	544	3.47	1250[b]	8.13
					0.18	20	3.65	1270[c]	8.31
					3.69	556	7.34	1826	12.00[d]
A2	10.0	68.95	0.215	8.5×10^{-5}	0.228	2180	0.228	2180[a]	0.443
(1/3x2/3x3 in)				6.2×10^{-5}	0.028	405	0.256	2585[e]	0.471
(8.5x17x76.2mm)	11.0	75.84	0	8.6×10^{-5}	0.124	1349	0.380	3934[e]	0.595
	12.5	85.68	0	2.0×10^{-4}	0.213	1002	0.593	4936[e]	0.808
	15.0	103.4	0.014	2.5×10^{-4}	0.811	1848	1.404[a]	6784[e]	1.619
	21.0	144.8	0.646	4.5×10^{-3}	28.75	4266	30.15	11050[h]	31.0
B1	21.0	144.8	5.34	1.4×10^{-3}	1.76	666	1.76	666[a]	7.10
(1/3x10/3x3 in)				8.8×10^{-4}	1.03	1005	2.79	1671[a]	
(8.5x85x76.2mm)				1.7×10^{-3}				3000[c]	
					1.72	1587	4.51	3258[a]	9.85[g]
								3525[h]	
B2	10.0	68.95	0.273[i]	8.6×10^{-5}	0.31	1644	0.31	1644[a]	0.58
(1/3x10/3x3 in)	↓			9.0×10^{-5}	0.14	1462	0.45	3106[e]	0.72
(8.5x85x76.2mm)	11.0	75.84	0	1.1×10^{-4}	0.16	1804	0.61	4910[e]	0.88
	12.5	85.68	0	2.0×10^{-4}	0.33	1364	0.94	6274[e]	1.21
	15.0	103.4	0.051	4.7×10^{-4}	1.00	1302[a]	1.93	7576[e]	1.98
	21.0	144.8	1.880	8.4×10^{-3}	16.47	1563	18.40	9139[h]	20.33
C1	23.3[k]	160.6	8[n]		1.7[n]	100[c]			
(1/3x10/3x3 in)							22.9[n]	138[d]	
(8.5x85x76.2mm)									
Central Hole									
1/3 in(8.5mm) dia.									
C2	10.0[k]	68.95	0.14[n]		0.62[n]	2808[a]	0.62[n]	2808[c]	0.76[n]
Same as C1	11.0[k]	75.84	0		0.40[n]	1290	1.02[n]	4098	1.16[n]
	12.5[k]	85.68	0		0.50[n]	1300[d]	1.52[n]	5398	1.66[n]
	15.0[k]	103.4	0.28[n]		0.82[n]	1148	2.34[n]	6546	2.76[n]
	18.0[k]	124.1	0.06[n]		3.31[n]	1630[a]	5.65[n]	8176[k]	6.13[n]
					0.89[n]	791[a]	6.54[n]	8967	7.02[n]
					1.05[n]	944[a]	7.59[n]	9911	8.07[n]
					1.12[n]	1339[d]	8.71[n]	11250	9.19[n]
					1.60[n]	1468	10.30	12718[h]	10.79
						6172[d]			
C3	21.0[k]	144.8	4.4[n]		1.5[n]	325[c]			
Same as C1							4.1[n]	397[h]	8.5[n]
D1	30.0	206.8							
D=0.96 in(24.4mm)									
d=0.64 in(16.2mm)									
R=0.19 in(0.46mm)									
D1-1	30.0	206.8	2.60[t]		0.30[t]	137	0.30[t]	137	2.90[t]
					0.20[t]	120	0.50[t]	239[k]	3.10[t]
D1-2	30.0	206.8	2.20[t]		0.26[t]	137	0.26[t]	137	2.46[t]
					0.22[t]	113	0.48[t]	250[c]	2.68[t]
							10.92[t]	305[d]	13.12[t]
D2-1	25.0	172.4	0.009[r]				0.006[r]	1371	0.015[r]
								1371[g]	2.17[t]

TABLE 6-2 (CONTINUED)

Test No. (Gage Section)	Loading Data: Stress (ksi)	Loading Data: Stress (MPa)	Loading Data: Plastic Strain (%)	Creep Data: Creep Rate (%/hr)	Creep Data: Increment Strain (%)	Creep Data: Increment Time (hr)	Creep Data: Accumulated Strain (%)	Creep Data: Accumulated Time (hr)	Permanent Strain (%)
D2-2	25.0	172.4	0.009[r]				0.006[r]	1240[c]	
								1371[d]	5.3[t]
D3	21.0	144.8	0.002[r]					5499[h]	
D4	10.0	68.95	0			406		406[e]	
	11.0	75.84	0			477		883[e]	
	12.5	85.68	0			434		1317[e]	
	15.0	103.4	0			404		1721[e]	
	21.0	144.8	0.001[r]		0.004[r]	433		2154[e]	
	25.0	172.4	0.003[r]		0.033[r]	1581[g]		3735[u]	
D4-1	One Notch of Specimen D4 To Be Sectioned.								
D4-2	25.0	172.4				2904[h]		5058[h]	
D5	23.0	158.4				1681[g]		1681	
D5-1	One Notch of Specimen D5 To Be Sectioned.								
D5-2	23.0	158.4				150		1831[d]	
D6	20.0	137.9			1.0[t]	4023[u]			
D6-1	To Be Sectioned.								
D6-2	20.0	137.9						7333[f]	
E1	20.0	137.9	7.77[n]	1.2×10^{-2}	1.10[n]	94	1.10[n]	94[a]	9.27[n]
	13.0[v]	89.64	±2.7	3.5×10^{-3}	2.27[n]	648	3.27[n]	742[y]	11.54[n]
					0.63[n]	167	4.00[n]	909[s]	12.17[n]
					0.58[n]	168	4.58[n]	1077[s]	12.75[n]
					0.57[n]	168	5.15[n]	1245[s]	13.32[n]
					0.46[n]	115	5.61[n]	1360[a]	13.78[n]
					0.79[n]	262	6.40[n]	1622[s]	14.57[n]
				3.0×10^{-3}	0.58[n]	190	6.98[n]	1812[s]	15.15[n]
					0.65[n]	215	7.63[n]	2027[s]	15.80[n]
					0.90[n]	263	8.53[n]	2290[s]	16.70[n]
				2.6×10^{-3}	0.49[n]	190	9.02[n]	2481[s]	17.19[n]
					0.52[n]	171	9.54[n]	2625[s]	17.71[n]
					0.77[n]	237	10.31[n]	2889[s]	18.48[n]
					1.81[n]	238	12.12[n]	3127[h]	20.29[n]
G-1	25.0	172.4	2.00[i]		0.88[i]	47[a]	0.88	47	2.47
				3.5×10^{-3}	1.12[i]	268[a]	2.00	315	4.00
					0.90[i]	170[a]	2.90[e]	485[g]	4.90
					0.65[i]	83	3.55	568[h]	5.60
G-2	21.0	144.8	0.43	3.9×10^{-4}	1.34	1195[a]	1.34	1195	1.77
(1/3x10/3x1 in)			0	1.0×10^{-4}	0.83	5520[a]	2.17	6715[e]	2.60
(8.5x85x25mm)	25.0	172.4	0.01	2.3×10^{-3}	1.80	700		7415	
					2.50	450[c]	4.67	7865	
					4.43	283[a]	6.60	8148	
						1827[l]		8552[d]	
BAW-1	25.0	172.4	0.25	8.3×10^{-3}	4.35[n]	477[a]	4.35	477	4.60[g]
B Type Specimen				1.1×10^{-2}	8.32[n]	765[a]	12.67	1242	12.92
With Central Axial				1.5×10^{-2}	3.42[n]	216[a]	16.09	1458	16.34
Weld					2.35[n]	71	18.44	1529	18.69
								1532[d]	
CAW-1	18.0	124.1	0.033[n]				0.77[n]	4487[f]	
C Type Specimen									
With Central Axial									
Weld									
DTW-1	Not Started.								
DTW-2	25.0	172.4	0.003[r]		0.003[r]	5035[e]			
DZTW-1	25.0	172.4			0.002[r]	978[d]			

TABLE 6-2 (CONTINUED)

Test No. (Gage Section)	Loading Data: Stress (ksi)	Loading Data: Stress (MPa)	Loading Data: Plastic Strain (%)	Creep Data: Creep Rate (%/hr)	Creep Data: Increment Strain (%)	Creep Data: Increment Time (hr)	Creep Data: Accumulated Strain (%)	Creep Data: Accumulated Time (hr)	Creep Data: Permanent Strain (%)
GAW-1	23.0	158.6	0.10[n]	5.1×10^{-3}	1.56[n]	1882	1.56[n]	188	1.65[n]
C Type Specimen				4.2×10^{-3}	1.93[n]	452[a]	3.59[n]	640	3.69[n]
With Axial				5.2×10^{-3}	1.64[n]	307[a]	5.13[n]	947	5.23[n]
Weld				5.3×10^{-3}	2.00[n]	379[a]	7.13[n]	1326[g]	7.23[n]
					2.21[n]	456[a]	9.34[n]	1782	9.44[n]
					3.17[n]	576[a]	12.52	2358	12.62[n]
					4.69	528[a]	17.21	2886	17.31[n]
					8.20	210	25.41	3096[d]	25.51[n]
BTW-1	21.0	144.8	0.17[n]	3.2×10^{-3}	1.29[n]	339[a]	1.29[n]	339	1.47[n]
B Type Specimen			0.01	3.2×10^{-3}	2.35[n]	718[a]	3.64[n]	1057[g]	3.82[n]
With Transverse					1.25[n]	474[a]	4.89[n]	1531	5.07[n]
Weld							5.67[n]	1724	
								1734[d]	
GTW-1	25.0	172.4	0.09	4.7×10^{-3}	1.62[n]	240[a]	1.62	240	1.71
G Type Specimen						208		448[d]	
With Transverse Weld									

[*] HT 9T2796, annealed 2000F (1094C)

[a] Interrupted for photographic measurement

[b] Transition at 0.2% OFFSET

[c] Transition at double minimum rate

[d] Rupture, R

[e] Stress raised (step-loaded test)

[f] Test in progress

[g] Crack initiated

[h] Test terminated, crack tearing

[i] Strain gage average, bending noted

[j] Specimen rotated 180° to investigate bending

[k] Net Section Stress, Gross Section Stress = 0.9 N.S.S.

[l] Time at final strain

[m] Average strain at central hole

[n] Average overall strain

[p] Test in preparation

[q] Specimen to be sectioned to determine damage at 78% of estimated rupture life

[r] Deflection of notch, inches (25.4 mm)

[s] Loaded and reload to determine retained bending.

[t] True strain = $\ln(A_o/A)$

[u] Test interrupted, 1/2 of specimen continued

[v] Nominal elastic bending stress

6.2.2 Eccentrically Loaded Specimens With Uniform Gage Section (304 SS, Heat 9T2796)

6.2.2.1 Test Piece Description

The Type E test piece design, as shown in Table 6.1, is used for this part of the test program.

6.2.2.2 Current Results

Specimen E-1 was loaded in bending and tension by an eccentric load at 0.36 inch (9.1 mm) from the vertical centerline of the gage section and at a distance of 12 inches (305 mm) from the horizontal centerline. Tensile stress was 20 ksi and the nominal elastic bending stress was $\pm$ 13 ksi. Yielding began on the higher stressed side at 23 percent of maximum loading, on the middle of the gage section at about 31 percent of maximum loading, and on the lower stressed side at about 64 percent of maximum loading. The plastic strain at full load, which is based on the nominal gage length of the straight section, was 7.77 $\pm$ 2.7 percent. Using the ORNL data,[1] for this heat of material the 10.47 percent plastic strain on loading the higher stressed side would be expected at 33 ksi. The actual stress, however, must relax with plastic flow when the centroid of the gage section moves toward the load line of action. To investigate the relaxation of the bending stress, the test specimen was unloaded and reloaded periodically to measure the elastic deflections (Table 6.2). The average permanent strains and the elastic bending deflections as functions of time are shown in Figure 6.2. The elastic bending deflection drops rapidly with plastic flow on loading and then gradually decreases with creep of the specimen. The creep curves for the tension-tension and tension-compression sides are shown in Figure 6.3. The creep rate is initially much higher on the tension-tension side, but the rate on each side gets closer together as creep strains are accumulated. The test was stopped at 3127 hours because a crack at the fillet was propagating rapidly. The rupture life for this specimen is plotted in Figure 6.4 at an average tensile stress of 20 ksi. The life is slightly lower than that of the base rupture data and lower than that estimated for the B-type specimens, which are similar in configuration.

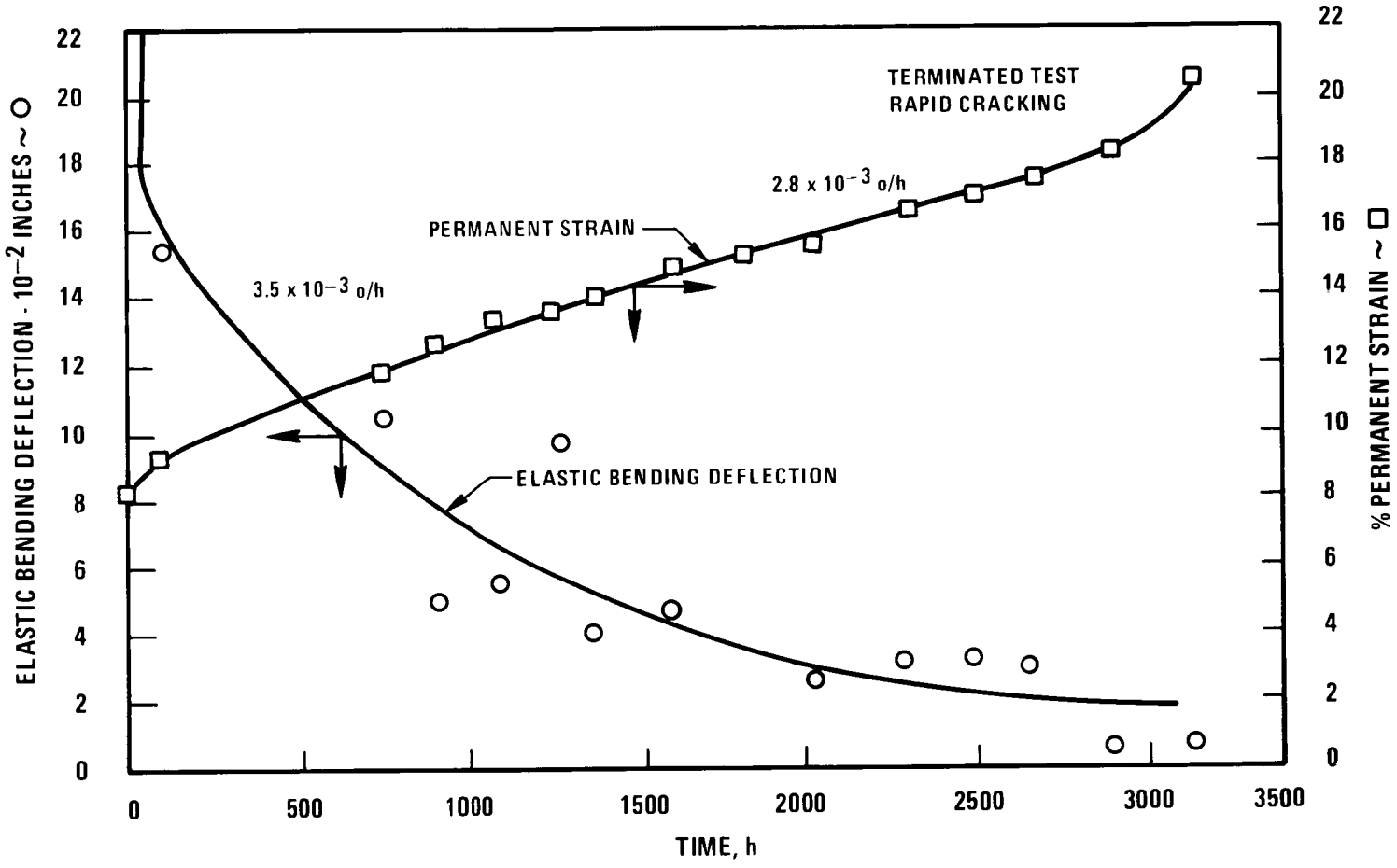

Figure 6.2 Influence of Permanent Strain on Elastic Bending Deflection

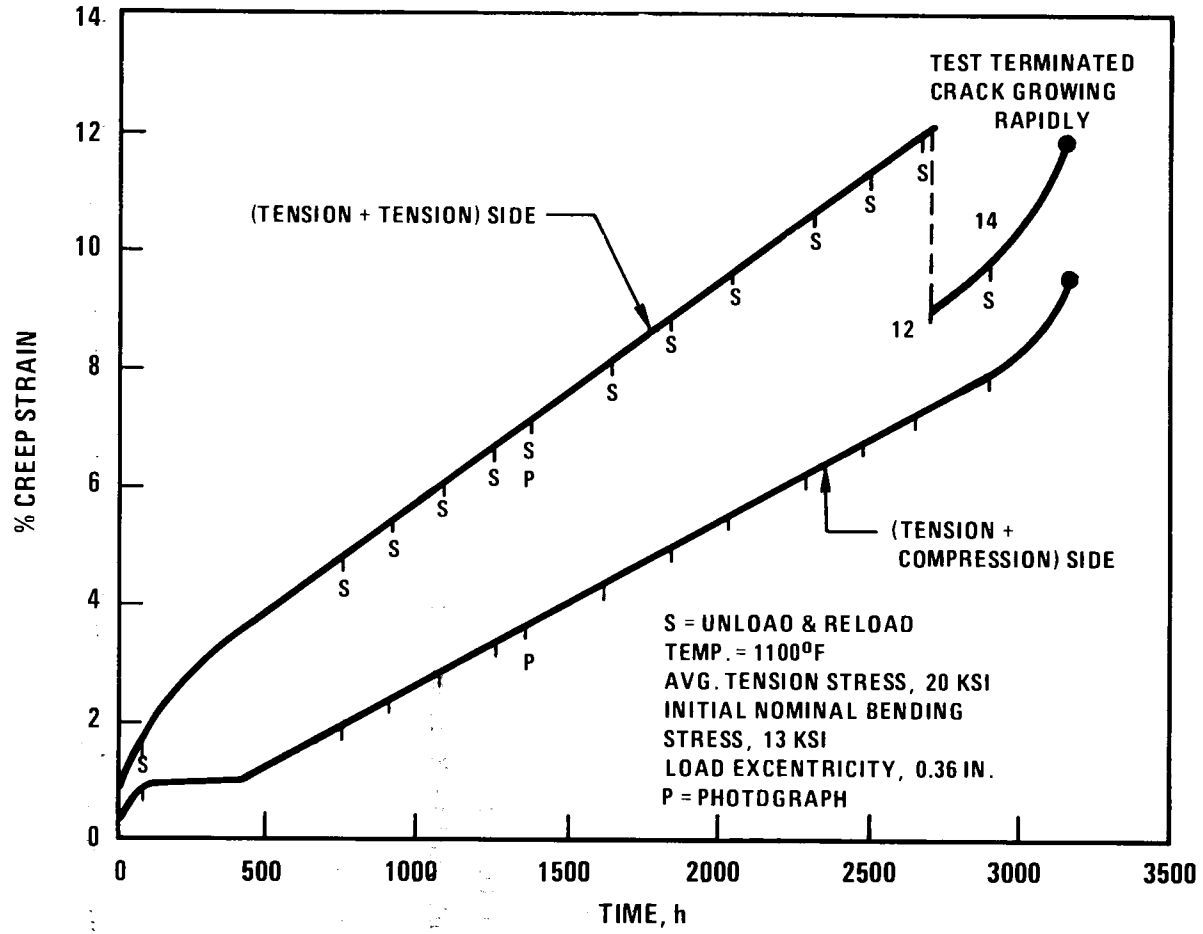

Figure 6.3 Overall Creep Extension Curves of E1 Under Tension and Bending

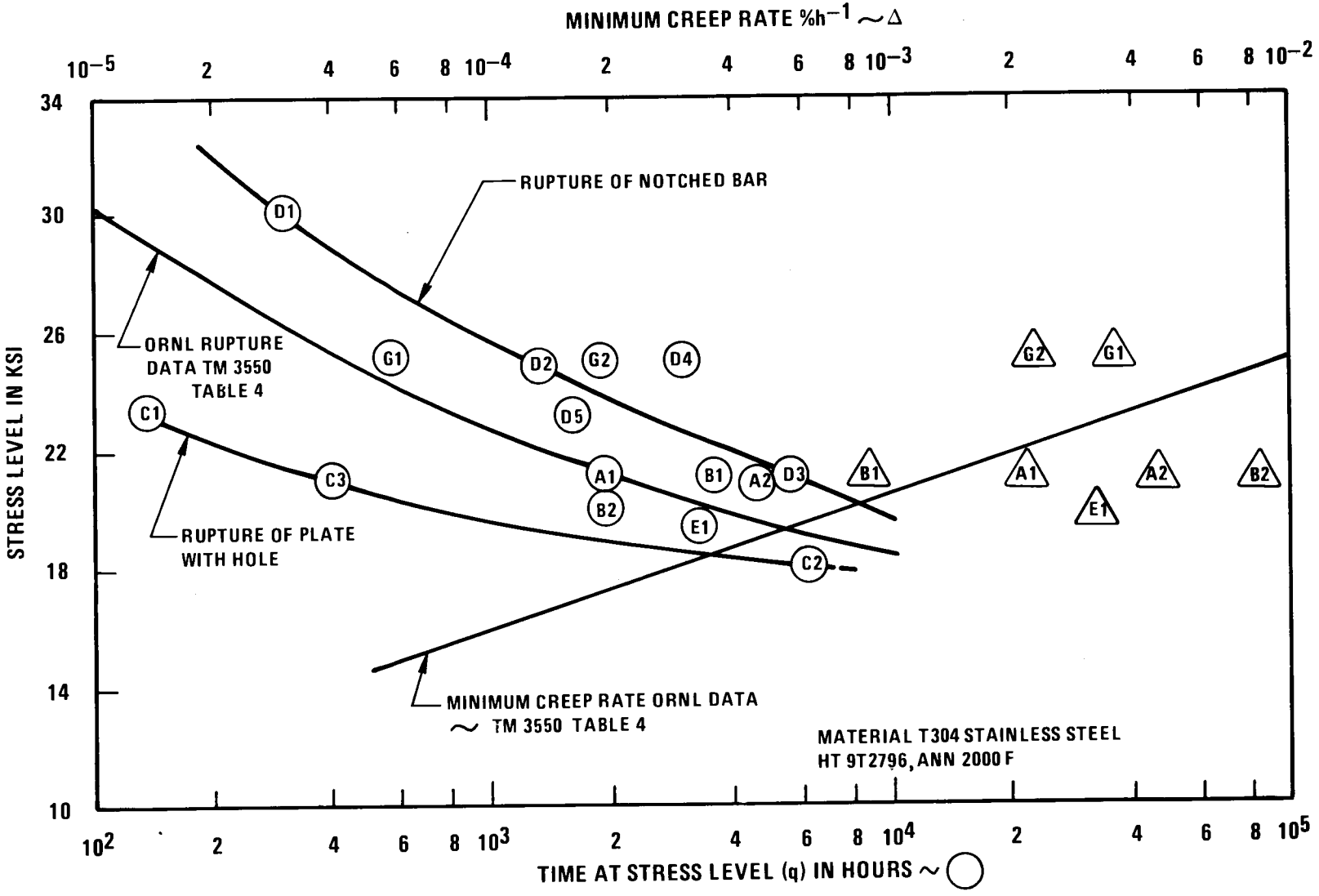

Figure 6.4 Basic Specimen Creep Data at 1100°F

6.2.3 Specimens with Welds (304 SS, Heat 9T2796)

6.2.3.1 Test Piece Description

The test piece designs used for this part of the program are described in Table 6.1.

6.2.3.2 Current Results

Circumferentially notched bar DTW-2 has completed over 5000 hours of testing. This is about double the rupture life of the unnotched weld metal reported by ORNL, as shown in Figure 6.5. The specimen will now be loaded to rupture at a higher stress of 28 ksi.

Axial weld specimen GAW-1 began to crack in the heat-affected zone (HAZ) at 1326 hours (Table 6.2), and extensive cracking continued at 2886 hours (Figure 6.6). The crack initiated in the HAZs on each side of the axial weld (Figure 6.6a) and grew more rapidly into the base metal. Due to the difference in the width of the weld on each side of the specimen, a different pattern is seen on the opposite side of the specimen (Figure 6.6b). Complete failure occurred 210 hours later, at 3096 hours.

6.3 TUBULAR SPECIMEN TESTING - K. C. Thomas, P. C. S. Wu, A. K. Dhalla

6.3.1 Test Piece Description

The tubular test pieces used in this program are Type 304 stainless steel, heat 9T2796, of 1.8-inch OD, 1.6-inch ID, and 8.7-inch length. However, thinner wall (1.7-inch OD and 1.6-inch ID) test pieces are planned for use in future tests to reduce the stress variation through the wall thickness during multiaxial testing.

6.3.2 Test Results and Planning (304 SS, Heat 9T2796)

A summary of the test results to date for constant load tests is presented in Table 6.3. Multiaxial variable load tests planned for Type 304 stainless steel are shown in Table 6.4, which also reports test data obtained on Specimen 13 during the current period.

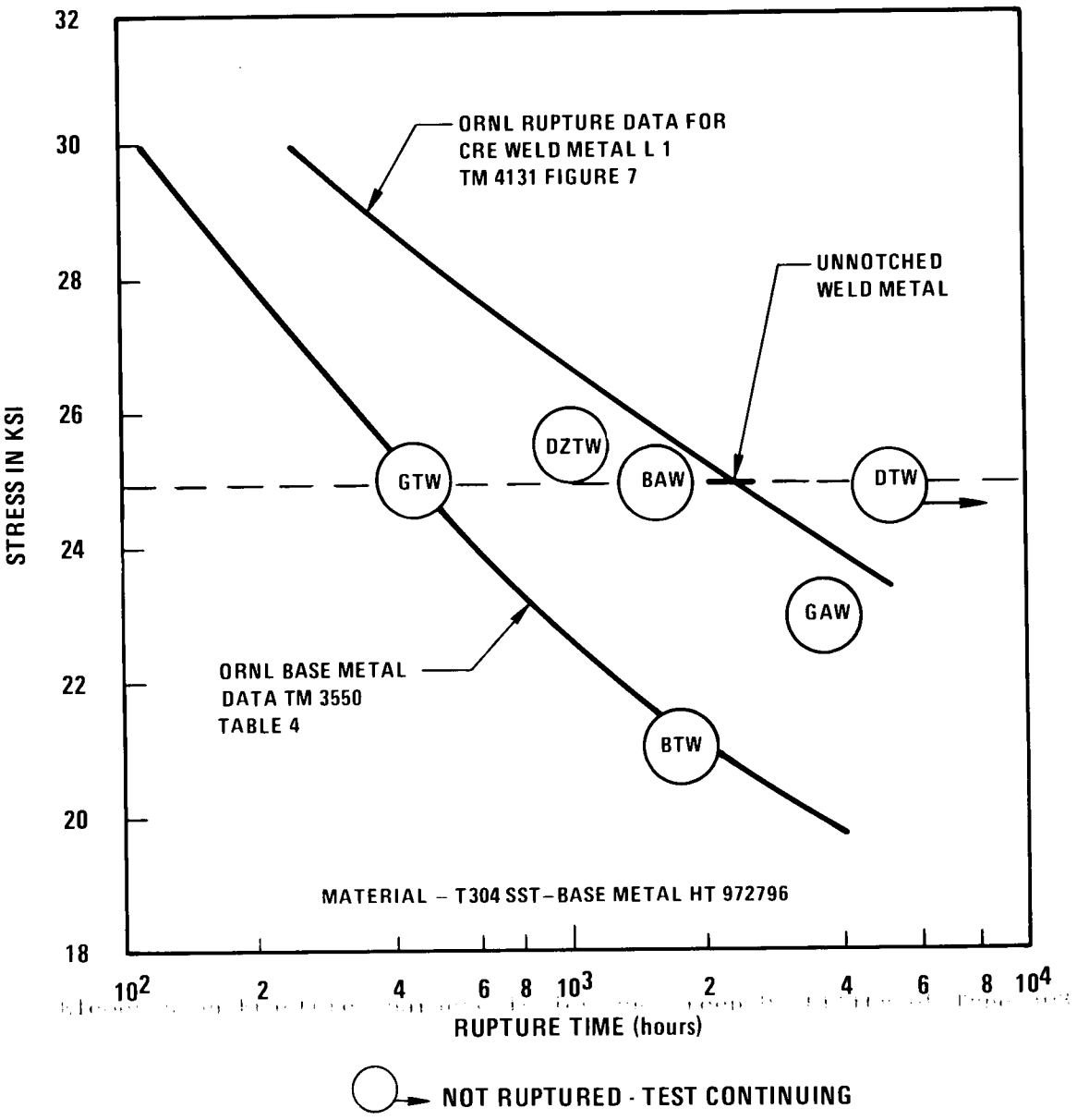

Figure 6.5 Basic Specimen Rupture Data for Welds at 1100°F

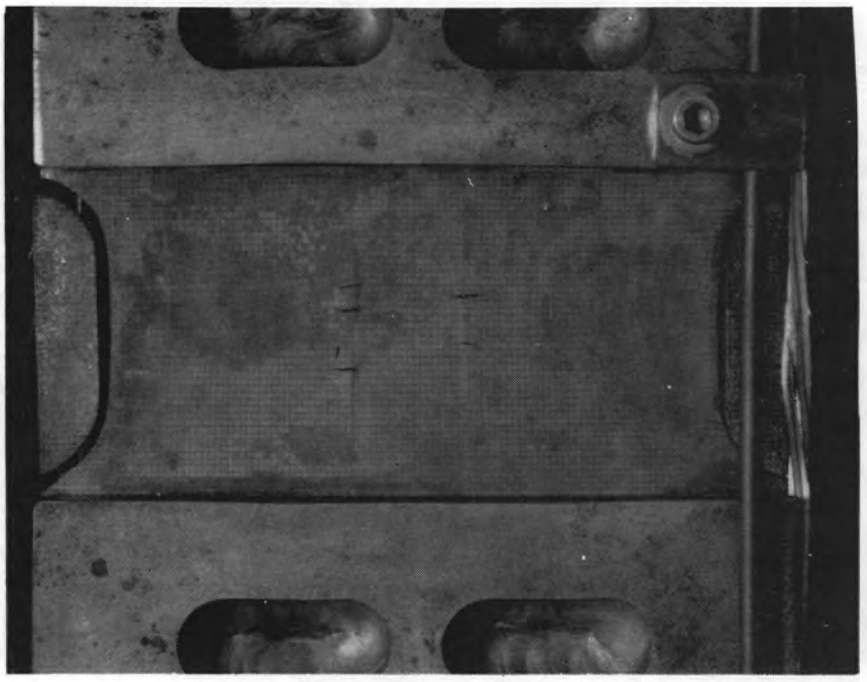

(a) VIEW OF CRACKING AT HEAT AFFECTED ZONES

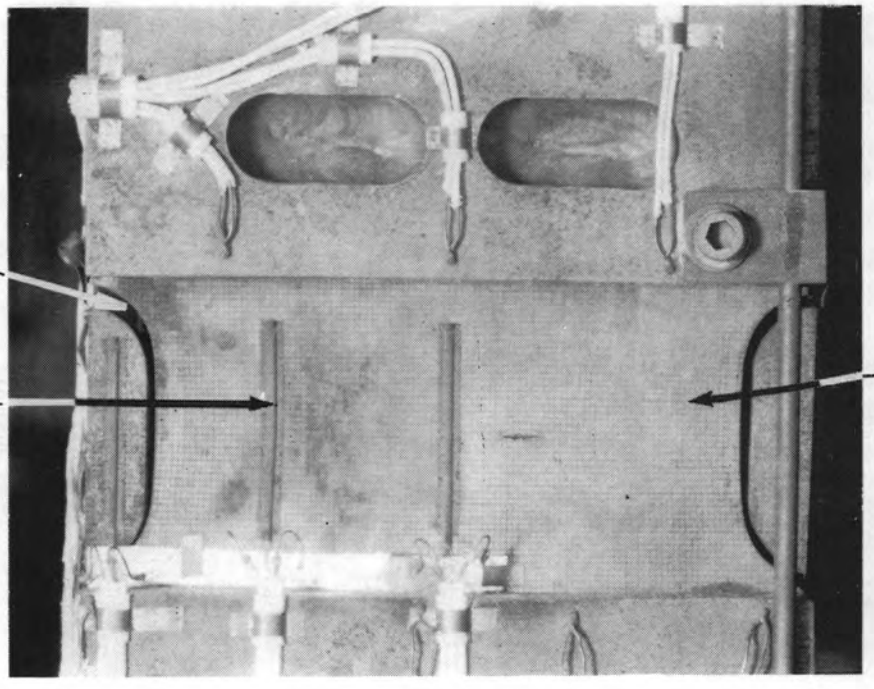

(b) VIEW OF CRACKING ON SIDE OPPOSITE (a)

Figure 6.6 Specimen GAW-1 After 2886 Hours at 23 KSI and 1100°F

TABLE 6-3. TYPE 304 STAINLESS STEEL TUBULAR TEST RESULTS

Uniaxial Creep Test Results

Test No.	Nominal Test Temperature (°F)	Axial Stress (psi)	Test Hours Accumulated	Axial Loading Strain (%)	Axial Creep Strain (%)	Total Axial Strain (%)
1B	1100	25,000	241.5	0.7988	3.5572	4.3660
2A	1100	10,000	2016	0.0490	0.0697	0.1187
2B	1100	10,000	2000	0.0780	0.0880	0.1660
3A	1100	20,000	336	- - -	0.9591	- - -
3B	1100	20,000	1990	0.1783	2.7468	2.9251
3C	1100	7,700	2002	0.0461	0.0534	0.0995
3D	1100	5,000	1721.3	0.0253	0.0089	0.0342
3F	1100	15,000	1556	0.4855	1.1224	1.1710

Multiaxial Creep Test Results

Test No.	Nominal Test Temp. (°F)	Axial Load (lbs)	Nominal Internal Pressure (psi)	Nominal Effective Stress (psi)	Nominal Principal Stress Ratio (σ_r/σ_z)	Test Time (hours)	Average[a] Loading Strain (%)		Nominal Average Creep Strain[a]			
							Axial	Hoop	Radial	Hoop	Axial	Effective
4A	1100	323.0	1209.5	10,000	2.0	1965.7	0.01048	0.02174	-0.12711	0.12466	0.00245	0.1453
5	1115	484.0	1814.3	15,000	2.0	1998.0	0.09208	0.08499	-0.57795	0.54670	0.03125	0.6499
6[c]	1100	0.0	2716.9	20,000	2.0	762.0	0.13321	2.71103	-2.12850	2.16000	-0.03150	2.4700
7A	1100	1211.0	1180.0	10,000	1.5	1648.0	0.04240	0.03521	-0.02101	0.01360	0.00741	0.0211
7[b]	1100	1211.0	1180.0	10,000	1.5							
8	1100	1515.0	2000.0	15,000	1.5	2009.3	0.19414	0.80047	-0.84800	0.71900	0.12900	0.9130
9[d]	1100	2018.6	2668.4	20,000	1.5	573.4	0.00541	0.02334	-3.74600	3.31000	0.43600	4.0900
10	1100	2670.0	1049.4	10,000	1.0	2033.8	0.04363	0.01994	-0.06130	0.03890	0.03330	0.0600
11	1100	4005.0	1574.0	15,000	1.0	2012.9	0.03288	0.07339	-0.48900	0.21100	0.27800	0.4720
12[d]	1100	5340.7	2353.0	20,000	1.0	1096.5	1.82117	0.99892	-2.82000	1.56000	1.26000	2.7900

(a) The axial loading strain is the average of two readings. The loop strain is the average of three readings.

(b) Test terminated due to instability of the strain measuring system.

(c) Sample rupture after 808 hours under the test condition.

(d) Test terminated because the sample has already reached tertiary creep stage.

TABLE 6-4. TYPE 304 STAINLESS STEEL TUBULAR SPECIMEN CREEP TEST RESULTS - MULTIAXIAL VARIABLE LOAD

Test Number	Nominal Test Temperature (°F)	Wall Thickness (0.001 In)	Nominal Effective Stress $\bar{\sigma}_e$ (psi)	Stress Ratio $\sigma_{hoop}/\sigma_{axial}$ σ_θ/σ_z	Test Time (hrs)	Nominal Average Loading Strain, (%)			Nominal Average Creep Strain, (%)		
						Axial	Hoop	Effective Loading Strain	Axial	Hoop	Effective Creep Strain
13	1100	50	10,000	1.5	1150	0.0211	0.0364	0.0211	0.0256	0.0413	0.0241
13 (Cont'd.)	1100	50	15,000	1.5	508	0.0606	0.2129	0.1266	0.0366	0.3213	0.2031
13 (Cont'd.)	1100	50	20,000	1.5	165	0.1406	0.8592	0.5321	0.1344	1.2059	0.7630
13 (Cont'd.)	1100	50	20,000	1.0							
14	1100	50	15,000	2.0							
14 (Cont'd.)	1100	50	15,000	1.5							
14 (Cont'd.)	1100	50	15,000	1.0							
14 (Cont'd.)	1100	50	15,000	2.0							
15	1100	50	10,000	2.0							
15 (Cont'd.)	1100	50	15,000	1.5							
15 (Cont'd.)	1100	50	20,000	1.0							
15 (Cont'd.)	1100	50	15,000	2.0							

A test plan has been prepared for examination of previously tested specimens to evaluate the effects of prior creep damage on yield strength, tensile strength, ductility, fatigue behavior, and microstructure. The initial tests of this study are shown in Table 6.5. These tests are being performed on the basis of machine availability and are of lower priority than the tests planned for Type 316 stainless steel. Since delays have been experienced in procuring the Type 316 stainless steel reference heat material, there has been an opportunity to initiate some of the Type 304 stainless steel post-test evaluation work during the current period. Two rupture specimens, surrounded by a 3-inch pipe to protect the furnace wiring when failure occurs, are being tested.

A final report was issued on the unusual occurrence in which multiaxial creep test No. 6 was terminated due to a sample burst. The specimen was under test at 1100°F and 20,000 psi effective stress, with 2717 psi internal pressure and zero axial load. The principal stress ratio ($\sigma_{hoop}/\sigma_{axial}$) of this test was 2:1, and the specimen burst during a routine pressure check after 808 hours under the test condition.

Based on a literature search and analysis of the test results, it is concluded that the rupture life for a tubular specimen under multiaxial load cannot be predicted simply by effective stress level based upon uniaxial creep-rupture time and tertiary creep initiation data. The following guidelines will be followed for the future test program at ARD:

1. The modified thin cylinder formula, based upon the equilibrium tube model, will be used to compute the stresses in the tubular test specimen.

2. Since the maximum principal stress (σ_{max}) correlates better than the effective stress (σ_{eff}) with stress rupture life of the internally pressurized tubular specimens, it will be used in specifying test durations. In addition, the effect of the stress ratio upon the creep-rupture time will be investigated further.

3. Multiaxial stress rupture data will be correlated with the uniaxial time to tertiary creep (0.2 percent offset) data instead of the uniaxial creep to rupture data. In addition, the creep-stress-rupture

TABLE 6-5. TYPE 304 STAINLESS STEEL TUBULAR SPECIMEN CREEP TEST - POST-TEST MATRIX

Test Number	Specimen History[a] Effective Stress, δ_e (ksi)	Stress Ratio (δ_σ/δ_z)	Axial Load (lb)	Internal Pressure (psi)	Post Test Plan
2A	10.0	0.0	5340	0	(b)
3C	7.7	0.0	4112	0	(b)
4A	10.0	2.0	323	1209	(c)
3B	20.0	0.0	10681	0	(d)
9	20.0	1.5	2018	2668	(d)
12	20.0	1.0	5340	2353	(d)
11	15.0	1.0	4005	1574	(d)
7A	10.0	1.5	1211	1180	(d)
2B	10.0	0.0	5340	0	(e)
3D	5.0	0.0	2670	0	(f)
10	10.0	1.0	2670	1049	(e)
1A[g]	25.0	0.0	6872	0	(h)
1B	25.0	0.0	6872	0	(h)
3A	20.0	0.0	10681	0	(h)
4	10.0	2.0	323	1207	(h)
6	20.0	2.0	0	2717	(h)
7	10.0	1.5	1212	1180	(h)
8	15.0	1.5	1515	2000	(h)

* Priority of testing is indicated by the order of listing in the table.

(a) All specimens tested at 1100°F for about 2000 hours.

(b) Tensile test to failure.

(c) Pressurize to failure.

(d) Creep-rupture test under the same prior creep test condition.

(e) Specimen step-loaded to effective stress levels of 15 and 20 ksi, respectively, for a period of 500 hours at each stress level.

(f) Specimen step-loaded to effective stress levels of 10, 15, and 20 ksi, respectively, for a period of 500 hours at each stress level.

(g) Test terminated due to over-temperature.

(h) Microstructural characterization. Microstructure and grain size distribution will be studied on specimens taken at longitudinal and transverse directions along the tubular specimens.

level, based on the uniaxial tertiary creep initiation data, will be conservatively reduced by 20 percent to avoid creep-rupture of future tubular test specimens.

4. Creep strain versus time relationships will be plotted on a daily basis for future tests. The tests will be terminated after the specimen is determined to have reached the tertiary creep stage based on the 0.2 percent offset criteria.

Two similar tests under the same effective stress (20,000 psi), but with different stress ratios (hoop stress/axial stress), were terminated after the tertiary creep stage had been reached for these two specimens. The third test, which was tested at lower stress levels, was terminated after the intended 2000-hour test period.

6.4 REFERENCES

1. Westinghouse Advanced Reactors Division, *"Validation of High Temperature Design Methods and Criteria, Quarterly Progress Report for Period Ending February 28, 1974,"* WARD-HT-3045-5, May 1974, Figure 3.7.

7. UNIVERSITY OF CINCINNATI

J. Moteff

7.1 INTRODUCTION

The objective of this program is to (a) evaluate the time, temperature and stress-dependent properties of reactor structural materials, (b) determine the relationship of these properties to the microstructure and (c) show the contribution of the microstructure to the microcracking and grain boundary sliding behavior during the normal plastic deformation at elevated temperatures. Special consideration is being given to operating conditions typical of nuclear reactor applications, including the knowledge that the radiation environment can influence the substructure of these metals, a circumstance which can lead to significant changes in the mechanical property behavior.

7.2 EXPERIMENTAL PROGRAM

Transmission electron microscopy has been used to study the deformation substructure resulting from creep, fatigue and tensile deformation at elevated temperatures. Creep and tensile data from ORNL (Heat Number 9T2796) was further evaluated through regression analysis in preparation for the correlation of the macroscopic deformation properties with the substructure results. Creep tests have been initiated on 304 Stainless Steel specimens in which the stress level is abruptly changed to another value and the tests subsequently terminated for TEM evaluation of the substructure. A family of creep

tests were performed on 304 Stainless Steel in which the tests were terminated at different strain levels for a TEM evaluation of the substructure developments as a function of the creep life. Work on the substructure developed in the fatigue deformation of Incoloy 800 is nearing completion. A family of fatigue tests on 304 SS conducted at ANL under a Thesis Parts Program were completed and the electron microstructure is presently being investigated. Other work in progress includes the determination of the influence of substructure on the room temperature hardness of fatigue tested specimens and a program on the hot-hardness and creep properties of three alloys obtained from the National Alloy Development Program.

7.2.1 Analysis of Relationships of Deformation Rate, Stress and Temperature for 304 Stainless Steel (R. Bhargava)

Work is being continued on the analysis of the creep and tensile data to determine the relationship between the deformation rate, temperature and stress for AISI 304 Stainless Steel (Reference Heat 9T2796). As reported previously[1] the strain rates obtained from the tensile tests and the minimum creep rates from the creep tests (ORNL data as reported by R. W. Swindeman, ORNL Metals and Ceramics Division) were converted into a Zener Hollomon type parameter, Z, according to the following equation:

$$Z = \dot{\varepsilon} \exp(Q_c/RT) \qquad [1]$$

where Q_c, Apparent Activation energy for creep = 85,000

Cals/mole. During an analysis similar to Garofalo's[2] a parameter $\text{Sinh}(\alpha\ \sigma_\tau/E)$ was evaluated and the data is plotted in Figure 7.1. In this plot of log Z versus log Sinh $(\alpha\ \sigma_\tau/E)$ which has been updated to include a total of 93 points a straight line can be drawn through the data points except for the ones at very high strain rates. At 538°C the tests conducted at strain rates higher than $\sim 10^{-5}$ sec^{-1} show a decrease in the true ultimate tensile stress. The tests particularly conducted at the strain rate of 8.3×10^{-2} sec^{-1} and at temperatures 538, 593, 650 and 704°C show a lower ultimate tensile strength than predicted by the straight line having a relationship of the form:

$$Z = \text{Constant } [\text{Sinh } (\alpha\ \sigma_\tau/E)]^n \qquad [2]$$

Such a behavior has been observed by both Swindeman[3] and Steichen[4,5] who have described the elevated temperature flow behavior of the 304 stainless steel at high strain rates in terms of mathematical models. The reasons for the drop in U.T.S at strain rates of 10^{-5} to 10^{-2} sec^{-1} has been postulated as adiabatic heating and dynamic strain aging. More work in this area is being done and the transmission electron microscopic examination will also help in finding the various reasons for the strain hardening/softening at these high strain rates. The results will be duly reported in future progress reports.

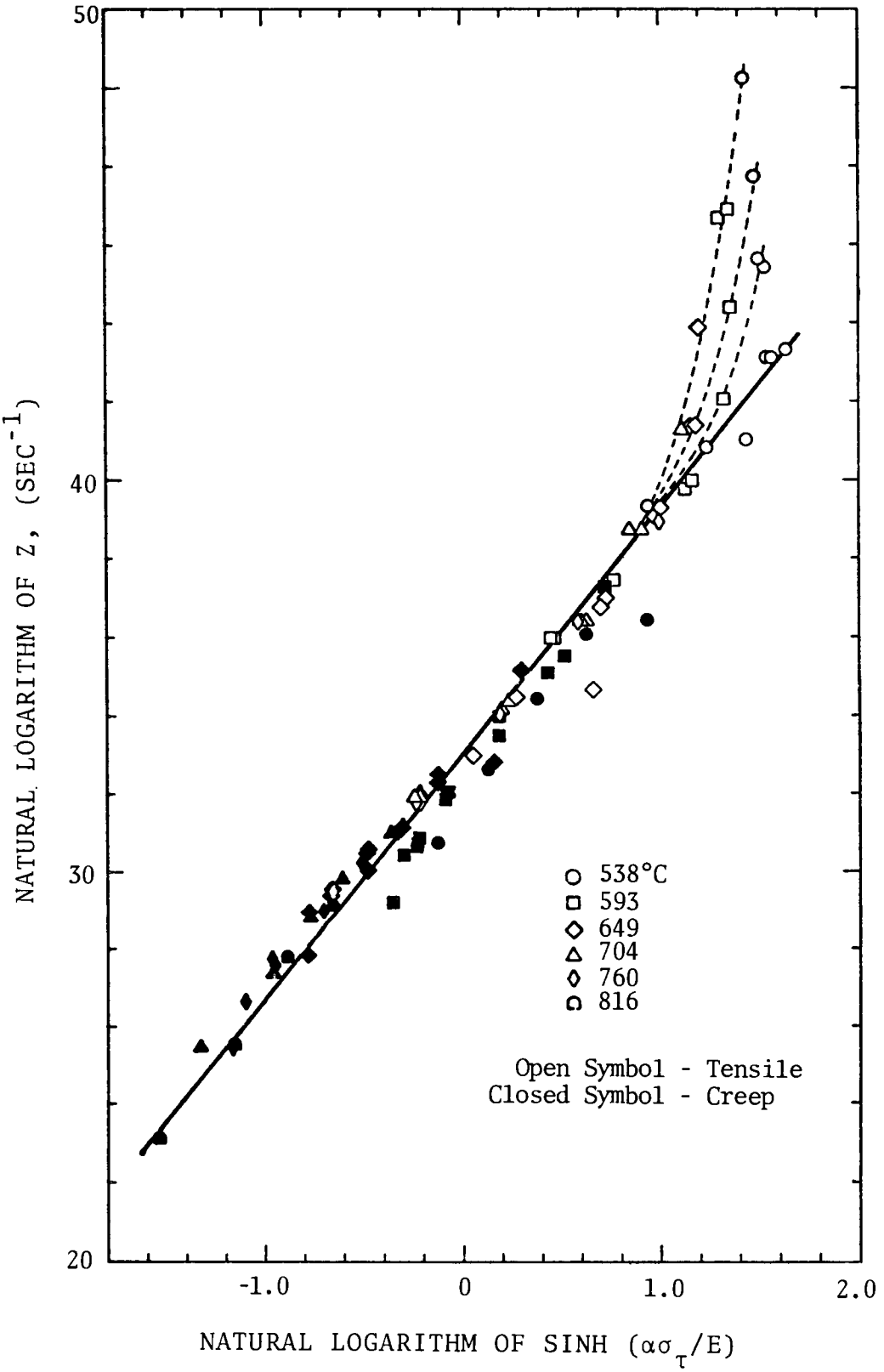

Plot of the Temperature Compensated Deformation Rate Z Versus the Hyperbolic SINE function of ($\alpha\ \sigma_\tau$/E) on a ℓn-ℓn scale. (AISI 304 SS, Reference Heat 9T2796).

Figure 7.1

7.2.2 Characterization of the Creep and Tensile Substructure of 304 Stainless Steel, Reference Heat 9T2796 (R. Bhargava)

The characterization of the substructure of the tensile and creep tested specimens of AISI 304 stainless steel (Reference Heat 9T2796) was initiated and some results were reported previously[1,6]. Figure 7.2 shows the various specimens that are selected for substructure evaluation. In this figure the Zener Hollomon type parameter, Z, is plotted versus the hyperbolic sine function of $(\alpha \sigma_\tau/E)$ on a log-log scale. The specimens chosen cover a range of test temperatures from 538°C to 816°C and a range of strain rates from 1.22×10^{-7} sec^{-1} to 8.33×10^{-2} sec^{-1}. Equivalently on a Z scale it will vary from 1.17×10^{11} sec^{-1} to 6.63×10^{21} sec^{-1}. Transmission electron microscopic examination of these 25 specimens has been nearly completed and the quantitative and qualitative analyses of various substructure features are being performed and will be reported in the next progress report.

7.2.3 Characterization of the Substructure During Early Stages of Creep of 304 Stainless Steel. (R. Bhargava)

In order to better understand the physical processes that undergo during the high temperature deformation of austenitic stainless steel a research program has been initiated. One heat (Heat No. G8607) of AISI 304 Stainless Steel was purchased from the Universal Cyclops Speciality Steel Division in the form of 5/8" dia x 36 ft. round rods. The creep specimens

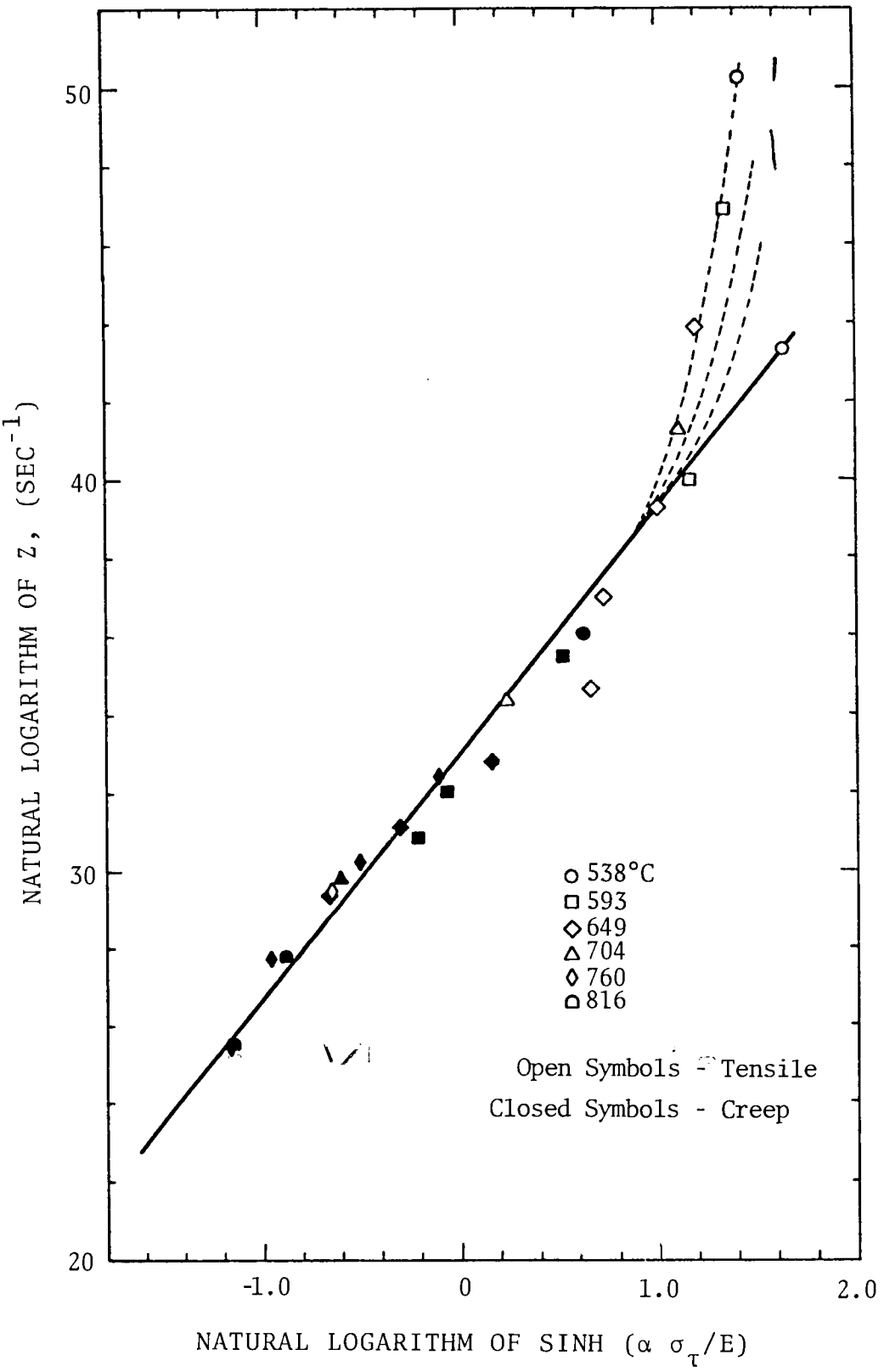

Plot of the Temperature Compensated Deformation Rate, Z Versus the Hyperbolic SINE Function of (α σ_τ/E) on a ℓn-ℓn scale showing the specimens chosen for TEM.

Figure 7.2

were machined from these rods. These specimens were reannealed at 1085°C for 1/2 hour in an Argon atmosphere. The vendor specified chemical compositions (wt%) of Heat G8607 and the Reference Heat 9T2796 are shown in Table 7.1.

In Figure 7.3 a strain versus time plot is shown for the series of tests that were performed. One specimen RUC-10 was tested at 1300°F and a stress of 25,000 psi (172.37 MPa) till rupture. The rest of the specimens were stopped at intermediate strains as indicated by the circles on the curve. The related data is shown in the insert on the same figure. All the specimens, i.e. RUC-3, RUC-4, RUC-5 and RUC-6 were cooled under load to freeze the dislocation substructure that was developed during testing. Transmission electron microscopy is being performed on these specimens and the results will be reported in future progress reports.

Originally it was planned to perform a series of creep tests at one temperature and one stress level and stop them at intermediate values of strain allowing only one of them to go till rupture. But it was found that this heat is very strong as compared to the reference heat 9T2796. The creep strength is about 90% greater than that of the reference heat for the same test conditions. Therefore, it was considered necessary to run some more short time creep tests to rupture and accumulate the creep-rupture data also. Table 7.2 shows the creep-rupture data of this heat of 304 stainless steel. All the tests were conducted at 1300°F (704°C) in air and the

TABLE 7.1

CHEMICAL ANALYSIS OF UC HEAT AND REFERENCE OF 304 STAINLESS STEEL

Element	Heat No. G8607 wt %	Heat No. 9T2796 wt %
C	0.069	0.047
Mn	1.57	1.22
Si	0.60	0.47
S	0.026	0.012
P	0.023	0.029
Cr	18.83	18.50
Ni	8.32	9.58
Cu	0.17	0.10
Mo	0.36	0.10
N	N.A.*	0.031
Co	N.A.*	0.05

*N.A. means not available.

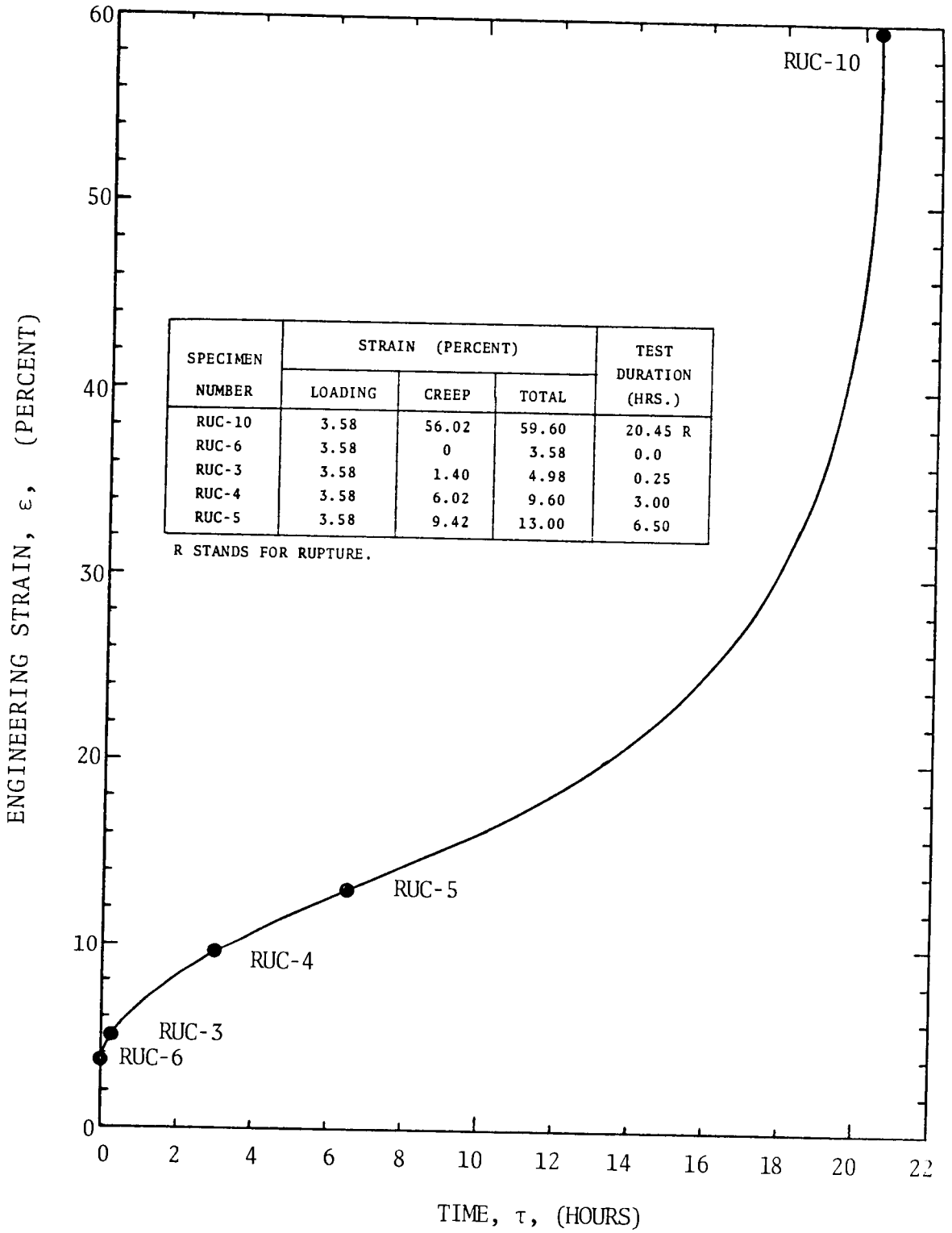

SPECIMEN NUMBER	STRAIN (PERCENT)			TEST DURATION (HRS.)
	LOADING	CREEP	TOTAL	
RUC-10	3.58	56.02	59.60	20.45 R
RUC-6	3.58	0	3.58	0.0
RUC-3	3.58	1.40	4.98	0.25
RUC-4	3.58	6.02	9.60	3.00
RUC-5	3.58	9.42	13.00	6.50

R STANDS FOR RUPTURE.

Plot of Strain Versus Time for Tests at a Stress of 25,000 psi (172.4 MPa) and a Temperature of 704°C. (AISI 304 SS, Heat G8607).

Figure 7.3

TABLE 7.2

STRESS-RUPTURE DATA OF 304 STAINLESS STEEL[a] AT 704°C

Specimen Number	Applied Stress (psi)	Applied Stress ($kg \cdot mm^{-2}$)	Strain on Loading (Percent)	End of Primary Strain (Percent)	End of Primary Time (hrs.)	End of Secondary Strain (Percent)	End of Secondary Time (hrs.)	Rupture Strain (Percent)	Rupture Life (hrs.)	Minimum Creep Rate (sec^{-1})
RUC-8	30,000	21.093	5.87	13.0	0.33	21.8	0.87	66.6	1.99	4.03×10^{-5}
RUC-9	20,000	14.062	1.58	3.6	10.0	4.8	32.0	60.5	100.7	1.51×10^{-7}
RUC-10	25,000	17.577	3.58	11.2	4.5	16.6	10.5	59.60	20.45	2.47×10^{-6}
RUC-1	15,000	10.546	0.07	0.57	29.0	0.85	85.0	21.0[b]	432[b]	1.34×10^{-8}

[a] UC Heat No. G8607

[b] Stopped the test after 21.0 percent Strain.

applied stress values ranged from 15,000 psi (103.42 MPa) to 30,000 psi (206.84 MPa). The applied stress and the rupture life are plotted in Figure 7.4 on log-log coordinates. For comparison the rupture life data for the reference heat 9T2796 has also been plotted. Parallel straight lines can be drawn through the data points as shown in the figure. In order to compare the steady state creep rates, it was found that the two heats show better correlation when the steady state creep rate $\dot{\varepsilon}_s$ (sec^{-1}) is plotted versus the true stress or, as in the present analysis a modulus compensated true stress parameter, σ_τ/E on log-log coordinates. This is shown in Figure 7.5 and again two parallel straight lines can be drawn through the data points. The creep rate $\dot{\varepsilon}_s$ at 30,000 psi, seems to increase at a faster rate than that predicted by the straight line equation. This behavior has been seen previously. Further work is being done to account for the increased strength of this heat.

7.2.4 Change in Stress Experiments (R. Bhargava)

In order to better understand the creep mechanisms the determination of the creep activation parameters is very helpful. During the analysis of relationships of deformation rates with stress and temperature for 304 stainless steel, it was found necessary to perform some additional creep tests of special nature. These will help in assessing the nature of the various deformation mechanisms that take place during elevated temperature deformation. Specimens from 1 inch plate

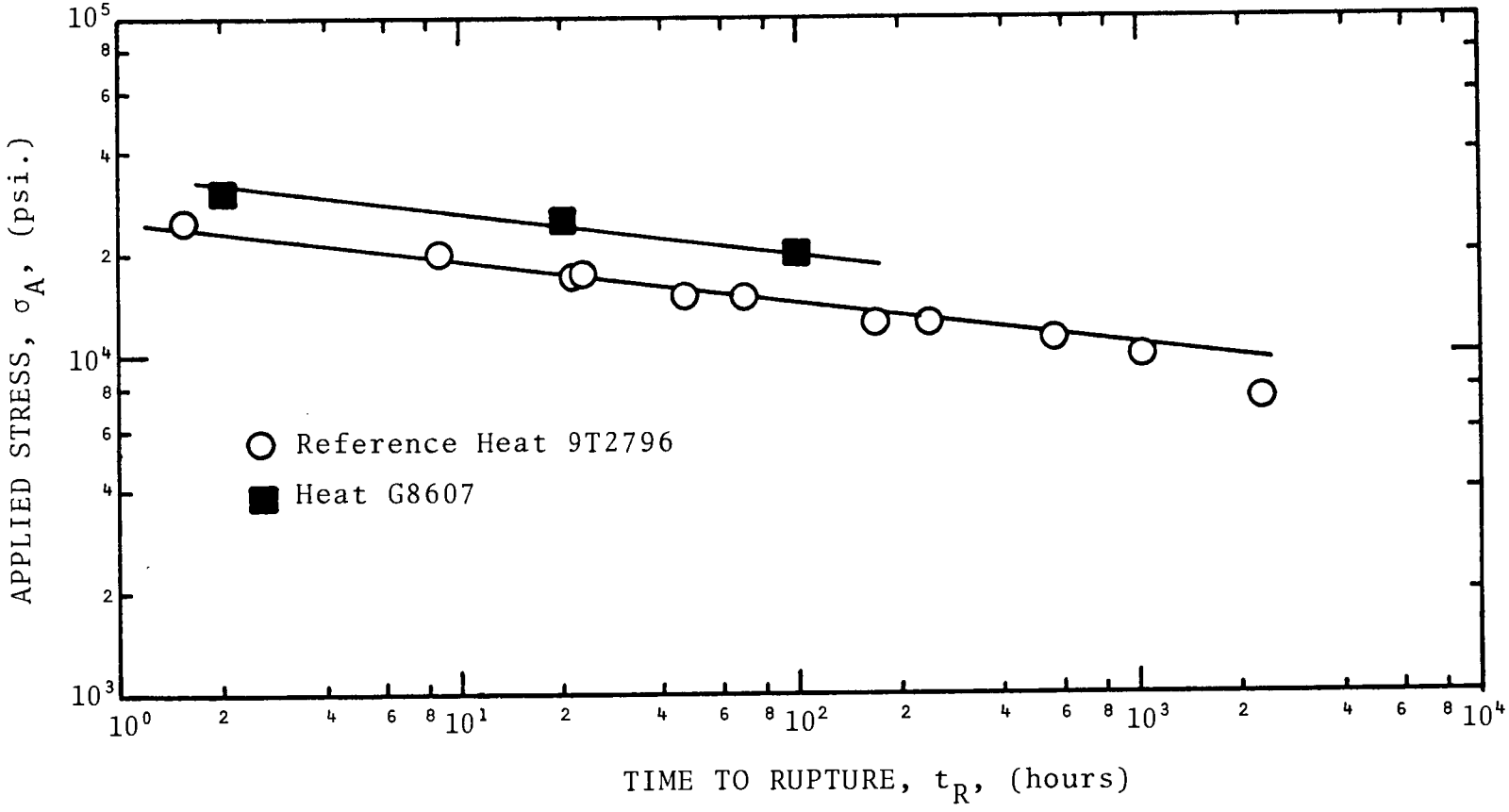

Plot of the Applied Stress Versus the Time to Rupture at 704°C (AISI 304 Stainless Steel).

Figure 7.4

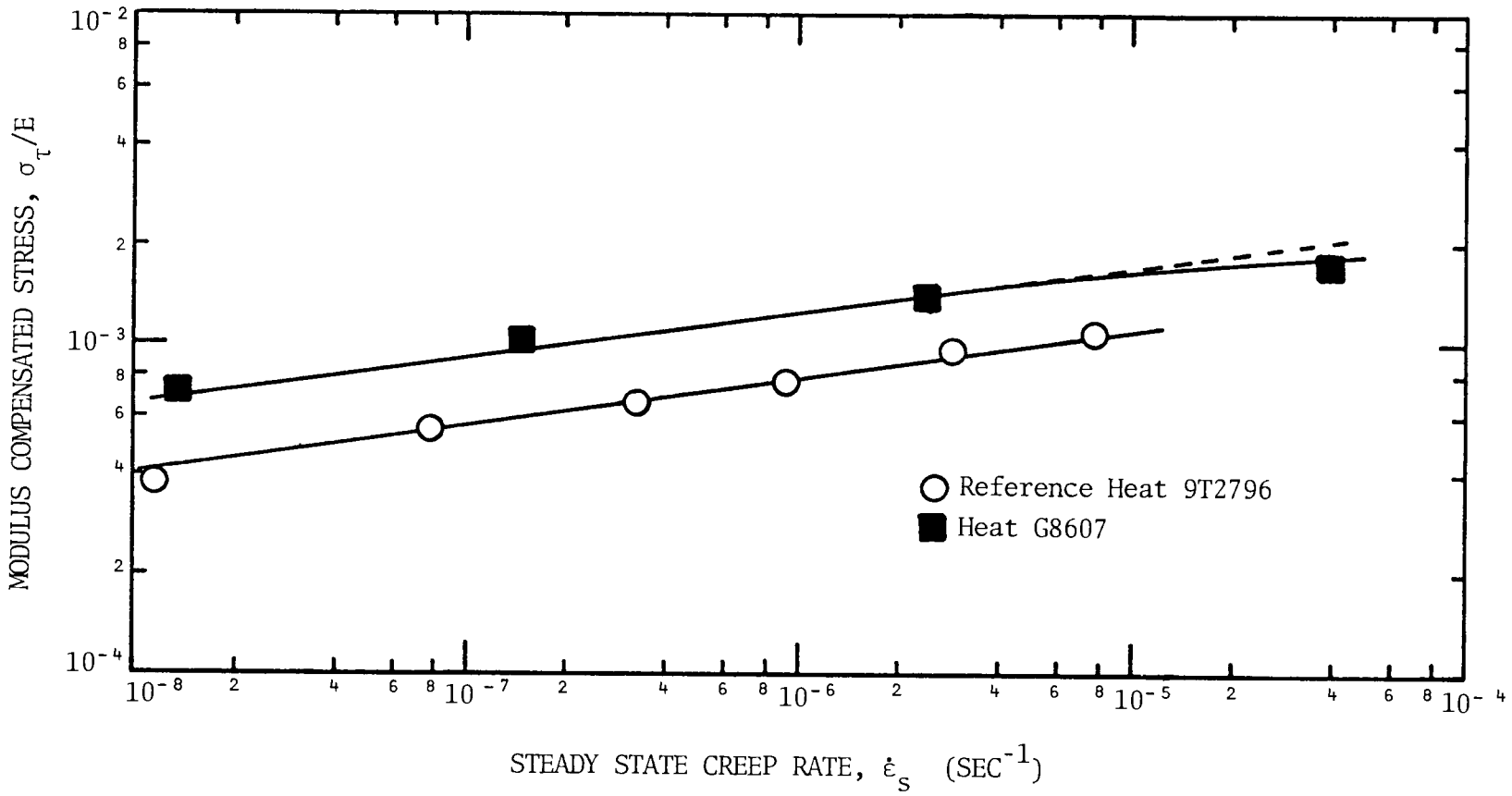

Plot of the Modulus Compensated Stress σ_τ/E Versus the Steady State Creep Rate, $\dot{\varepsilon}_s$ at 704°C (AISI 304 Stainless Steel).

Figure 7.5

of the Reference Heat 9T2796 of AISI 304 stainless steel will be used for these experiments. These specimens were reannealed at 1085°C for 1/2 hour in an Argon atmosphere. In this program, the specimens will be subjected to changes in stress to determine the subsequent creep rate changes to estimate the internal stresses that are developed during deformation and to estimate the activation volume. Most of these preliminary tests are planned to be performed at one temperature.

7.2.5 Deformation Substructure of Incoloy 800 Tested in the Low Cycle Fatigue Mode (H. Nahm)

The substructure of Incoloy 800 low cycle fatigue specimens which were tested[7] in the strain-controlled push-pull mode at 760°C is nearing completion. Preliminary results for tests performed at two strain rates and various strain levels, as plotted in Figure 7.6 and tabulated in Table 7.3, shows that the average cell or subgrain intercept, λ, and the modulus compensated saturation stress, $\Delta\sigma/2G$, may be related by the following equation:

$$\lambda = A(\Delta\sigma/2G)^n \qquad [3]$$

where $\Delta\sigma/2$ represents the saturation stress level, G is the shear modulus at 760°C and A is a constant.

In comparing the substructure developed in the fatigue mode with that developed in specimens tested in a unidirectional mode (i.e., tensile and creep) it is noted that the exponent n has a value of about -2.7 in fatigue whereas the value of n

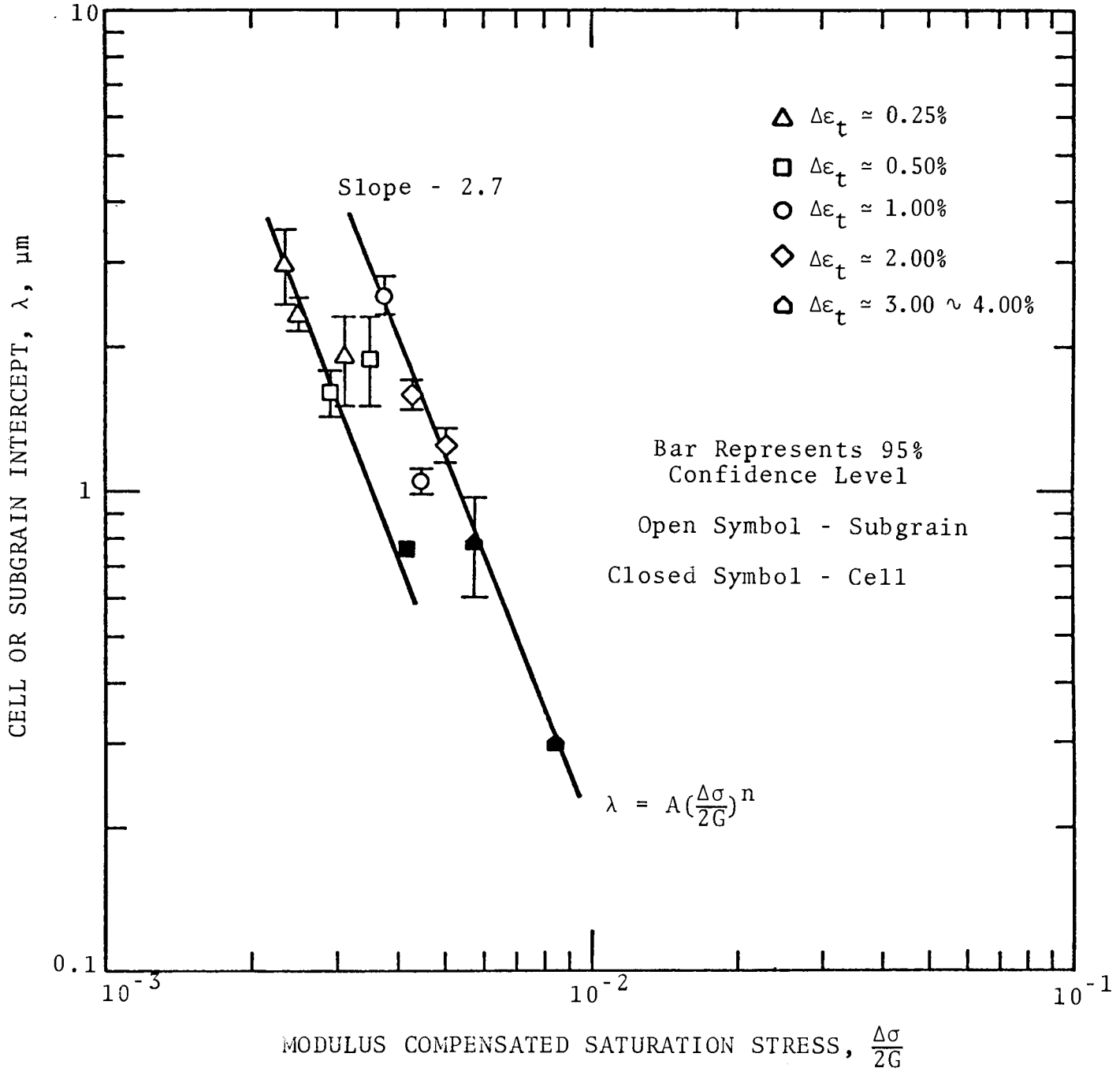

Relationship between Cell or Subgrain Intercept and Modulus Compensated Stress of Incoloy 800 Tested in Low Cycle Fatigue.

Figure 7.6

TABLE 7.3

FATIGUE AND SUBSTRUCTURE PROPERTIES OF INCOLOY 800 AT 760°C

Spec. No.	Strain Rate $\dot{\varepsilon}$, sec^{-1}	Plastic Strain Range $\Delta\varepsilon_p$, Pct.	Modulus Compensated[a] Saturation Stress $\Delta\sigma/2G$	$\Delta\sigma/2E$	Average Subgrain[b] Intercept λ, μm	Average Mobile[b] Dislocation Density ρ, cm^{-2}	Subgrain[b] Misorientation θ, Degrees
2C75	4×10^{-3}	3.53	5.69×10^{-3}	2.05×10^{-3}	0.78 ± 0.19	$(5.23 \pm 2.17) \times 10^{9}$	N.M.
2B26	4×10^{-3}	1.61	5.08×10^{-3}	1.83×10^{-3}	1.26 ± 0.18	N.M.	0.54 ± 0.12
2F6	4×10^{-3}	0.66	4.48×10^{-3}	1.61×10^{-3}	1.05 ± 0.05	$(4.98 \pm 0.95) \times 10^{9}$	0.76 ± 0.19
2W23	4×10^{-3}	0.24	3.49×10^{-3}	1.53×10^{-3}	1.89 ± 0.41	$(3.32 \pm 0.80) \times 10^{9}$	0.76 ± 0.32
2D28	4×10^{-3}	0.08	3.07×10^{-3}	1.11×10^{-3}	1.90 ± 0.40	$(3.30 \pm 0.40) \times 10^{9}$	0.42 ± 0.08
2G79	4×10^{-3}	0.07	2.48×10^{-3}	8.93×10^{-4}	2.33 ± 0.19	$(2.46 \pm 0.51) \times 10^{9}$	0.69 ± 0.18
2K35	4×10^{-4}	1.66	4.28×10^{-3}	1.54×10^{-3}	1.61 ± 0.10	$(5.39 \pm 0.31) \times 10^{9}$	0.85 ± 0.20
2H32	4×10^{-4}	0.72	3.76×10^{-3}	1.35×10^{-3}	2.55 ± 0.24	$(1.93 \pm 0.23) \times 10^{9}$	0.59 ± 0.22
2I33	4×10^{-4}	0.28	2.94×10^{-3}	1.06×10^{-3}	1.60 ± 0.16	$(3.25 \pm 0.30) \times 10^{9}$	0.90 ± 0.31
2H80	4×10^{-4}	0.08	2.35×10^{-3}	8.46×10^{-4}	2.98 ± 0.56	$(1.11 \pm 0.25) \times 10^{9}$	0.67 ± 0.14

[a] Elastic Modulus at 760°C ($E = 21.06 \times 10^{6}$, $G = 7.58 \times 10^{6}$ psi) is obtained from the International Nickel Company (Technical Bulletin T-40).

[b] The errors indicates the 95 percent confidence level (λ,ρ among the plates, θ among the measurements).

is -1 below a critical stress level in creep/tensile and -2 above this critical stress level. This observation for the case of Incoloy 800 as well as the apparent strong dependence of the subgrain size on the strain amplitude is consistent with the data reported by Challenger and Moteff[8] on 316 stainless steel also tested in the elevated temperature fatigue mode. The values for n, in the case of 316 stainless steel, varied from -1 at the low stress levels to -2.8 at the high stress levels.

The dependence of the free dislocation density on the saturation stress is presented in Figure 7.7. Here the square root of the dislocation density $\sqrt{\rho}$ is plotted as a function of the modulus compensated saturation stress and the trend suggests that the classical work hardening equation

$$\Delta\sigma = \Delta\sigma_o + \alpha\, Gb\sqrt{\rho} \qquad [4]$$

is a reasonable approximation to the experimental data. Since additional data are being generated on the dislocation densities of Incoloy 800 at other test conditions, the constants in Equation [4] will be evaluated at a later time.

The density of dislocations bound in sub-boundaries, ρ_{SB}, can be estimated by means of the equation

$$\rho_{SB} \simeq 3\theta/b\lambda \qquad [5]$$

where b is the Burgers vector of dislocations forming sub-boundaries and θ is the mean subgrain misorientation. The subgrain intercept, λ, has been presented previously.

Since the inter-relationship of the dislocation substruc-

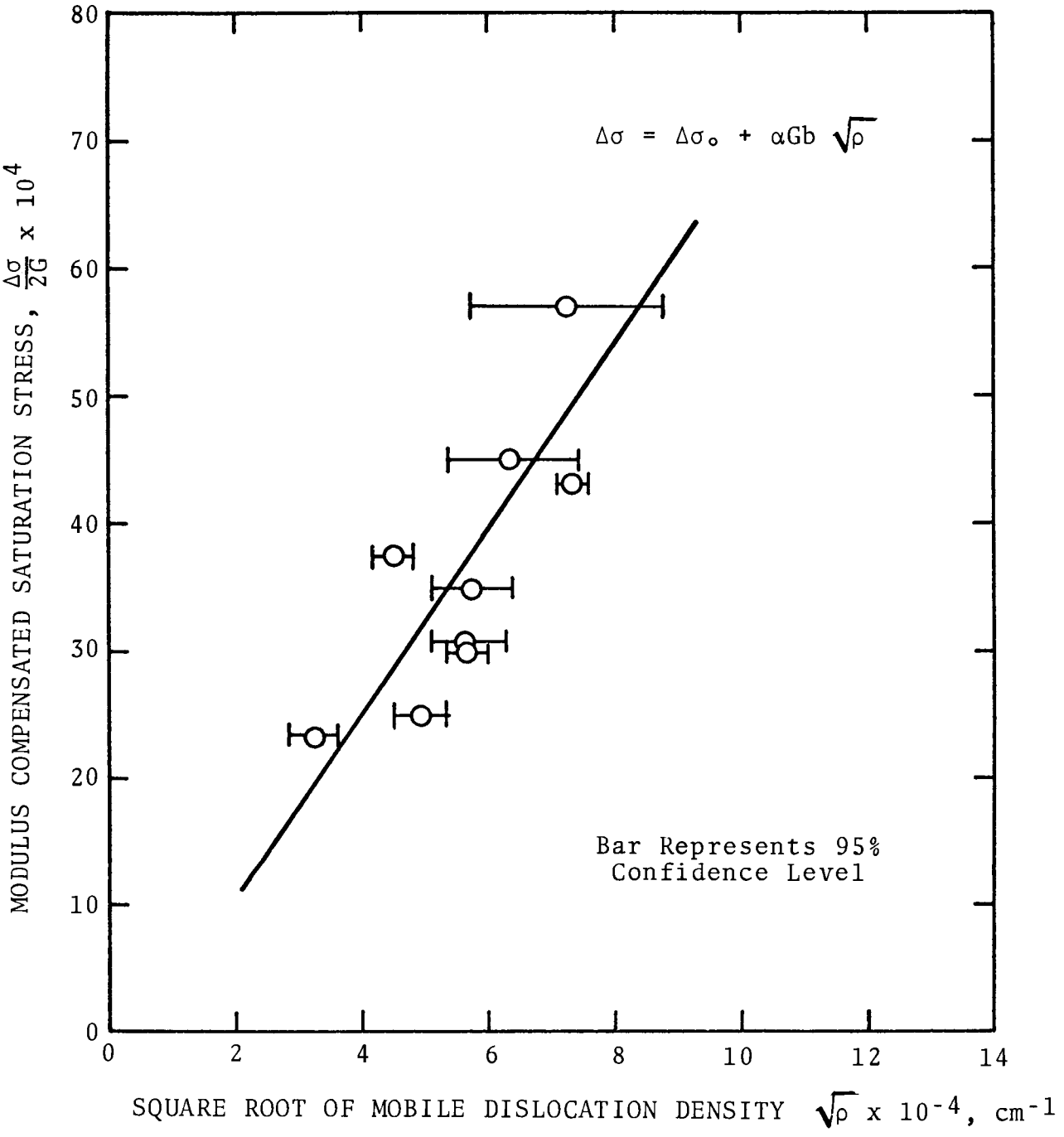

Plot of Modulus Compensated Stress Versus Dislocation Density of Incoloy 800 Tested in Low Cycle Fatigue at 760°C.

Figure 7.7

tural parameters of total dislocations (ρ_T), free dislocations (ρ_m), bound dislocations (ρ_{SB}), subgrain (or cell) intercepts (λ) and misorientation angles (θ) plays an important role in the development of a better understanding of the creep-fatigue properties, particular attention will be given to improving the experimental quantitative data of these parameters. These relationships have been shown for the case of metals such as iron, iron-3 percent silicon, aluminum, aluminum-5.5 percent magnesium and α-zirconium by Orlova and Cadek[9] and on 316 stainless steel by Sikka, Nahm, and Moteff[10].

In the present analysis on Incoloy 800, the misorientation angles between adjoining subgrains was experimentally determined by measuring the Kikuchi line shift[11] as the image shown with the smallest selected area aperture was traversed across the subgrain boundary. Preliminary results of the misorientation angle as a function of the subgrain intercept are listed in Table 7.3 and plotted in Figure 7.8. Since all the specimens which were used in this investigation were tested to failure, it is not surprising that the misorientation angles are relatively insensitive to the subgrain intercept.

Further evaluations of the hexagonal dislocation networks in the sub-boundaries of fatigue tested Incoloy 800 are made by using the $\bar{g} \cdot \bar{b} = 0$ analysis criterion. The set of four micrographs presented in Figure 7.9 shows that the individual dislocations out of contrast in micrographs 7.9B, C, and D

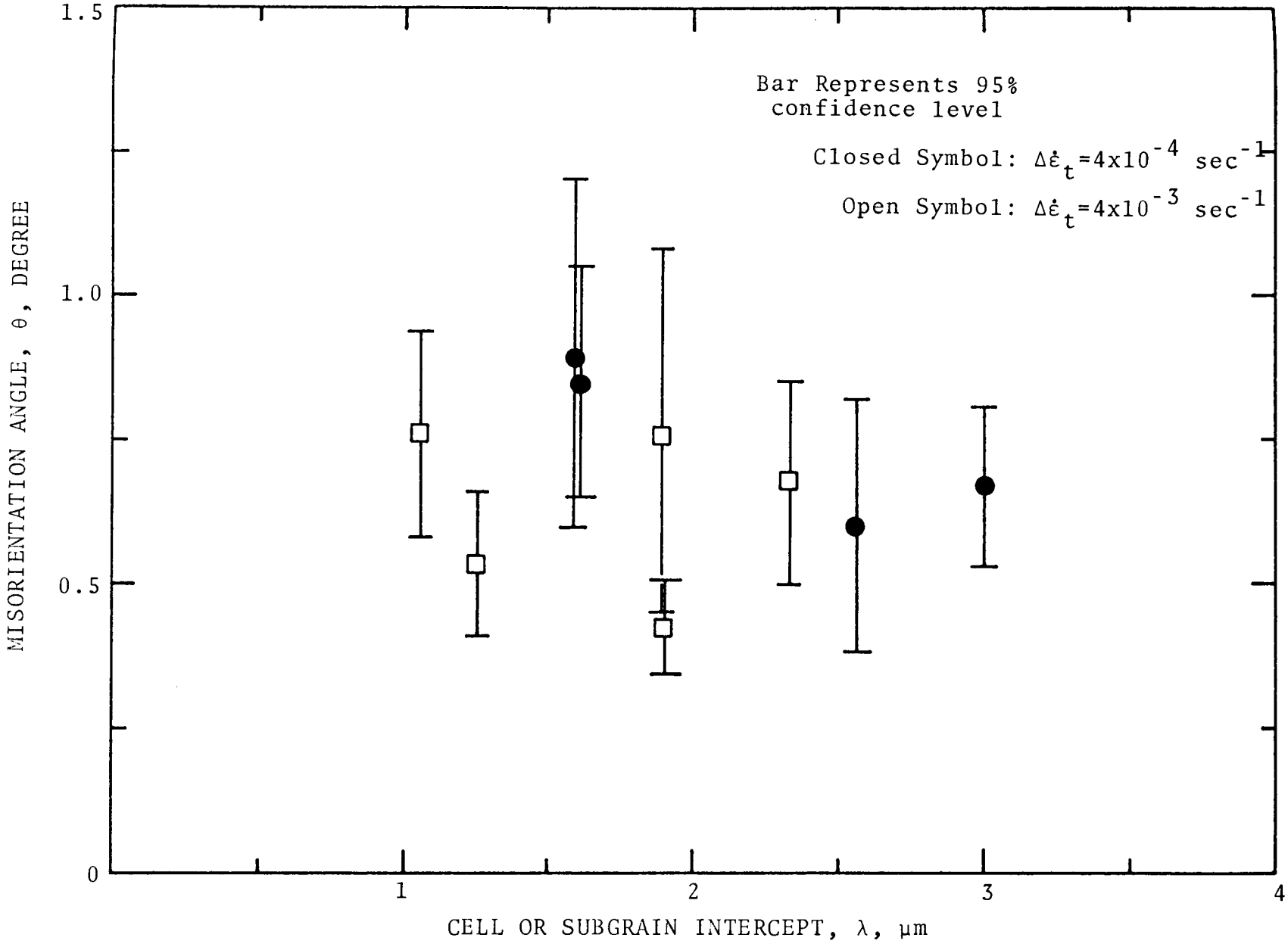

Plot of Misorientation Angle versus Cell or Subgrain Intercept of Incoloy 800 Tested in Low Cycle Fatigue at 760°C.

Figure 7.8

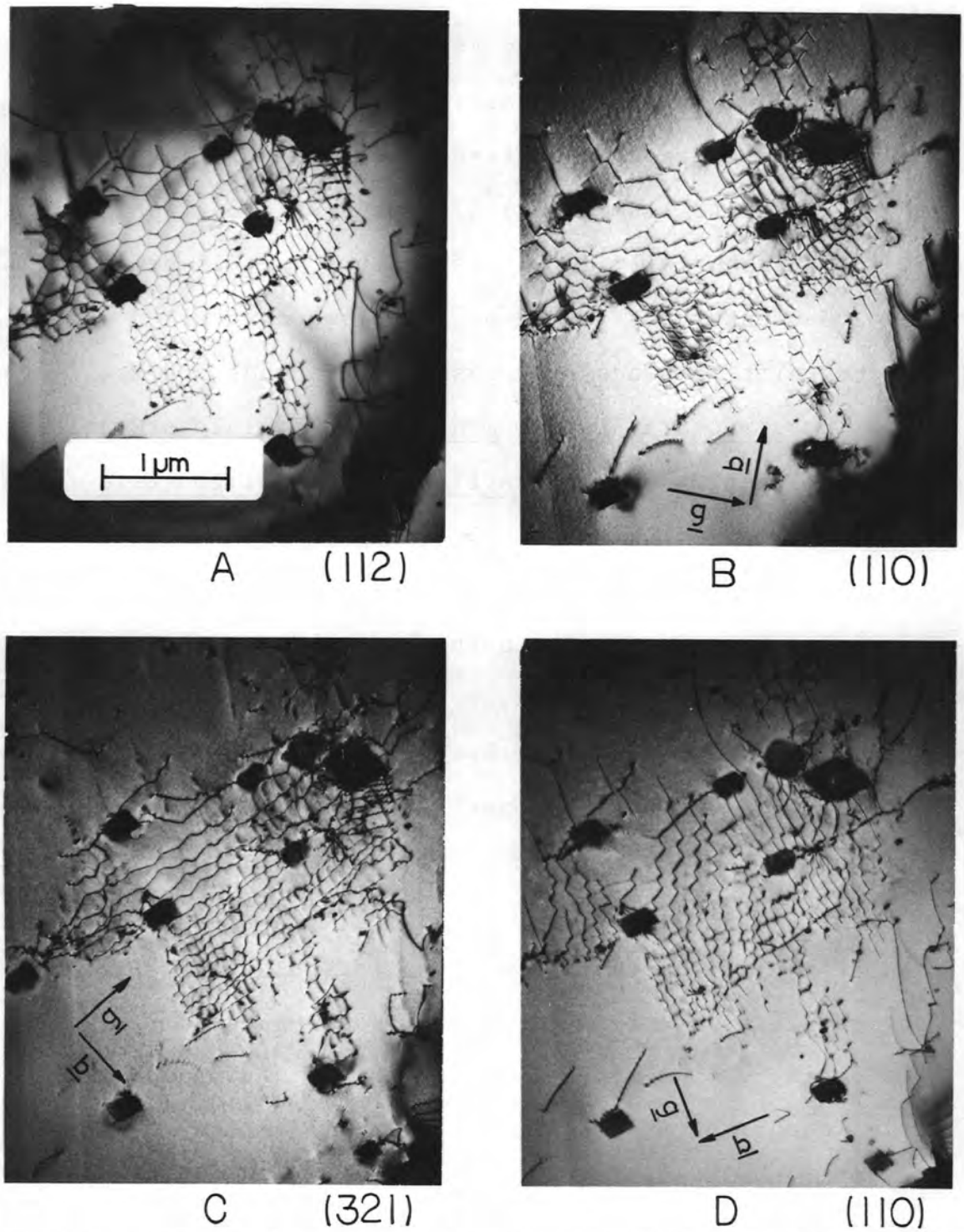

Characterization of a Low Angle Boundary by the Identification of Individual Dislocations Using $g \cdot b = 0$ Criterion in Incoloy 800 Tested in Low Cycle Fatigue (2H32, $\Delta\varepsilon_t$ = 0.99%, $\Delta\dot{\varepsilon}_t = 4 \times 10^{-4}$, N_f = 854).

Figure 7.9

are perpendicular to the operating $\bar{g}$ vector and parallel to the Burgers vector $\bar{b}$. The micrograph shown in Figure 7.9A is taken in an electron multi-beam condition. The sub-boundary is found to lie on a (111) type crystallographic plane and to be essentially of a twist nature. It is believed that this sub-boundary is formed by the climb-controlled stress induced knitting process proposed by Lindroos and Miekk-oja[12]

7.2.6 Substructural Development of 304 Stainless Steel as A Function of the Fraction of the Fatigue Life (H. Nahm)

A special set of low cycle fatigue tests were performed at Argonne National Laboratory* under the provisions of a Thesis Parts Program. The purpose of these tests were to supply plastically deformed specimens (304 Stainless Steel, Heat No. 9T2796) which have been tested up to different fractions of the fatigue life under identical test conditions of temperature (649°C), strain range (2%) and strain rate (4×10^{-3} sec^{-1}). The number of cycles at the termination of the respective fatigue tests are given in Table 7.4. Preliminary observations suggest that clearly developed cells form sometime during 0.75 to 6.75 cycle(s) on test, with some cell formation occurring even at 2.75 cycles. Although cells are formed within about 1.1 percent of the 722 cyclic life of this material and consequently contributes to the observed strain hardening, some additional hardening may be attributed

*Fatigue Laboratory, Materials Science Division

TABLE 7.4

TEST SEQUENCE FOR 304 STAINLESS STEEL LCF[a]

SUBSTRUCTURAL DEVELOPMENT EVALUATIONS

ANL Test Number	Specimen Number	Number of Cycles At Test Interruption[b] N_f, cycles	Fraction of Fatigue Life N/N_f, Percent	General Substructural Features[c]
709	T337	722	100	Well defined cells Uniform distribution of dislocations Large misorientation angles
---	----	∿350	48.50	Work in Progress
---	----	∿80	11.08	Work in Progress
711	T338	6 3/4	1.07	Relatively clear cell Small misorientation angles
713	T339	2 3/4	0.38	Some cell formation in localized areas
717	T343	3/4	0.10	Inhomogeneous distribution of dislocations
719	T344	1/4	0.04	Work in Progress

(a) Material: AISI 304 Stainless Steel, Heat No. 9T2796
Heat Treatment: Solution annealed at 1092°C for 30 minutes and aged at 593°C for 1000 hours
Test Temperature: 649°C (1200°F)
Total Strain Range: $\Delta\dot{\varepsilon}_t \simeq 2\%$
Strain Rage: $\Delta\dot{\varepsilon}_t \simeq 4 \times 10^{-3}$ sec^{-1}

(b) All tests were terminated in the tensile mode with the exception of the 1/4 cycle case which was terminated in the compression mode. All tests were initiated in the compression mode.

(c) Specimen cooling rate on completion of test is estimated to be greater than about 90°C min^{-1} from 650 to about 100°C.

to the strengthening of the sub-boundaries, as possible barriers to dislocation motion, through the increase in misorientation angle with time on test. Since work is still in progress on this mini-research program, the final conclusions will be established at a later time.

7.3 REFERENCES

1. ORNL-5103, "Mechanical Properties Test Data for Structural Materials" quarterly progress report for period ending October 31, 1974, pp. 326-334.

2. F. Garofalo, Trans. AIME, 227, (1963), p. 351.

3. R. W. Swindeman, J. of Eng. Matls. and Technology, Trans. of the ASME.

4. J. M. Steichen, J. of Eng. Matls. and Technology, Trans. of the ASME, July 1973, pp. 182-185.

5. J. M. Steichen, J. of Testing and Evaluation, 1, (1973), pp. 520-523.

6. ORNL-4998, "Mechanical Properties Test Data for Structural Materials" quarterly progress report for period ending July 31, 1974, p. 306.

7. J. B. Conway, J. T. Berling, and R. H. Stentz, Met. Trans., 3, (1972) p. 1633.

8. K. D. Challenger and J. Moteff, Met. Trans., 3, (1972), p. 1675.

9. Orlová, A., and Čadek, J., 1973, Phil. Mag., 28, p. 891.

10. V. K. Sikka, H. Nahm and J. Moteff, Accepted for publication in

11. S. Kikuchi, Japan J. Phys., 5, (1926), p. 83.

12. V.K. Lindroos and H.M. Miekk-oja, Phil. Mag.,16,(1957)593.

This work is supported by the U.S. Energy Research and Development Agency under Contract AT(11-1)-2107 with the University of Cincinnati.

UNIVERSITY OF CALIFORNIA, LOS ANGELES

(No report.)

8. GENERAL ELECTRIC COMPANY

D. Weinstein

8.1 INTRODUCTION

The principal objective of mechanical properties testing at the General Electric Company is to characterize the behavior of 2¼Cr-1Mo and austenitic stainless steels in sodium environments relevent to LMFBR steam generators and intermediate heat transport systems. Under conditions predicted for the intermediate sodium system of the CRBRP, 2¼Cr-1Mo will lose carbon to the system and be weakened. The carbon will tend to carburize and embrittle stainless steel components in other portions of the system. The effects of a carburizing environment on creep rupture properties of Type 316 stainless steel will be evaluated along with an assessment of creep-fatigue interactions. In addition, studies of fatigue crack propagation rates in carburizing sodium will be performed in order to assess environmental effects under pertinent intermediate sodium loop loading conditions. The loss of carbon from 2¼Cr-1Mo steel components can result in increased creep rates of the decarburized surface layer with the possibility of ratchetting under cyclic straining. These effects will be evaluated for base metal and weld metal in a decarburizing sodium environment.

8.2 MECHANICAL PROPERTIES OF STAINLESS STEEL IN CARBURIZING SODIUM - J. F. Copeland

8.2.1 Background

The objective of this program is to experimentally verify and supplement ASME Code design values for austenitic stainless steels to be used in LMFBR Intermediate Heat Transport Systems (IHTS). The effects of sodium carburization on creep-rupture lives and deformation rates, as well as the influence of creep-fatigue interaction and of tension hold time at peak stresses (30 min.), will be evaluated. Additionally, the effect of environment and other design-related parameters on the fatigue crack propagation rate will be determined in high carbon sodium using a fracture

mechanics approach. Frequency (0.5 and 0.05 cpm) and hold time (1 min.) effects will be determined over a range of ΔK values in air and in carburizing sodium. This study will include the influence of continuous carburization in sodium at a crack tip during cycling and stressing since even a heavy thickness component could conceivably be degraded by this mechanism. A possible mechanism for the influence of carburizing sodium on crack initiation and propagation is illustrated in Figure 8.1. Such data will be utilized for assessing and ensuring the integrity of LMFBR IHTS components in carburizing liquid sodium environments.

Initial tests will be performed on Type 316 stainless steel at 950°F in carbon-saturated sodium after approximately 1000 hr. specimen pre-exposures. The degree of carburization expected[1] is a case depth of about 5 mils with a surface carbon content of approximately 1-1.5 wt. %. This carburization corresponds to that expected (Figure 8.2)[2] for the 30 year CRBR IHTS design life with a 2¼Cr-1Mo steel carbon source. GE experience with bimetallic sodium test loops (Steam Generator Test Rig,[3] PA15 Loop 3,[4,5] B&W Model Steam Generator,[6] and EBR II secondary sodium system vent-line[2]) has verified that such surface carburization of stainless steel components does occur.

Two types of tests will be performed, in addition to initial material characterizations: (a) tubular creep and creep-fatigue tests that give rupture times, deformation rates, and rupture ductilities, and (b) ASTM E399 fracture mechanics bend tests to give fatigue crack propagation rates. Under (a), specimens, shown in Figure 8.3, will be filled with sodium and a carbon source and sealed prior to testing. Control specimens will be filled with argon. For part (b), testing will be performed in flowing sodium (Loop A, previously employed in carburization studies). Control tests will be performed in air. Cyclic frequency will be low and will include the determination of hold-time effects.

8.2.2 Current Progress

Testing facility modifications have been designed and are being implemented. Capital equipment for this new task is currently being procured. Type 316 annealed material has been received, and material

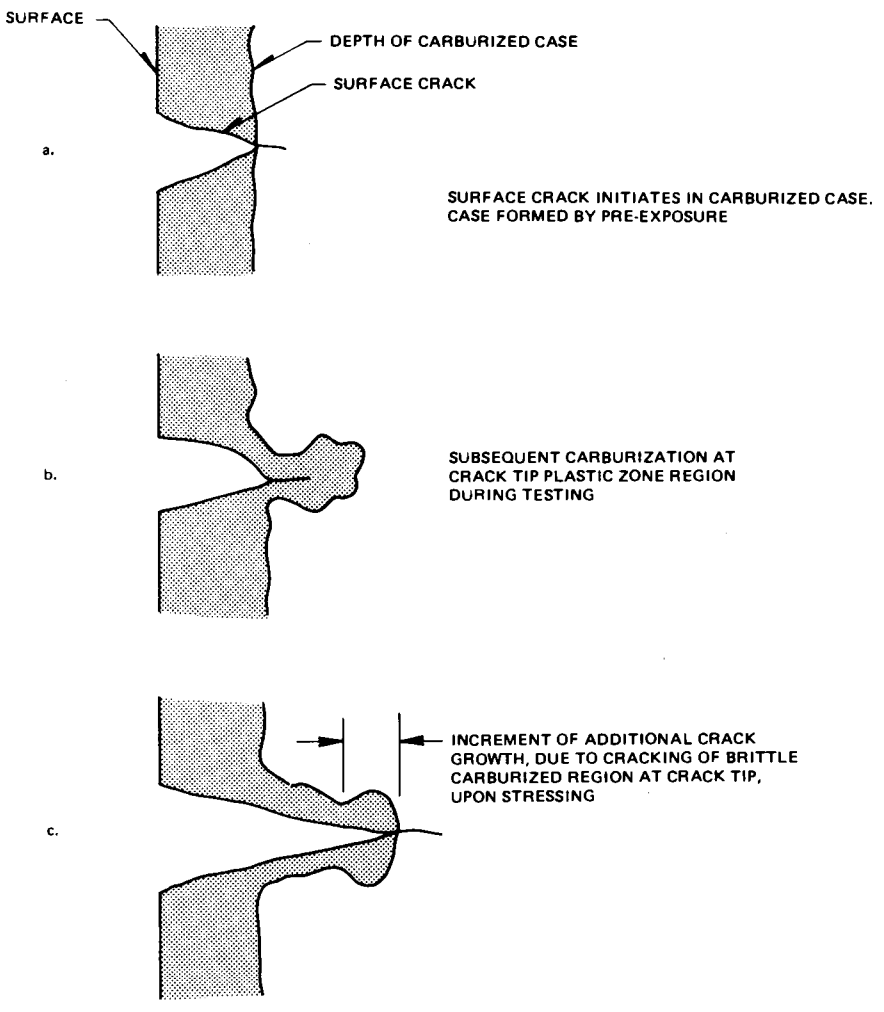

FIGURE 8.1 SCHEMATIC REPRESENTATION OF THE MECHANISM OF CRACK INITIATION AND GROWTH FOR FATIGUE SPECIMENS CARBURIZED BY PRE-EXPOSURE AND TESTED IN CARBURIZING ENVIRONMENT. EFFECTS ON BOTH CRACK INITIATION AND PROPAGATION, SINCE THE CRACK IS ALWAYS GROWING THROUGH CARBURIZING MATERIAL EXPOSED TO SODIUM.

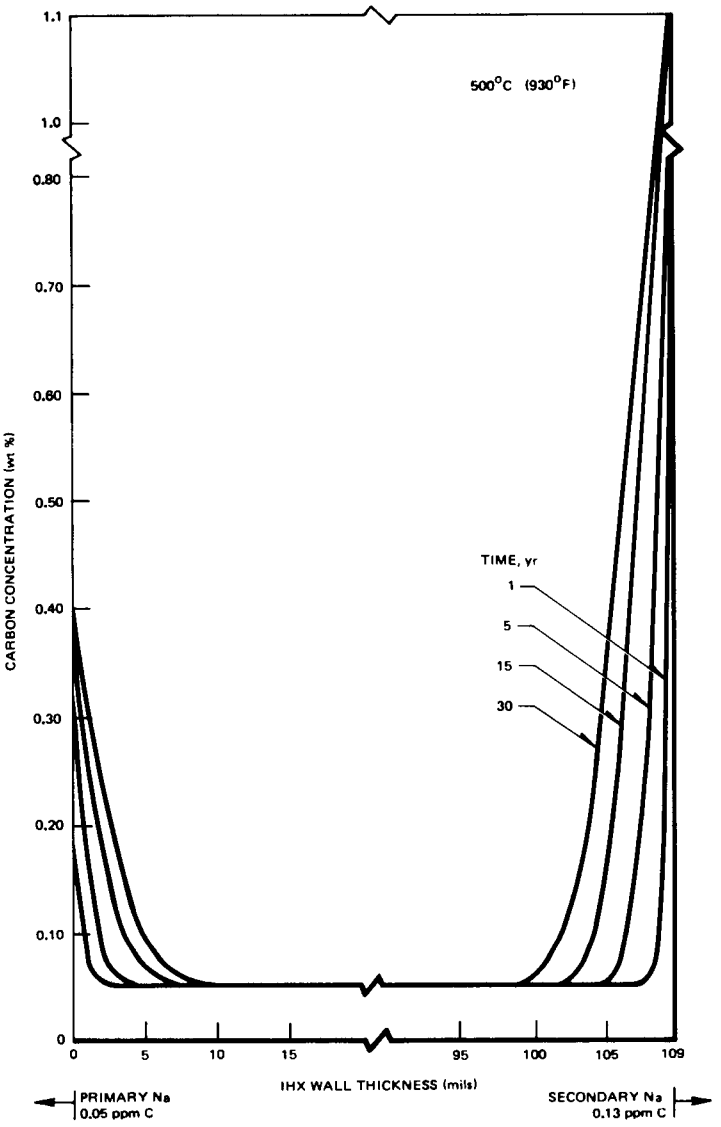

FIGURE 8.2 CARBON CONCENTRATION-DISTANCE PROFILES ACROSS TYPE-304 STAINLESS STEEL IHX PIPING AFTER EXPOSURE TO PRIMARY-AND SECONDARY-SYSTEM SODIUM CONTAINING 0.05 AND 0.13 ppm CARBON, RESPECTIVELY, FOR UP TO 30 yr AT 500°C. ANL NEG No. MSD-58582; REF 2.

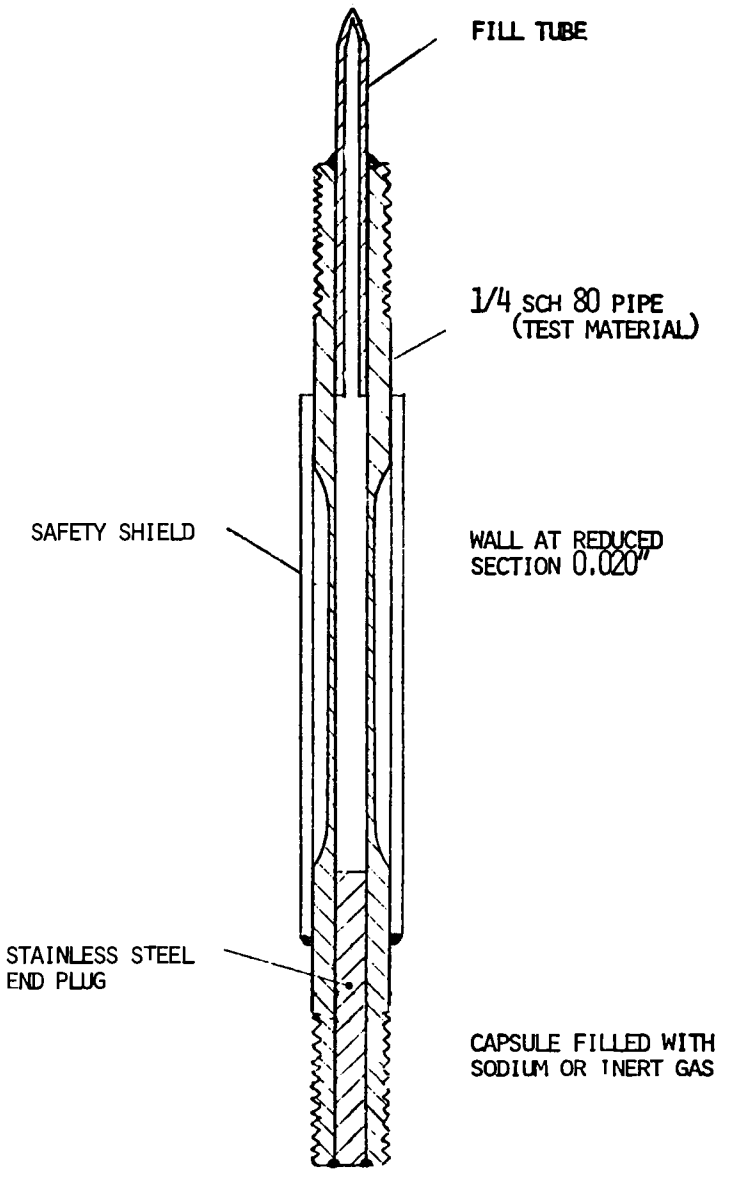

FIGURE 8.3 UNIAXIAL CREEP/FATIGUE SPECIMEN

characterization and specimen fabrication is completed. Chemical composition and tensile test results are given in Tables 8.1 and 8.2. These characterization results indicate no material irregularities, and specimen pre-exposure and aging is proceeding. The type (a) control specimens will have 1000 hr. of aging on January 15, 1975, and testing will be initiated at that time. The other type (a) specimens are currently being filled with sodium from Loop A. The thermal aging of these specimens should be completed in early February 1975. Arrangements are nearing completion for the testing of two sets of type (a) specimens at Battelle Memorial Institute. The remaining specimens will be tested at GE. Fatigue precracking of the type (b) specimens will be completed by early February 1975. These specimens will then be pre-exposed to high carbon sodium in Loop A prior to testing. The testing of type (b) specimens should initiate in March 1975.

8.3 DECARBURIZATION KINETICS AND DESIGN METHODS VERIFICATION TESTING - G. J. Licina

8.3.1 Background

The objective of this program is to define the decarburization kinetics of 2¼Cr-1Mo base metal and weld metal exposed to 950°F sodium, and to evaluate the response of these materials to interrupted creep loading, as encountered during steam generator transients.

One of the major concerns with the use of 2¼Cr-1Mo for sodium-heated steam generators is its susceptibility to decarburization. Recently, it has been shown that the decarburization kinetics of 2¼Cr-1Mo base metal are sufficiently slow to permit its use for steam generator tubing in the CRBRP with only a small (10%) design stress penalty.[7,8] This small design penalty is possible because the creep/rupture properties of 2¼Cr-1Mo are relatively insensitive to bulk carbon content until the level drops below 0.03 - 0.04% C, a value which will not be reached in the design life of steam generator tubes under CRBRP secondary sodium conditions.

Table 8.1 Type 316 Stainless Steel Annealed Test Material Characterization-Chemical Composition (wt. %)

1/4 Sched. 80 pipe ((a) Tests)	C	Mn	P	S	Si	Cu	Ni	Cr	Mo	N
Ladle	0.056	1.63	0.029	0.015	0.56	0.08	13.32	17.24	2.40	-
Check	0.055	1.63	0.018	0.010	0.70	0.05	13.40	17.47	2.67	0.038
5/8 in. Plate ((b) Tests)										
Ladle	0.042	1.66	0.015	0.008	0.60	-	13.40	17.50	2.69	-
Check	0.053	1.59	0.009	0.013	0.54	0.06	13.37	17.22	2.37	0.050

Table 8.2 Type 316 Stainless Steel Annealed Test Material Characterization-Tensile Tests

	0.2% Y.S. (ksi.)	U.T.S. (ksi.)	% El. (2")	% R.A.
1/4 Sched. 80 Pipe ((a) Tests)*				
Room Temp.	39.4	90.4	50.0	55.3
	43.5	88.7	44.0	48.5
950°F	25.1	69.4	28.5	36.3
	24.0	71.2	32.5	36.6
5/8 in. Plate ((b) Tests)**				
Room Temp.	38.0	88.7	45.9	77.0
	39.3	89.4	53.6	77.4
950°F	21.1	70.6	36.5	66.4
	21.8	74.1	41.3	61.3

* 0.35 in. O.D. X 0.020 in. wall X 2 in. reduced section

** 0.25 in. Dia. X 2 in. reduced section

Since the allowable stresses for a welded tube are based on the strength properties of the weakest part of that tube, a "weak" weld in a steam generator tube would govern the allowable stress for the entire tube. A limited number of creep tests on weld metal decarburized (at 1650°F for 6 hours in wet H_2) to 0.02% C showed that rupture life was approximately one-half that of base metal decarburized to the same level.[9]

Contemporary ASME Code rules for elastic and inelastic analysis methods require a consideration of creep/fatigue interactions for high temperature components to accomodate the effects of transient loading. However, the Code does not cover degradation of mechanical properties caused by the service environment. Hence, steam generator design must account for the existence, nature, and magnitude of environmentally-induced mechanical property changes. From the upper limit of the predicted decarburization rate constant and from the dependence of strength on carbon content,[10] Table 8.3 was prepared to illustrate the reduction of allowable stress (S_o from ASME Code Case 1592) for a given temperature and wall thickness. Although the decarburization of 2¼Cr-1Mo is such that only a small reduction in allowable stress is necessary for 950°F service, the increased creep rates of a decarburized surface layer and the possibility of ratchetting under cyclic straining must be considered. Table 8.4 outlines the test matrix planned to investigate these effects.

8.3.2 Current Progress

Figure 8.4 describes the test rig for the biaxial creep rupture studies in sodium. As shown, eight samples are simultaneously pressurized to selected stress levels from an external source. Four pins are isolated from the sodium, while the other four pins will be exposed to the decarburizing environment. Low pressure switches in the gas line detect specimen failure. These switches then stop a timer and cycle counter, as well as isolate the pot from the pressurization system and vent the pressure. As indicated by the test matrix, the effects of interruption and a decarburizing sodium environment on the rupture life of 2¼Cr-1Mo tubing and weld metal will be evaluated. Start-up of this test and the uniaxial, interrupted creep tests is envisioned for the next quarter.

Table 8.3 Reduction in Allowable Stress for 2¼Cr-1Mo Tubing* in Sodium

Temperature (F)	Allowable Stress, ksi**	Wall Thickness (mils)	Decrease in Carbon Content (wt%)	Reduction of S_o (%)
900	10.9	95	.023	4
		109	.021	4
		120	.019	3
950	8.4	95	.044	10
		109	.039	9
		120	.036	8
975	7.2(est)	95	.059	15
		109	.053	14
		120	.049	13
1000	6.3	95	.078	23
		109	.070	21
		120	.065	19

* Assume .625 in OD

** From ASME Code Case 1592

Table 8.4 Design Methods Verification Testing-2¼Cr-1Mo Test Matrix

Temp., °F	Stress, Ksi	Product Form	Test Mode	Environment	No.	Data	Facility	Test Time
950°F	25	Pipe	Uniaxial Creep (84hr.), Stress peak to 45Ksi (1hr.) Environment Inside Air Outside	Sodium/Ti	2	Creep Rates; Effect of Interruption	SATEC Machines	1000hr. max.
				Argon	2			
	35			Sodium/Ti	2			
				Argon	2			
	45		Uniaxial Creep	Sodium/Ti	2	Creep Rates		
				Argon	2			
	25			Sodium/Ti	2			
				Argon	2			
	35			Sodium/Ti	2			
				Argon	2			
	35	Tube	Biaxial-Cyclic Presurization (+10Ksi) Environment Outside; Argon Inside	Sodium/Ti	1	Rupture Time (& Cycles)	Decarb Pot #2	1000hr. max.
				Argon	1			

Table 8.4 Test Matrix (Cont'd.)

Temp., °F	Stress, Ksi	Product Form	Test Mode	Environment	No.	Data	Facility	Test Time
950°F	40	Tube	Biaxial-Cyclic Presurization (+10Ksi) Environment Outside; Argon Inside	Sodium/Ti	3*	Rupture Time (& Cycles)	Decarb Pot #2	1000hr. max.
				Argon	3*			
	45			Sodium/Ti	3*			
				Argon	3*			
	35	Weld Metal		Sodium/Ti	1			
				Argon	1			
	40			Sodium/Ti	3*			
				Argon	3*			
	45			Sodium/Ti	3*			
				Argon	3*			
	35	Tube	Stress Rupture (Internal Pressurization) Environment Outside; Argon Inside	Sodium/Ti	1	Rupture Time		
				Argon	1			
	40			Sodium/Ti	3*			
				Argon	3*			

*One each, unexposed, ∿ 500 pre-exposed, and ∿ 1000hr. pre-exposed samples.

Table 8.4 Test Matrix (Cont'd.)

Temp., °F	Stress, Ksi	Product Form	Test Mode	Environment	No.	Data	Facility	Test Time
950°F	45	Tube	Stress Rupture (Internal Pressurization) Environment Outside; Argon Inside	Sodium/Ti	3*	Rupture Time	Decarb Pot #2	1000hr. max.
					3*			
	35	Weld Metal		Sodium/Ti	1			
				Argon	1			
	40			Sodium/Ti	3*			
				Argon	3*			
	45			Sodium/Ti	3*			
				Argon	3*			

*One each, unexposed, ∿ 500 pre-exposed, and ∿ 1000hr. pre-exposed samples.

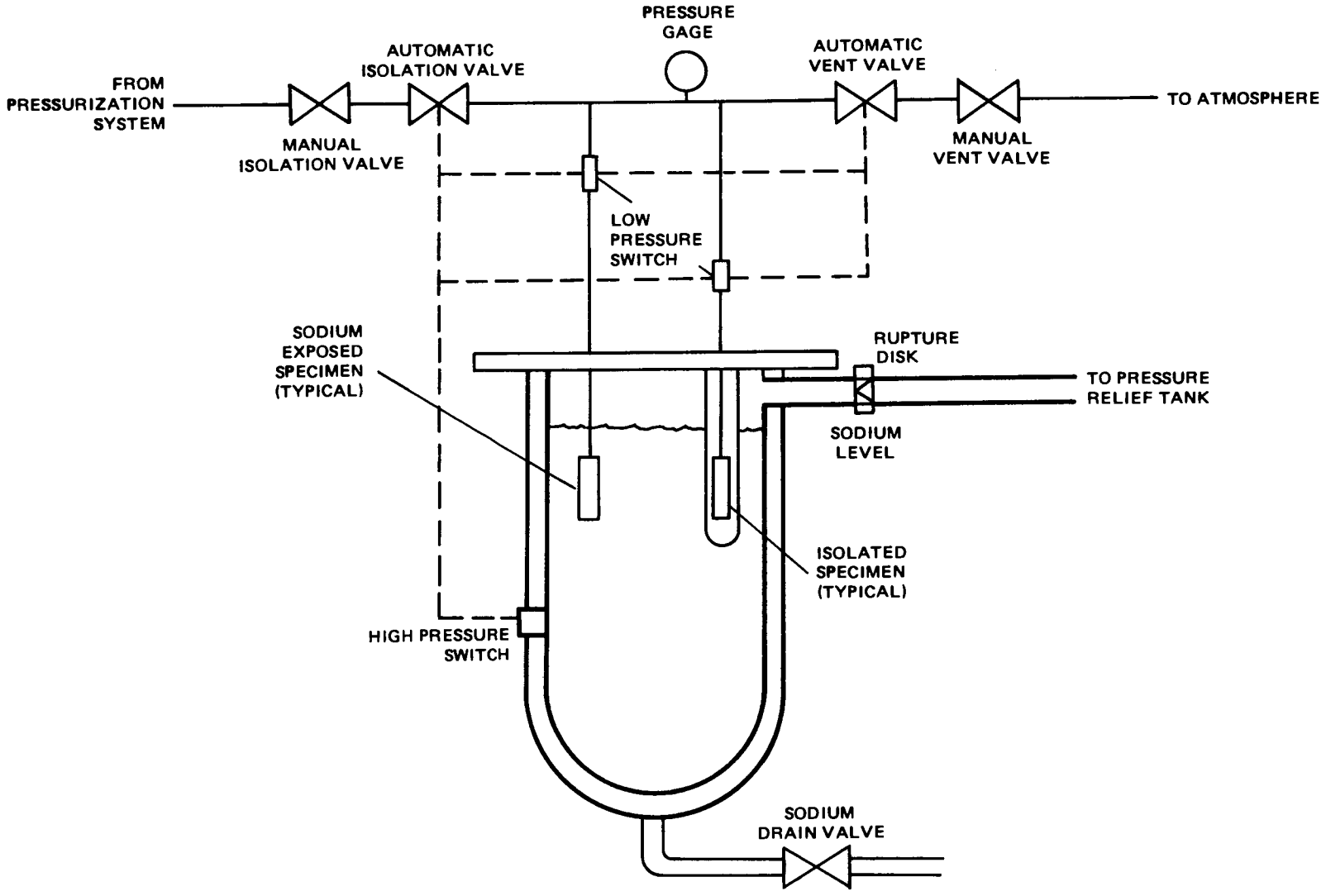

FIGURE 8.4 APPARATUS FOR BIAXIAL CREEP RUPTURE TESTS IN SODIUM

8.4 REFERENCES

1. "LMFBR Heat Exchanger Materials Development Program". Second Quarterly Report, Sept.-Nov. 1972, GEAP-13919-2, AEC Contract AT(04-3)-189 Proj. Agree. 60, December 1972.
2. R. B. Snyder, K. Natesan, and T. F. Kassner, "A Generalized Method of Computing Carbon-Diffusion Profiles in Austenitic Stainless Steels Exposed to a Sodium Environment", ANL-8015, AEC Contract W-31-109-Eng-38, June 1973.
3. J. L. Krankota, "Carburization of Stainless Steel Rupture Discs in SGTR," GE letter report, August 1, 1974.
4. M. C. Rowland and D. E. Plumlee, "Sodium Mass Transfer: XXII - Metallurgical Examination of the Test Loops," GEAP-4838, October 1965.
5. Summary Report - Sodium Mass Transfer Program: "Effects of Sodium Exposure on the Corrosion and Strength of Stainless Steel", GEAP-10394, August 1971.
6. D. W. Koch and P. J. Kovach, "Materials Examination of a Model Sodium Heated Steam Generator", BAW-1280-37, June 1966.
7. J. L. Krankota and J. S. Armijo, "Decarburization Kinetics of Low Alloy Ferritic Steels in Sodium", Met. Trans., September 1972.
8. W. E. Ray, Sodium Technology Program Progress Report, WARD-3045T1-7, January 1973.
9. D. F. Atkins, "The Mechanical Properties of Decarburized 2¼Cr-1Mo Steel", Atomics International Report TR-095-330-029, September 1971.
10. G. J. Licina and J. F. Copeland, "A Review of 2¼Cr-1Mo Steel for Steam Generator Applications in the Clinch River Breeder Reactor", GEAP-20589, October 1974.

INDEX

ORNL-5104
UC-79b, -h, -k
(Liquid Metal Fast
Breeder Reactors)

INTERNAL DISTRIBUTION

(3) Central Research Library
ORNL — Y-12 Technical Library
Document Reference Section
(10) Laboratory Records Department
Laboratory Records, ORNL RC
ORNL Patent Office
R. J. Beaver
M. Bender
R. G. Berggren
J. J. Blass
M. K. Booker
C. R. Brinkman
D. A. Canonico
J. Corum
W. R. Corwin
F. L. Culler
J. E. Cunningham
J. H. DeVan
D. P. Edmonds
G. Fee
M. H. Fontana
W. R. Gall
B. L. Greenstreet
J. C. Griess, Jr.
J. P. Hammond
W. O. Harms
R. L. Heestand
(5) M. R. Hill
D. O. Hobson
F. J. Homan
H. Inouye
P. R. Kasten
J. F. King
R. T. King
R. L. Klueh
K. C. Liu
C. T. Liu
A. L. Lotts
(3) W. R. Martin
W. J. McAfee
H. E. McCoy
H. C. McCurdy
C. J. McHargue
J. Merkle
(5) P. Patriarca
S. Peterson
H. Postma
C. E. Pugh
P. L. Rittenhouse
D. N. Robinson
T. Roche
J. L. Scott
Myrtleen Sheldon
V. K. Sikka
G. M. Slaughter
W. J. Stelzman
J. P. Strizak
R. W. Swindeman
D. B. Trauger
T. N. Washburn
J. R. Weir, Jr.
G. D. Whitman
T. Yahr
Walter Kohn (consultant)
W. C. Leslie (consultant)
John Moteff (consultant)
J. A. Pask (consultant)
J. W. Prados (consultant)
G. V. Smith (consultant)

EXTERNAL DISTRIBUTION

ERDA DIVISION OF REACTOR RESEARCH AND DEVELOPMENT, Washington, DC 20545

(2) Director

ERDA OAK RIDGE OPERATIONS OFFICE, P.O. Box E, Oak Ridge, TN 37830

Research and Technical Support Division
Director, Reactor Division

ERDA TECHNICAL INFORMATION CENTER, Office of Information Services, P.O. Box 62, Oak Ridge, TN 37830

(309) For distribution as shown in TID-4500 Distribution Category, UC-79b (Fuels and Materials Engineering Development); UC-79h (Structural Materials and Design Engineering); UC-79k (Components)

☆U. S. GOVERNMENT PRINTING OFFICE: 1974-748-189/173